

# **Numerical approximation of cardiac electro-fluid-mechanical models: coupling strategies for large-scale simulation**

THÈSE N° 8731 (2018)

PRÉSENTÉE LE 19 JUILLET 2018

À LA FACULTÉ DES SCIENCES DE BASE  
CHAIRE DE MODÉLISATION ET CALCUL SCIENTIFIQUE  
PROGRAMME DOCTORAL EN MATHÉMATIQUES

ÉCOLE POLYTECHNIQUE FÉDÉRALE DE LAUSANNE

POUR L'OBTENTION DU GRADE DE DOCTEUR ÈS SCIENCES

PAR

**Antonello GERBI**

acceptée sur proposition du jury:

Prof. J. Krieger, président du jury  
Prof. A. Quarteroni, Dr L. Dede', directeurs de thèse  
Prof. L. Pavarino, rapporteur  
Prof. R. Krause, rapporteur  
Prof. F. Nobile, rapporteur



ÉCOLE POLYTECHNIQUE  
FÉDÉRALE DE LAUSANNE

Suisse  
2018





Le cœur a ses raisons  
que la raison ne connaît point.

The heart has its reasons  
which reason does not know.

— Blaise Pascal



# Acknowledgements

Several people have played an important role in my PhD, and in particular in the writing of this thesis. These people will always have my deepest gratitude. In the following, I will try to thank them even if *this section is too small to contain* them all.

First of all, I wish to thank my advisor, Prof. Alfio Quarteroni, for giving me the chance to obtain my PhD in the Chair of Modeling and Scientific Computing (CMCS) at EPFL, and to work on such a fascinating and inspirational topic as cardiovascular modeling. I am also truly grateful to my co-advisor, Prof. Luca Dede', for being an irreplaceable point of reference during the PhD. Without any doubt, his knowledge and his patience have been fundamental for me during these years: I would not have been able to get past the darkest hours without his support.

I would also like to thank MER Simone Deparis and Prof. Andrea Manzoni for their help in several circumstances, and for the (sometimes much needed) discussions on non-scientific topics.

I am thankful to the members of the jury, Prof. Fabio Nobile, Prof. Luca Pavarino, and Prof. Rolf Krause, for having carefully read this manuscript and for providing useful comments and feedbacks, and to Prof. Joachim Krieger, who committed himself as president of the jury.

My family deserves a very special acknowledgement for the unconditional support I received during these years. I have always found revealing the fact that, in the Italian language, “to support” (supportare) and “to stand” (sopportare) share the same etymology. I consider myself lucky to have such wonderful parents which have been doing both things for me so well, even if quite often I was not as good as them in turn.

Doing a PhD, at times, feels like being at war: if I survived this experience, I definitely owe it to the “brothers in arms” which I had on my side during these years. More specifically, I must thank the following people. My PhD-soulmate Nico, with whom I shared three different offices, a fridge, and countless cigarette breaks. He has always been patient enough to listen to my many boring complaints and to give me precious advices in turn. Barte, for our side projects and our crypto-discussions. Ste, with whom I both cried and laughed about our academic lives' difficulties. Pego, for having considerably helped me improving my terrible aim.

Outside this inner circle, I wish to thank the many colleagues and people met in Lausanne

## Acknowledgements

---

which shared this experience with me in different ways. Davide, Fede, and Claudia for their help and knowledge, especially in the beginning of the PhD. Andrea, for giving me a roof on the head during the first days in Lausanne. Cate, for the blessing of a real moka coffee at work. Giacomo, for the many discussions ranging from politics to tv series. Paolo for his sarcasm and Robert for his not-so-teutonic humor. Ana, for being a true thesis mate, making me feel less lonely during the last part of the PhD. Isa and Giorgia for sharing the body pain the days after *condition physique*. Ruy for being the nicest landlord possible. My last flatmate Jakob and his team from ECAL for throwing unexpected house parties at our place.

Last, but not least, I am deeply grateful to the “Su la testa!” association in Milan and to the dozens (if not hundreds) of wonderful people working, volunteering, and participating over there. It has been a second family to me since I was a teenager and, even at a distance, it kept alive several important sides of myself during the PhD. It would be way too long to list everybody, but I feel I have to mention at least the *Selfiests* group, and in particular the other two musketeers and D’artagnan.

This work is dedicated to all of you.

*Lausanne, June 2018*

A. G.

# Abstract

The mathematical modeling of the heart involves several challenges, which are intrinsically related to the complexity of its function. A satisfactory cardiac model must be able to describe a wide range of different processes, such as the evolution of the transmembrane potential in the myocardium, the deformation caused by the muscles contraction, and the dynamics of the blood inside the heart chambers. In this work, we focus on the coupling of the electrophysiology, the active and the passive mechanics, and the fluid dynamics of the blood in the left ventricle (LV) of the human heart. The models describing the previously mentioned processes are called “single core models”, and can be regarded as the building blocks of an “integrated model”.

In this thesis, we first review the isolated single core mathematical models for the description of the LV function, and discuss their space and time discretizations with particular emphasis on the coupling conditions. We consider both implicit and semi-implicit schemes for the time discretization. The fully discretized single core problems thus obtained are then combined to define integrated electromechanics and electrofluidmechanics problems. We then focus on the numerical coupling strategy for the electromechanics solver in the framework of the active strain formulation. First, we propose a monolithic strategy where the discretized core models are solved simultaneously; then, several novel segregated strategies, where the discretized core models are solved sequentially, are proposed and systematically compared with each other. The segregated strategies are obtained by exploiting a Godunov splitting scheme, which introduces a first order error on the solution. We show that, while the monolithic approach is more accurate and more stable for relatively large timesteps, segregated approaches allow to solve the integrated problem much more efficiently in terms of computational resources. Moreover, with segregated approaches, it is possible to use different timesteps for the different core models in a staggered fashion, thus further improving the computational efficiency of the schemes.

The monolithic and the segregated strategies for the electromechanics are used to solve a benchmark problem with idealized geometry: the results are then compared in terms of accuracy and efficiency. We numerically confirm that the segregated strategies are accurate at least of order one. In light of the results obtained, we employ the proposed strategies to simulate the electromechanics of a subject-specific LV for a full heartbeat. We simulate both healthy and pathological scenarios: in the latter case, we account for an ischemic necrosis of the tissue and analyze several clinical indicators such as

## Acknowledgements

---

pressure-volume loops and the end systolic pressure-volume relationship. Finally, we use the proposed strategies to simulate the electrofluidmechanics of a realistic LV during the systolic phase of the heartbeat.

When defining the integrated cardiac models, we establish a preprocess pipeline aimed at preparing geometries and data for both idealized and subject-specific simulations. The pipeline is successfully used for the setting up of large scale simulations in a high performance computing framework, where the (strong and weak) scalability of the proposed coupling strategies is assessed.

*Keywords:* heart modelling; coupled problem; electromechanics model; electromechano-fluid model; monolithic scheme; segregated scheme; staggered scheme; finite element method; patient-specific simulations.

# Résumé

La modélisation mathématique du coeur soulève plusieurs défis, intrinsèquement liés à la complexité de ses fonctions. Un modèle cardiaque satisfaisant doit être capable de décrire une large gamme de processus différents, comme l'évolution du potentiel transmembranaire dans le myocarde, la déformation causée par la contraction des muscles, et la dynamique du sang à l'intérieur des cavités cardiaques. Dans ce travail, nous nous concentrons sur le couplage entre l'électrophysiologie, les mécaniques actives et passives, et la dynamique des fluides du sang dans le ventricule gauche (LV) du coeur humain. Les modèles décrivant les processus précédemment mentionnés sont appelés "modèles noyau" et peuvent être vus comme les blocs de construction d'un "modèle intégré".

Dans cette thèse, nous revoyons tout d'abord les modèles mathématiques noyau isolé pour la description des fonctions du LV, and nous discutons leurs discrétisations spatiales et temporelles avec une accentuation sur les conditions de couplage. Nous considérons à la fois des schémas implicites et explicites pour la discrétisation temporelle. Les problèmes noyau entièrement discrétisés ainsi obtenus sont ensuite combinés pour définir des problèmes d'électromécanique et d'électrofluidomécanique intégrés. Nous nous concentrons ensuite sur la stratégie de couplage numérique pour les solveurs électromécaniques dans le cadre de la formulation de la souche active. Tout d'abord, nous proposons une stratégie monolithique où les modèles noyau discrétisés sont résolus simultanément ; ensuite, plusieurs nouvelles stratégies séparé, où les modèles noyau discrétisés sont résolus séquentiellement, sont comparées les unes aux autres. Les stratégies séparé sont obtenues en exploitant un schéma de fragmentation de Godunov, qui introduit une erreur de premier ordre sur la solution. Nous montrons que, tandis que l'approche monolithique est plus précise et plus stable pour des pas de temps relativement grands, les approches segregated permettent de résoudre le problème intégré bien plus efficacement en termes de ressources computationnelles. De plus, avec les approches séparé, il est possible d'utiliser différents pas de temps pour les différents modèles noyau d'une manière échelonnée. Cela améliore encore l'efficacité computationnelle des schémas numériques.

Les stratégies monolithique et séparé pour l'électromécanique sont utilisées pour résoudre des problèmes de référence avec des géométries idéalisées : les résultats sont ensuite comparés en termes de précision et d'efficacité. Nous confirmons numériquement que les stratégies séparé ont une précision d'ordre au moins un. À la lumière des résultats obtenus, nous utilisons les stratégies proposées pour simuler l'électromécanique d'un LV

## Acknowledgements

---

spécifique à un patient pendant toute la durée d'un battement de coeur. Nous simulons à la fois les scénarios sains et pathologiques : dans le deuxième cas, nous considérons une nécrose ischémique du tissu et nous analysons plusieurs indicateurs cliniques tels que les boucles pression-volume et la relation pression-volume systolique. Finalement, nous utilisons les stratégies proposées pour simuler l'électrofluidomécanique d'un LV réaliste pendant la phase systolique d'un battement de coeur.

Lorsque nous définissons les modèles cardiaques intégrés, nous déterminons une pipeline de pré-traitement ayant pour but de préparer les géométries et les données, à la fois pour les simulations idéalisées et pour les simulations spécifiques à un patient. La pipeline est utilisée avec succès pour la mise en place de simulations à grande échelle dans le cadre de calcul de haute performance, où l'évolutivité (faible et forte) des stratégies de couplage proposées est évaluée.

*Mots clés:* modélisation du coeur; problème de couplage; modèle électromécanique; modèle électrofluidomécanique; schéma monolithique; schéma séparé; schéma échelonnée; méthode des éléments finis; simulations spécifiques aux patients.



# Contents

|  |            |
|--|------------|
| <b>Acknowledgements</b>                                    | <b>v</b>   |
| <b>Abstract (English/Français)</b>                         | <b>vii</b> |
| <b>Contents</b>  | <b>xi</b>  |
| <b>List of Figures</b>                                     | <b>xv</b>  |
| <b>List of Tables</b>                                      | <b>xxi</b> |
| <b>Introduction</b>  | <b>1</b>   |
| <br>   |            |
| <b>I Mathematical and numerical modeling</b>               | <b>7</b>   |
| <br>   |            |
| <b>1 Mathematical models for the human heart</b>           | <b>9</b>   |
| 1.1 Heart function . . . . .                               | 9          |
| 1.2 Electrophysiology models . . . . .                     | 10         |
| 1.2.1 Ionic models for single cells . . . . .              | 11         |
| 1.2.2 Bidomain and monodomain models . . . . .             | 14         |
| 1.3 Myocardium mechanical models . . . . .                 | 19         |
| 1.3.1 Passive mechanics . . . . .                          | 20         |
| 1.3.2 Active mechanics . . . . .                           | 25         |
| 1.3.3 Mechanical activation . . . . .                      | 29         |
| 1.4 Blood flow modeling . . . . .                          | 31         |
| 1.4.1 Blood dynamics: 3D model . . . . .                   | 32         |
| 1.4.2 Endocardial pressure: 0D model . . . . .             | 35         |
| <br>   |            |
| <b>2 Numerical approximation</b>                           | <b>39</b>  |
| 2.1 Space discretization . . . . .                         | 39         |
| 2.1.1 Ionic model . . . . .                                | 41         |
| 2.1.2 Bidomain and monodomain equations . . . . .          | 43         |
| 2.1.3 Mechanical activation . . . . .                      | 45         |
| 2.1.4 Passive and active mechanics . . . . .               | 45         |
| 2.1.5 Fluid geometry and Navier-Stokes equations . . . . . | 46         |

|            |   |            |
|------------|---|------------|
| 2.2        | Time discretization . . . . .   | 48         |
| 2.2.1      | Implicit and semi-implicit schemes . . . . .  | 50         |
| 2.2.2      | Discretization of the 0D fluid model . . . . .  | 58         |
| <b>3</b>   | <b>Preprocessing</b>  | <b>59</b>  |
| 3.1        | Mesh generation . . . . .   | 59         |
| 3.1.1      | Idealized geometry . . . . .  | 60         |
| 3.1.2      | Image processing and segmentation . . . . .   | 62         |
| 3.1.3      | Cardiac atlas . . . . .   | 64         |
| 3.2        | Fibers and sheets distribution . . . . .  | 65         |
| 3.3        | Prestress . . . . .   | 69         |
| 3.4        | A critical discussion on the preprocess pipeline . . . . .  | 71         |
| <b>II</b>  | <b>Electromechanics</b>   | <b>75</b>  |
| <b>4</b>   | <b>Algorithms for the EM of the LV</b>  | <b>77</b>  |
| 4.1        | Fully monolithic strategy $(\mathcal{I}_I \mathcal{E}_I \mathcal{A}_I \mathcal{M}_I)$ . . . . .                             | 77         |
| 4.1.1      | Preconditioning the monolithic problem . . . . .  | 79         |
| 4.2        | Segregated schemes . . . . .  | 80         |
| 4.2.1      | Partially segregated strategy $(\mathcal{I}_I \mathcal{E}_I \mathcal{A}_I) - (\mathcal{M}_I)$ . . . . .                     | 82         |
| 4.2.2      | Partially segregated strategy $(\mathcal{I}_{SI} \mathcal{E}_{SI} \mathcal{A}_{SI}) - (\mathcal{M}_I)$ . . . . .            | 84         |
| 4.2.3      | Fully segregated strategy $(\mathcal{I}_{SI}) - (\mathcal{E}_{SI}) - (\mathcal{A}_{SI}) - (\mathcal{M}_I)$ . . . . .        | 85         |
| <b>5</b>   | <b>Numerical simulations</b>  | <b>87</b>  |
| 5.1        | Free contraction benchmark . . . . .  | 87         |
| 5.1.1      | Convergence with respect to time discretization . . . . .   | 91         |
| 5.1.2      | Scalability test and $h$ -refinement . . . . .  | 105        |
| 5.2        | Subject-specific LV: the full heartbeat . . . . .   | 110        |
| 5.3        | Application to a pathological scenario: LV with ischemic necrosis . . . . .   | 115        |
| <b>III</b> | <b>Electrofluidmechanics</b>  | <b>123</b> |
| <b>6</b>   | <b>Algorithms for the EFM of the LV</b>   | <b>125</b> |
| 6.1        | The FSI problem . . . . .   | 125        |
| 6.2        | Fully monolithic strategy $(\mathcal{I}_I \mathcal{E}_I \mathcal{A}_I \mathcal{M}_I \mathcal{G}_I \mathcal{F}_I)$ . . . . . | 127        |
| 6.2.1      | Preconditioning the monolithic problem . . . . .  | 129        |
| 6.3        | Segregated strategies . . . . .   | 130        |
| <b>7</b>   | <b>Numerical simulations</b>  | <b>133</b> |
| 7.1        | Realistic LV: systolic phase . . . . .  | 134        |
| 7.2        | Comparison of computational costs . . . . .   | 140        |

|  |            |
|--|------------|
| <b>Conclusions</b>                                 | <b>145</b> |
| <b>A Matrix calculus</b>                           | <b>149</b> |
| <b>B Models</b>                                    | <b>151</b> |
| B.1 Ionic model and ionic currents terms . . . . . | 151        |
| B.2 Monodomain and bidomain . . . . .              | 153        |
| B.3 Mechanical activation . . . . .                | 154        |
| B.4 Mechanics . . . . .                            | 155        |
| <b>Bibliography</b>                                | <b>159</b> |
| <b>Curriculum Vitae</b>                            | <b>183</b> |



# List of Figures

|     |   |    |
|-----|---|----|
| 1.1 | Anterior view of a frontal section of the heart. . . . .  | 10 |
| 1.2 | Ion channels in a cardiac cell. In the figure, $K^+$ , $Na^+$ , and $Ca^{2+}$ are channels allowing the corresponding ion to cross the membrane, while $Na^+/Ca^{2+}$ is an exchanger which transports three $Na^+$ ions for each $Ca^{2+}$ ion. Image taken from [Marbán, 2002]. . . . .   | 11 |
| 1.3 | Evolution of the transmembrane electric potential in a cardiac cell, stimulated with an external electric current. The figure highlights the following phases: 1) the <i>resting</i> phase, when the potential remains at its rest value of approximately $v = -90$ mV until the cell is stimulated; 2) the <i>depolarization</i> phase, when the cascade effect of electrochemical reactions drives the opening of the ionic channels on the membrane, ultimately causing a spike in the potential which switches sign; 3) the <i>short repolarization</i> phase, when the potential shortly decreases immediately after the spike; 4) the <i>plateau</i> phase, when the net flux of electric charge due to the ions flowing inward/outward with respect to the cell membrane is zero; 5) the <i>repolarization</i> phase, when the channels, the ionic concentrations and the potential slowly return to the rest configuration. . . . . | 13 |
| 1.4 | Myocardial tissue at the microscale, showing the disposition of the fibers in the muscle. Image taken from [Akhgari et al., 2017]. . . . .  | 14 |
| 1.5 | Representation of a membrane channel activated by the membrane tension due to the deformation of the muscle. The open channel allows the ions to flow inward/outward resulting in a SAC. . . . .  | 17 |
| 1.6 | a) An ideal left ventricle muscle. b) A cardiac tissue block showing the fibers' orientation through its thickness. c) Fiber orientation projected on different slides. Image from [Holzapfel and Ogden, 2009]. . . . .   | 19 |
| 1.7 | Isovolumic strain energy of the form $\mathcal{W}_{vol}(J) = \frac{B}{2}(J - 1) \log(J)$ , represented as a function of $J$ . $\mathcal{W}_{vol}$ is nonnegative, convex, and it attains its global minimum in $J = 1$ . . . . .  | 21 |
| 1.8 | A simplified representation of the boundaries of the LV. These are the endocardium (blue), the epicardium (red) and the base (green). The pericardium (grey) contains the whole heart, and covers part of the LV epicardium in the figure. . . . .  | 23 |
| 1.9 | The two ventricles in relaxed (left) and contracted (right) configurations. . . . .   | 26 |

## List of Figures

---

|      |  |    |
|------|--|----|
| 1.10 | The active strain decomposition of the strain tensor $\mathbf{F}$ . . . . .  | 27 |
| 1.11 | Sagittal (top row) and axial (bottom row) views of the LV at three different moments of the heartbeat. The thickness of the LV walls increases significantly during the systolic phase. . . . .  | 28 |
| 1.12 | Crossbridge dynamics determining the cardiomyocytes contraction: an active site on actin is exposed as $Ca^{2+}$ binds troponin (top left); the myosin head forms a crossbridge bond with actin (top right); the myosin head bends releasing ADP and phosphate (bottom). . . . .   | 30 |
| 1.13 | Circulation of the blood in the heart. For what regards the left side of the heart, the oxygenated blood coming from the lungs flows from the LA to the LV in the diastolic phase (with the aortic valve closed), and from the LV into the aorta in the systolic phase (with the mitral valve closed). . . .   | 32 |
| 1.14 | The aortic and mitral valves (left side of the heart), and the pulmonary and tricuspid valves (right side of the heart). . . . .   | 35 |
| 1.15 | The Wiggers diagram [Katz, 2010] of the left heart depicting the aortic, ventricular, and atrial pressures and the ventricular volume, as well as the four phases of the cardiac cycle. . . . .  | 36 |
| 2.1  | Meshes of the $\Omega_0^s$ and the $\Omega_0^f$ domains. The interface $\Gamma_0^{endo}$ between the two is highlighted. . . . .   | 40 |
| 3.1  | Prolate ellipsoid geometries for two distinct sets of parameters, representing a canine LV (left) as in [Guccione et al., 1995], and a human LV (right) as in [Wang et al., 2013]. . . . .   | 61 |
| 3.2  | An overview of the 3D MRI images along three orthogonal slices, as given by the 3D Slicer software. The pulmonary artery is clearly visible in the central slice, while the LV with the sinus of Valsalva and the aorta can be seen in the right slice. . . . .  | 62 |
| 3.3  | The segmented LV after several smoothing steps, overlayed on three slices of a subset of the MRI shown in Figure 3.2. . . . .  | 63 |
| 3.4  | The full-heart cardiac atlas colored by the first four modes obtained from the PCA analysis of the shape of the cardiac components of multiple subjects [Hoogendoorn et al., 2013]. From this perspective, the LV is located at the bottom right corner of each image. . . . .   | 64 |
| 3.5  | Fibers field (top left) generated for the subject-specific mesh, and the mesh boundaries (top right), together with a close-up of a transmural slice of the myocardium with fibers, sheets and normals (bottom). Angles $\alpha_{endo}$ and $\alpha_{epi}$ are highlighted at the endocardium and epicardium, respectively. . . . .  | 65 |
| 3.6  | Stages of the fibers generation rule algorithm, for the subject specific geometry. In the top row, we show the scalar potential $\Phi$ (top left), its gradient $\nabla_0 \Phi$ before normalization (top), and the centerline direction $\mathbf{k}_c^\parallel$ (top right). In the second row, the field $\mathbf{k}_{s_0}^\perp$ (bottom left), the unrotated fiber field $\tilde{\mathbf{f}}_0$ (bottom), and the final result $\mathbf{f}_0$ (bottom right). . . . . | 66 |

|      |  |    |
|------|--|----|
| 3.7  | Mesh of the idealized prolate LV geometry (top left), together with the fibers (top) and the sheets (top right) fields. The finer meshes (b) and (c) are obtained by hierarchical refinement of the coarsest mesh (a). . . . .   | 67 |
| 3.8  | Mesh of the patient-specific geometry (left), together with the fibers (center) and the sheets (right) fields. . . . .   | 68 |
| 3.9  | Meshes of the cardiac atlas myocardium and blood geometries (left), together with the fibers (center) and the sheets (right) fields. . . . .   | 69 |
| 3.10 | The preprocess pipeline aiming at collecting the data required for the simulations. From the top left corner, counter-clockwise: the generation of the mesh, preceded by the segmentation of medical images in case of subject-specific geometries, produces the myocardium mesh file (and the blood one in the electrofluidmechanics case); the fibers and the sheets fields are defined in the nodes (depending on the FEM polynomial order $r$ ) of the myocardium mesh; the mesh and the fields are used to generate the prestress and the initial displacement. . . . . | 72 |
| 4.1  | Graphical representation of the time advancement for the $(\mathcal{I}_I \mathcal{E}_I \mathcal{A}_I) - (\mathcal{M}_I)$ and the $(\mathcal{I}_{SI} \mathcal{E}_{SI} \mathcal{A}_{SI}) - (\mathcal{M}_I)$ schemes. . . . .   | 83 |
| 4.2  | Graphical representation of the time advancement for the $(\mathcal{I}_{SI}) - (\mathcal{E}_{SI}) - (\mathcal{A}_{SI}) - (\mathcal{M}_I)$ scheme. . . . .  | 85 |
| 5.1  | Transmembrane potential $v$ at times $T = 2.4$ ms (first row), $T = 4.8$ ms (second row), $T = 7.2$ ms (third row), and AT (fourth row) obtained with the $(\mathcal{I}_I \mathcal{E}_I \mathcal{A}_I \mathcal{M}_I)$ strategy and timesteps $\tau = 8 \times 10^{-5}$ s (left), $\tau = 16 \times 10^{-5}$ s (center), and $\tau = 24 \times 10^{-5}$ s (right). . . . .  | 88 |
| 5.2  | Evolution of the transmembrane potential $v$ (left y-axis), the fibers shortening $\gamma_f$ , and the ionic variables $w_1$ , $w_2$ , $w_3$ (right y-axis) in a point located on the apex, during the free contraction benchmark. . . . .   | 89 |
| 5.3  | Deformed myocardium at six different times during the free contraction benchmark, coloured by the displacement magnitude $\ \mathbf{d}_{s,h}\ _2$ and compared with the reference domain $\Omega_0^s$ . . . . .  | 90 |
| 5.4  | Errors in $L^2(\Omega_0^s)$ (left) and $L^\infty(\Omega_0^s)$ (right) norms of the potentials $\hat{v}_h^\tau$ (top) and of the displacements $\hat{\mathbf{d}}_{s,h}^\tau$ (bottom) obtained using $(\mathcal{I}_I \mathcal{E}_I \mathcal{A}_I \mathcal{M}_I)$ with timestep $\tau$ , at times $T = 24$ ms (blue), $T = 48$ ms (green) and $T = 96$ ms (red) in logarithmic scale. The errors for both BDF1 (dashed lines) and BDF2 (solid lines) are reported, together with linear and quadratic reference slopes. . . . .  | 91 |
| 5.5  | Evolution of the transmembrane potential $v_h^\tau$ in the apex obtained using $(\mathcal{I}_I \mathcal{E}_I \mathcal{A}_I) - (\mathcal{M}_I)$ (top) and $(\mathcal{I}_{SI} \mathcal{E}_{SI} \mathcal{A}_{SI}) - (\mathcal{M}_I)$ (bottom) for different $\tau$ and $N_{sub} = 1$ (and hence $\Delta t = \tau$ ). The close-ups highlight the instant in which the depolarization wave reaches the apex. . . . .   | 92 |

|      |   |     |
|------|---|-----|
| 5.6  | Evolution of the fibers shortening $\gamma_h^\tau$ in the apex obtained using $(\mathcal{I}_I \mathcal{E}_I \mathcal{A}_I) - (\mathcal{M}_I)$ (top) and $(\mathcal{I}_{SI} \mathcal{E}_{SI} \mathcal{A}_{SI}) - (\mathcal{M}_I)$ (bottom) for different $\tau$ and $N_{sub} = 1$ (and hence $\Delta t = \tau$ ). The close-ups highlight the instant in which the calcium concentration reaches the threshold and $\gamma_h^\tau$ starts to decrease.   | 93  |
| 5.7  | Evolution of the displacement in the Z direction $\mathbf{d}_{s,h}^\tau \cdot \mathbf{e}_3$ in the apex obtained using $(\mathcal{I}_I \mathcal{E}_I \mathcal{A}_I) - (\mathcal{M}_I)$ (top) and $(\mathcal{I}_{SI} \mathcal{E}_{SI} \mathcal{A}_{SI}) - (\mathcal{M}_I)$ (bottom) for different $\tau$ and $N_{sub} = 1$ (and hence $\Delta t = \tau$ ). The close-ups highlight the instant in which the apex starts moving.  | 94  |
| 5.8  | Evolution of the displacement in the Z direction $\mathbf{d}_{s,h}^\tau \cdot \mathbf{e}_3$ in the apex obtained using $(\mathcal{I}_I \mathcal{E}_I \mathcal{A}_I) - (\mathcal{M}_I)$ (top) and $(\mathcal{I}_{SI} \mathcal{E}_{SI} \mathcal{A}_{SI}) - (\mathcal{M}_I)$ (bottom) for different $N_{sub}$ and $\tau = \hat{\tau}$ (and hence $\Delta t = N_{sub} \hat{\tau}$ ). The close-ups highlight the instant in which the apex starts moving.   | 95  |
| 5.9  | Errors in $L^2(\Omega_0)$ (left) and $L^\infty(\Omega_0)$ (right) norms of the potentials $v_h^\tau$ (top) and of the displacements $\mathbf{d}_{s,h}^\tau$ (bottom) at times $T = 24$ ms (blue), $T = 48$ ms (green) and $T = 96$ ms (red) obtained by solving the problem with $(\mathcal{I}_I \mathcal{E}_I \mathcal{A}_I) - (\mathcal{M}_I)$ and timestep $\tau$ , in logarithmic scale against $N_{sub}$ .   | 96  |
| 5.10 | Errors in $L^2(\Omega_0^s)$ (left) and $L^\infty(\Omega_0^s)$ (right) norms of the potentials $v_h^\tau$ (top) and of the displacements $\mathbf{d}_{s,h}^\tau$ (bottom) obtained using $(\mathcal{I}_I \mathcal{E}_I \mathcal{A}_I) - (\mathcal{M}_I)$ with timestep $\tau$ and $N_{sub} = 1$ , at times $T = 24, 48, 96$ ms in logarithmic scale.   | 97  |
| 5.11 | Errors in $L^2(\Omega_0^s)$ (left) and $L^\infty(\Omega_0^s)$ (right) norms of the potentials $v_h^\tau$ (top) and of the displacements $\mathbf{d}_{s,h}^\tau$ (bottom) obtained using $(\mathcal{I}_I \mathcal{E}_I \mathcal{A}_I) - (\mathcal{M}_I)$ with timestep $\tau$ and $N_{sub} = 1, 2, 4, 8, 16$ , at time $T = 96$ ms in logarithmic scale.   | 98  |
| 5.12 | Errors in $L^2(\Omega_0^s)$ (left) and $L^\infty(\Omega_0^s)$ (right) norms of the potentials $v_h^\tau$ and of the displacements $\mathbf{d}_{s,h}^\tau$ obtained using $(\mathcal{I}_{SI} \mathcal{E}_{SI} \mathcal{A}_{SI}) - (\mathcal{M}_I)$ (first and third rows) and $(\mathcal{I}_{SI}) - (\mathcal{E}_{SI}) - (\mathcal{A}_{SI}) - (\mathcal{M}_I)$ (second and fourth rows) with timestep $\tau$ and $N_{sub} = 1$ , at times $T = 24, 48, 96$ ms in logarithmic scale.  | 99  |
| 5.13 | Errors in $L^2(\Omega_0^s)$ (left) and $L^\infty(\Omega_0^s)$ (right) norms of the potentials $v_h^\tau$ (top) and of the displacements $\mathbf{d}_{s,h}^\tau$ (bottom) obtained using $(\mathcal{I}_{SI} \mathcal{E}_{SI} \mathcal{A}_{SI}) - (\mathcal{M}_I)$ (first and third rows) and $(\mathcal{I}_{SI}) - (\mathcal{E}_{SI}) - (\mathcal{A}_{SI}) - (\mathcal{M}_I)$ (second and fourth rows) with timestep $\tau$ and $N_{sub} = 1, 2, 4, 8, 16$ , at time $T = 96$ ms in logarithmic scale.   | 100 |
| 5.14 | Errors in $L^2(\Omega_0^s)$ (left) and $L^\infty(\Omega_0^s)$ (right) norms of the displacements $\mathbf{d}_{s,h}^\tau$ obtained using $(\mathcal{I}_I \mathcal{E}_I \mathcal{A}_I) - (\mathcal{M}_I)$ (first row), $(\mathcal{I}_{SI} \mathcal{E}_{SI} \mathcal{A}_{SI}) - (\mathcal{M}_I)$ (second row), and $(\mathcal{I}_{SI}) - (\mathcal{E}_{SI}) - (\mathcal{A}_{SI}) - (\mathcal{M}_I)$ (third row) with fixed mechanics timestep $\Delta t = N_{sub} \tau$ at time $T = 96$ ms, in logarithmic scale against $N_{sub}$ .  | 101 |
| 5.15 | Errors in $L^2(\Omega_0^s)$ norm of the displacements $\mathbf{d}_{s,h}^\tau$ obtained with $(\mathcal{I}_I \mathcal{E}_I \mathcal{A}_I) - (\mathcal{M}_I)$ (left), $(\mathcal{I}_{SI} \mathcal{E}_{SI} \mathcal{A}_{SI}) - (\mathcal{M}_I)$ (center) and $(\mathcal{I}_{SI}) - (\mathcal{E}_{SI}) - (\mathcal{A}_{SI}) - (\mathcal{M}_I)$ (right) at time $T = 96$ ms, for every $\tau$ and $N_{sub}$ considered, in logarithmic scale against the wall time. The errors obtained with $(\mathcal{I}_I \mathcal{E}_I \mathcal{A}_I \mathcal{M}_I)$ are also reported in each figure. | 104 |



|      |   |     |
|------|---|-----|
| 5.16 | Strong scalability for $(\mathcal{I}_I \mathcal{E}_I \mathcal{A}_I \mathcal{M}_I)$ : the average number of Newton iterations $\bar{N}^N$ (top left) and GMRES iterations $\bar{N}^G$ (top right), the average time spent for the assembly and application of the preconditioner $\bar{T}^P$ (bottom left), and the total wall time $T^W$ (bottom right). The total number of DoFs amounts to 37'038'536. . . . .  | 106 |
| 5.17 | Strong scalability for $(\mathcal{I}_{SI})-(\mathcal{E}_{SI})-(\mathcal{A}_{SI})-(\mathcal{M}_I)$ : the total wall time $T^W$ (top left), the average number of Newton iterations $\bar{N}^N$ (top) and GMRES iterations $\bar{N}^G$ (top right), the average assembly time for the preconditioner $\bar{T}^P$ (bottom left) and the Jacobian matrix (bottom), and the GMRES average time $\bar{T}^G$ for the solution of the mechanics problem (bottom right). . . . . | 107 |
| 5.18 | Weak scalability for $(\mathcal{I}_{SI})-(\mathcal{E}_{SI})-(\mathcal{A}_{SI})-(\mathcal{M}_I)$ : the total wall time $T^W$ (top left), the average number of Newton iterations $\bar{N}^N$ (top) and GMRES iterations $\bar{N}^G$ (top right), the average assembly time for the preconditioner $\bar{T}^P$ (bottom left) and the Jacobian matrix (bottom), and the GMRES average time $\bar{T}^G$ for the solution of the mechanics problem (bottom right). . . . .   | 108 |
| 5.19 | Transmembrane potential and displacement magnitude obtained by using the five idealized meshes. . . . .   | 109 |
| 5.20 | Transmembrane potential at different times (top row) and activation time (bottom row) for the subject-specific simulation. . . . .  | 111 |
| 5.21 | Deformed subject-specific geometry and displacement field at different times, compared with the reference domain $\Omega_0$ , for the full heartbeat simulation. . . . .  | 112 |
| 5.22 | Stress components $\sigma_{ss}$ (left) and $\sigma_{ff}$ (right) depicted on three slices of the deformed domain at different times. . . . .  | 113 |
| 5.23 | LV internal volumes (top left) and endocardial pressures (bottom left) versus time, with pV loops (right) for the subject-specific simulations with all the strategies considered (the parameter $N_{sub}$ used is indicated in legend with a subscript). . . . .   | 114 |
| 5.24 | Transmembrane potential at times $T = 150, 200, 250$ ms for the small (top row), medium (middle row), and large (bottom row) necrotic regions for the simulations using the monodomain equation. . . . .  | 116 |
| 5.25 | AT for the simulations with the small (left), medium (center), and large (right) necrotic regions. The results obtained by using the bidomain equations (top row) and the monodomain equation (bottom row) are both reported. . . . .   | 117 |
| 5.26 | Fibers shortening at times $T = 150, 200, 250$ ms for the small (top row), medium (middle row), and large (bottom row) necrotic regions. . . . .  | 118 |
| 5.27 | Deformed subject-specific geometry and displacement field at times $T = 150, 200, 250$ ms for the small (top row), medium (middle row), and large (bottom row) necrotic regions. . . . .  | 119 |
| 5.28 | Stress component $\sigma_{ff}$ at times $T = 150, 200, 250$ ms for the small (top row), medium (middle row), and large (bottom row) necrotic regions. . . . .   | 120 |

## List of Figures

---

|      |  |     |
|------|--|-----|
| 5.29 | LV internal volumes (top left) and endocardial pressures (bottom left) versus time, with pV loops (right) for the . . . . .  | 121 |
| 5.30 | The pV loops and the ESPVR for the healthy and the three pathological cases. . . . .   | 122 |
| 6.1  | The boundaries $\Gamma_{t,D}^f$ and $\Gamma_{t,N}^f$ on which we impose the essential (“Dirichlet”) condition for the continuity of the domain and the fluid velocities, and the natural (“Neumann”) condition. . . . .  | 126 |
| 7.1  | Transmembrane potential (top row) at three different times and activation time (bottom row) from different viewpoints. . . . .   | 135 |
| 7.2  | Fibers shortening (left) and displacement magnitude of the deformed myocardium (center) and blood (right) domains. . . . .   | 136 |
| 7.3  | The fluid subregion considered to calculate the ventricular volume and the averaged pressure, obtained by clipping the fluid domain in correspondance of the myocardium base. . . . .  | 137 |
| 7.4  | The volume (top left) and the averaged pressure (bottom left) in the same subregion over time and the partial pV loop (right). . . . .   | 137 |
| 7.5  | Blood velocity magnitude (left) and pressure field with fixed (center) and variable (right) scales on a slice of the fluid domain. . . . .   | 138 |
| 7.6  | Streamlines (top row) and velocity vector field (bottom row) on the blood deformed domain, at three different times. . . . .   | 139 |
| 7.7  | Strong scalability for $(\mathcal{I}_1\mathcal{E}_1\mathcal{A}_1\mathcal{M}_1\mathcal{G}_1\mathcal{F}_1)$ : the total wall time $T^W$ (top left), the average number of Newton iterations $\bar{N}^N$ (top right), the average assembly time for the preconditioner $\bar{T}^P$ (bottom left), and the average GMRES solution time $\bar{T}^G$ (bottom right). . . . . | 142 |

# List of Tables

|     |   |     |
|-----|---|-----|
| 2.1 | List of finite element functions and vectors, grouped by model. The domain in which the functions are defined is also indicated. . . . .  | 42  |
| 3.1 | List of meshes used in this thesis, with their number of vertices, tetrahedra, and average edge length. . . . .   | 73  |
| 5.1 | The average number of Newton ( $\bar{N}^N$ ) and GMRES ( $\bar{N}^G$ ) iterations for the solution of the monolithic problem $(\mathcal{I}_I\mathcal{E}_I\mathcal{A}_I\mathcal{M}_I)$ , and the total wall time ( $T^W$ , in minutes) for the benchmark simulations, for each $\tau (= \Delta t)$ considered. . . . .   | 102 |
| 5.2 | The average number of Newton ( $\bar{N}^N$ ) and GMRES ( $\bar{N}^G$ ) iterations for the solution of the mechanics problem and the total wall time ( $T^W$ , in minutes) for the benchmark simulations, for each segregated strategy, $\tau$ (in $10^{-5}$ s), and $N_{sub}$ considered. . . . .   | 103 |
| 5.3 | Strong scalability for $(\mathcal{I}_{SI})-(\mathcal{E}_{SI})-(\mathcal{A}_{SI})-(\mathcal{M}_I)$ : the number of CPUs, the Vertices/CPU ratio, and the DoFs/CPU ratio for the mechanics problem.   | 107 |
| 5.4 | Weak scalability for $(\mathcal{I}_{SI})-(\mathcal{E}_{SI})-(\mathcal{A}_{SI})-(\mathcal{M}_I)$ : the level of hierarchical refinement, the number of vertices and tetrahedra for each idealized mesh, the number of CPUs, the Vertices/CPU ratio, and the DoFs/CPU ratio for the mechanics problem. . . . .  | 108 |
| 5.5 | The mechanics timestep $\Delta t$ (in $10^{-5}$ s), the average number of Newton ( $\bar{N}^N$ ) and GMRES ( $\bar{N}^G$ ) iterations, and the total wall time ( $T^W$ , in minutes) for the simulation of the heartbeat with final time $T = 0.073$ s with the subject-specific mesh, using the four strategies considered and $N_{sub} = 1, 5, 10$ . . . . .                        | 115 |
| 5.6 | EDV, ESV, SV, LVEF, and ESPVR for the healthy and the pathological cases. . . . .   | 122 |
| 7.1 | Top table: the number of vertices for the myocardium, the fluid, and the common interface meshes. Middle table: the number of DoFs for each single core problem. Bottom table: the number of DoFs and DoFs per CPU for the $(\mathcal{IEA})$ (electrophysiology + mechanical activation), $(\mathcal{MGF})$ (FSI), and $(\mathcal{IEAMGF})$ (electrofluidmechanics) problems. . . . . | 134 |

## List of Tables

---

|     |   |     |
|-----|---|-----|
| 7.2 | The average number of Newton ( $\overline{N}^N$ ) and GMRES ( $\overline{N}^G$ ) iterations for the solution of the monolithic problem ( $\mathcal{I}_I \mathcal{E}_I \mathcal{A}_I \mathcal{M}_I \mathcal{G}_I \mathcal{F}_I$ ), and the total wall time ( $T^W$ , in minutes) for the electrofluidmechanics simulations, for each $\tau (= \Delta t)$ considered. . . . . | 140 |
| 7.3 | The average number of Newton ( $\overline{N}^N$ ) and GMRES ( $\overline{N}^G$ ) iterations for the solution of the mechanics problem and the total wall time ( $T^W$ , in minutes) for the electrofluidmechanics simulations, for each segregated strategy, and $N_{sub}$ considered and $\tau = 8 \times 10^{-5}$ s. . . . .  | 141 |
| B.1 | Values of the coefficients used for the minimal model [Bueno-Orovio et al., 2008]. The coefficients indicated in scientific notation were rescaled from the original work, from [ms] to [s]. . . . .  | 151 |
| B.2 | Coefficient used for the monodomain (top table) and the bidomain (bottom table) equations. . . . .  | 153 |
| B.3 | Coefficients of the truncated Fourier series approximating the force-length relationship (top table); minimum, maximum, and reference sarcomere length, calcium threshold and the tuning parameters. The parameter $\hat{\mu}_A$ used for each of the four heartbeat phases is specified. . . . .   | 154 |
| B.4 | Parameters for the nearly incompressible Holzapfel-Ogden strain energy function (top table); density and boundary conditions coefficients (mid and bottom tables). . . . .  | 155 |

# Introduction

The heart performs two simple, yet fundamental, tasks: it pumps the deoxygenated blood to the lungs to get oxygen and release carbon dioxide, while it simultaneously pushes the oxygen rich blood into the arteries delivering it to tissues and organs [Levick, 2013]. Cardiovascular related diseases represent the leading causes of death in the whole world [Murray et al., 2014]: while advancements in medical practice are continuously improving patients conditions and diseases outcomes, recent progresses in the mathematical modeling of the cardiac function allow to perform realistic cardiovascular numerical simulations [Eriksson et al., 2013, Colli Franzone et al., 2015a, Gerbi et al., 2017, Göktepe and Kuhl, 2010, Krause et al., 2012, Nordsletten et al., 2011, Quarteroni et al., 2017a, Quarteroni et al., 2017b, Rossi, 2014, Sugiura et al., 2012, Trayanova, 2011, Usyk et al., 2002], thus providing medical doctors and clinicians with valuable diagnostic and predictive tools. Moreover, clinical data and the application of image segmentation techniques to Magnetic Resonance Imaging (MRI) and Computed Tomography (CT) scans feed, as inputs, the mathematical models, thus allowing numerical simulations in a *subject-specific* framework [Augustin et al., 2016, Coupé et al., 2011, Crozier et al., 2016, Gerbi et al., 2017, Krause et al., 2015, Lee et al., 2010, Plotkowiak et al., 2008, Potse et al., 2014, Quarteroni et al., 2017b, Smith et al., 2011, Takizawa et al., 2010]; in addition, uncertainty quantification techniques allow to estimate the models parameters and data, and to cope with their variability [Eck et al., 2016, Eriksson et al., 2013, Manzoni et al., 2016, Pagani, 2017, Sankaran and Marsden, 2011].

The heart function is the result of several physical processes taking place at different spatial scales, i.e. at the cellular, tissue, and organ levels. The muscle contraction, by which the two ventricles pump the blood in arteries and veins during the systole, is set off by a complex intracellular mechanism (the *mechanical activation*) causing the shortening of the myocardium muscle fibers (structures defining the anisotropy of the myocardium at the cellular level), which are in turn triggered by an electric wave propagating through the tissues (the *action potential*). The contraction of the ventricles, in coordination with the valves opening/closing, ensures the flowing of the blood in the circulatory system at each heartbeat. We hence identify the following main processes: electrophysiology (which drives the action potential), mechanical activation (or active mechanics), (passive) mechanics, and fluid dynamics. In the mathematical modeling,

these isolated (single) processes have to be properly integrated; we refer to this as an “integrated heart model” [Quarteroni et al., 2017a]. The models for the electrophysiology, the active and the passive mechanics, and the fluid dynamics are referred to as “single core models”, and are expressed by systems of Ordinary Differential Equations (ODEs) and Partial Differential Equations (PDEs). Although their individual behavior is nowadays quite understood, further theoretical studies and analysis are still needed to better understand their interactions [Chapelle et al., 2009, Costabal et al., 2017, Eriksson et al., 2013, Gerbi et al., 2017, Quarteroni et al., 2017b, Rocha et al., 2009].

The focus of this thesis is on the electrofluidmechanics mathematical and numerical modeling of the left ventricle (LV). The models used for the description of the physical processes are the monodomain and bidomain equations [Colli Franzone et al., 2006, Hunter et al., 1997, Potse et al., 2006, Sainte-Marie et al., 2006] together with the minimal Bueno-Orovio ionic model [Bueno-Orovio et al., 2008] for the electrophysiology. For the passive mechanics, we use the popular Holzapfel-Ogden model [Holzapfel and Ogden, 2009] together with the active strain approach [Ambrosi et al., 2011, Ambrosi and Pezzuto, 2012], the latter endowed with a recently proposed model for the transmurally heterogeneous thickening of the myocardium [Barbarotta et al., 2017] in the framework of the active strain formulation. The mechanical activation model provides then a coupling between the electrophysiology and the mechanics by describing the shortening of the myocardial fibers [Gerbi et al., 2017, Ruiz-Baier et al., 2014], triggered by a change in the ionic concentrations in the cardiac cells, namely the intracellular calcium concentration. For the description of the fluid, we consider two cases: a 3D “full” model, and a 0D “reduced” one. In the latter case, we use simple ODE-based models for the fluid pressure acting on the endocardium (the interface between the myocardium and the blood) as is done, e.g., in [Hirschvogel et al., 2017, Rossi, 2014] thus obtaining an “electromechanics” model of the LV. In the former case, the incompressible Navier-Stokes equations for a Newtonian fluid [Gervasio et al., 2006, Quarteroni et al., 2010] are employed thus obtaining a Fluid-Structure Interaction (FSI) problem [Formaggia et al., 2010, Forti, 2016, Nobile, 2001], and we refer to the integrated model thus obtained as one for the “electrofluidmechanics” of the LV.

The numerical approximation of the single core models is carried out by means of the Finite Element Method (FEM) for the space discretization while Backward Differentiation Formulas (BDFs) are used for the time discretization [Quarteroni et al., 2010]. We consider both implicit and semi-implicit schemes, the latter consisting in the partial evaluation of the nonlinear terms with an approximation of the unknowns (extrapolation) of the same order of the BDF scheme [Cellier and Kofman, 2006, Gervasio et al., 2006]. Once the isolated discretized models are obtained, a central topic which we thoroughly investigate in this thesis is the numerical strategy used for the integrated models, i.e. the way by which we solve the isolated problems with respect to each other. Indeed, the discretized integrated problems can be formulated by either a *monolithic* approach, where the approximated equations are assembled in a single large system and simultaneously solved,

---

or a *segregated* approach, where the approximated equations are solved sequentially (in a suitable specified order). We refer to the solvers for the integrated problems as monolithic and segregated solvers, respectively. Monolithic solvers usually show better accuracy and stability properties with respect to segregated ones; however, they are typically (much) more computationally demanding. Segregated solvers, on the other hand, usually require less computational resources at the cost of a reduced accuracy due to an introduced splitting error. Segregated solvers for the electromechanics of the LV are very common, and are investigated in [Augustin et al., 2016, Baillargeon et al., 2014, Chapelle et al., 2009, Göktepe and Kuhl, 2010, Land et al., 2012, Rossi, 2014, Usyk et al., 2002], where the electrophysiology and the mechanics problems are solved separately. In [Dal et al., 2011, Dal et al., 2013, Gerbi et al., 2017, Hirschvogel et al., 2017], monolithic solvers are used instead. We formulate here a monolithic solver [Gerbi et al., 2017] and three novel segregated solvers [Gerbi et al., 2018] for the electromechanics problem, and then extend them to the electrofluidmechanics case. A distinguishing feature of our approach is that the numerical coupling is performed on the electromechanics problem within the active strain framework and with a physically meaningful transmurally variable orthotropic activation validated in [Barbarotta et al., 2017]. We systematically compare the numerical results obtained by means of the segregated solvers with those of the monolithic solver for some physically meaningful benchmark problems, and we show that the segregated schemes are first order accurate. We again remark that one of the main novelties of the solvers here proposed is due to the use of the active strain instead of the active stress. Indeed, contrarily to the results obtained in [Niederer and Smith, 2008] where the active stress approach is used, numerical instabilities do not arise when segregating the electrophysiology and the mechanics blocks. Our segregated solvers are formulated in a way that different timestep sizes for the electrophysiology and the mechanics can be used, thus leading to the so-called *staggered* algorithms. The use of different timestep sizes for the time discretization of the single core models is indeed more natural for segregated approaches. Moreover, this is physically motivated as each single core model features very different time scales: namely, the electrophysiology requires a small timestep size while the mechanics yields stable and accurate results also for relatively coarse time discretizations. Regarding the computational efficiency, we show that the segregated solvers allow dramatic reductions of the computational costs with respect to the monolithic scheme. This is particularly true for a segregated solver in which the equations for the ionic concentrations, the monodomain, the mechanical activation, the mechanics, and the fluid are fully decoupled and a timestep size of an order of magnitude larger is used for the mechanics (or the FSI in the electrofluidmechanics case) with respect to the electrophysiology.

When solving the discretized single core and integrated problems, suitable preconditioners must be employed for the efficient solution of the large linear systems stemming from the discretization of the problems. This is particularly true in the case of the monolithic solvers, where an effective preconditioner is necessary to even ensure the convergence

of the method for the solution of the linear system. Moreover, using a monolithic black box preconditioner (typical examples being Multigrid [Briggs et al., 2000] or Additive Schwarz [Quarteroni and Valli, 1996] preconditioners) would lead to the loss of information related to the differential problem associated to a single core model and, consequently, to “poor” performances in the solution of the linear system. With this aim, we develop two monolithic preconditioners (for the monolithic electromechanics and electrofluidmechanics) exploiting such information at the block level, that is we define a preconditioner which exploits the physics of the coupled problem at the level of the block structure. This is obtained by an inexact factorization of the Jacobian of the monolithic algebraic linear problem, which allows to precondition separately each single core model rather than the whole integrated problem. The proposed preconditioner is an extension of the FaCSI preconditioner for FSI problems proposed in [Deparis et al., 2016b]. In particular, the results that we obtain confirm that the the block corresponding to the mechanics, which is strongly nonlinear and highly anisotropic, is the most troublesome regarding the preconditioning approach [Colli Franzone et al., 2015a, Pavarino et al., 2015], thus representing the bottleneck of our simulations. The monolithic solvers are tested in High Performance Computing (HPC) framework with meshes featuring millions of vertices and thousands of processing units in order to assess the weak and the strong scalability of the proposed preconditioners and solvers; analogous tests are performed with the segregated solvers to allow the comparison of the different strategies for large scale simulations.

The integrated models require several different information (data) to be effectively used, namely the ventricle geometry, the fibers distribution, and other physical parameters such as the conductivity of the tissue or the End Diastolic Pressure (EDP). This aspect is particularly important if one aims at simulating a realistic subject-specific scenario; still obtaining data with noninvasive in vivo measurements is a complex task which is not routinely performed in clinical procedures, and is under study in several medical fields [Kircher et al., 1990, Provost et al., 2011, Zhang et al., 2006]. Moreover, even when these data are available, often additional procedures have to be performed to exploit them in the so-called *preprocess pipeline*. This aims at obtaining the data that are needed to feed the solvers as inputs. In this work, the preprocess pipeline includes the generation of the computational geometries, the approximation of the fibers field in the myocardium, and the estimation of the internal stresses in the myocardium when the latter is in mechanical equilibrium under the action of the pressure exerted by the blood. More in detail, the preprocess pipeline that we consider includes procedures for the discretization of the geometries starting from medical images obtained with techniques such as the MRI. The mesh thus obtained, together with additional information on the fibers orientation, is then exploited for the definition of the fibers in the whole myocardium by using a rule-based algorithm [Bayer et al., 2012, Rossi, 2014]. Finally, given the geometry, the fibers, and the EDP, the computation of the *prestress* allows to estimate the internal distribution of the stresses at the end of the diastolic phase, which we always consider



---

as the starting time for our simulations. The advantage of defining this pipeline is also given by the possibility of generating these data “offline” for each given geometry and parameters set, instead of carrying out this somewhat computationally expensive tasks.

After having assessed the accuracy and the efficiency of the proposed electromechanics solvers we show that they can be seamlessly used, after having performed the preprocess pipeline, also for large scale subject-specific simulations with geometries segmented from MRI images. In the electromechanics case, a full heartbeat is simulated by modeling the pressure at the endocardium during the four phases in which the LV heartbeat is conventionally split, i.e. the isovolumic contraction, the ejection, the isovolumic relaxation, and the filling phases. The results thus obtained show that the proposed methods are able to produce results which match physiological data, specifically in terms of conduction velocities, displacements, stresses, and pressure. Pressure-volume loops, common and synthetic representations of the LV function [Klabunde, 2011], are also produced and discussed. We then simulate, with the same subject-specific geometry, a pathological condition known as (ischemic) necrosis, characterized by a reduction in the blood supply to the myocardial tissues [Griffin et al., 2008] which causes a shortage in the oxygen supply required for the cellular metabolism and ultimately the death of the cells of the affected portion of tissue. The necrosis is modeled by locally modifying the models for the electrophysiology and for the mechanical activation, while we stress that the same solver and parameters of the healthy case are used. In this case, we also produce several medical indicators and compare them with physiological data. Finally, in the electrofluidmechanics case, the LV systole (which includes the isovolumic contraction and the ejection phases) is simulated on a realistic geometry, by which we obtain physiological values for the blood velocity and pressure.

This thesis is organized in three parts and along the following chapters.

## *I Mathematical and numerical modeling*

**Chapter 1:** we describe in detail the physical processes taking place in the LV during the heartbeat and we recall the mathematical core models for the electrophysiology, the active and the passive mechanics, and the fluid dynamics which are used throughout the thesis. Particular emphasis is put on the interactions (the coupling conditions, in mathematical terms) between the core models in both the electromechanics and the electrofluidmechanics case.

**Chapter 2:** we carry out the space and time discretizations of the single core models by using the FEM and BDFs, the latter with both implicit and semi-implicit time schemes.

**Chapter 3:** the techniques employed to generate the data to be used as input for the proposed solvers are outlined. These data include the approximated geometries (i.e. the meshes), the myocardium fibers and sheets distribution representing the local anisotropy directions, and the myocardium stresses at the initial time (i.e. the

prestress).

### II *Electromechanics*

**Chapter 4:** we propose, discuss, and analyze monolithic, segregated, and staggered solvers for the electromechanics problem. The segregated and the staggered solvers correspond to a Godunov splitting scheme [Godunov, 1959] and we show that first order accuracy is guaranteed when using them.

**Chapter 5:** we report the numerical results obtained with the proposed methods. These include in particular error convergence analysis, the error being computed with respect to the solution given by the monolithic solver with a small timestep size. We then carry out several tests to assess the weak and the strong scalability for varying timestep sizes. Finally, we use the solvers to simulate the electromechanics of a subject-specific LV during a full heartbeat. In the latter case we also model and simulate a pathological scenario, where part of the myocardium is affected by an ischemic necrosis.

### III *Electrofluidmechanics*

**Chapter 6:** the proposed strategies for the electromechanics of the LV are extended to the electrofluidmechanics problem. Since interactions of the fluid with models other than the mechanics are not considered, the extension consists in replacing the mechanics core model with the FSI core model.

**Chapter 7:** we report and discuss the numerical results obtained with the proposed strategies for the simulation of the LV electrofluidmechanics with a realistic geometry. In this case, we limit the simulation to the systolic phase due to the complexity of simulating the full heartbeat.

Finally, we draw our Conclusions and outline several possible future developments.

All the numerical methods described in this thesis have been implemented by the author in the open source finite element library LifeV <sup>1</sup>. This thesis contains results which have already been accepted or submitted for publication (see [Gerbi et al., 2017, Gerbi et al., 2018, Landajuela et al., 2017]).

---

<sup>1</sup><http://www.lifev.org>

# Mathematical and numerical modeling

## Part I



# 1 Mathematical models for the human heart

In this review chapter we describe the physical processes taking place in the LV during a heartbeat and the main mathematical models for their description. These include the electrophysiology and the passive/active mechanics in the myocardium (i.e. the heart muscle), and the blood dynamics in the chambers. For each process, we introduce the variables of interest and give a brief review of the mathematical models employed to describe the evolution of such variables, as well as their mutual interactions.

## 1.1 Heart function

The heart is composed of four chambers, the left and the right ventricles and atria. Its function is to pump the blood through the circulatory system: the right side pushes the deoxygenated blood to the lungs to pick up oxygen and get rid of carbon dioxide, while the left side pushes the oxygen rich blood in the arteries to get it delivered to tissues and organs (see Figure 1.1) [Opie, 2004]. It is estimated that the heart pumps some five million liters of blood during an average lifetime [Jarvik, 1981].

The contraction of the ventricles, which are responsible for pumping the blood, is triggered by a series of electrochemical reactions occurring in the myocardium. The stimuli initiating these reactions are generated at the sinoatrial (SA) node [Brooks and Lu, 1972] – a group of cells located on the right atrium wall – which acts as a natural pacemaker and delivered through the so called Purkinje fibers network, as depicted in Figure 1.1. The contraction is carried out by means of the excitable contractile cardiac muscle cells, called cardiomyocytes. The latter are composed of myofibrils, long bundles of sarcomeres (the basic unit of striated muscle tissue) forming bonds with each other by means of calcium ions  $[Ca^{2+}]$  molecules [Hoffman and Crane, 1960]. Once these bonds have taken place, the shortening of the cardiomyocytes drives the tissue contraction at the organ level. The evolution of the electric field through the cardiomyocytes depends on a delicate balance between the *transmembrane potential* – i.e. the potential difference

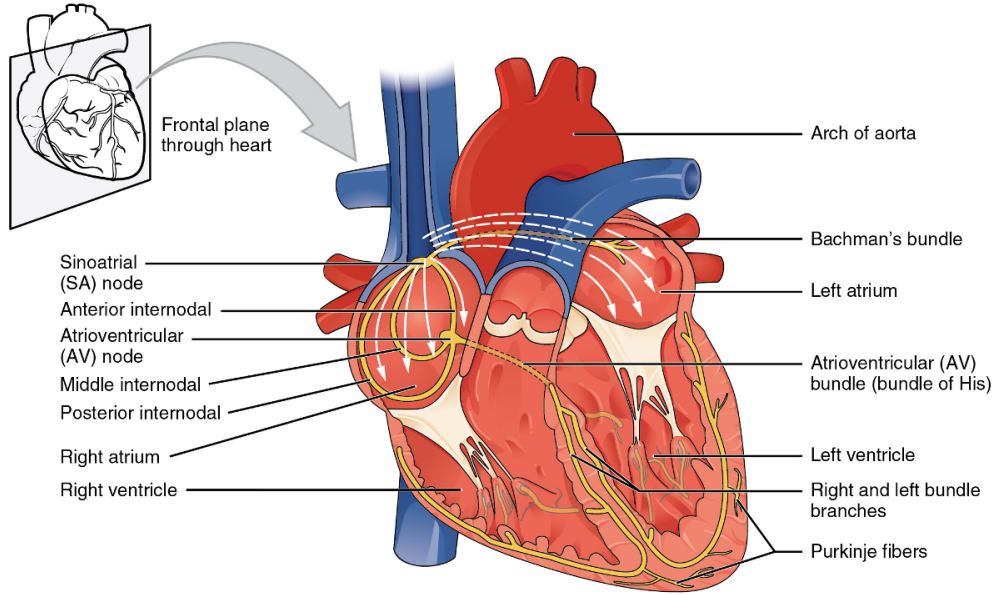


Figure 1.1 – Anterior view of a frontal section of the heart.

across the membrane separating the inner and the outer parts of the cells – and the concentration of different ionic species like the calcium.

In the context of a full heartbeat, the contraction takes place in the *systolic* phase (see Figure 1.15) causing the LV pressure to increase while the aortic and the mitral valves are both closed. When the LV pressure reaches the value of the outer aortic pressure measured on the other side of the aortic valve, the latter opens allowing the oxygenated blood to flow in the arteries [Altman and Dittmer, 1971]. After the ejection of blood starts, the LV undergoes a relaxation in the *diastolic* phase, during which it is filled with the blood coming from the left atrium (LA) and passing through the mitral valve.

In the following, we analyze in detail the models that we use to capture the main features of these physical processes.

## 1.2 Electrophysiology models

The myocardium cells are organized in membranes; these are characterized by channels (or gates) which provide direct intercellular communications between the cytoplasmic compartments of two adjacent cells [Colli Franzone et al., 2006, Hoyt et al., 1989]. Different ionic species flow through the cellular membrane, depending on the electric transmembrane potential  $v$ . At equilibrium, the ionic flux is zero and a resting state for  $v$  can be defined; if an external electrical stimulus is applied to the cell, a complex system of reactions generates an action potential, which propagates through the myocardium. A detailed description of such phenomena can be found e.g. in [Colli Franzone et al.,

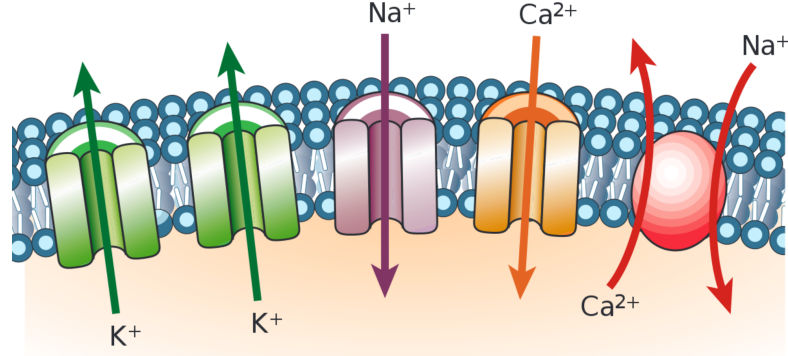


Figure 1.2 – Ion channels in a cardiac cell. In the figure,  $K^+$ ,  $Na^+$ , and  $Ca^{2+}$  are channels allowing the corresponding ion to cross the membrane, while  $Na^+/Ca^{2+}$  is an exchanger which transports three  $Na^+$  ions for each  $Ca^{2+}$  ion. Image taken from [Marbán, 2002].

2006, Keener and Sneyd, 1998].

### 1.2.1 Ionic models for single cells

By considering a single cell membrane and a single ionic species with concentration  $c(t)$ , its flux  $\mathbf{J}$  through the membrane can be obtained by the superposition of two effects: a component due to the gradient of the ion's concentration (according to the Fick's law) and a second one due to the generated electric field  $\nabla v$ . In mathematical terms:

$$\mathbf{J} = \mathbf{J}_c + \mathbf{J}_e = \mathbf{D} \left( \nabla c + c \frac{zF}{RT} \nabla v \right), \quad (1.1)$$

where  $\mathbf{D}$  is the conductivity tensor,  $T$  is the membrane's temperature, and  $z$  is the charge of the ionic species;  $F$  and  $R$  are, respectively, the Faraday's and the ideal gas constants. By setting  $\mathbf{J} = \mathbf{0}$  in (1.1) and integrating in  $(x_{int}, x_{ext})$ , where  $x_{int}$  and  $x_{ext}$  are the coordinates of the inside and the outside of the cell, respectively, the resting (or Nernst) potential of the specific ion can be obtained:

$$v_S = \frac{RT}{zF} \log \left( \frac{c_{ext}}{c_{int}} \right),$$

with  $c_{ext}$  and  $c_{int}$  being the ion's concentrations in the exterior and in the interior of the cell, respectively. Therefore, when  $v \neq v_S$ , an electric current density flows through the membrane; according to Ohm's law, this current is modeled as:

$$I_S = \bar{g}_S(v - v_S),$$

where the conductivity of the membrane  $\bar{g}_S$  has to be properly modeled.

The main factors in the determination of  $\bar{g}_S$  are the channels on the cell, which allow the flux to pass through the membrane (see Figure 1.2). The simplest model for these channels [Colli Franzone et al., 2006] is based on the assumption that they can be either open or closed. By denoting the total number of channels per unit area as  $[T] = [O] + [C]$ , where  $[O]$  and  $[C]$  are the open and closed channels per unit area respectively, the *gating variable*  $w = \frac{[O]}{[T]}$  are defined as the fraction of channels which are open. Taking into account  $M$  kinds of channels for a specific ion, and defining the gating variables  $w_j \in [0, 1]$ ,  $j = 1, \dots, M$  associated to  $S$ , the conductivity takes then the following form:

$$\bar{g}_S = g_S \varphi(v), \quad \text{with} \quad \varphi(v) := \prod_{j=1}^M w_j^{S_j}(v).$$

The number  $M$  of gating variables depends on the particular species considered, as well as on the particular *ionic model* at hand. In general,  $S_j$  represents the number of channel subunits of the  $j$ -th type [Keener and Sneyd, 1998]. Among the numerous works attempting to model heart muscle cells, we recall simple models such as the Aliev-Panfilov ( $M = 1$ ) [Aliev and Panfilov, 1996], the minimal model ( $M = 3$ ) [Bueno-Orovio et al., 2008], or the more realistic Luo-Rudy ( $M = 6$ ) [Luo and Rudy, 1991, Luo and Rudy, 1994] and the ten Tusscher ( $M = 13$ ) [ten Tusscher et al., 2004] models. All of these aim at describing ventricular cells, even if the same framework applies to different kinds of cells, as in the case of the Noble model ( $M = 3$ ) [Noble, 1962] for the Purkinje fibers.

Typically, each gating variable  $w_j$  is the solution of an ordinary differential equation (ODE) of the form:

$$\frac{dw_j}{dt} = \alpha_j(v)(w_j^\infty(v) - w_j) + \beta_j(v)w_j, \quad (1.2)$$

$\alpha_j, \beta_j$  being the probability of channel opening and closing, respectively, while  $w_j^\infty$  is such that  $w_j = \frac{\alpha_j}{\alpha_j - \beta_j} w_j^\infty$  at the equilibrium. In the case of multiple ionic species, the total ionic current density  $I^{ion}$  can be obtained by summing the contribution given by  $p$  different species. By using the Hodgkin-Huxley [Hodgkin and Huxley, 1952] formalism, we write:

$$I^{ion}(v, \mathbf{w}, \mathbf{c}) = \sum_{k=1}^p g_k(\mathbf{c}) \prod_{j=1}^{M_k} w_j^{S_{kj}}(v - v_k(\mathbf{c})), \quad (1.3)$$

where, as previously stated,  $\mathbf{c} = (c_1, \dots, c_p)$  are variables which represent the intracellular concentration of the ions and  $\mathbf{w} = (w_1, \dots, w_{M_p})$  are the gating variables. The 0D equations which describe the evolution of the transmembrane potential in a single cell



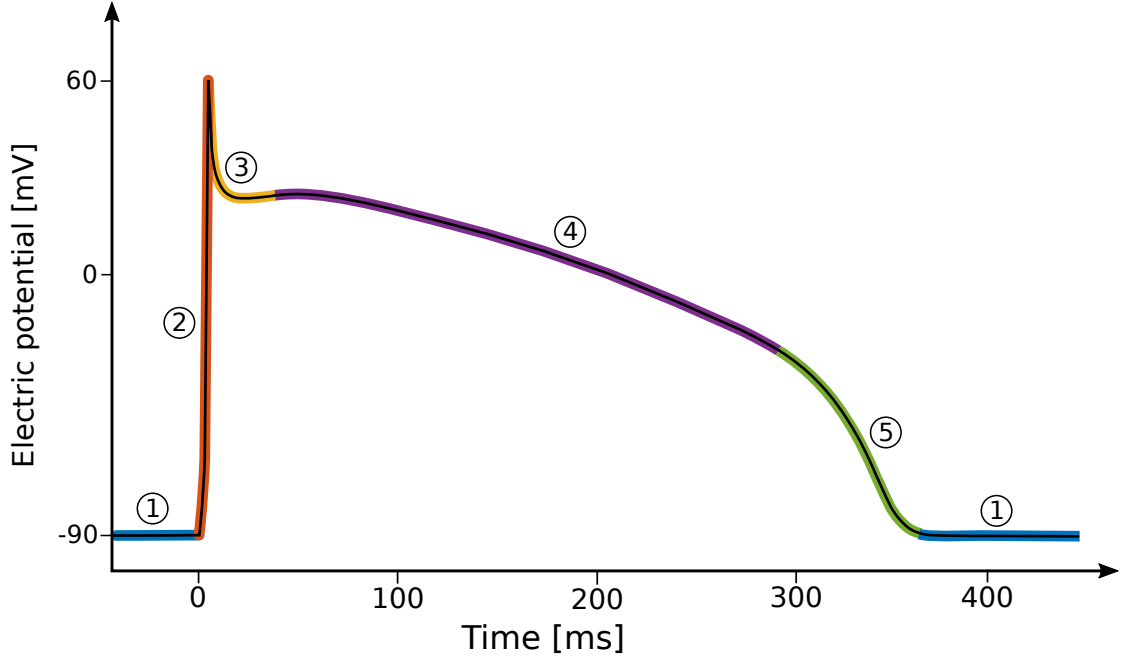


Figure 1.3 – Evolution of the transmembrane electric potential in a cardiac cell, stimulated with an external electric current. The figure highlights the following phases: 1) the *resting* phase, when the potential remains at its rest value of approximately  $v = -90$  mV until the cell is stimulated; 2) the *depolarization* phase, when the cascade effect of electrochemical reactions drives the opening of the ionic channels on the membrane, ultimately causing a spike in the potential which switches sign; 3) the *short repolarization* phase, when the potential shortly decreases immediately after the spike; 4) the *plateau* phase, when the net flux of electric charge due to the ions flowing inward/outward with respect to the cell membrane is zero; 5) the *repolarization* phase, when the channels, the ionic concentrations and the potential slowly return to the rest configuration.

hence read:

$$\begin{cases} \frac{dv}{dt} = \frac{1}{C_m}(I^{app} - I^{ion}(v, \mathbf{w}, \mathbf{c})) & t \in (0, T], \\ \frac{d\mathbf{w}}{dt} = \mathbf{R}(v, \mathbf{w}) & t \in (0, T], \\ \frac{d\mathbf{c}}{dt} = \mathbf{S}(v, \mathbf{w}, \mathbf{c}) & t \in (0, T], \\ v = v_0, \quad \mathbf{w} = \mathbf{w}_0, \quad \mathbf{c} = \mathbf{c}_0 & t = 0. \end{cases} \quad (1.4)$$

where  $T$  is the final time considered,  $C_m$  is the membrane capacitance,  $I^{app}$  is an external current density, the function  $\mathbf{R}$  is usually of the form specified in Eq. (1.2), while the function  $\mathbf{S}$  describes the evolution of the ion concentration and depends on the considered ionic model. We report in Figure 1.3 the evolution of the transmembrane potential  $v$  in a cardiac cell as modeled with Eq. (1.4) with different phases highlighted.

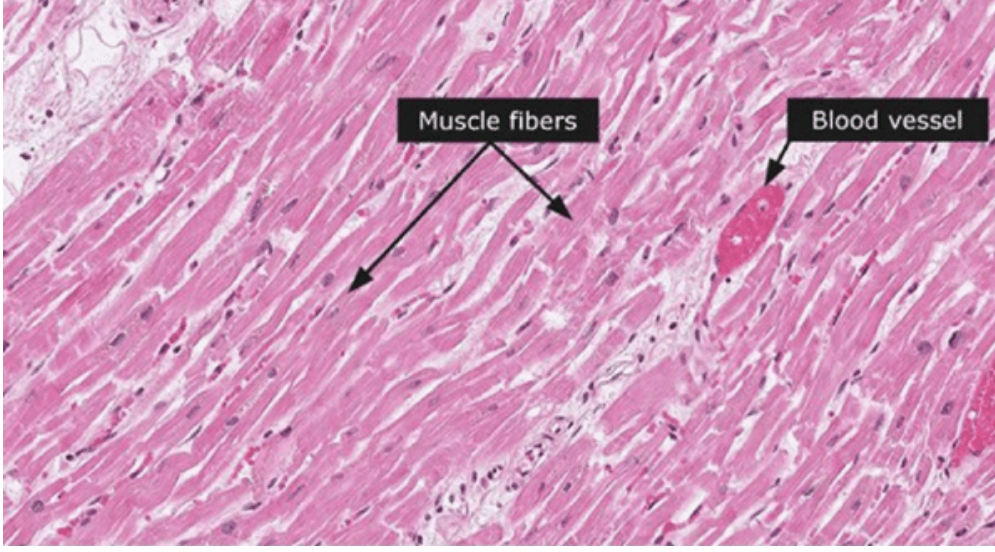


Figure 1.4 – Myocardial tissue at the microscale, showing the disposition of the fibers in the muscle. Image taken from [Akhgari et al., 2017].

For the sake of simplicity we will be using the minimal model of [Bueno-Orovio et al., 2008] which is characterized by 3 gating variables only; nevertheless, it is suitable to reproduce action potential morphologies and can be tuned to mimic the behavior of other complex models such as the ten Tusscher [Rossi, 2014]. Moreover, in view of the subsequent numerical discretization of the continuous model, this choice will allow to contain the computational cost since the equations of the ionic model will be solved in each degree of freedom of the discretized geometry.

### 1.2.2 Bidomain and monodomain models

Once the electrophysiological model of a single cell has been set up, it is possible to model the behavior of a multi-cell tissue; however, rather than considering such tissue as made of individual cells, the homogenization theory [Colli Franzone et al., 2006] suggests that the extra-cellular and the intra-cellular regions can be considered as two continuous, geometrically coincident domains which we denote by  $\Omega_0^s$  (see Section 1.3).

The myocardium is a highly anisotropic material composed of fibers [Costa et al., 1999, Fernandez-Teran and Hurle, 1982, Gilbert et al., 2007, Hoshino et al., 1983]. Fibers are in turn composed of cardiomyocytes, organized in groups, firmly tied up in collagen (see Figure 1.4). Since the electrical and the structural properties of the myocardium depend on a local frame of reference, we define the three vector fields  $\mathbf{f}_0 = \mathbf{f}_0(\mathbf{X}_s)$ ,  $\mathbf{s}_0 = \mathbf{s}_0(\mathbf{X}_s)$  and  $\mathbf{n}_0 = \mathbf{n}_0(\mathbf{X}_s) \forall \mathbf{X}_s \in \Omega_0^s$ , which identify the fibers and the collagen sheets directions, and the fibers-sheets normal (i.e. the vector normal to the plane identified by  $\mathbf{f}_0$  and  $\mathbf{s}_0$ ), respectively. The anisotropy of the myocardium is then encoded in the conductivity

tensors  $\mathbf{D}_E$  and  $\mathbf{D}_I$  for the extra-cellular and the intra-cellular domains, respectively, for which we set:

$$\begin{aligned}\mathbf{D}_E &= \sigma_{E,t} \mathbf{I} + (\sigma_{E,l} - \sigma_{E,t}) \mathbf{f}_0 \otimes \mathbf{f}_0, \\ \mathbf{D}_I &= \sigma_{I,t} \mathbf{I} + (\sigma_{I,l} - \sigma_{I,t}) \mathbf{f}_0 \otimes \mathbf{f}_0,\end{aligned}$$

where  $\sigma_{E,t}, \sigma_{E,l}$  ( $\sigma_{I,t}, \sigma_{I,l}$ ) are the extra-cellular (intra-cellular) conductivities in the directions transversal and longitudinal with respect to the fibers, respectively.

By redefining the transmembrane potential as  $v = v_I - v_E$ , where  $v_I$  and  $v_E$  are the internal and external potentials with respect to a common point, respectively, the transmembrane current per unit volume is:

$$J_m = \chi \left( C_m \frac{\partial v}{\partial t} + I^{ion}(v, \mathbf{w}, \mathbf{c}) \right),$$

where  $\chi$  is the membrane surface area per unit volume. By denoting with  $\mathbf{J}_I = -\mathbf{D}_I \nabla v_I$  and  $\mathbf{J}_E = -\mathbf{D}_E \nabla v_E$  the intra/extra-cellular current densities and following Section 1.2.1 regarding the modeling of the concentrations and the gating variables, the so called bidomain model [Franzone et al., 2005] in parabolic-parabolic formulation reads:

$$\begin{cases} \chi \left[ C_m \frac{\partial v}{\partial t} + I^{ion}(v, \mathbf{w}, \mathbf{c}) \right] = \nabla_0 \cdot (\mathbf{D}_I \nabla_0 v_I) & \text{in } \Omega_0^s \times (0, T], \\ \chi \left[ -C_m \frac{\partial v}{\partial t} - I^{ion}(v, \mathbf{w}, \mathbf{c}) \right] = \nabla_0 \cdot (\mathbf{D}_E \nabla_0 v_E) + I^{app} & \text{in } \Omega_0^s \times (0, T], \\ \frac{\partial \mathbf{w}}{\partial t} = \mathbf{R}(v, \mathbf{w}) & \text{in } \Omega_0^s \times (0, T], \\ \frac{\partial \mathbf{c}}{\partial t} = \mathbf{S}(v, \mathbf{w}, \mathbf{c}) & \text{in } \Omega_0^s \times (0, T], \\ (\mathbf{D}_{I,E} \nabla_0 v_{I,E}) \cdot \mathbf{N}_s = 0 & \text{on } \partial\Omega_0^s \times (0, T], \\ v = v_0, \quad \mathbf{w} = \mathbf{w}_0, \quad \mathbf{c} = \mathbf{c}_0 & \text{in } \Omega_0^s \times \{0\}, \end{cases} \quad (1.5)$$

where  $\mathbf{N}_s$  is the outward normal vector with respect to the surface  $\partial\Omega_0^s$ , and  $I^{app}$  is an applied extracellular current per unit volume, satisfying the compatibility condition

$$\int_{\Omega_0^s} I^{app} \, d\Omega_0^s = 0.$$

The bidomain model is often rewritten in an equivalent form in terms of  $v$  and  $v_E$ : in such a case, which is also the formulation that we consider, the equations in parabolic-elliptic

form [Landajuela et al., 2017] read:

$$\left\{ \begin{array}{ll} \chi \left[ C_m \frac{\partial v}{\partial t} + I^{ion}(v, \mathbf{w}, \mathbf{c}) \right] = \nabla_0 \cdot (\mathbf{D}_I \nabla_0(v + v_E)) + I^{app} & \text{in } \Omega_0^s \times (0, T], \\ -\nabla_0 \cdot (\mathbf{D}_I \nabla_0 v) - \nabla_0 \cdot ((\mathbf{D}_I + \mathbf{D}_E) \nabla_0 v_E) = 0 & \text{in } \Omega_0^s \times (0, T], \\ \frac{\partial \mathbf{w}}{\partial t} = \mathbf{R}(v, \mathbf{w}) & \text{in } \Omega_0^s \times (0, T], \\ \frac{\partial \mathbf{c}}{\partial t} = \mathbf{S}(v, \mathbf{w}, \mathbf{c}) & \text{in } \Omega_0^s \times (0, T], \\ (\mathbf{D}_I \nabla_0(v + v_E)) \cdot \mathbf{N}_s = 0 & \text{on } \partial\Omega_0^s \times (0, T], \\ (\mathbf{D}_I \nabla_0 v + (\mathbf{D}_I + \mathbf{D}_E) \nabla_0 v_E) \cdot \mathbf{N}_s = 0 & \text{on } \partial\Omega_0^s \times (0, T], \\ v = v_0, \quad \mathbf{w} = \mathbf{w}_0, \quad \mathbf{c} = \mathbf{c}_0 & \text{in } \Omega_0^s \times \{0\}, \end{array} \right. \quad (1.6)$$

A simpler model, called monodomain model, is often used instead of Eq. (1.5). The monodomain model is obtained from the bidomain model by assuming that the anisotropy ratio of the two media is the same, that is

$$\mathbf{D}_I = \lambda \mathbf{D}_E,$$

for  $\lambda \in \mathbb{R}^+$ . This model is intrinsically simpler than the bidomain model and is able to reproduce the electrophysiology phenomena inducing the muscle contraction. However, the monodomain model is not deemed to be suitable to describe phenomena for which the current in the extracellular domain influences the transmembrane potential and the ionic currents, as occurs for example during cardiac fibrillation and other pathological cases [Potse et al., 2006]. The monodomain model reads:

$$\left\{ \begin{array}{ll} \chi \left[ C_m \frac{\partial v}{\partial t} + I_{ion}(v, \mathbf{w}, \mathbf{c}) \right] = \nabla_0 \cdot (\mathbf{D}_M \nabla_0 v) + I^{app} & \text{in } \Omega_0^s \times (0, T], \\ \frac{\partial \mathbf{w}}{\partial t} = \mathbf{R}(v, \mathbf{w}), & \text{in } \Omega_0^s \times (0, T], \\ \frac{\partial \mathbf{c}}{\partial t} = \mathbf{S}(v, \mathbf{w}, \mathbf{c}) & \text{in } \Omega_0^s \times (0, T], \\ (\mathbf{D}_M \nabla_0 v) \cdot \mathbf{N}_s = 0 & \text{on } \partial\Omega_0^s \times (0, T], \\ v = v_0, \quad \mathbf{w} = \mathbf{w}_0, \quad \mathbf{c} = \mathbf{c}_0 & \text{in } \Omega_0^s \times \{0\}. \end{array} \right. \quad (1.7)$$

where

$$\begin{aligned} \mathbf{D}_M &= \mathbf{D}_I(\mathbf{D}_I + \mathbf{D}_E)^{-1} \mathbf{D}_I \\ &\approx \sigma_t \mathbf{I} + (\sigma_l - \sigma_t) \mathbf{f}_0 \otimes \mathbf{f}_0. \end{aligned}$$

In [Colli Franzone et al., 2006], a rigorous derivation of (1.7) is provided. Compared to Eq. (1.5), this simplification entails a simpler model and hence, once approximated, reduced computational costs; moreover, it is proven that, under specific conditions, problem (1.7) has a unique solution [Rossi, 2014].

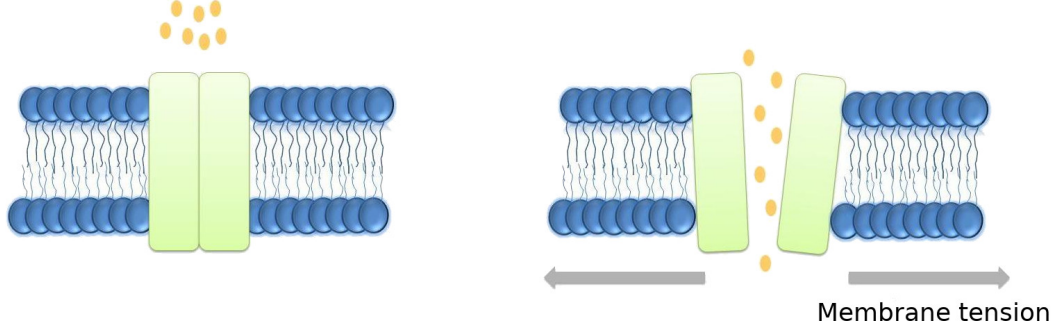


Figure 1.5 – Representation of a membrane channel activated by the membrane tension due to the deformation of the muscle. The open channel allows the ions to flow inward/outward resulting in a SAC.

In Eqs. (1.6)-(1.7) additional terms might be considered. First of all, if the domain  $\Omega_0^s$  is subject to a deformation, as in our case, we need to include the dependence of the diffusive term on the strain tensor  $\mathbf{F}$ , where:

$$\mathbf{F} = \nabla_0 \mathbf{x}_s = \frac{\partial \mathbf{x}_s}{\partial \mathbf{X}_s} = \mathbf{I} + \frac{\partial \mathbf{d}_s}{\partial \mathbf{X}_s}$$

is the deformation gradient,  $\mathbf{X}_s$  and  $\mathbf{x}_s = \mathbf{X}_s + \mathbf{d}_s$  being the reference and the deformed coordinates, respectively. Indeed in such a case the diffusive term in the first equation of (1.7) takes the form [Colli Franzone et al., 2015b, Nordsletten et al., 2011]:

$$\nabla_0 \cdot (J \mathbf{F}^{-1} \mathbf{D}_M \mathbf{F}^{-T} \nabla_0 v), \quad (1.8)$$

with  $J = \det(\mathbf{F})$ , and analogously in Eq. (1.6). Moreover, stretch activated currents (SAC) might be included to consider the electric currents triggered by the deformation of the myocardium [Kamkin et al., 2000, Davis et al., 1992], as shown in Figure 1.5. In general, it accounts to introducing a term of the form [Colli Franzone et al., 2015b, Trayanova et al., 2010]:

$$I_{SAC} = I_{SAC}(v, \mathbf{c}, \mathbf{d}_s). \quad (1.9)$$

In this work, we consider the dependence of the diffusion on the deformation of the domain. We however neglect, for simplicity, the role of SAC currents: nonetheless we remark that considering the term (1.9), in the context of the integrated problem, does not change the coupling of the core models because a feedback from the mechanics is already included by means of Eq. (1.8). More detailed studies on the topic of the bioelectrical effects of mechanical feedbacks were carried out in [Colli Franzone et al., 2016b, Colli Franzone et al., 2017, Colli Franzone et al., 2016a].

We conclude this Section by writing the weak formulation of the bidomain model in

parabolic-elliptic form and of the monodomain model [Bourgault et al., 2009]. For the sake of simplicity, from now on, the vector  $\mathbf{w} = \{w^l\}_{l=1}^{N_I}$  will comprehend both the gating variables and the ionic concentrations. Indeed, in the case of the minimal model [Bueno-Orovio et al., 2008], they both satisfy an equation in the form (1.2), which we rewrite in vector form as

$$\frac{\partial \mathbf{w}(t)}{\partial t} + \mathbf{U}(v(t))\mathbf{w}(t) = \mathbf{Q}(v(t)).$$

We hence multiply the first two equations in (1.6) by a test function  $\psi_s \in H^1(\Omega_0^s)$  and the third one by  $\phi_s \in [L^2(\Omega_0^s)]^{N_I}$ , and integrate over the domain. By Integrating by parts, we obtain the weak formulation of the bidomain model: find  $v(t) \in H^1(\Omega_0^s)$ ,  $v_E(t) \in H^1(\Omega_0^s)/\mathbb{R}$ ,  $\mathbf{w}(t) \in [L^2(\Omega_0^s)]^{N_I}$  such that

$$\begin{aligned} \int_{\Omega_0^s} \chi \left[ C_m \frac{\partial v}{\partial t} + I_{ion}(v, \mathbf{w}, \mathbf{c}) \right] \psi_s \, d\Omega_0^s + \int_{\Omega_0^s} (\mathbf{D}_I \nabla_0(v + v_E)) : \nabla_0 \psi_s \, d\Omega_0^s \\ = \int_{\Omega_0^s} I^{app} \psi_s \, d\Omega_0^s, \quad \text{for all } t \in (0, T], \\ \int_{\Omega_0^s} (\mathbf{D}_I \nabla_0 v) : \nabla_0 \psi_s \, d\Omega_0^s + \int_{\Omega_0^s} ((\mathbf{D}_I + \mathbf{D}_E) \nabla_0 v_E) : \nabla_0 \psi_s \, d\Omega_0^s = 0, \quad \text{for all } t \in (0, T], \\ \int_{\Omega_0^s} \frac{\partial \mathbf{w}}{\partial t} \cdot \phi_s \, d\Omega_0^s + \int_{\Omega_0^s} \mathbf{U}(v) \mathbf{w} \cdot \phi_s \, d\Omega_0^s = \int_{\Omega_0^s} \mathbf{Q}(v) \cdot \phi_s \, d\Omega_0^s, \\ v(0) = v_0, \quad \mathbf{w}(0) = \mathbf{w}_0, \end{aligned}$$

for every  $\psi_s \in H^1(\Omega_0^s)$  and every  $\phi_s \in [L^2(\Omega_0^s)]^{N_I}$ . The function  $v_E$  belongs to the quotient space  $H^1(\Omega_0^s)/\mathbb{R}$  because it is defined up to a constant in this formulation.

In the case of the monodomain model, the weak formulation reads: find  $v(t) \in H^1(\Omega_0^s)$ ,  $\mathbf{w}(t) \in [L^2(\Omega_0^s)]^{N_I}$

$$\begin{aligned} \int_{\Omega_0^s} \chi \left[ C_m \frac{\partial v}{\partial t} + I_{ion}(v, \mathbf{w}, \mathbf{c}) \right] \psi_s \, d\Omega_0^s + \int_{\Omega_0^s} (\mathbf{D}_M \nabla_0 v) : \nabla_0 \psi_s \, d\Omega_0^s \\ = \int_{\Omega_0^s} I^{app} \psi_s \, d\Omega_0^s, \quad \text{for all } t \in (0, T], \\ \int_{\Omega_0^s} \frac{\partial \mathbf{w}}{\partial t} \cdot \phi_s \, d\Omega_0^s + \int_{\Omega_0^s} \mathbf{U}(v) \mathbf{w} \cdot \phi_s \, d\Omega_0^s = \int_{\Omega_0^s} \mathbf{Q}(v) \cdot \phi_s \, d\Omega_0^s, \\ v(0) = v_0, \quad \mathbf{w}(0) = \mathbf{w}_0, \end{aligned}$$

for every  $\psi_s \in H^1(\Omega_0^s)$  and every  $\phi_s \in [L^2(\Omega_0^s)]^{N_I}$ .

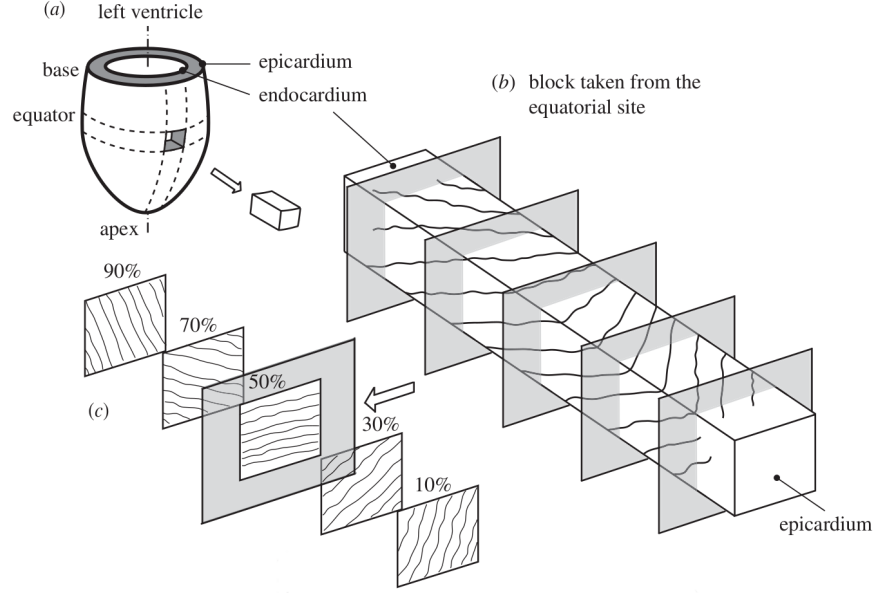


Figure 1.6 – a) An ideal left ventricle muscle. b) A cardiac tissue block showing the fibers' orientation through its thickness. c) Fiber orientation projected on different slides. Image from [Holzapfel and Ogden, 2009].

### 1.3 Myocardium mechanical models

The LV, among the four cardiac chambers, is by far the most studied from both the physiological and the mathematical points of view: this is due to the fact that the vigorous contraction of its walls is responsible for pumping oxygenated blood to tissues all over the body through the circulatory system and it is in first instance responsible for the function of the organs. The LV is endowed with the thickest walls among the other chambers and the muscle forming them is composed of cardiomyocytes. As explained in Section 1.2, the tissue is composed of fibers: at the macroscopical level, fibers are arranged in a helical fashion and their orientation varies transmurally from the epicardium to the endocardium (see Figure 1.6).

The mechanical models for the myocardial tissue are based on the finite elasticity theory, since the myocardium undergoes large deformations throughout the heartbeat. In this framework, the unknown displacement  $\mathbf{d}_s$  is determined by solving the momentum conservation equation:

$$\begin{cases} \rho_s \frac{\partial^2 \mathbf{d}_s}{\partial t^2} - \nabla_0 \cdot \mathbf{P}(\mathbf{d}_s) = \mathbf{0}, & \text{in } \Omega_0^s \times (0, T] \\ + \text{boundary conditions,} \\ + \text{initial conditions,} \end{cases} \quad (1.10)$$

where  $\rho_s$  is the density of the material and the first Piola-Kirchhoff stress tensor  $\mathbf{P}$

accounts for the properties of the considered material. Boundary and initial conditions must be assigned in Eq. (1.10) to ensure the well posedness of the problem, and will be specified later. Tensor  $\mathbf{P}$  is often expressed in terms of the right Cauchy-Green tensor  $\mathbf{C} = \mathbf{F}^T \mathbf{F}$ .

Under the additional assumption that the myocardium is a hyperelastic material [Ogden, 1997], the relationship between the stress and the strain derives from a strain energy density function  $\mathcal{W} = \mathcal{W}(\mathbf{C})$ ; this accounts to assume that:

$$\mathbf{P} = \frac{\partial \mathcal{W}(\mathbf{C})}{\partial \mathbf{F}}. \quad (1.11)$$

### 1.3.1 Passive mechanics

In this section we outline the models employed for the passive behavior of the myocardium. We describe in particular the state of the art strain energy function for the left ventricle tissue in a nearly-incompressible formulation. The mechanics problem is then formulated and endowed with initial and boundary conditions.

#### Strain energy function

It is convenient to express the anisotropic components of  $\mathcal{W}$  in a form which is invariant with respect to the frame of reference. With this aim, we introduce the following invariants of the tensor  $\mathbf{C}$ :

$$\begin{aligned} \mathcal{I}_1 &= \text{tr}(\mathbf{C}), \\ \mathcal{I}_2 &= \frac{1}{2} \left[ \mathcal{I}_1^2 - \text{tr}(\mathbf{C}^2) \right], \\ \mathcal{I}_3 &= \det(\mathbf{C}), \\ \mathcal{I}_{4p} &= \mathbf{C} : \mathbf{p}_0 \otimes \mathbf{p}_0 = \mathbf{p} \cdot \mathbf{p}, \\ \mathcal{I}_{8pq} &= \mathbf{C} : \mathbf{p}_0 \otimes \mathbf{q}_0 = \mathbf{p} \cdot \mathbf{q}, \quad \mathbf{p}, \mathbf{q} \in \{\mathbf{f}, \mathbf{s}, \mathbf{n}\}. \end{aligned}$$

The subscript 0 means that the quantity is considered with respect to the reference domain, while the vectors  $\mathbf{f}$ ,  $\mathbf{s}$ , and  $\mathbf{n}$  were defined in Section 1.2. The typical behavior of biological tissue is such that the response of the material in terms of internal stresses is very strong, compared to a relatively small deformation; many models in literature [Demiray, 1976, Humphrey and Yin, 1987, Humphrey et al., 1990, Costa et al., 2001, Schmid et al., 2006] provide an expression for  $\mathcal{W}$  in terms of exponential type in the invariants of  $\mathbf{C}$ , for which the energy grows quickly as the structure is deformed with respect to its resting state. The state of the art of such models was obtained using experimental shear test data from [Dokos et al., 2002]; in the model proposed in [Holzapfel and Ogden, 2009] the



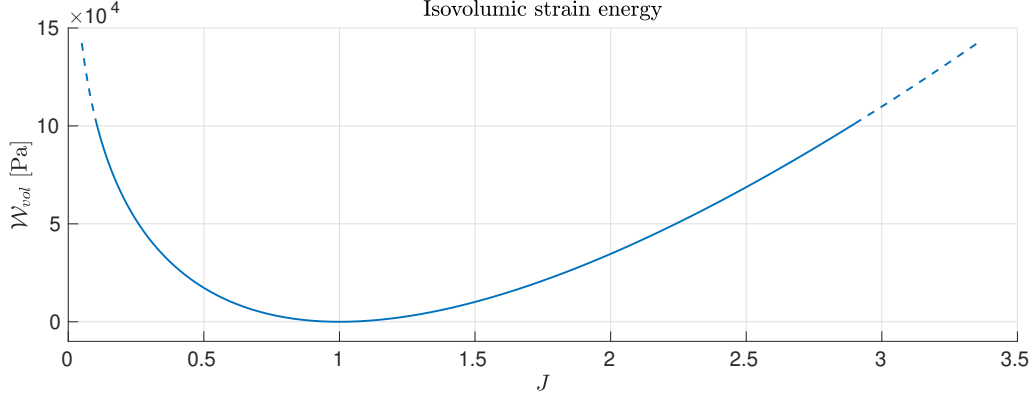


Figure 1.7 – Isovolumic strain energy of the form  $\mathcal{W}_{vol}(J) = \frac{B}{2}(J-1)\log(J)$ , represented as a function of  $J$ .  $\mathcal{W}_{vol}$  is nonnegative, convex, and it attains its global minimum in  $J = 1$ .

strain energy function  $\mathcal{W}$  takes the form:

$$\mathcal{W}(\mathbf{C}) = \mathcal{W}_1(\mathcal{I}_1) + \mathcal{W}_{4f}(\mathcal{I}_{4f}) + \mathcal{W}_{4s}(\mathcal{I}_{4s}) + \mathcal{W}_{8fs}(\mathcal{I}_{8fs}), \quad (1.12)$$

where

$$\begin{aligned} \mathcal{W}_1(\mathcal{I}_1) &= \frac{a}{2b} e^{b(\mathcal{I}_1-3)}, \\ \mathcal{W}_{4f}(\mathcal{I}_{4f}) &= \frac{a_f}{2b_f} \left[ e^{b(\mathcal{I}_{4f}-1)^2} - 1 \right], \\ \mathcal{W}_{4s}(\mathcal{I}_{4s}) &= \frac{a_s}{2b_s} \left[ e^{b(\mathcal{I}_{4s}-1)^2} - 1 \right], \\ \mathcal{W}_{8fs}(\mathcal{I}_{8fs}) &= \frac{a_{fs}}{2b_{fs}} \left[ e^{b_{fs}\mathcal{I}_{8fs}^2} - 1 \right], \end{aligned}$$

and

$$\langle x \rangle = \begin{cases} x & \text{if } x > 0, \\ 0 & \text{otherwise,} \end{cases}$$

indicates the positive part of  $x$  and its role consists in switching off the contributions to the stresses of the fibers and sheets when the material is under compression along their directions [Holzapfel and Ogden, 2015].

#### Nearly-incompressible formulation

Biological tissues are mostly composed of water, and therefore can be considered as incompressible. However, in the case of the myocardium, volume changes have been observed [Yin et al., 1996] even if these are fairly moderate [Cheng et al., 2005], ranging from 2% to 15%. For this reason, a nearly-incompressible formulation is often adopted

[Barbarotta et al., 2017, Rossi, 2014, Simo and Taylor, 1991], as it allows moderate volume variations; at the same time, the resulting problem is simpler than in the case of the incompressible formulation as the pressure is neglected. The nearly-incompressible formulation prescribes a decomposition of the strain tensor into an isochoric (or isovolumetric)  $\bar{\mathbf{F}}$  and a volumetric  $\mathbf{F}_v$  part as:

$$\mathbf{F} = \mathbf{F}_v \bar{\mathbf{F}}, \quad \text{with} \quad \mathbf{F}_v = J^{\frac{1}{3}} \mathbf{I} \quad \text{and} \quad \bar{\mathbf{F}} = J^{-\frac{1}{3}} \mathbf{F}, \quad (1.13)$$

where  $J = \det(\mathbf{F})$  represents the volume change of an infinitesimal block (and hence  $\det(\bar{\mathbf{F}}) = 1$ ). Together with (1.13), an additional term depending on  $J$  has to be considered in the definition of the strain energy function, in order to enforce the incompressibility constraint:

$$\begin{aligned} \mathcal{W}(\mathbf{C}, J) &= \mathcal{W}_{iso}(\mathbf{C}, J) + \mathcal{W}_{vol}(J) \\ &= \mathcal{W}_1(\bar{\mathcal{I}}_1) + \mathcal{W}_{4f}(\mathcal{I}_{4f}) + \mathcal{W}_{4s}(\mathcal{I}_{4s}) + \mathcal{W}_{8fs}(\mathcal{I}_{8fs}) + \mathcal{W}_{vol}(J), \end{aligned} \quad (1.14)$$

where  $\bar{\mathcal{I}}_1 = J^{-\frac{2}{3}} \mathcal{I}_1$  is the first invariant of the tensor  $\bar{\mathbf{C}} = \bar{\mathbf{F}}^T \bar{\mathbf{F}}$ . Indeed, since the isochoric part of the energy function  $\mathcal{W}_{iso}$  is that of an incompressible material (as is assumed in [Holzapfel and Ogden, 2009]), one should evaluate its terms in the invariants of  $\bar{\mathbf{C}}$  instead of  $\mathbf{C}$ ; however, it is shown in [Sansour, 2008] that the evaluation of the anisotropic terms must be performed with respect to the invariants of  $\mathbf{C}$  to avoid unphysical deformations.

In order to enforce the incompressibility constraint, the term  $\mathcal{W}_{vol}$  grows as the deformation deviates from being isochoric. A common choice [Pezzuto, 2013] is that of a function bounded from below, convex, and whose slope in  $J = 1$  is null, for instance:

$$\mathcal{W}_{vol}(J) = \frac{B}{2} (J - 1) \log(J),$$

where the penalization factor  $B$  is called *bulk modulus*. The term  $\mathcal{W}_{vol}$  is shown in Figure 1.7 as a function of  $J$ .

### Initial and boundary conditions

In order to ensure uniqueness for Eq. (1.10), initial and boundary conditions have to be assigned. The latter are imposed on the boundaries depicted in Figure 1.8, and are chosen to take into account for the interaction with the blood on the endocardium (the inner surface of the myocardium), for the tension due to the continuity of the heart muscle on the base (the imaginary surface identified by a plane orthogonal to the LV centerline cutting it in the upper part) and for the presence of the pericardium, a sac containing the heart enclosed in the pericardial cavity [Spodick, 1996]. In particular, following [Hirschvogel et al., 2017], we use visco-elastic generalized Robin boundary conditions;

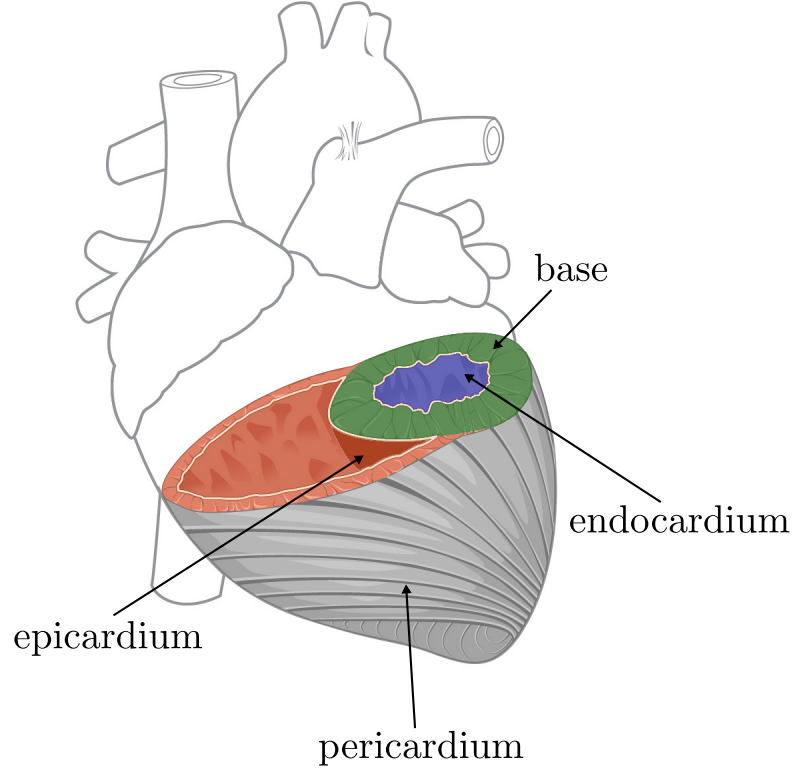


Figure 1.8 – A simplified representation of the boundaries of the LV. These are the endocardium (blue), the epicardium (red) and the base (green). The pericardium (grey) contains the whole heart, and covers part of the LV epicardium in the figure.

thus, the complete mechanics problem reads:

$$\left\{ \begin{array}{ll} \rho_s \frac{\partial^2 \mathbf{d}_s}{\partial t^2} - \nabla_0 \cdot \mathbf{P}(\mathbf{d}_s) = \mathbf{0} & \text{in } \Omega_0^s \times (0, T], \\ (\mathbf{N}_s \otimes \mathbf{N}_s) \left( K_{\perp}^{\eta} \mathbf{d}_s + C_{\perp}^{\eta} \frac{\partial \mathbf{d}_s}{\partial t} \right) \\ + (\mathbf{I} - \mathbf{N}_s \otimes \mathbf{N}_s) \left( K_{\parallel}^{\eta} \mathbf{d}_s + C_{\parallel}^{\eta} \frac{\partial \mathbf{d}_s}{\partial t} \right) + \mathbf{P}(\mathbf{d}_s) \mathbf{N}_s = \mathbf{0} & \text{on } \Gamma_0^{\eta} \times (0, T], \\ \mathbf{P}(\mathbf{d}_s) \mathbf{N}_s = p^{endo}(t) \mathbf{N}_s & \text{on } \Gamma_0^{endo} \times (0, T], \\ \mathbf{d}_s = \mathbf{d}_{s,0}, \quad \frac{\partial \mathbf{d}_s}{\partial t} = \dot{\mathbf{d}}_{s,0} & \text{in } \Omega_0^s \times \{0\}. \end{array} \right. \quad (1.15)$$

The boundary  $\partial\Omega_0^s$  is partitioned into the three surfaces  $\Gamma_0^{base}$ ,  $\Gamma_0^{endo}$ , and  $\Gamma_0^{epi}$ , corresponding to those indicated in Figure 1.8. For  $\eta \in \{base, epi\}$  we assign parameters  $K_{\perp}^{\eta}, K_{\parallel}^{\eta}, C_{\perp}^{\eta}, C_{\parallel}^{\eta} \in \mathbb{R}^+$ , where  $K_j^{\eta}$  and  $C_j^{\eta}$  are the spring stiffnesses and the dashpot viscosities per unit reference surface area, respectively. Subscripts  $\perp$  and  $\parallel$  indicate whether the condition is applied in the normal or in the tangential direction. On the endocardium, on the other hand, the pressure  $p^{endo}(t)$  (still prescribed at this stage) is imposed. Finally,

vector  $\mathbf{d}_{s,0}$  denotes the initial displacement and  $\dot{\mathbf{d}}_{s,0}$  its temporal rate of change.

In order to obtain the weak formulation of Eq.(1.15) we multiply by a vector valued test function  $\boldsymbol{\psi}_s \in [H^1(\Omega_0^s)]^3$ , and integrate in  $\Omega_0^s$  thus obtaining: find  $\mathbf{d}_s(t) \in [H^1(\Omega_0^s)]^3$  such that

$$\begin{aligned} & \int_{\Omega_0^s} \rho_s \frac{\partial^2 \mathbf{d}_s}{\partial t^2} \cdot \boldsymbol{\psi}_s \, d\Omega_0^s + \int_{\Omega_0^s} \mathbf{P}(\mathbf{d}_s) : \nabla_0 \boldsymbol{\psi}_s \, d\Omega_0^s \\ & + \sum_{\eta \in \{ept, base\}} \int_{\Gamma_0^\eta} \left[ (\mathbf{N}_s \otimes \mathbf{N}_s) \left( K_\perp^\eta \mathbf{d}_s + C_\perp^\eta \frac{\partial \mathbf{d}_s}{\partial t} \right) \right. \\ & \quad \left. (\mathbf{I} - \mathbf{N}_s \otimes \mathbf{N}_s) \left( K_\parallel^\eta \mathbf{d}_s + C_\parallel^\eta \frac{\partial \mathbf{d}_s}{\partial t} \right) \right] : \nabla_0 \boldsymbol{\psi}_s \, d\Omega_0^s, \\ & = \int_{\Gamma_0^{endo}} p^{endo} \mathbf{N}_s \cdot \boldsymbol{\psi}_s \, d\Gamma_0^{endo}, \quad \text{for all } t \in (0, T], \\ & \mathbf{d}_s(0) = \mathbf{d}_{s,0}, \quad \frac{\partial \mathbf{d}_s}{\partial t}(0) = \dot{\mathbf{d}}_{s,0}, \end{aligned} \tag{1.16}$$

for every  $\boldsymbol{\psi}_s \in [H^1(\Omega_0^s)]^3$ .

### Prestress

A common problem which has to be considered in the mathematical modeling of fluid-structure interaction (FSI) phenomena is that the reference geometry of the structure does not necessarily correspond to a stress-free configuration. In our case, this is due to the fact that at the initial time  $t = 0$  the blood pressure  $\bar{p}^{endo} = p^{endo}(0) > 0$  exerts a force on the endocardium walls and hence the net force acting on the myocardium is nonzero. This implies that solving problem (1.15) with a physiological endocardial pressure  $\bar{p}^{endo} > 0$  would give rise to non-physiological displacements as the internal stresses are not in equilibrium with the intraventricular blood's pressure. To take into account this behavior, two strategies have been proposed in literature to address this issue:

*Pressure preload* [Eriksson et al., 2013, Rossi, 2014, Takizawa et al., 2010, Tezduyar et al., 2008]: the reference geometry  $\Omega_0$  is loaded with the prescribed pressure  $\bar{p}^{endo}$ . This is done by iteratively solving the steady variant of the mechanics problem (1.15) while gradually incrementing the pressure until it reaches the desired value  $\bar{p}^{endo}$ . The displacement field so obtained is then used as an initial datum  $\mathbf{d}_{s,0}$  for the unsteady problem.

*Pressure prestress* [Hsu and Bazilevs, 2011, Takizawa et al., 2012]: one computes an internal stresses distribution such that the reference geometry is in equilibrium with the blood pressure  $\bar{p}^{endo}$ . An additive decomposition of the stress tensor  $\tilde{\mathbf{P}} = \mathbf{P}(\mathbf{d}_s) + \mathbf{P}_0$  is

operated, where the prestress tensor  $\mathbf{P}_0$  is determined to ensure a null displacement  $\mathbf{d}_{s,0}$  in correspondance of the assigned pressure  $\bar{p}^{endo}$ .

We use the pressure prestress approach since in the preload one the procedure returns a configuration which might be significantly different with respect to the initial geometry, as shown in [Hsu and Bazilevs, 2011]. In order to compute  $\mathbf{P}_0$  according to this approach, we proceed as in [Gerbi et al., 2017] by adapting the method proposed in [Hsu and Bazilevs, 2011] to our model. In particular, we look for a vector  $\hat{\mathbf{d}}_{s,0}$  and a tensor  $\mathbf{P}_0$  such that

$$\begin{cases} -\nabla_0 \cdot \mathbf{P}(\hat{\mathbf{d}}_{s,0}) = \nabla_0 \cdot \mathbf{P}_0 & \text{in } \Omega_0^s, \\ (\mathbf{N}_s \otimes \mathbf{N}_s) K_{\perp}^{\eta} \hat{\mathbf{d}}_{s,0} + (\mathbf{I} - \mathbf{N}_s \otimes \mathbf{N}_s) K_{\parallel}^{\eta} \hat{\mathbf{d}}_{s,0} + \mathbf{P}(\hat{\mathbf{d}}_{s,0}) \mathbf{N}_s = 0 & \text{on } \Gamma_0^{\eta}, \\ (\mathbf{P}(\hat{\mathbf{d}}_{s,0}) + \mathbf{P}_0) \mathbf{N}_s = \bar{p}^{endo} \mathbf{N}_s & \text{on } \Gamma_0^{endo}, \end{cases} \quad (1.17)$$

with  $\hat{\mathbf{d}}_{s,0} \approx \mathbf{0}$ . We then use the stress tensor  $\tilde{\mathbf{P}}(\mathbf{d}) = \mathbf{P}(\mathbf{d}_s) + \mathbf{P}_0$  in place of  $\mathbf{P}(\mathbf{d}_s)$  in the first equation of problem (1.15), and set  $\mathbf{d}_{s,0} = \hat{\mathbf{d}}_{s,0}$ ,  $\dot{\mathbf{d}}_{s,0} = \mathbf{0}$ . With this choice, since the pair  $(\hat{\mathbf{d}}_{s,0}, \mathbf{P}_0)$  is a solution of Eq. (1.17), the myocardium is in mechanical equilibrium at  $t = 0$ .

The weak formulation of Eq. (1.17) reads: find  $\hat{\mathbf{d}}_{s,0} \in [H^1(\Omega_0^s)]^3$  and  $\mathbf{P}_0 \in [L^2(\Omega_0^s)]^{3 \times 3}$  such that

$$\begin{aligned} \int_{\Omega_0^s} \mathbf{P}(\hat{\mathbf{d}}_{s,0}) : \nabla_0 \boldsymbol{\psi}_s \, d\Omega_0^s + \sum_{\eta \in \{epi, base\}} \int_{\Gamma_0^{\eta}} [(\mathbf{N}_s \otimes \mathbf{N}_s) K_{\perp}^{\eta} \mathbf{d}_s + (\mathbf{I} - \mathbf{N}_s \otimes \mathbf{N}_s) K_{\parallel}^{\eta} \mathbf{d}_s] : \nabla_0 \boldsymbol{\psi}_s \, d\Omega_0^s, \\ = \int_{\Gamma_0^{endo}} \bar{p}^{endo} \mathbf{N}_s \cdot \boldsymbol{\psi}_s \, d\Gamma_0^{endo} - \int_{\Omega_0^s} \mathbf{P}_0 : \boldsymbol{\psi}_s \, d\Omega_0^s, \end{aligned}$$

for every  $\boldsymbol{\psi}_s \in [H^1(\Omega_0^s)]^3$ .

#### 1.3.2 Active mechanics

A fundamental property of the myocardium is the ability to actively change its own configuration even without any externally applied load, as depicted in Figure 1.9; indeed, the mechanical activation induced by the electrophysiology is responsible for such activation. Two main approaches have been proposed in order to model this phenomenon, called *active stress* [Smith et al., 2004, Panfilov et al., 2005, Göktepe and Kuhl, 2010] and *active strain* [Ambrosi and Pezzuto, 2012, Cherubini et al., 2008, Giansesio and Musesti, 2017a, Taber and Perucchio, 2000, Nardinocchi and Teresi, 2007, Nobile et al., 2012]. Both the active stress and active strain models exhibit advantages and disadvantages. Our work is based on the active strain formulation as this approach leads to a problem which enjoys better mathematical properties including admitting the existence of solutions.

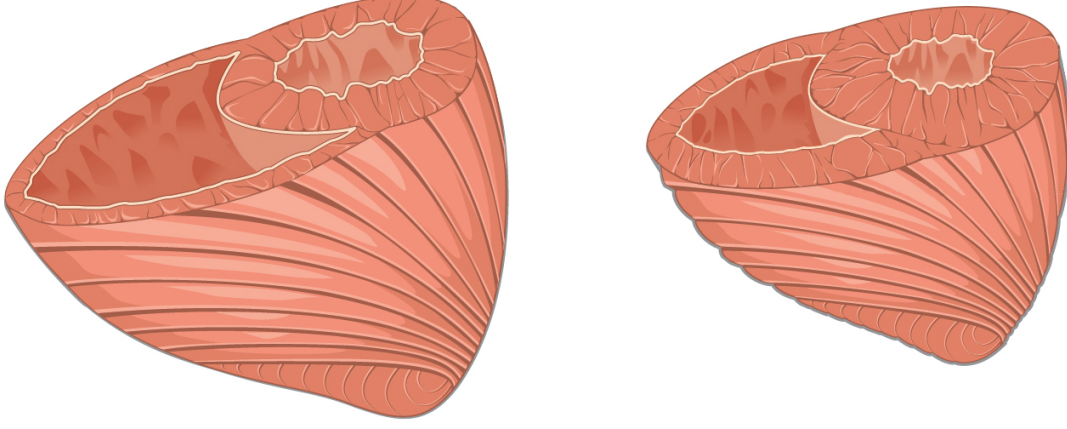


Figure 1.9 – The two ventricles in relaxed (left) and contracted (right) configurations.

Conversely, the active stress approach leads to more complicated formulations of the mechanical problem. An in-depth discussion of the topic can be found in [Ambrosi and Pezzuto, 2012].

From now on, for clarity, we refer to the passive (or elastic) component of the stress tensor as  $\mathbf{P}_E$ , whereas we denote with  $\mathbf{P}$  the tensor including both the active and the passive contributions (see also Appendix B.4).

### Active stress

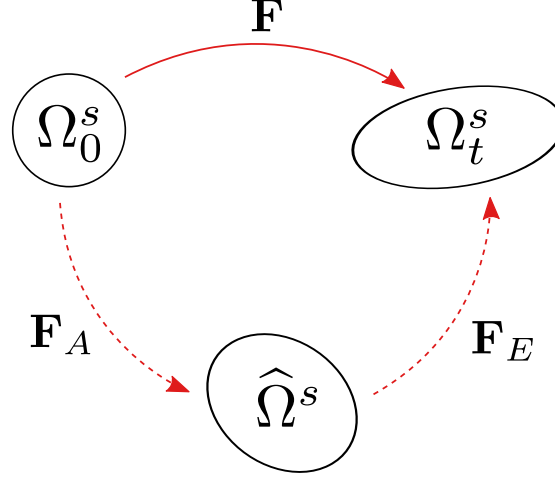
A common and simple way to take into account the active role of the cardiomyocytes consists in assuming an additive decomposition of the stress tensor  $\mathbf{P}$  as:

$$\mathbf{P} = \mathbf{P}_A + \mathbf{P}_E,$$

where  $\mathbf{P}_A$  and  $\mathbf{P}_E$  represent the active and the passive components of the stress, respectively. Such assumption is widely used for simulations of the electromechanical activity of the heart [Nash and Hunter, 2000, Sainte-Marie et al., 2006, Göktepe and Kuhl, 2010]; in these works, the active stress tensor is modeled as

$$\frac{1}{\rho_s} \mathbf{P}_A = T_A \mathbf{f} \otimes \mathbf{f}_0,$$

where  $T_A$  represents the magnitude of the stress in the fibers direction due to the electrical stimulus, while  $\mathbf{P}_E$  is the first Piola-Kirchhoff tensor used to model the passive mechanics, defined in (1.11).


 Figure 1.10 – The active strain decomposition of the strain tensor  $\mathbf{F}$ .

### Active strain

This approach considers the decomposition of the active and passive components of the deformation tensor  $\mathbf{F}$  as in [Lee and Liu, 1967]; such decomposition is applied to the isochoric part of this tensor, thus reading:

$$\mathbf{F} = \mathbf{F}_E \mathbf{F}_A = \mathbf{F}_v \bar{\mathbf{F}}_E \mathbf{F}_A,$$

where we identified the passive (isochoric)  $\bar{\mathbf{F}}_E$  and the active  $\mathbf{F}_A$  deformations, while  $\mathbf{F}_v$  is defined in Eq. (1.13). Within this approach, a virtual intermediate state  $\hat{\Omega}^s$ , representing the active part of the deformation between the reference domain  $\Omega_0^s$  and the deformed one  $\Omega_t^s$  (see Figure. 1.10), is introduced. The domain  $\hat{\Omega}^s$  is reached from  $\Omega_0^s$  by applying a prescribed active transformation (which we will specify later) represented by the tensor  $\mathbf{F}_A$ . On the other hand, the material's elastic response to the prescribed active transformation is embedded in the tensor  $\mathbf{F}_E$  and finally transforms  $\hat{\Omega}^s$  into  $\Omega_t^s$ . The tensor  $\mathbf{P}$  in  $\Omega_0^s$  with respect to the total displacement  $\mathbf{d}_s$  of the tissue is then obtained by applying a pull-back to the stress computed in the intermediate state  $\hat{\Omega}^s$ , i.e.:

$$\mathbf{P} = \det(\mathbf{F}_A) \mathbf{P}_E \mathbf{F}_A^{-T}. \quad (1.18)$$

The following models for the active tensor  $\mathbf{F}_A$  are available in literature:

- **Transversely isotropic activation**

Since myocytes do not change their volume significantly during contraction and the deformation mainly occurs in the fibers direction [Boyett et al., 1991], it is assumed that

$$\mathbf{F}_A = \gamma_1 \mathbf{f}_0 \otimes \mathbf{f}_0 + \gamma_2 (\mathbf{I} - \mathbf{f}_0 \otimes \mathbf{f}_0).$$

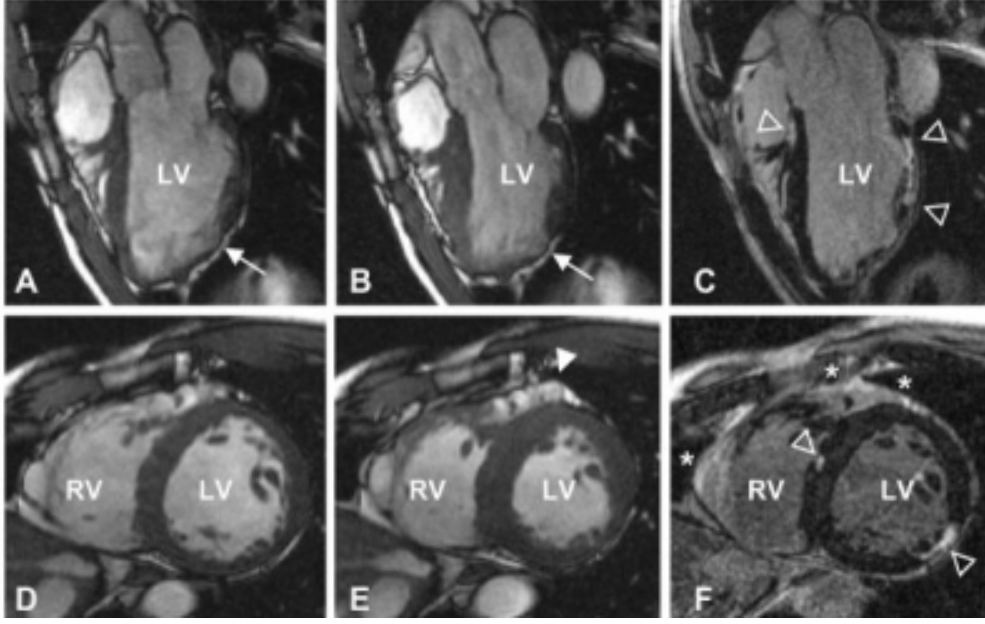


Figure 1.11 – Sagittal (top row) and axial (bottom row) views of the LV at three different moments of the heartbeat. The thickness of the LV walls increases significantly during the systolic phase.

By imposing an isochoric deformation, one finds that  $\gamma_2 = \frac{1}{\sqrt{\gamma_1}}$ . Hence, the only independent variable is  $\gamma = \gamma_1$ , which represents the shortening of the fibers provided by the electrophysiological model;  $\gamma$  is a function of time and spatial coordinates in  $\Omega_0$  through the transmembrane potential  $v$ .

- **Orthotropic activation**

An alternative approach [Rossi et al., 2014] considers the following form for the active tensor  $\mathbf{F}_A$ :

$$\mathbf{F}_A = \mathbf{I} + \gamma_f \mathbf{f}_0 \otimes \mathbf{f}_0 + \gamma_s \mathbf{s}_0 \otimes \mathbf{s}_0 + \gamma_n \mathbf{n}_0 \otimes \mathbf{n}_0,$$

where

$$\begin{cases} \gamma_n = k' \left( \frac{1}{\sqrt{1 + \gamma_f}} - 1 \right), \\ \gamma_s = \frac{1}{(1 + \gamma_f)(1 + \gamma_n)} - 1. \end{cases} \quad (1.19)$$

The function  $\gamma_f$  represents the microscopic deformation in the fibers direction and depends on the transmembrane potential  $v$ , while  $k'$  is a parameter that relates the shortening at the microscale to that of the macroscale. The advantage introduced with this model is that it is able to capture the systolic wall thickening [Rossi, 2014] occurring during the systolic phase, as depicted in Figure 1.11.



- **Transmurally non-homogeneous orthotropic activation**

The orthotropic activation fails however to reproduce the heterogeneity of the deformation in the myocardium [Rossi et al., 2014]. Indeed, the different orientation and lever arm of the fibers at the endocardium and at the epicardium is such that the thickening is increased at the endocardium. In light of these observations, a new set of relations based on Eq. (1.19) was proposed in [Barbarotta, 2014, Barbarotta et al., 2017] to overcome this issue. In this case,  $k'$  is no longer a fixed parameter, but a function of the transmural coordinate instead. The proposed equation reads:

$$k'(\lambda) = \bar{k}' \left( \bar{k}_{endo} \frac{\lambda - \lambda_{epi}}{\lambda_{endo} - \lambda_{epi}} + \bar{k}_{epi} \frac{\lambda - \lambda_{endo}}{\lambda_{epi} - \lambda_{endo}} \right),$$

where  $\lambda \in [\lambda_{endo}, \lambda_{epi}]$  is the transmural coordinate and the parameters  $\bar{k}'$ ,  $\bar{k}_{endo}$ , and  $\bar{k}_{epi}$  are tuned depending on the specific case.

In [Giantesio and Musesti, 2017b], it is observed that the correct way to use the active strain approach is that of expliciting the dependence on  $\mathbf{F}_A$  directly in the strain energy function definition and perform the derivation (1.11) with respect to  $\mathbf{F}$ , instead of  $\mathbf{F}_E$  (see Appendix B.4) as is done e.g. in [Giantesio and Musesti, 2017a, Hernández-Gascón et al., 2013, Rossi et al., 2012]. Indeed, if  $\mathbf{F}_A$  depends on the displacement  $\mathbf{d}_s$  (and hence on  $\mathbf{F}$ ) as will be the case in this work, an additional term appears in the definition of  $\mathbf{P}_E$ . Nonetheless, since such dependence is not trivial to explicit in our case, we choose to disregard this additional term. The final form of the first Piola-Kirchhoff stress tensor, which we denote as  $\mathbf{P} = \mathbf{P}(\mathbf{d}_s, \gamma_f)$  to highlight the dependence on the shortening of the fibers, including both the active and the passive contribution, is detailed in Appendix B.4.

#### 1.3.3 Mechanical activation

In order to use the active strain approach, we need to define the shortening of the fibers  $\gamma_f$  once the solution of the electrophysiological problem is obtained. The model to determine  $\gamma_f$  should describe the so called crossbridge cycle [Huxley and Kress, 1985], by which myosin heads and actin (two motor proteins located on the sarcomeres) create a bond followed by a traction caused by the bending of myosin (see Figure 1.12).

Simple models [Rossi, 2014] define it as the solution of an ODE of the form:

$$\frac{d\gamma_f}{dt} = C_1\theta - C_2\gamma_f,$$

where  $C_1$  and  $C_2$  are suitable constants while  $\theta$  can represent either the transmembrane potential  $v$  or one of the gating variables  $w_j$ . However, even if this model is able to capture the smooth mechanical activation, there is no direct connection with experimental data. Other models try to describe the complex dynamics taking place inside the sarcomeres

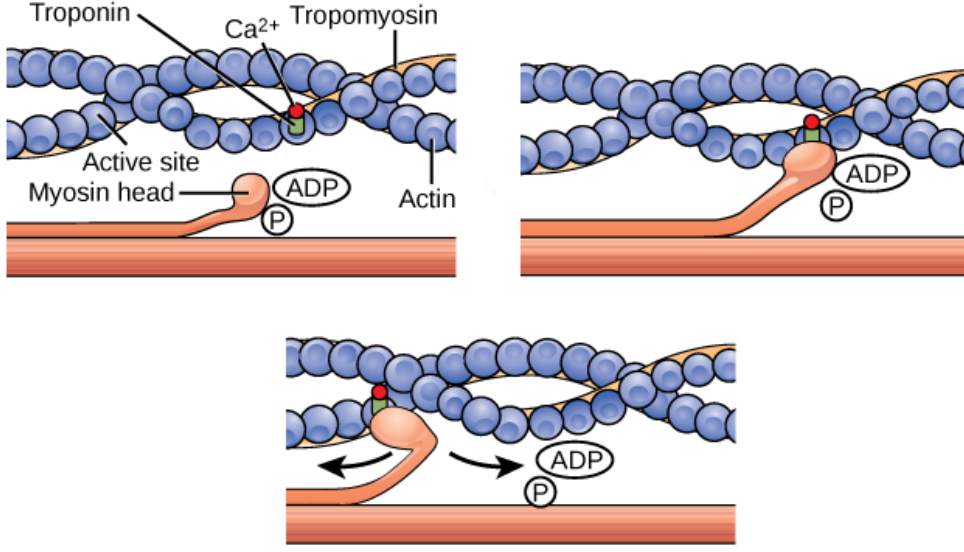


Figure 1.12 – Crossbridge dynamics determining the cardiomyocytes contraction: an active site on actin is exposed as  $Ca^{2+}$  binds troponin (top left); the myosin head forms a crossbridge bond with actin (top right); the myosin head bends releasing ADP and phosphate (bottom).

[Regazzoni et al., 2017], however these usually represent a system of ODEs which features a large number of degrees of freedom, making their use for large scale geometries unfeasible. Again in [Ruiz-Baier et al., 2014], the authors propose an activation law following the work in [Stålhand et al., 2011] and based on principles of internal state theory. It is assumed, as in other works [Hunter et al., 1997], that the shortening of the fibers is mainly due to the calcium ions concentration level  $c = [Ca^{2+}]$ . The model proposed in [Ruiz-Baier et al., 2014], modified with the addition of a diffusion term in [Gerbi et al., 2017], reads:

$$\begin{cases} \frac{\partial \gamma_f}{\partial t} - \frac{\varepsilon}{g(c)} \Delta_0 \gamma_f = \frac{1}{g(c)} \Phi(c, \gamma_f, \mathbf{d}_s) & \text{in } \Omega_0^s \times (0, T], \\ \nabla_0 \gamma_f \cdot \mathbf{N}_s = 0 & \text{on } \partial \Omega_0^s \times (0, T], \\ \gamma_f = 0 & \text{in } \Omega_0^s \times \{0\}. \end{cases} \quad (1.20)$$

Here,  $g(c) = \hat{\mu}_A c^2$ , while the active force  $\Phi(c, \gamma_f, \mathbf{d}_s)$  is defined as:

$$\Phi(c, \gamma_f, \mathbf{d}_s) = H_{c_0}(c) \alpha (c - c_0)^2 R_{FL}(I_{4f}) + \sum_{j=1}^5 (-1)^j (j+1)(j+2) I_{4f} \gamma_f^j,$$

where  $H_{c_0}(c)$  is the Heaviside function centered in the calcium threshold  $c_0$ . The function  $R_{FL}$  is the sarcomere force-length relationship [Gordon et al., 1966, Ruiz-Baier et al.,

2014], which takes the following form:

$$R_{FL}(x) = \chi_{[SL_{min}, SL_{max}]}(\sqrt{x}l_0) \left\{ \frac{d_0}{2} + \sum_{n=1}^3 [d_n \sin(\sqrt{x}l_0) + e_n \cos(\sqrt{x}l_0)] \right\},$$

where  $l_0$  stands for the initial sarcomere length (SL),  $SL_{min}$  and  $SL_{max}$  are the sarcomere's minimum and maximum lengths respectively,  $c_n$  and  $d_n$  are coefficients of a truncated Fourier series fitted to match experimental length-force relations, and  $\alpha, \hat{\mu}_A, \varepsilon \in \mathbb{R}^+$  are parameters which have to be suitably tuned and personalized.

The weak formulation of Eq (1.20) reads: given  $c(t) \in L^2(\Omega_0^s)$  and  $\mathbf{d}_s(t) \in H^1(\Omega_0^s)$  find  $\gamma_f(t) \in H^1(\Omega_0^s)$  such that

$$\begin{aligned} \int_{\Omega_0^s} \frac{\partial \gamma_f}{\partial t} \psi_s \, d\Omega_0^s - \int_{\Omega_0^s} \frac{\varepsilon}{g(c)} \nabla_0 \gamma_f : \nabla_0 \psi_s \, d\Omega_0^s \\ = \int_{\Omega_0^s} \frac{1}{g(c)} \Phi(c, \gamma_f, \mathbf{d}_s) \psi_s \, d\Omega_0^s, \quad \text{for all } t \in (0, T], \\ \gamma_f(0) = 0, \end{aligned}$$

for every  $\psi_s \in H^1(\Omega_0^s)$ .

With respect to the formulation used in [Rossi, 2014], as already done in [Gerbi et al., 2017], we added the diffusive term  $\varepsilon \Delta_0 \gamma_f$  in Eq. (1.20) to yield a model in the form of a PDE. While this is not strictly motivated by physical considerations, it can be interpreted as the upscaling of the microscopic activation at the macroscopic continuum level of the tissue. Moreover, this choice yields a more regular solution  $\gamma_f$  in terms of the space variable  $\mathbf{X}_s$ , from which the numerical approximation will also benefit. Eq. (1.20) will be the activation model used in this work, as it succesfully captures the main features of cellular shortening [Gerbi et al., 2017].

## 1.4 Blood flow modeling

The most important function of the LV is that of pushing the blood to flow into the circulatory system to provide all sort of vital substances to the cells (see Figure 1.13). While the modeling of the blood dynamics is a relevant and complex topic per se, involving issues such as the newtonian assumption for the blood [Cho and Kensey, 1991, Janela et al., 2010, Johnston et al., 2004], in this work we are mainly interested in modeling the fluid in order to take into account for its interaction with the endocardium walls. As will be detailed in the following sections, we model this interaction in two different ways: a) by using the Navier-Stokes equations in Arbitrary Lagrangian Eulerian (ALE) formulation, thus obtaining an integrated full order electrofluidmechanics problem; b) by modeling the pressure at the endocardium only, using a reduced 0D model.

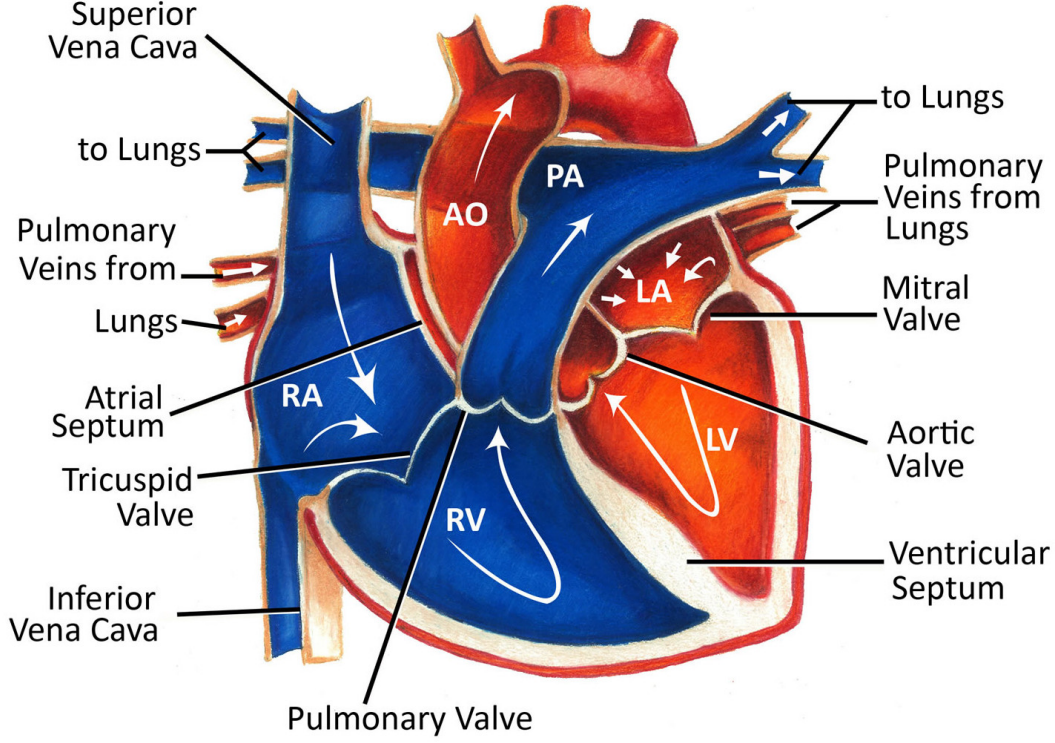


Figure 1.13 – Circulation of the blood in the heart. For what regards the left side of the heart, the oxygenated blood coming from the lungs flows from the LA to the LV in the diastolic phase (with the aortic valve closed), and from the LV into the aorta in the systolic phase (with the mitral valve closed).

#### 1.4.1 Blood dynamics: 3D model

Blood is composed mainly by red blood cells suspended in the plasma, the latter constituting about 55% of the blood volume [Dill and Costill, 1974]; since plasma is mostly composed by water, blood in large vessels can be modeled as a Newtonian fluid [Formaggia et al., 2010]. Hence, we consider the Navier-Stokes equations in ALE formulation (see, among the others, [Bazilevs et al., 2013, Crosetto, 2011, Crosetto et al., 2011a, Formaggia et al., 2010, Nobile, 2001]), as we will be dealing with a moving fluid domain  $\Omega_t^f$ . In this framework, we first identify the reference structure and fluid domains  $\Omega_0^s$ ,  $\Omega_0^f$  and their common interface as  $\Gamma_0^{endo} = \partial\Omega_0^s \cap \partial\Omega_0^f$ ; then, the current fluid domain is defined as

$$\Omega_t^f = \left\{ \mathbf{x}_f = \mathcal{A}_t(\mathbf{X}_f) \mid \mathbf{X}_f \in \Omega_0^f \right\},$$

with the time-dependent map  $\mathcal{A}_t$  determined by the following harmonic extension (Laplace) problem:

$$\begin{cases} -\Delta_0 \mathbf{d}_f = \mathbf{0} & \text{in } \Omega_0^f, \\ \mathbf{d}_f = \mathbf{d}_s(t) & \text{on } \Gamma_0^{endo}, \\ \nabla_0 \mathbf{d}_f \mathbf{N}_f = 0 & \text{on } \partial\Omega_0^f \setminus \Gamma_0^{endo}, \end{cases} \quad (1.21)$$

for all  $t > 0$ . The vector  $\mathbf{N}_f$  is the outward directed unit vector normal to the fluid domain surface, while the map  $\mathcal{A}_t(\mathbf{X}_f) = \mathbf{X}_f + \mathbf{d}_f$  at time  $t$  is determined once a displacement  $\mathbf{d}_s(t)$  is given. The ALE-NS equations then read:

$$\begin{cases} \rho_f \frac{\partial \mathbf{u}}{\partial t} \Big|_{\mathbf{X}_f} + \rho_f ((\mathbf{u} - \mathbf{v}) \cdot \nabla) \mathbf{u} - \nabla \cdot \boldsymbol{\sigma}_f(\mathbf{u}, p) = \mathbf{0} & \text{in } \Omega_t^f, t \in (0, T], \\ \nabla \cdot \mathbf{u} = 0 & \text{in } \Omega_t^f, t \in (0, T], \\ \mathbf{u} \circ \mathcal{A}_t = \frac{\partial \mathbf{d}_s}{\partial t} & \text{on } \Gamma_t^{endo}, t \in (0, T], \\ \mathbf{u} = \mathbf{u}_D & \text{on } \Gamma_{t,D}^f, t \in (0, T], \\ \boldsymbol{\sigma}_f \mathbf{n}_f = \mathbf{g}_N & \text{on } \Gamma_{t,N}^f, t \in (0, T], \\ \mathbf{u} = \mathbf{u}_0 & \text{in } \Omega_0^f, t = 0. \end{cases} \quad (1.22)$$

where

$$\frac{\partial}{\partial t} \Big|_{\mathbf{X}_f} = \frac{\partial}{\partial t} + \mathbf{v} \cdot \nabla \quad \text{and} \quad \mathbf{v} = \frac{\partial \mathbf{d}_f}{\partial t}.$$

The vectors  $\mathbf{v}$  and  $\mathbf{u}$  represent the velocity of the fluid domain and of the fluid itself; in our case, it is determined by the deformation of the myocardium at the interface  $\Gamma_0^{endo}$  which is in turn caused by the propagation of the action potential. The Cauchy stress tensor for the fluid is defined as

$$\boldsymbol{\sigma}_f(\mathbf{u}, p) = \mu_f (\nabla \mathbf{u} + (\nabla \mathbf{u})^T) - p \mathbf{I},$$

where  $\mu_f$  is the dynamic viscosity of the fluid and  $p$  the pressure. Finally, the domain boundaries are defined as  $\Gamma_t^{endo} = \mathcal{A}_t(\Gamma_0^{endo})$ ,  $\Gamma_{t,N}^f = \mathcal{A}_t(\Gamma_{0,N}^f)$ , and  $\Gamma_{t,D}^f = \mathcal{A}_t(\Gamma_{0,D}^f)$  with  $\Gamma_0^{endo} \cup \Gamma_{0,N}^f \cup \Gamma_{0,D}^f = \partial\Omega_0^f$ , while  $\mathbf{n}_f$  is the outward surface normal in the deformed configuration. The third equation in (1.22) accounts for the continuity of the fluid and the domain velocities at the endocardium.

The weak formulation of Eq.(1.21) reads: given  $\mathbf{d}_s(t) \in [H^{-1/2}(\Gamma_0^{endo})]^3$ , find

$\mathbf{d}_f \in [H^1(\Omega_0^f)]^3$  such that

$$\begin{aligned} \int_{\Omega_0^f} \nabla_0 \mathbf{d}_f : \nabla_0 \psi_f \, d\Omega_t^f &= 0, & t \in (0, T], \\ \mathbf{d}_f &= \mathbf{d}_s(t), & \text{on } \Gamma_0^{endo}, \, t \in (0, T]. \end{aligned}$$

for every  $\psi_f \in [H^1(\Omega_0^f)]^3$ . Regarding Eq.(1.22), it reads: given  $\frac{\partial \mathbf{d}_s}{\partial t} \in [H^{-1/2}(\Gamma_0^{endo})]^3$  and  $\frac{\partial \mathbf{d}_f}{\partial t} \in [H^1(\Omega_t^f)]^3$ , find  $\mathbf{u}_f \in [H^1(\Omega_t^f)]^3$ ,  $p \in L^2(\Omega_t^f)$ , and  $\boldsymbol{\lambda} \in [H^{-1/2}(\Gamma_0^{endo})]^3$  such that

$$\begin{aligned} \int_{\Omega_t^f} \rho_f \left( \frac{\partial \mathbf{u}}{\partial t} \Big|_{\mathbf{x}_f} + \left( \left( \mathbf{u} - \frac{\partial \mathbf{d}_f}{\partial t} \right) \cdot \nabla \right) \mathbf{u} \right) : \psi_f \, d\Omega_t^f \\ + \int_{\Omega_t^f} \boldsymbol{\sigma}_f(\mathbf{u}, p) : \nabla \psi_f \, d\Omega_t^f &= \int_{\Gamma_N^f} \mathbf{g}_N \cdot \psi_f \, d\Gamma_{t,N}^f, & t \in (0, T], \\ \int_{\Omega_t^f} \phi_f \nabla \cdot \mathbf{u} \, d\Omega_t^f &= 0, & t \in (0, T], \\ \int_{\Gamma_0^{endo}} (\mathbf{u} \circ \mathcal{A}_t) \cdot \psi_\Gamma \, d\Gamma_0^{endo} &= \int_{\Gamma_0^{endo}} \frac{\partial \mathbf{d}_s}{\partial t} \cdot \psi_\Gamma \, d\Gamma_0^{endo}, & t \in (0, T], \\ \mathbf{u} &= \mathbf{u}_D & \text{on } \Gamma_{t,D}^f, \, t \in (0, T], \\ \mathbf{u}(0) &= \mathbf{u}_0, \end{aligned} \tag{1.23}$$

for every  $\psi_f \in [H^1(\Omega_t^f)]^3$ ,  $\phi_f \in L^2(\Omega_t^f)$ , and  $\psi_\Gamma \in [H^{-1/2}(\Gamma_0^{endo})]^3$ . When Eq. (1.15) is coupled with Eq. (1.21) and (1.22) we obtain an FSI model. In such a case, the boundary condition in Eq. (1.15) on the interface  $\Gamma_0^{endo}$  must be properly adapted in order to impose the continuity of the structure and the fluid stresses. The condition hence reads:

$$\mathbf{P}(\mathbf{d}_s, \gamma_f) \mathbf{N}_s = -\boldsymbol{\sigma}_f(\mathbf{u}, p) \mathbf{n}_f = -\boldsymbol{\lambda}, \tag{1.24}$$

As a consequence, we add a term to the momentum conservation equation in both (1.16) and (1.23) to weakly impose the continuity of the stresses (see e.g. [Bazilevs et al., 2008, Forti, 2016, Forti et al., 2016, Gee et al., 2011, Hron and Turek, 2006]). These terms are defined as follows:

$$\int_{\Gamma_0^{endo}} \boldsymbol{\lambda} \cdot \psi_s \, d\Gamma_0^{endo}, \quad \int_{\Gamma_0^{endo}} \boldsymbol{\lambda} \cdot (\psi_f \circ \mathcal{A}_t) \, d\Gamma_0^{endo}, \tag{1.25}$$

in (1.16) and (1.23), respectively. The function  $\boldsymbol{\lambda} \in [H^{-1/2}(\Gamma_0^{endo})]^3$  is an auxiliary variable defined on  $\Gamma_0^{endo}$ , and can be regarded as a Lagrange multiplier used to enforce the continuity of the velocities at the interface.

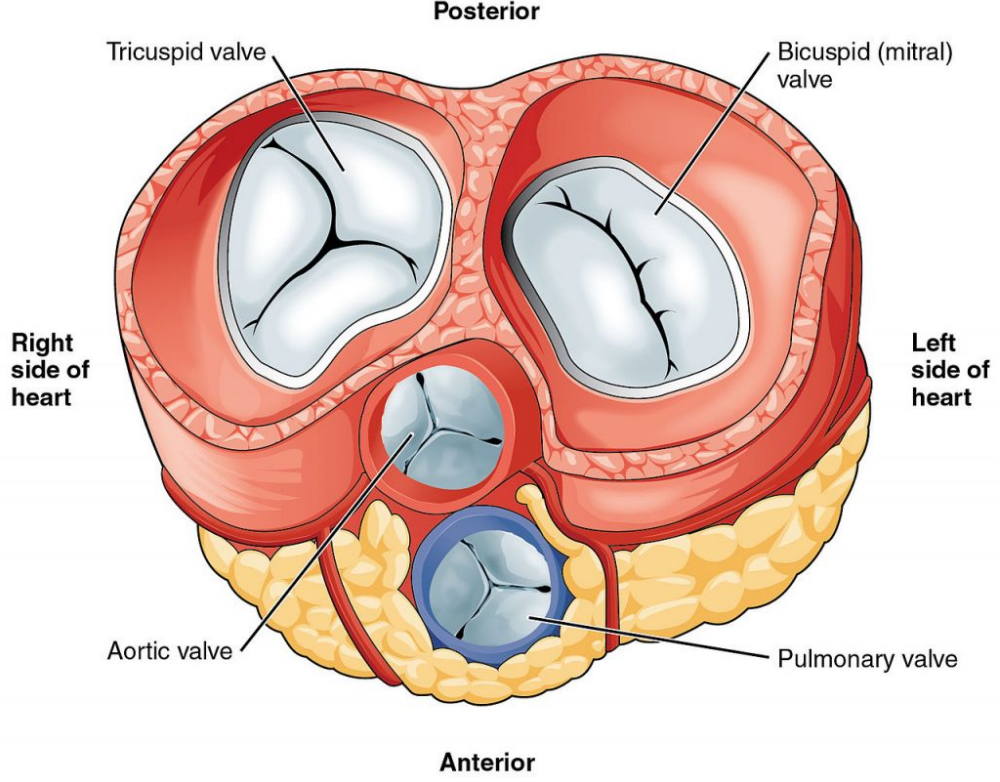


Figure 1.14 – The aortic and mitral valves (left side of the heart), and the pulmonary and tricuspid valves (right side of the heart).

### 1.4.2 Endocardial pressure: 0D model

A model of reduced complexity for the fluid in the LV can be obtained by modeling the endocardial pressure only. We assume in particular that it is uniform on the whole endocardial wall and we denote such value by  $p^{endo}(t)$ , since it does not depend on the space variable. The evolution of  $p^{endo}(t)$  depends on a number of factors: some of them, such as the interaction of the cardiac valves – depicted in Figure 1.14 – with the fluid, are not taken into account in this model. Hence, in order to acknowledge the effect of their state (either open or close), we consider the four phases in which the heartbeat is conventionally split (see Figure 1.15).

Depending on the phase of the heartbeat, we solve different 0D models based on ODEs following [Eriksson et al., 2013, Rossi, 2014, Usyk et al., 2002]. These are, in order:

- Isovolumic contraction: the early stages of the LV contraction drive an increment of the endocardial pressure  $p^{endo}$  from the End Diastolic Pressure (EDP)  $p_{EDP}^{endo}$  (about 10 mmHg) to the value measured in the aorta  $p^{ao}$  (about 85 mmHg). We

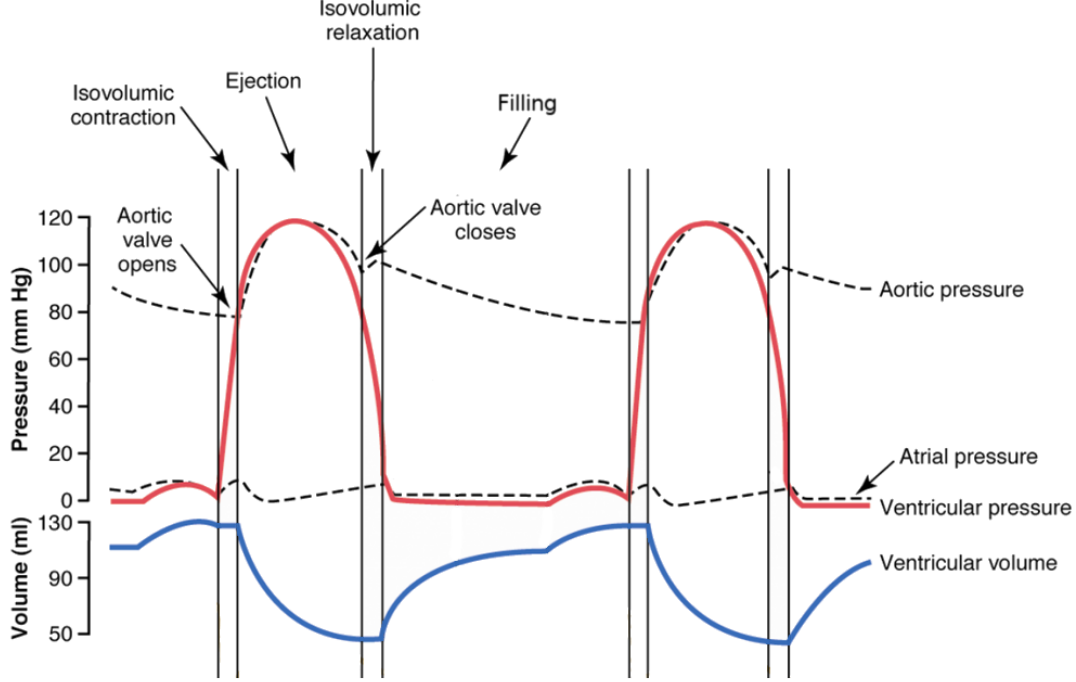


Figure 1.15 – The Wiggers diagram [Katz, 2010] of the left heart depicting the aortic, ventricular, and atrial pressures and the ventricular volume, as well as the four phases of the cardiac cycle.

determine  $p^{endo}$  as the solution of

$$\frac{dV^{endo}}{dt}(p^{endo}) = 0, \quad t \in (0, T_1], \quad (1.26)$$

where  $V^{endo}(0)$  is set to the initial LV volume. Thus, we require that the ventricular volume  $V^{endo}$  remains constant;  $T_1 = T_1(p^{endo})$  is the earliest time occurrence at which  $p^{endo} \geq p^{ao}$ ;

- Ejection: the ventricular volume decreases due to the contraction of the LV forcing the blood to flow through the aortic valve. For this phase we use a two elements windkessel 0D model [Westerhof et al., 2009] in the form:

$$C \frac{dp^{endo}}{dt} = -\frac{p^{endo}}{R} - \frac{dV^{endo}}{dt}, \quad t \in (T_1, T_2], \quad (1.27)$$

with  $p^{endo}(T_1) = p^{ao}$ , where the parameters  $C, R > 0$  represent the capacitance and resistance of the electric circuit analogy mimicking the blood flow in the aorta. The phase ends when  $p^{endo}$  become smaller than  $p^{ao}$ , thus causing the closing of the aortic valve. Since we do not model the evolution of the aortic pressure over time, we set in Eq. (1.27)  $T_2 = T_2(V^{endo})$  as soon as  $\frac{dV^{endo}}{dt} \geq 0$ ;



- Isovolumic relaxation: the endocardial pressure  $p^{endo}$  decreases as a consequence of the LV early relaxation while  $V^{endo}$  remains constant and is treated similarly to the isovolumic contraction. We denote the final time of this phase as  $T_3 = T_3(p^{endo})$ , the occurrence at which  $p^{endo} \leq p_{min}^{endo}$  (about 5 mmHg);
- Filling: the pressure drop in the LV causes the opening of the mitral valve, which in turn causes an increment of  $V^{endo}$  due to the blood flowing inside the LV, until both the pressure  $p^{endo}$  and the volume  $V^{endo}$  reach the EDP values. We model this phase by linearly increasing  $p^{endo}$  until it attains the initial value  $p_{EDP}^{endo}$  at the time  $\bar{T}_3 = 0.7$  s, and by keeping its value constant from  $\bar{T}_3$  to the final time  $T = 0.8$  s, that is by imposing

$$\frac{dp^{endo}}{dt} = \varsigma, \quad t \in (T_3, T], \quad (1.28)$$

where

$$\begin{cases} \varsigma = \frac{p_{EDP}^{endo} - p^{endo}(T_3)}{\bar{T}_3 - T_3}, & \text{if } t \in (T_3, \bar{T}_3], \\ \varsigma = 0, & \text{otherwise.} \end{cases} \quad (1.29)$$



## 2 Numerical approximation

In this chapter, we approximate the single core models for the electrophysiology (1.6), (1.7), the mechanical activation (1.20), for the myocardium mechanics (1.15), and the fluid geometry (1.21), and dynamics (1.22) with respect to the space and time independent variables. We use in particular the Finite Element Method (FEM) for the space discretization while Backward Differentiation Formulas (BDF) are employed for the time discretization [Quarteroni et al., 2010] by considering both implicit and semi-implicit schemes.

### 2.1 Space discretization

The FEM discretization of the differential equations introduced in Chapter 1 allows us to obtain systems of ODEs for each core model. With this aim, we first consider two meshes composed of pairwise disjoint tetrahedra  $\mathcal{T}_{s,h}$  and  $\mathcal{T}_{f,h}$ , corresponding to the structure and the fluid domains, respectively, such that  $\cup_{K_s \in \mathcal{T}_{s,h}} K_s = \Omega_0^s$  and  $\cup_{K_f \in \mathcal{T}_{f,h}} K_f = \Omega_0^f$ , where  $h$  is the maximum size of the tetrahedra. We only consider the case of unstructured meshes, conforming at the common interface  $\Gamma_0^{endo}$  [Thompson et al., 1998] that is  $\mathcal{T}_{s,h}|_{\Gamma_0^{endo}} = \mathcal{T}_{f,h}|_{\Gamma_0^{endo}}$  as in Figure 2.1. Then, we define the following finite dimensional spaces of real valued functions and their size:

$$\begin{aligned}\mathcal{X}_{s,h}^r &= \left\{ v \in C^0(\bar{\Omega}_0^s) : v|_{K_s} \in \mathbb{P}^r(K_s) \forall K_s \in \mathcal{T}_{s,h} \right\}, \quad N_{s,r}^{\text{dof}} = \dim(\mathcal{X}_{s,h}^r), \\ \mathcal{X}_{f,h}^r &= \left\{ v \in C^0(\bar{\Omega}_0^f) : v|_{K_f} \in \mathbb{P}^r(K_f) \forall K_f \in \mathcal{T}_{f,h} \right\}, \quad N_{f,r}^{\text{dof}} = \dim(\mathcal{X}_{f,h}^r);\end{aligned}$$

$\mathbb{P}^r(K_s)$  ( $\mathbb{P}^r(K_f)$ ) is the set of polynomials of degree smaller than or equal to  $r$  in the element  $K_s$  ( $K_f$ ), and

$$\mathcal{X}_{\Gamma,h}^r = \mathcal{X}_{s,h}^r|_{\Gamma_0^{endo}} = \mathcal{X}_{f,h}^r|_{\Gamma_0^{endo}}, \quad N_{\Gamma,r}^{\text{dof}} = \dim(\mathcal{X}_{\Gamma,h}^r);$$

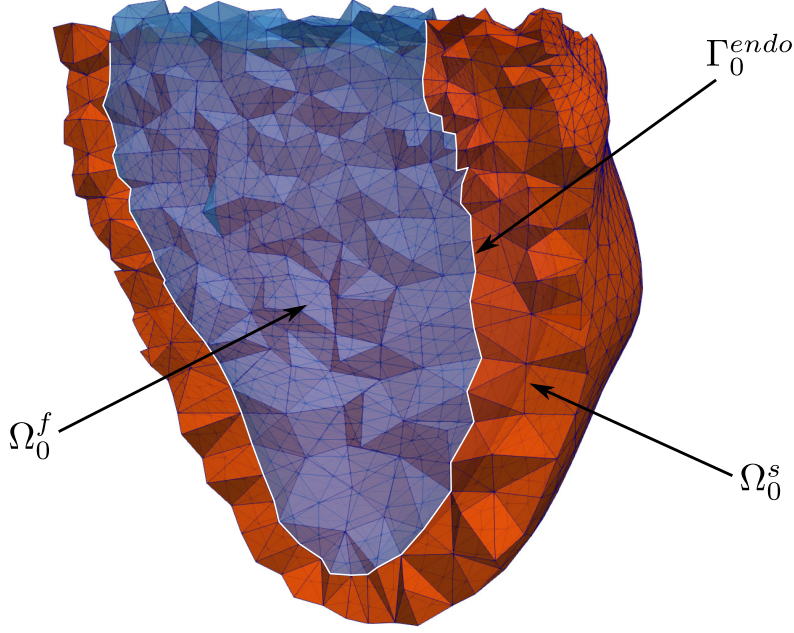


Figure 2.1 – Meshes of the  $\Omega_0^s$  and the  $\Omega_0^f$  domains. The interface  $\Gamma_0^{endo}$  between the two is highlighted.

$\mathcal{X}_{s,h}^r|_{\Gamma_0^{endo}}$  and  $\mathcal{X}_{f,h}^r|_{\Gamma_0^{endo}}$  denote the restriction of  $\mathcal{X}_{s,h}^r$  and  $\mathcal{X}_{f,h}^r$  to  $\Gamma_0^{endo}$ , respectively. Moreover, we set:

$$\mathbf{x}_{s,h}^r = [\mathcal{X}_{s,h}^r]^3, \quad \mathbf{x}_{f,h}^r = [\mathcal{X}_{f,h}^r]^3, \quad \mathbf{x}_{\Gamma,h}^r = [\mathcal{X}_{\Gamma,h}^r]^3,$$

The common interface between the structure and the fluid domains  $\Gamma_0^{endo}$  is the support of the functions belonging to  $\mathcal{X}_{\Gamma,h}^r$ . By indicating with  $\{\psi_{s,j}\}_{j=1}^{N_{s,r}^{dof}}$ ,  $\{\psi_{f,j}\}_{j=1}^{N_{f,r}^{dof}}$ , and  $\{\psi_{\Gamma,j}\}_{j=1}^{N_{\Gamma,r}^{dof}}$  three basis for  $\mathcal{X}_{s,h}^r$ ,  $\mathcal{X}_{f,h}^r$ , and  $\mathcal{X}_{\Gamma,h}^r$ , respectively, it holds:

$$\begin{aligned} \mathcal{X}_{s,h}^r &= \text{span}(\psi_{s,1}, \dots, \psi_{s,N_{s,r}^{dof}}) = \text{span}(\{\psi_{s,j}\}_{j=1}^{N_{s,r}^{dof}}), \\ \mathcal{X}_{s,h}^r &= \text{span}\left(\{\psi_{s,j}^1\}_{j=1}^{N_{s,r}^{dof}}, \{\psi_{s,j}^2\}_{j=1}^{N_{s,r}^{dof}}, \{\psi_{s,j}^3\}_{j=1}^{N_{s,r}^{dof}}\right), \quad \psi_{s,j}^k = \psi_{s,j} \mathbf{e}_k, \\ \mathcal{X}_{f,h}^r &= \text{span}(\psi_{f,1}, \dots, \psi_{f,N_{f,r}^{dof}}) = \text{span}(\{\psi_{f,j}\}_{j=1}^{N_{f,r}^{dof}}), \\ \mathcal{X}_{f,h}^r &= \text{span}\left(\{\psi_{f,j}^1\}_{j=1}^{N_{f,r}^{dof}}, \{\psi_{f,j}^2\}_{j=1}^{N_{f,r}^{dof}}, \{\psi_{f,j}^3\}_{j=1}^{N_{f,r}^{dof}}\right), \quad \psi_{f,j}^k = \psi_{f,j} \mathbf{e}_k, \\ \mathcal{X}_{\Gamma,h}^r &= \text{span}(\psi_{\Gamma,1}, \dots, \psi_{\Gamma,N_{\Gamma,r}^{dof}}) = \text{span}(\{\psi_{\Gamma,j}\}_{j=1}^{N_{\Gamma,r}^{dof}}), \\ \mathcal{X}_{\Gamma,h}^r &= \text{span}\left(\{\psi_{\Gamma,j}^1\}_{j=1}^{N_{\Gamma,r}^{dof}}, \{\psi_{\Gamma,j}^2\}_{j=1}^{N_{\Gamma,r}^{dof}}, \{\psi_{\Gamma,j}^3\}_{j=1}^{N_{\Gamma,r}^{dof}}\right), \quad \psi_{\Gamma,j}^k = \psi_{\Gamma,j} \mathbf{e}_k, \end{aligned} \tag{2.1}$$

where  $\mathbf{e}_k$  is the  $k$ -th unit vector of  $\mathbb{R}^3$ . For the sake of clearness, we will use the same index for the basis of every space in (2.1) even if their number may be different. In particular, regarding the vector valued basis functions for  $\mathcal{X}_{s,h}^r$ ,  $\mathcal{X}_{f,h}^r$ , and  $\mathcal{X}_{\Gamma,h}^r$ , we will write:

$$\begin{aligned} \psi_{s,j} & \text{ for } j = j_s + (k-1)N_{s,r}^{\text{dof}} = 1, \dots, 3N_{s,r}^{\text{dof}}, \quad (j_s = 1, \dots, N_{s,r}^{\text{dof}}, k = 1, 2, 3), \\ \psi_{f,j} & \text{ for } j = j_f + (k-1)N_{f,r}^{\text{dof}} = 1, \dots, 3N_{f,r}^{\text{dof}}, \quad (j_f = 1, \dots, N_{f,r}^{\text{dof}}, k = 1, 2, 3), \\ \psi_{\Gamma,j} & \text{ for } j = j_\Gamma + (k-1)N_{\Gamma,r}^{\text{dof}} = 1, \dots, 3N_{\Gamma,r}^{\text{dof}}, \quad (j_\Gamma = 1, \dots, N_{\Gamma,r}^{\text{dof}}, k = 1, 2, 3). \end{aligned}$$

We then denote by  $\{\mathbf{X}_j^s\}_{j=1}^{N_{s,r}^{\text{dof}}}$ ,  $\{\mathbf{X}_j^f\}_{j=1}^{N_{f,r}^{\text{dof}}}$ ,  $\{\mathbf{X}_j^\Gamma\}_{j=1}^{N_{\Gamma,r}^{\text{dof}}}$  the set of the Degrees of Freedom (DoFs) associated to  $\mathcal{X}_{s,h}^r, \mathcal{X}_{s,h}^r$ , to  $\mathcal{X}_{f,h}^r, \mathcal{X}_{f,h}^r$ , and to  $\mathcal{X}_{\Gamma,h}^r, \mathcal{X}_{\Gamma,h}^r$ , respectively.

Functions in both  $\mathcal{X}_{s,h}^r$  and  $\mathcal{X}_{f,h}^r$  can be projected, at the algebraic level, on  $\mathcal{X}_{\Gamma,h}^r$  by using the following operators:

$$\begin{aligned} \Pi_\Gamma^s & \in \mathbb{R}^{N_{\Gamma,r}^{\text{dof}} \times N_{s,r}^{\text{dof}}} : \bar{\mathbf{v}}_s \longmapsto \Pi_\Gamma^s \bar{\mathbf{v}}_s, \\ \Pi_\Gamma^f & \in \mathbb{R}^{N_{\Gamma,r}^{\text{dof}} \times N_{f,r}^{\text{dof}}} : \bar{\mathbf{v}}_f \longmapsto \Pi_\Gamma^f \bar{\mathbf{v}}_f, \end{aligned}$$

where  $\bar{\mathbf{v}}_s$  ( $\bar{\mathbf{v}}_f$ ) is a vector containing the nodal values of  $\mathbf{v}_s \in \mathcal{X}_{s,h}^r$  ( $\mathbf{v}_f \in \mathcal{X}_{f,h}^r$ );  $\Pi_\Gamma^s$  ( $\Pi_\Gamma^f$ ) maps the degrees of freedom of  $\mathcal{X}_{s,h}^r$  ( $\mathcal{X}_{f,h}^r$ ) belonging to  $\Gamma_0^{\text{endo}}$  to those of  $\mathcal{X}_{\Gamma,h}^r$ . In matrix form, the operators can be written as

$$(\Pi_\Gamma^s)_{ij} = \begin{cases} 1 & \text{if } \mathbf{X}_i^\Gamma = \mathbf{X}_j^s, \\ 0 & \text{otherwise,} \end{cases} \quad (\Pi_\Gamma^f)_{ij} = \begin{cases} 1 & \text{if } \mathbf{X}_i^\Gamma = \mathbf{X}_j^f, \\ 0 & \text{otherwise.} \end{cases}$$

Finally, we set

$$\mathbf{\Pi}_\Gamma^s = \text{diag}(\Pi_\Gamma^s, \Pi_\Gamma^s, \Pi_\Gamma^s), \quad \mathbf{\Pi}_\Gamma^f = \text{diag}(\Pi_\Gamma^f, \Pi_\Gamma^f, \Pi_\Gamma^f).$$

Once these definitions have been established, we can finally introduce the trial solutions in the Galerkin-FEM subspace  $v_h, v_{E,h}, \gamma_h, \mathbf{d}_{s,h}, \mathbf{d}_{f,h}, \mathbf{u}_h, p_h$ , and  $\boldsymbol{\lambda}_h$ , whose definition is reported in Table 2.1, approximating  $v, v_E, \gamma_f, \mathbf{d}_s, \mathbf{d}_f, \mathbf{u}, p$ , and  $\boldsymbol{\lambda}$ , respectively; moreover, we denote by  $\bar{\mathbf{v}}_h, \bar{\mathbf{v}}_{E,h}, \bar{\gamma}_h, \bar{\mathbf{d}}_{s,h}, \bar{\mathbf{d}}_{f,h}, \bar{\mathbf{u}}_{f,h}$ , and  $\bar{\boldsymbol{\lambda}}_h$  the vectors containing the nodal values of the aforementioned functions. We remark that, from now on, we drop the subscript from  $\gamma_f$  to avoid confusion with the one used to distinguish the fluid displacement from the structure displacement.

### 2.1.1 Ionic model

The ionic model does not explicitly depend on the space variable, however its equations depend on the value of  $v$  which is not uniform in  $\Omega_0^s$ . Thus, we write the equations of the ionic model in each nodal value  $\mathbf{X}_j^s, j = 1, \dots, N_{s,r}^{\text{dof}}$ . The semi-discrete formulation

| Model                             | Label         | Domain                   | FE function  | FE vector  |
|-----------------------------------|---------------|--------------------------|--|--|
| Ionic                             | $\mathcal{I}$ | $\Omega_0^s$             | $w_h^l(t) = \sum_{j=1}^{N_{s,r}^{\text{dof}}} w_j^l(t) \psi_{s,j}, \quad w_j^l(t) \approx w_l(\mathbf{X}_j^s, t)$  | $\bar{\mathbf{w}}^l(t) = \left\{ w_j^l(t) \right\}_{j=1}^{N_{s,r}^{\text{dof}}}$<br>$\bar{\mathbf{w}}(t) = \left\{ \mathbf{w}^l(t) \right\}_{l=1}^{N_I}$ |
| Mono/<br>bidomain                 | $\mathcal{E}$ | $\Omega_0^s$             | $v_h(t) = \sum_{j=1}^{N_{s,r}^{\text{dof}}} v_j(t) \psi_{s,j}, \quad v_j(t) \approx v(\mathbf{X}_j^s, t),$<br>$v_{E,h}(t) = \sum_{j=1}^{N_{s,r}^{\text{dof}}} v_{E,j}(t) \psi_{s,j}, \quad v_{E,j}(t) \approx v(\mathbf{X}_j^s, t)$                          | $\bar{\mathbf{v}}(t) = \{v_j(t)\}_{j=1}^{N_{s,r}^{\text{dof}}}$<br>$\bar{\mathbf{v}}_E(t) = \{v_{E,j}(t)\}_{j=1}^{N_{s,r}^{\text{dof}}}$                 |
| Activation                        | $\mathcal{A}$ | $\Omega_0^s$             | $\gamma_h(t) = \sum_{j=1}^{N_{s,r}^{\text{dof}}} \gamma_j(t) \psi_{s,j}, \quad \gamma_j(t) \approx \gamma_f(\mathbf{X}_j^s, t)$  | $\bar{\gamma}(t) = \{\gamma_j(t)\}_{j=1}^{N_{s,r}^{\text{dof}}}$   |
| Structure<br>displacement         | $\mathcal{M}$ | $\Omega_0^s$             | $\mathbf{d}_{s,h}(t) = \sum_{j=1}^{3N_{s,r}^{\text{dof}}} d_{s,j}(t) \psi_{s,j}, \quad d_{s,j}(t) \approx \mathbf{d}_s(\mathbf{X}_j^s, t) \cdot \mathbf{e}_k$  | $\bar{\mathbf{d}}_s(t) = \{d_{s,j}(t)\}_{j=1}^{3N_{s,r}^{\text{dof}}}$   |
| Fluid<br>displacement             | $\mathcal{G}$ | $\Omega_0^f$             | $\mathbf{d}_{f,h}(t) = \sum_{j=1}^{3N_{f,r}^{\text{dof}}} d_{f,j}(t) \psi_{f,j}, \quad d_{f,j}(t) \approx \mathbf{d}_f(\mathbf{X}_j^f, t) \cdot \mathbf{e}_k$  | $\bar{\mathbf{d}}_f(t) = \{d_{f,j}(t)\}_{j=1}^{3N_{f,r}^{\text{dof}}}$   |
| Fluid<br>velocity and<br>pressure | $\mathcal{F}$ | $\Omega_t^f$             | $\mathbf{u}_h(t) = \sum_{j=1}^{3N_{f,r}^{\text{dof}}} u_j(t) \psi_{f,j}, \quad u_j(t) \approx \mathbf{u}(\mathbf{x}_j^f, t) \cdot \mathbf{e}_k$<br>$p_h(t) = \sum_{j=1}^{N_{f,r}^{\text{dof}}} p_j(t) \psi_{f,j}, \quad p_j(t) \approx p(\mathbf{x}_j^f, t)$ | $\bar{\mathbf{u}}(t) = \{u_j(t)\}_{j=1}^{3N_{f,r}^{\text{dof}}}$<br>$\bar{\mathbf{p}}(t) = \{p_j(t)\}_{j=1}^{N_{f,r}^{\text{dof}}}$                      |
| Lagrange<br>multipliers           | $\mathcal{L}$ | $\Gamma_0^{\text{endo}}$ | $\lambda_h(t) = \sum_{j=1}^{3N_{\Gamma,r}^{\text{dof}}} \lambda_j(t) \psi_{\Gamma,j}, \quad \lambda_j(t) \approx \lambda(\mathbf{X}_j^\Gamma, t) \cdot \mathbf{e}_k$   | $\bar{\lambda}(t) = \{\lambda_j(t)\}_{j=1}^{3N_{\Gamma,r}^{\text{dof}}}$   |

Table 2.1 – List of finite element functions and vectors, grouped by model. The domain in which the functions are defined is also indicated.

of the ionic model hence reads: given  $\bar{\mathbf{v}}(t)$ , find  $\bar{\mathbf{w}}(t)$  such that

$$\begin{cases} \dot{\bar{\mathbf{w}}}(t) + \mathbb{U}(\bar{\mathbf{v}}(t))\bar{\mathbf{w}}(t) = \mathbf{Q}(\bar{\mathbf{v}}(t)), & t \in (0, T], \\ \bar{\mathbf{w}}(0) = \bar{\mathbf{w}}_0, \end{cases} \quad (2.2)$$

where the diagonal matrix  $\mathbb{U}$  and the vector  $\mathbf{Q}$  are defined as

$$\begin{aligned} \mathbb{U}_{ii}(\bar{\mathbf{v}}) &= \alpha_l(v_i) - \beta_l(v_i), \\ \mathbf{Q}_i(\bar{\mathbf{v}}) &= \alpha_l(v_i)w_l^\infty(v_i), \end{aligned}$$

with  $i = lN_{s,r}^{\text{dof}} + j$ , for  $l = 1, \dots, N_I$ ,  $j = 1, \dots, N_{s,r}^{\text{dof}}$ . Regarding the minimal model, for which  $N_I = 3$ , the form of the terms  $\alpha_l$ ,  $\beta_l$ ,  $w_l^\infty$  is stated in Appendix B.1.

### 2.1.2 Bidomain and monodomain equations

By using the FEM for the space discretization of the monodomain equation we obtain the following semi-discrete problem: given  $\bar{\mathbf{w}}(t)$  and  $\bar{\mathbf{d}}_s(t)$ , find  $\bar{\mathbf{v}}(t)$  such that

$$\begin{cases} \mathbb{M}^s \dot{\bar{\mathbf{v}}}(t) + \mathbb{K}_M(\bar{\mathbf{d}}_s(t))\bar{\mathbf{v}}(t) + \mathbf{I}^{ion}(\bar{\mathbf{v}}(t), \bar{\mathbf{w}}(t)) = \mathbb{M}^s \mathbf{I}^{app}(t), & t \in (0, T], \\ \bar{\mathbf{v}}(0) = \bar{\mathbf{v}}_0, \end{cases} \quad (2.3)$$

where

$$\begin{aligned} \mathbb{M}_{ij}^s &= \int_{\Omega_0^s} \psi_{s,j} \psi_{s,i} \, d\Omega_0^s, \\ \mathbf{I}_i^{app}(t) &= I^{app}(\mathbf{X}_i^s, t), \\ \mathbb{K}_{M,ij}(\bar{\mathbf{d}}_s) &= \int_{\Omega_0^s} (J_h \mathbf{F}_h^{-1} \mathbf{D}_M \mathbf{F}_h^{-T} \nabla_0 \psi_{s,j}) \cdot \nabla_0 \psi_{s,i} \, d\Omega_0^s, \\ \mathbf{I}_i^{ion}(\bar{\mathbf{v}}, \bar{\mathbf{w}}) &= \int_{\Omega_0^s} I^{ion}(v_h, w_h^1, \dots, w_h^{N_I}) \psi_{s,i} \, d\Omega_0^s, \end{aligned}$$

for  $i, j = 1, \dots, N_{s,r}^{\text{dof}}$  and  $\mathbf{F}_h = \frac{\partial \mathbf{d}_h}{\partial \mathbf{X}_s}$ ,  $J_h = \det(\mathbf{F}_h)$ , while the initial value is set to  $\bar{\mathbf{v}}_{0,h} = \left\{ v_0(\mathbf{X}_j^s) \right\}_{j=1}^{N_{s,r}^{\text{dof}}}$ . On the other hand, the bidomain problem reads: given  $\bar{\mathbf{w}}(t)$  and  $\bar{\mathbf{d}}_s(t)$ , find  $(\bar{\mathbf{v}}(t), \bar{\mathbf{v}}_E(t))$  such that

$$\begin{cases} \mathbb{M}^s \dot{\bar{\mathbf{v}}}(t) + \mathbb{K}_I(\bar{\mathbf{d}}_s(t))(\bar{\mathbf{v}}(t) + \bar{\mathbf{v}}_E(t)) + \mathbf{I}^{ion}(\bar{\mathbf{v}}(t), \bar{\mathbf{w}}(t)) = \mathbb{M}^s \mathbf{I}^{app}(t), & t \in (0, T], \\ \mathbb{K}_I(\bar{\mathbf{d}}_s(t))\bar{\mathbf{v}}(t) + \left( \mathbb{K}_I(\bar{\mathbf{d}}_s(t)) + \mathbb{K}_E(\bar{\mathbf{d}}_s(t)) \right) \bar{\mathbf{v}}_E(t) = \mathbf{0}, & t \in (0, T], \\ \bar{\mathbf{v}}(0) = \bar{\mathbf{v}}_0, \\ \bar{\mathbf{v}}_E(0) = \bar{\mathbf{v}}_{E,0}, \end{cases} \quad (2.4)$$

## Chapter 2. Numerical approximation

---

where

$$(\mathbb{K}_{I,E})_{ij}(\bar{\mathbf{d}}_s) = \int_{\Omega_0^s} (J_h \mathbf{F}_h^{-1} \mathbf{D}_{I,E} \mathbf{F}_h^{-T} \nabla_0 \psi_{s,j}) \cdot \nabla_0 \psi_{s,i} \, d\Omega_0^s.$$

The bidomain model in the form of Eq. (2.4) is however not well posed, since the vector  $\bar{\mathbf{v}}_E$  is defined up to an additive constant; in order to close the problem, we force a single entry of vector  $\bar{\mathbf{v}}_E$  to take the value 0, by properly modifying the global system matrix corresponding to the second equation of (2.4).

Regarding the numerical integration of the term  $\mathbf{I}^{ion}$ , at least two possibilities are considered in literature [Pathmanathan et al., 2010, Pathmanathan et al., 2012] for the evaluation of the ionic current at the quadrature nodes. In the first one, called State Variable Interpolation (SVI) [Pathmanathan et al., 2012, Patelli et al., 2017] the variables  $v_h, w_h^1, \dots, w_h^{N_I}$  are evaluated (“interpolated”) at the quadrature nodes  $\tilde{\mathbf{x}}_q^s, q = 1, \dots, N_Q$ , that is

$$\begin{aligned} & \int_{\Omega_0^s} I^{ion} (v_h, w_h^1, \dots, w_h^{N_I}) \psi_{s,i} \, d\Omega_0^s \\ & \approx \sum_{q=1}^{N_Q} I^{ion} \left( \sum_{j=1}^{N_{s,r}^{dof}} v_j, \psi_{s,j}(\tilde{\mathbf{x}}_q^s), \sum_{j=1}^{N_{s,r}^{dof}} w_j^1 \psi_{s,j}(\tilde{\mathbf{x}}_q^s), \dots, \sum_{j=1}^{N_{s,r}^{dof}} w_j^{N_I} \psi_{s,j}(\tilde{\mathbf{x}}_q^s) \right) \omega_q. \end{aligned}$$

This approach corresponds to the standard Galerkin-FEM method. In the second one, known as Ionic Current Interpolation (ICI) [Krishnamoorthi et al., 2013, Pathmanathan et al., 2010], the currents are first evaluated in the degrees of freedom and then interpolated at the quadrature nodes:

$$\begin{aligned} & \int_{\Omega_0^s} I^{ion} (v_h, w_h^1, \dots, w_h^{N_I}) \psi_{s,i} \, d\Omega_0^s, \\ & \approx \sum_{q=1}^{N_Q} \sum_{j=1}^{N_{s,r}^{dof}} I^{ion} (v_j, w_j^1, \dots, w_j^{N_I}) \psi_{s,j}(\tilde{\mathbf{x}}_q^s) \omega_q. \end{aligned}$$

The aim of ICI is that of reducing the computational cost associated to the assembly of the ionic currents term in the SVI case. However, since the computational resources bottleneck in the assembly of the integrated problems considered in this work is represented by the mechanics problem, we rely on the SVI approach.

We also remark that since the ionic currents (zero order) term in both Eq. (2.3) and Eq. (2.4) dominates the diffusion (second order) one, a known numerical issue [Burman and Ern, 2003] may occur and cause numerical instabilities; to avoid them, we use a lumped mass matrix  $\mathbb{M}^L$  in place of  $\mathbb{M}^s$ .



### 2.1.3 Mechanical activation

As already noted, the terms in Eq. (1.20) depend on the calcium concentration  $c(t)$ ; we hence identify with  $\hat{l} \in N_I$  the index such that  $w^{\hat{l}}(t) = c(t)$ . The semi-discrete formulation of (1.20) then reads: given  $\bar{\mathbf{w}}(t)$  and  $\bar{\mathbf{d}}_s(t)$ , find  $\bar{\boldsymbol{\gamma}}(t)$  such that

$$\begin{cases} \mathbb{M}^s \dot{\bar{\boldsymbol{\gamma}}}(t) + \varepsilon \mathbb{K}_\gamma(\bar{\mathbf{w}}(t)) \bar{\boldsymbol{\gamma}}(t) + \boldsymbol{\Phi}(\bar{\mathbf{w}}(t), \bar{\boldsymbol{\gamma}}(t), \bar{\mathbf{d}}_s(t)) = \mathbf{0} & t \in (0, T], \\ \bar{\boldsymbol{\gamma}}(0) = \mathbf{0}, \end{cases} \quad (2.5)$$

where:

$$\begin{aligned} (\mathbb{K}_\gamma)_{ij}(\bar{\mathbf{w}}) &= \int_{\Omega_0^s} \frac{\varepsilon}{\mu_A(w_h^{\hat{l}})^2} \nabla_0 \psi_j \cdot \nabla_0 \psi_i \, d\Omega_0^s, \\ \boldsymbol{\Phi}_i(\bar{\mathbf{w}}, \bar{\boldsymbol{\gamma}}, \bar{\mathbf{d}}_s) &= - \int_{\Omega_0^s} \frac{1}{\mu_A(w_h^{\hat{l}})^2} \Phi(w_h^{\hat{l}}, \gamma_h, \mathbf{d}_{s,h}) \psi_i \, d\Omega_0^s, \end{aligned}$$

for  $i, j = 1, \dots, N_{s,r}^{\text{dof}}$ .

### 2.1.4 Passive and active mechanics

The semi-discrete formulation of the mechanics problem (1.10) is: given  $p^{\text{endo}}(t)$  or  $\bar{\boldsymbol{\lambda}}(t)$ , and  $\bar{\boldsymbol{\gamma}}(t)$ , find  $\bar{\mathbf{d}}_s(t)$  such that

$$\begin{cases} \rho_s \mathbb{M}_3^s \ddot{\bar{\mathbf{d}}}_s(t) + \mathbb{F} \dot{\bar{\mathbf{d}}}_s(t) + \mathbb{G} \bar{\mathbf{d}}_s(t) + \mathbf{S}(\bar{\mathbf{d}}_s(t), \bar{\boldsymbol{\gamma}}(t)) = \boldsymbol{\rho} & t \in (0, T], \\ \bar{\mathbf{d}}_s(0) = \bar{\mathbf{d}}_0, \quad \dot{\bar{\mathbf{d}}}_s(0) = \mathbf{0}, \end{cases} \quad (2.6)$$

where

$$\begin{aligned} \mathbb{M}_{3,ij}^s &= \int_{\Omega_0^s} \boldsymbol{\psi}_{s,j} \cdot \boldsymbol{\psi}_{s,i} \, d\Omega_0^s, \\ \mathbb{F}_{ij}^k &= \sum_{\eta \in \{\text{epi}, \text{base}\}} \int_{\Gamma_0^\eta} \left( C_\perp^\eta(\mathbf{N}_s \otimes \mathbf{N}_s) + C_\parallel^\eta(\mathbf{I} - \mathbf{N}_s \otimes \mathbf{N}_s) \right) \boldsymbol{\psi}_{s,j} \cdot \boldsymbol{\psi}_{s,i} \, d\Gamma_0^\eta, \\ \mathbb{G}_{ij}^k &= \sum_{\eta \in \{\text{epi}, \text{base}\}} \int_{\Gamma_0^\eta} \left( K_\perp^\eta(\mathbf{N}_s \otimes \mathbf{N}_s) + K_\parallel^\eta(\mathbf{I} - \mathbf{N}_s \otimes \mathbf{N}_s) \right) \boldsymbol{\psi}_{s,j} \cdot \boldsymbol{\psi}_{s,i} \, d\Gamma_0^\eta, \\ \mathbf{S}_i(\bar{\mathbf{d}}, \bar{\boldsymbol{\gamma}}) &= \int_{\Omega_0^s} \mathbf{P}(\mathbf{d}_h, \gamma_h) : \nabla_0 \boldsymbol{\psi}_{s,i} \, d\Omega_0^s, \end{aligned}$$

for  $i, j = 1, \dots, 3N_{s,r}^{\text{dof}}$ . Regarding  $\boldsymbol{\rho}$ , it takes two different forms depending if we are considering the electromechanics problem coupled with a given pressure, or the full electrofluidmechanics problem. In the first case, we set

$$\rho_i(t) = \int_{\Gamma_0^{\text{endo}}} p^{\text{endo}}(t) \mathbf{N}_s \cdot \boldsymbol{\psi}_{s,i} \, d\Gamma_0^{\text{endo}}, \quad \text{for } i = 1, \dots, 3N_{s,r}^{\text{dof}},$$

whereas we assume that the only force acting on  $\Gamma_0^{endo}$  is the pressure, considered homogeneous on the interface. On the other hand, if we consider the electrofluidmechanics model,  $\boldsymbol{\rho}$  is used to account for the continuity of the normal component of the stresses, which is imposed weakly as in [Deparis et al., 2016b, Forti, 2016, Forti et al., 2016]; in such a case, recalling (1.24), we define  $\boldsymbol{\rho}$  as

$$\boldsymbol{\rho}(\bar{\boldsymbol{\lambda}}(t)) = \boldsymbol{\Pi}_s^f \bar{\boldsymbol{\lambda}}(t),$$

where

$$\boldsymbol{\Pi}_s^f = \boldsymbol{\Pi}_\Gamma^{sT} \boldsymbol{\Pi}_\Gamma^f.$$

The discretized prestress problem (1.17) can also be written by using the same terms defined for the mechanics problem. Thus, it reads: given  $\bar{p}^{endo} = p^{endo}(0)$ , find  $(\hat{\mathbf{d}}_0, \mathbf{P}_0)$  such that

$$\mathbb{G} \hat{\mathbf{d}}_{s,0} + \mathbf{S}(\hat{\mathbf{d}}_{s,0}) = \bar{\mathbf{p}}^{endo} - \mathbf{S}_0,$$

where  $\mathbf{S}$  does not depend on  $\bar{\gamma}$  since the latter is zero at the initial time, and

$$\mathbf{S}_{0,i} = \int_{\Omega_0^s} \mathbf{P}_0 : \nabla_0 \boldsymbol{\psi}_{s,i} \, d\Omega_0^s, \quad \bar{\mathbf{p}}_i^{endo} = \int_{\Omega_0^s} \bar{p}^{endo}(0) \mathbf{N}_s \cdot \boldsymbol{\psi}_{s,i} \, d\Omega_0^s,$$

for  $i = 1, \dots, 3N_{s,r}^{\text{dof}}$ .

### 2.1.5 Fluid geometry and Navier-Stokes equations

We write the approximated harmonic extension problem (1.21) (steady for each fixed  $t$ ) at first in the following simple form: given  $\bar{\mathbf{d}}_{s,h}(t)$ , find  $\bar{\mathbf{d}}_{f,h}(t)$  such that

$$\begin{cases} \mathbb{K}_G \bar{\mathbf{d}}_{f,h} = \mathbf{0}, \\ \boldsymbol{\Pi}_\Gamma^f \bar{\mathbf{d}}_{f,h} = \boldsymbol{\Pi}_\Gamma^s \bar{\mathbf{d}}_{s,h}, \end{cases} \quad (2.7)$$

with

$$\mathbb{K}_{G,ij} = \int_{\Omega_0^f} \nabla_0 \boldsymbol{\psi}_{f,j} \cdot \nabla_0 \boldsymbol{\psi}_{f,i} \, d\Omega_0^f,$$

for  $i, j = 1, \dots, 3N_{f,r}^{\text{dof}}$ . In order to impose the condition on  $\Gamma_0^{endo}$ , we set

$$\tilde{\mathbb{K}}_G = \mathbb{K}_G|_{\Gamma_0^{endo}}, \quad \boldsymbol{\Pi}_f^s = \boldsymbol{\Pi}_\Gamma^{fT} \boldsymbol{\Pi}_\Gamma^s = \boldsymbol{\Pi}_s^{fT},$$

where  $\mathbb{K}_G|_{\Gamma_0^{endo}}$  is obtained from  $\mathbb{K}_G$  by setting  $\mathbb{K}_{G,\widehat{ij}} = \delta_{\widehat{ij}}$  (the Dirac delta) for every  $\widehat{i} = i_s + (k-1)N_{f,r}^{\text{dof}}$  such that  $\mathbf{X}_{i_s}^f \in \Gamma_0^{endo}$ ; this operation is used to enforce the essential condition on the fluid-structure interface. In this way, we can recast Eq. (2.7) as:

$$\widetilde{\mathbb{K}}_G \bar{\mathbf{d}}_f - \mathbf{\Pi}_f^s \bar{\mathbf{d}}_s = \mathbf{0}. \quad (2.8)$$

We conclude this section by writing the semi-discrete Navier-Stokes equations in ALE formulation (1.22). The problem thus reads: given  $\dot{\bar{\mathbf{d}}}_f(t)$  and  $\dot{\bar{\mathbf{d}}}_s(t)$ , find  $(\bar{\mathbf{u}}(t), \bar{\mathbf{p}}(t), \bar{\boldsymbol{\lambda}}(t))$  such that

$$\begin{cases} \rho_f \mathbb{M}_3^f \dot{\bar{\mathbf{u}}}(t) + \mu_f \mathbb{A} \bar{\mathbf{u}}(t) + \rho_f \mathbb{C}(\bar{\mathbf{u}}(t) - \dot{\bar{\mathbf{d}}}_f(t)) \bar{\mathbf{u}}(t) + \mathbb{B}^T \bar{\mathbf{p}}(t) + \mathbf{\Pi}_\Gamma^{fT} \bar{\boldsymbol{\lambda}}_h(t) = \mathbf{0} & t \in (0, T], \\ \mathbb{B} \bar{\mathbf{u}}(t) = \mathbf{0}, \\ -\mathbf{\Pi}_\Gamma^s \dot{\bar{\mathbf{d}}}_s(t) + \mathbf{\Pi}_\Gamma^f \bar{\mathbf{u}}(t) = \mathbf{0}, \\ \bar{\mathbf{u}}(0) = \mathbf{u}_0, \quad \dot{\bar{\mathbf{u}}}(0) = \mathbf{0}, \end{cases} \quad (2.9)$$

where the terms are:

$$\begin{aligned} \mathbb{M}_{3,ij}^f &= \int_{\Omega_t^f} \boldsymbol{\psi}_{f,j} \cdot \boldsymbol{\psi}_{f,i} \, d\Omega_t^f, \\ \mathbb{A}_{ij} &= \int_{\Omega_t^f} (\nabla \boldsymbol{\psi}_{f,j} + (\nabla \boldsymbol{\psi}_{f,j})^T) : \nabla \boldsymbol{\psi}_{f,i} \, d\Omega_t^f, \\ \mathbb{C}_{ij}(\bar{\mathbf{u}} - \dot{\bar{\mathbf{d}}}_f) &= \int_{\Omega_t^f} ((\mathbf{u}_h - \dot{\mathbf{d}}_{f,h}) \cdot \nabla) \boldsymbol{\psi}_{f,j} \cdot \boldsymbol{\psi}_{f,i} \, d\Omega_t^f, \end{aligned}$$

for  $i, j = 1, \dots, 3N_{f,r}^{\text{dof}}$ , and

$$\mathbb{B}_{ij} = \int_{\Omega_t^f} \nabla \cdot \boldsymbol{\psi}_{f,j} \boldsymbol{\psi}_{f,i} \, d\Omega_t^f$$

for  $i = 1, \dots, N_{f,r}^{\text{dof}}$ ,  $j = 1, \dots, 3N_{f,r}^{\text{dof}}$ .

In Eq. (2.9), additional terms have to be considered. Indeed, it is well known that if incompatible function spaces in the inf-sup sense for the velocity and pressure variables are chosen, as is the case for (2.1), stabilization terms need to be introduced [Quarteroni, 2010], such as those given by the Streamline Upwind Petrov-Galerkin (SUPG) stabilization [Brooks and Hughes, 1982]. On the other hand, a numerical stabilization is required at high Reynolds regimes: in such cases, in order to avoid a very fine spatial discretization and hence a large computational cost, the Variational Multiscale (VMS) method can be exploited leading to the VMS-LES [Forti, 2016, Hughes et al., 2000, Hughes et al., 2001, Bazilevs et al., 2007] – LES standing for Large Eddy Simulation – or the VMS-SUPG [Forti and Dedè, 2015] methods. This allows to take into account the effect of the small scales without actually solving them. In this work, since the Reynolds number

## Chapter 2. Numerical approximation

---

for the blood in the ventricle is around  $2 - 3 \times 10^3$  [Krittian et al., 2010], the fluid is not in the turbulent regime and we will use for simplicity the SUPG stabilization. This accounts to adding the terms  $\mathbf{S}_M^{SUPG}(\bar{\mathbf{u}}, \bar{\mathbf{p}})$  and  $\mathbf{S}_C^{SUPG}(\bar{\mathbf{u}}, \bar{\mathbf{p}})$  to the left hand side of the first and of the second equation of Eq. (2.9), respectively, where:

$$\mathbf{S}_{M,i}^{SUPG}(\bar{\mathbf{u}}, \bar{\mathbf{p}}) = \int_{\Omega_t^f} \left( \rho_f ((\mathbf{u}_h \cdot \nabla) \boldsymbol{\psi}_{f,i}) \cdot \tau_M(\mathbf{u}_h) \mathbf{r}_M(\mathbf{u}_h, p_h) + (\nabla \cdot \boldsymbol{\psi}_{f,i}) \tau_C(\mathbf{u}_h) r_C(\mathbf{u}_h) \right) d\Omega_t^f, \quad (2.10)$$

for  $i = 1, \dots, 3N_{f,r}^{\text{dof}}$ ,

$$\mathbf{S}_{C,i}^{SUPG}(\bar{\mathbf{u}}, \bar{\mathbf{p}}) = \int_{\Omega_t^f} \nabla \boldsymbol{\psi}_{f,i} \cdot \tau_M(\mathbf{u}_h) \mathbf{r}_M(\mathbf{u}_h, p_h) d\Omega_t^f, \quad (2.11)$$

for  $i = 1, \dots, N_{s,r}^{\text{dof}}$  and

$$\begin{aligned} \mathbf{r}_M(\mathbf{u}_h, p_h) &= \rho_f \dot{\mathbf{u}}_h + \rho_f (\mathbf{u}_h - \dot{\mathbf{d}}_{f,h}) \cdot \nabla \mathbf{u}_h + \nabla p_h - \mu_f \Delta \mathbf{u}_h, \\ r_C(\mathbf{u}_h) &= \nabla \cdot \mathbf{u}_h, \\ \tau_M(\mathbf{u}_h) &= \left( \frac{\sigma^2 \rho_f^2}{\Delta t^2} + \frac{\rho_f^2}{h_{K_f}^2} |\mathbf{u}_h|^2 + \frac{\mu_f^2}{h_{K_f}^4} C_r \right)^{-\frac{1}{2}}, \\ \tau_C(\mathbf{u}_h) &= \frac{h_{K_f}^2}{\tau_M(\mathbf{u}_h)}. \end{aligned}$$

$h_{K_f}$  denotes the diameter of the element  $K_f \in \mathcal{T}_{f,h}$ , while  $C_r$  is a constant obtained by an inverse inequality [Quarteroni and Valli, 1994].  $\sigma$  and  $\Delta t$  denote the order of the time discretization and the timestep size (see Section 2.2).

## 2.2 Time discretization

We use Backward Differentiation Formulas (BDFs) for the time discretization of the semi-discrete unsteady single core problems obtained in Section 2.1 by considering both implicit and semi-implicit schemes. In order to better illustrate our methodology, we set

$$\mathbf{z} = (\bar{\mathbf{w}}, \bar{\mathbf{v}}, \bar{\mathbf{v}}_E, \bar{\boldsymbol{\gamma}}, \bar{\mathbf{d}}_s, \bar{\mathbf{d}}_f, \bar{\mathbf{u}}, \bar{\mathbf{p}}, \bar{\boldsymbol{\lambda}})^T,$$

where each block corresponds to the nodal values of the finite element functions associated to one of the core model considered, in the most general case (i.e. the electrofluidmechanics problem with the bidomain equations). We then rewrite the unsteady semi-discrete

problems in a generalized form as:

$$\begin{cases} \mathcal{B}_i \mathbf{z}_i(t) + \mathbf{T}_i(\mathbf{z}(t)) = \mathbf{H}_i(t) & t \in (0, T], & i = 1, 2, 4, 5, 7, \\ \mathbf{z}_i(0) = \mathbf{z}_{i,0}, & & i = 1, 2, 4, 5, 7, \\ \dot{\mathbf{z}}_5(0) = \mathbf{0}, & & \end{cases} \quad (2.12)$$

where

$$\begin{aligned} \mathbf{z}_1 &= \overline{\mathbf{w}}, & \mathbf{z}_2 &= \overline{\mathbf{v}}, & \mathbf{z}_4 &= \overline{\boldsymbol{\gamma}}, & \mathbf{z}_5 &= \overline{\mathbf{d}}_s, & \mathbf{z}_7 &= \overline{\mathbf{u}}, \\ \mathcal{B}_1 &= \mathbb{I} \frac{d}{dt}, & \mathcal{B}_2 &= \mathbb{M}^s \frac{d}{dt}, & \mathcal{B}_4 &= \mathbb{M}^s \frac{d}{dt}, & \mathcal{B}_5 &= \rho_s \mathbb{M}_3^s \frac{d^2}{dt^2}, & \mathcal{B}_7 &= \rho_f \mathbb{M}_3^f \frac{d}{dt}, \end{aligned}$$

and the terms  $\mathbf{T}_i$  and  $\mathbf{H}_i$  are specific of the corresponding core model. In order to obtain a fully discretized formulation using the BDF scheme we exploit the following approximation of the time derivatives:

$$\begin{aligned} \frac{d}{dt} \mathbf{z}_i(t^{n+1}) &\approx \frac{1}{\Delta t} \left( \vartheta_0^I \mathbf{z}_i^{n+1} - \mathbf{z}_i^I \right), & \mathbf{z}_i^I &= \sum_{k=1}^{\sigma} \vartheta_k^I \mathbf{z}_i^{n-k+1}, & i &= 1, 2, 4, 5, 7, \\ \frac{d^2}{dt^2} \mathbf{z}_5(t^{n+1}) &\approx \frac{1}{(\Delta t)^2} \left( \vartheta_0^{II} \mathbf{z}_5^{n+1} - \mathbf{z}_5^{II} \right), & \mathbf{z}_5^{II} &= \sum_{k=1}^{\sigma+1} \vartheta_k^{II} \mathbf{z}_5^{n-k+1}, \end{aligned} \quad (2.13)$$

where  $\Delta t = \frac{T}{N_T}$  is the timestep length,  $N_T$  being the number of timesteps, while the parameters  $\vartheta_k^I, \vartheta_k^{II}, k = 0, \dots, \sigma$  depend on the order  $\sigma$  of the BDF scheme.

In the implicit case, we obtain the nonlinear problems in the form:

$$\mathbf{A}_i(\mathbf{z}^{n+1}) = \mathbf{h}_i^{n+1}, \quad n = \sigma, \dots, N_T - 1, \quad (2.14)$$

with  $\mathbf{z}^n$  assigned for  $n = 0, \dots, \sigma$ . Even though the time discretization was carried out the unsteady problems corresponding to  $i = 1, 2, 4, 5, 7$  only, the form of Eq. (2.14) clearly holds for the steady problems too (i.e. the equations for  $\overline{\boldsymbol{\gamma}}, \overline{\mathbf{d}}_f, \overline{\mathbf{p}},$  and  $\overline{\boldsymbol{\lambda}}$ ). We will hence consider, from now on, Eq. (2.14) for  $i = 1, \dots, 9$ . In the semi-implicit case, on the other hand, we extrapolate the variables in the nonlinear terms  $\mathbf{A}_i(\mathbf{z}^{n+1})$  by means of the Newton-Gregory backward polynomials [Cellier and Kofman, 2006] – as is done, e.g., for the Navier-Stokes equations in [Gervasio et al., 2006] – thus yielding a linear system at each timestep. The extrapolated variables are evaluated as a linear combination of the variables at previous timesteps, with an approximation of the same order  $\sigma$  of the BDF scheme:

$$\mathbf{z}_i(t^{n+1}) \approx \mathbf{z}_i^* = \sum_{k=1}^{\sigma} \beta_k \mathbf{z}_i^{n-k+1}.$$

We thus avoid the nonlinear terms by partially evaluating  $\mathbf{A}_i$  in the extrapolated variable

$\mathbf{z}^*$ , i.e. we approximate the nonlinear term as

$$\mathbf{A}_i(\mathbf{z}^{n+1}) \approx \sum_{j=1}^9 \mathbb{A}_i^j(\mathbf{z}^*) \mathbf{z}_j^{n+1} + \tilde{\mathbf{A}}_i(\mathbf{z}^*). \quad (2.15)$$

By recalling Eq. (2.14), we hence obtain a system in the form:

$$\sum_{j=1}^9 \mathbb{A}_{i,j}(\mathbf{z}^*) \mathbf{z}_j^{n+1} = \mathbf{b}_i^{n+1}, \quad n = \sigma, \dots, N_T - 1,$$

with  $\mathbf{z}^n$  assigned for  $n = 0, \dots, \sigma$  and  $\mathbf{b}_i^{n+1} = \mathbf{h}_i^{n+1} - \tilde{\mathbf{A}}_i(\mathbf{z}^*)$ .

### 2.2.1 Implicit and semi-implicit schemes

Now that the general framework in which we discretize in time the semi-discrete problems has been established, we list the fully discrete formulations used for each core model. In the case of the electrophysiology and of the mechanical activation, both implicit and semi-implicit schemes are proposed. Regarding the mechanics, all the semi-implicit formulations that were tested (not reported) proved not to be stable unless extremely small timesteps were employed, and we hence consider the implicit scheme only. This will however affect also the choice of the scheme for the fluid, since the full FSI part of the problem will be in all cases solved in a monolithic fashion: this choice was made to avoid the so called *added mass effect* [Bathe et al., 1999, Le Tallec and Mouro, 2001, Nobile, 2001, Causin et al., 2005], which is typical of loosely coupled time advancing schemes for haemodynamics problems, where the densities of the fluid and the structure are comparable. As a consequence, for coherence with the mechanics scheme, the fluid will always be solved with an implicit scheme.

#### Ionic model

The fully discretized formulation of the ionic model with the implicit scheme takes, at each timestep, the following form

$$\frac{\vartheta^I}{\Delta t} \bar{\mathbf{w}}^{n+1} + \mathbb{U}(\bar{\mathbf{v}}^{n+1}) \bar{\mathbf{w}}^{n+1} - \mathbf{Q}(\bar{\mathbf{v}}^{n+1}) = \frac{1}{\Delta t} \bar{\mathbf{w}}^I. \quad (2.16)$$

Eq. (2.16) depends both on  $\bar{\mathbf{w}}^{n+1}$  (linearly) and on  $\bar{\mathbf{v}}^{n+1}$  (nonlinearly). If the mono/bidomain is solved at once with the ionic model in a monolithic fashion, the Newton method for (2.16) reads

$$\begin{cases} \mathbb{J}_{\mathcal{I},k}^{n+1} \delta \bar{\mathbf{w}}_{k+1}^{n+1} + \mathbb{J}_{\mathcal{IE},k}^{n+1} \delta \bar{\mathbf{v}}_{k+1}^{n+1} = -\mathbf{r}_{\mathcal{I},k}^{n+1}, \\ \bar{\mathbf{w}}_{k+1}^{n+1} = \bar{\mathbf{w}}_k^{n+1} + \delta \bar{\mathbf{w}}_{k+1}^{n+1}, \end{cases}$$

where the increment  $\delta \bar{\mathbf{v}}_{k+1}^{n+1} = \mathbf{v}_{k+1}^{n+1} - \mathbf{v}_k^{n+1}$  is determined by the simultaneous application of the Newton method to the mono/bidomain equations, and

$$\begin{aligned}\mathbb{J}_{\mathcal{I},k}^{n+1} &= \frac{\vartheta^{\mathbf{I}}}{\Delta t} \mathbb{I} + \mathbb{U}(\bar{\mathbf{v}}_k^{n+1}), \\ \mathbb{J}_{\mathcal{E},k}^{n+1} &= \partial_v \mathbb{U}(\bar{\mathbf{v}}_k^{n+1}) - \partial_v \mathbf{Q}(\bar{\mathbf{v}}_k^{n+1}), \\ \mathbf{r}_{\mathcal{I},k}^{n+1} &= \frac{\vartheta_0^{\mathbf{I}}}{\Delta t} \bar{\mathbf{w}}_k^{n+1} + \mathbb{U}(\bar{\mathbf{v}}_k^{n+1}) \bar{\mathbf{w}}_k^{n+1} - \mathbf{Q}(\bar{\mathbf{v}}_k^{n+1}) - \frac{1}{\Delta t} \bar{\mathbf{w}}^{\mathbf{I}},\end{aligned}$$

where  $\partial_v \mathbb{U} \in \mathbb{R}^{\tilde{N} \times \tilde{N}}$  is a diagonal matrix with  $\tilde{N} = N_I N_{s,r}^{\text{dof}}$ , and  $\partial_v \mathbf{Q} \in \mathbb{R}^{\tilde{N} \times N_{s,r}^{\text{dof}}}$ ; the latter are defined as

$$\begin{aligned}(\partial_v \mathbb{U}^l)_{ii}(\bar{\mathbf{v}}) &= \alpha'_l(v_i) - \beta'_l(v_i), \\ (\partial_v \mathbf{Q}^l)_{ii}(\bar{\mathbf{v}}) &= \alpha'_l(v_i) w_l^\infty(v_i) + \alpha_l(v_i) (w_l^\infty)'(v_i), \\ \partial_v \mathbb{U} &= \text{diag}(\partial_v \mathbb{U}^1, \dots, \partial_v \mathbb{U}^{N_I}), \quad \partial_v \mathbf{Q} = (\partial_v \mathbf{Q}^1, \dots, \mathbf{Q}^{N_I})^T,\end{aligned}$$

for  $i = 1, \dots, N_{s,r}^{\text{dof}}$ ,  $l = 1, \dots, N_I$ .

If we choose to solve Eq. (2.16) in a segregated fashion with respect to the mono/bidomain equations, before the transmembrane potential  $\bar{\mathbf{v}}^{n+1}$  has been determined, we use in its place the value  $\bar{\mathbf{v}}^*$  extrapolated from the previous timesteps. Thus, in such case, we rewrite Eq. (2.16) as

$$\left( \frac{\vartheta_0^{\mathbf{I}}}{\Delta t} \mathbb{I} + \mathbb{U}(\bar{\mathbf{v}}^*) \right) \bar{\mathbf{w}}^{n+1} = \frac{1}{\Delta t} \bar{\mathbf{w}}^{\mathbf{I}} + \mathbf{Q}(\bar{\mathbf{v}}^*). \quad (2.17)$$

We highlight that Eq. (2.17) is a linear system of equations in  $\bar{\mathbf{w}}^{n+1}$  and can hence be solved directly without resorting to the Newton method. Moreover, since the linear system is diagonal, all the equations are uncoupled and can be solved independently. Incidentally, the derivation of a semi-implicit scheme for the ionic model also leads to Eq. (2.17).

### Monodomain and bidomain equations

Several approaches have been proposed and used to solve the monodomain and the bidomain equations, usually together with the equations for the ionic model. For instance, explicit schemes [Heidenreich et al., 2010, Rossi, 2014], implicit schemes [Munteanu and Pavarino, 2009, Potse et al., 2006, Whiteley, 2006], and the so-called implicit-explicit (IMEX) schemes [Ascher et al., 1997, Colli Franzone et al., 2015a, Spiteri and Dean, 2008] have been used in literature. However, explicit and IMEX schemes they tend to have undesirable time-step restrictions to ensure stabilities. In the following, we formulate both an implicit scheme and a semi-implicit one.

## Chapter 2. Numerical approximation

We first consider the monodomain equation which, after having replaced  $\mathbb{M}^s$  with  $\mathbb{M}^L$  as explained in Section 2.1.2, takes the following form in the implicit case

$$\frac{\vartheta^I}{\Delta t} \mathbb{M}^L \bar{\mathbf{v}}^{n+1} + \mathbb{K}_M(\bar{\mathbf{d}}_s^{n+1}) \bar{\mathbf{v}}^{n+1} + \mathbf{I}^{ion}(\bar{\mathbf{v}}^{n+1}, \bar{\mathbf{w}}^{n+1}) = \frac{1}{\Delta t} \mathbb{M}^L \bar{\mathbf{v}}^I + \mathbb{M}^L \mathbf{I}^{app}(t^{n+1}), \quad (2.18)$$

while the Newton method employed to solve it reads

$$\begin{cases} \mathbb{J}_{\mathcal{E},k}^{n+1} \delta \bar{\mathbf{w}}_{k+1}^{n+1} + \mathbb{J}_{\mathcal{E},k}^{n+1} \delta \bar{\mathbf{v}}_{k+1}^{n+1} + \mathbb{J}_{\mathcal{E},\mathcal{M},k}^{n+1} \delta \bar{\mathbf{d}}_{s,k+1}^{n+1} = -\mathbf{r}_{\mathcal{E},k}^{n+1}, \\ \bar{\mathbf{v}}_{k+1}^{n+1} = \bar{\mathbf{v}}_k^{n+1} + \delta \bar{\mathbf{v}}_{k+1}^{n+1}, \end{cases} \quad (2.19)$$

where

$$\begin{aligned} \mathbb{J}_{\mathcal{E},k}^{n+1} &= \partial_{\mathbf{w}} \mathbf{I}^{ion}(\bar{\mathbf{v}}_k^{n+1}, \bar{\mathbf{w}}_k^{n+1}), \\ \mathbb{J}_{\mathcal{E},k}^{n+1} &= \frac{\vartheta^I}{\Delta t} \mathbb{M}^L + \mathbb{K}_M(\bar{\mathbf{d}}_{s,k}^{n+1}) + \partial_v \mathbf{I}^{ion}(\bar{\mathbf{v}}_k^{n+1}, \bar{\mathbf{w}}_k^{n+1}), \\ \mathbb{J}_{\mathcal{E},\mathcal{M},k}^{n+1} &= \partial_{\mathbf{d}_s} \mathbb{K}_M(\bar{\mathbf{d}}_{s,k}^{n+1}, \bar{\mathbf{v}}_k^{n+1}), \\ \mathbf{r}_{\mathcal{E},k}^{n+1} &= \frac{\vartheta^I}{\Delta t} \mathbb{M}^L \bar{\mathbf{v}}_k^{n+1} + \mathbb{K}_M(\bar{\mathbf{d}}_{s,k}^{n+1}) \bar{\mathbf{v}}_k^{n+1} + \mathbf{I}^{ion}(\bar{\mathbf{v}}_k^{n+1}, \bar{\mathbf{w}}_k^{n+1}) \\ &\quad - \frac{1}{\Delta t} \mathbb{M}^L \bar{\mathbf{v}}^I - \mathbb{M}^L \mathbf{I}^{app}(t^{n+1}), \end{aligned}$$

and in particular

$$\begin{aligned} (\partial_{\mathbf{w}} \mathbf{I}^{ion,l})_{ij}(\bar{\mathbf{v}}, \bar{\mathbf{w}}) &= \int_{\Omega_0^s} \frac{\partial I^{ion}(v_h, w_h^1, \dots, w_h^{N_I})}{\partial w_h^l} \psi_{s,j} \psi_{s,i} \, d\Omega_0^s, \\ (\partial_v \mathbf{I}^{ion})_{ij}(\bar{\mathbf{v}}, \bar{\mathbf{w}}) &= \int_{\Omega_0^s} \frac{\partial I^{ion}(v_h, w_h^1, \dots, w_h^{N_I})}{\partial v_h} \psi_{s,j} \psi_{s,i} \, d\Omega_0^s, \\ (\partial_{\mathbf{d}_s} \mathbb{K}_M)_{ij}(\bar{\mathbf{d}}, \bar{\mathbf{v}}) &= \int_{\Omega_0^s} \left( \frac{\partial (J_h \mathbf{F}_h^{-1} \mathbf{D}_M \mathbf{F}_h^{-T} \nabla_0 v_h)}{\partial \mathbf{F}_h} \right) [\nabla_0 \psi_{s,j}] \cdot \nabla_0 \psi_{s,i} \, d\Omega_0^s, \end{aligned} \quad (2.20)$$

where we denote by  $\mathbf{Z}[\mathbf{B}]$  the contraction of the third order tensor  $\mathbf{Z}$  with the second order one  $\mathbf{B}$  (see Appendix A). The definition of  $\frac{\partial I^{ion}}{\partial w_h^l}$ ,  $\frac{\partial I^{ion}}{\partial v_h}$  (for the minimal model) and of  $\left( \frac{\partial (J_h \mathbf{F}_h^{-1} \mathbf{D}_M \mathbf{F}_h^{-T} \nabla_0 v)}{\partial \mathbf{F}_h} \right) [\nabla_0 \psi_{s,j}]$  are reported in Appendix B.1 and B.2, respectively.

We also consider the case in which the displacement is given, and hence remove in Eq. (2.18) the dependence on  $\bar{\mathbf{d}}_s^{n+1}$  by evaluating the stiffness matrix  $\mathbb{K}$  in the extrapolated displacement  $\bar{\mathbf{d}}_s^*$ . This yields to discarding the last term on the left hand side of Eq. (2.19), and to change accordingly the residual  $\mathbf{r}_{\mathcal{E},k}^{n+1}$ . Finally, we consider the following semi-



implicit scheme

$$\begin{aligned} \frac{\vartheta^I}{\Delta t} \mathbb{M}^L \bar{\mathbf{v}}^{n+1} + \mathbb{K}_M(\bar{\mathbf{d}}_s^*) \bar{\mathbf{v}}^{n+1} + \sum_{l=1}^{N_I} \mathbf{I}_{w^l}^{ion}(\bar{\mathbf{v}}^*, \bar{\mathbf{w}}^*) \bar{\mathbf{w}}^{n+1} + \mathbf{I}_v^{ion}(\bar{\mathbf{v}}^*, \bar{\mathbf{w}}^*) \bar{\mathbf{v}}^{n+1} \\ = \frac{1}{\Delta t} \mathbb{M}^L \bar{\mathbf{v}}^n + \mathbb{M}^L \mathbf{I}^{app}(t^{n+1}) - \tilde{\mathbf{I}}^{ion}(\bar{\mathbf{v}}^*, \bar{\mathbf{w}}^*), \end{aligned} \quad (2.21)$$

where we applied an additive decomposition of the form (2.15) to the ionic currents term. To this aim, we propose a splitting of the  $I^{ion}$  function which is reported in Appendix B.1.

The fully discretized bidomain equations, obtained with the implicit time scheme, take instead the form

$$\begin{aligned} \frac{\vartheta^I}{\Delta t} \mathbb{M}^L \bar{\mathbf{v}}^{n+1} + \mathbb{K}_I(\bar{\mathbf{d}}_s^{n+1})(\bar{\mathbf{v}}^{n+1} + \bar{\mathbf{v}}_E^{n+1}) + \mathbf{I}^{ion}(\bar{\mathbf{v}}^{n+1}, \bar{\mathbf{w}}^{n+1}) \\ = \frac{1}{\Delta t} \mathbb{M}^L \bar{\mathbf{v}}^I + \mathbb{M}^L \mathbf{I}^{app}(t^{n+1}), \\ \mathbb{K}_I(\bar{\mathbf{d}}_s^{n+1}) \bar{\mathbf{v}}^{n+1} + (\mathbb{K}_I(\bar{\mathbf{d}}_s^{n+1}) + \mathbb{K}_E(\bar{\mathbf{d}}_s^{n+1})) \bar{\mathbf{v}}_E^{n+1} = \mathbf{0}, \end{aligned}$$

whereas in this case the Newton method for its solution reads

$$\begin{cases} \mathbb{J}_{\mathcal{E}_L, k}^{n+1} \delta \bar{\mathbf{w}}_{k+1}^{n+1} + \mathbb{J}_{\mathcal{E}_{11}, k}^{n+1} \delta \bar{\mathbf{v}}_{k+1}^{n+1} + \mathbb{J}_{\mathcal{E}_{12}, k}^{n+1} \delta \bar{\mathbf{v}}_{E, k+1}^{n+1} + \mathbb{J}_{\mathcal{E}_{\mathcal{M}_1}, k}^{n+1} \delta \bar{\mathbf{d}}_{s, k+1}^{n+1} = -\mathbf{r}_{\mathcal{E}_1, k}^{n+1}, \\ \mathbb{J}_{\mathcal{E}_{21}, k}^{n+1} \delta \bar{\mathbf{v}}_{k+1}^{n+1} + \mathbb{J}_{\mathcal{E}_{22}, k}^{n+1} \delta \bar{\mathbf{v}}_{E, k+1}^{n+1} + \mathbb{J}_{\mathcal{E}_{\mathcal{M}_2}, k}^{n+1} \delta \bar{\mathbf{d}}_{s, k+1}^{n+1} = \mathbf{0}, \\ \bar{\mathbf{v}}_{k+1}^{n+1} = \bar{\mathbf{v}}_k^{n+1} + \delta \bar{\mathbf{v}}_{k+1}^{n+1}, \\ \bar{\mathbf{v}}_{E, k+1}^{n+1} = \bar{\mathbf{v}}_{E, k}^{n+1} + \delta \bar{\mathbf{v}}_{E, k+1}^{n+1}, \end{cases} \quad (2.22)$$

where

$$\begin{aligned} \mathbb{J}_{\mathcal{E}_{11}, k}^{n+1} &= \frac{\vartheta^I}{\Delta t} \mathbb{M}^L + \mathbb{K}_I(\bar{\mathbf{d}}_{s, k}^{n+1}) + \partial_v \mathbf{I}^{ion}(\bar{\mathbf{v}}_k^{n+1}, \bar{\mathbf{w}}_k^{n+1}), \\ \mathbb{J}_{\mathcal{E}_{12}, k}^{n+1} &= \mathbb{J}_{\mathcal{E}_{21}, k}^{n+1} = \mathbb{K}_I(\bar{\mathbf{d}}_{s, k}^{n+1}), \\ \mathbb{J}_{\mathcal{E}_{22}, k}^{n+1} &= \mathbb{K}_I(\bar{\mathbf{d}}_{s, k}^{n+1}) + \mathbb{K}_E(\bar{\mathbf{d}}_{s, k}^{n+1}), \\ \mathbb{J}_{\mathcal{E}_{\mathcal{M}_1}, k}^{n+1} &= \partial_{\mathbf{d}_s} \mathbb{K}_I(\bar{\mathbf{d}}_{s, k}^{n+1}, \bar{\mathbf{v}}_k^{n+1} + \bar{\mathbf{v}}_{E, k}^{n+1}), \\ \mathbb{J}_{\mathcal{E}_{\mathcal{M}_2}, k}^{n+1} &= \partial_{\mathbf{d}_s} \mathbb{K}_I(\bar{\mathbf{d}}_{s, k}^{n+1}, \bar{\mathbf{v}}_k^{n+1}) + \mathbb{K}_I(\bar{\mathbf{d}}_{s, k}^{n+1}, \bar{\mathbf{v}}_{E, k}^{n+1}) + \mathbb{K}_E(\bar{\mathbf{d}}_{s, k}^{n+1}, \bar{\mathbf{v}}_{E, k}^{n+1}), \\ \mathbf{r}_{\mathcal{E}_1, k}^{n+1} &= \frac{\vartheta^I}{\Delta t} \mathbb{M}^L \bar{\mathbf{v}}^{n+1} + \mathbb{K}_I(\bar{\mathbf{d}}_s^{n+1})(\bar{\mathbf{v}}^{n+1} + \bar{\mathbf{v}}_E^{n+1}) + \mathbf{I}^{ion}(\bar{\mathbf{v}}^{n+1}, \bar{\mathbf{w}}^{n+1}) \\ &\quad - \frac{1}{\Delta t} \mathbb{M}^L \bar{\mathbf{v}}^I - \mathbb{M}^L \mathbf{I}^{app}(t^{n+1}). \end{aligned}$$

The definition of matrices  $\partial_{\mathbf{d}_s} \mathbb{K}_I$  and  $\partial_{\mathbf{d}_s} \mathbb{K}_E$  is analogous to that of  $\partial_{\mathbf{d}_s} \mathbb{K}_M$ , provided that the tensors  $\mathbf{D}_I$  and  $\mathbf{D}_E$  are used in place of  $\mathbf{D}_M$ . The semi-implicit scheme for the

bidomain equations [Ethier and Bourgault, 2008] reads

$$\begin{aligned} \frac{\vartheta^I}{\Delta t} \mathbb{M}^L \bar{\mathbf{v}}^{n+1} + \mathbb{K}_I(\bar{\mathbf{d}}_s^*)(\bar{\mathbf{v}}^{n+1} + \bar{\mathbf{v}}_E^{n+1}) + \sum_{l=1}^{N_I} \mathbf{I}_{w^l}^{ion}(\bar{\mathbf{v}}^*, \bar{\mathbf{w}}^*) \bar{\mathbf{w}}^{n+1} + \mathbf{I}_v^{ion}(\bar{\mathbf{v}}^*, \bar{\mathbf{w}}^*) \bar{\mathbf{v}}^{n+1} \\ = \frac{1}{\Delta t} \mathbb{M}^L \bar{\mathbf{v}}^n + \mathbb{M}^L \mathbf{I}^{app}(t^{n+1}) - \tilde{\mathbf{I}}^{ion}(\bar{\mathbf{v}}^*, \bar{\mathbf{w}}^*), \end{aligned} \quad (2.23)$$

$$\mathbb{K}_I(\bar{\mathbf{d}}_s^*) \bar{\mathbf{v}}^{n+1} + \left( \mathbb{K}_I(\bar{\mathbf{d}}_s^{n+1}) + \mathbb{K}_E(\bar{\mathbf{d}}_s^{n+1}) \right) \bar{\mathbf{v}}_E^{n+1} = \mathbf{0}.$$

### Mechanical activation

The mechanical activation equation with the implicit scheme for the time discretization, and the Newton method for this case respectively read

$$\frac{\vartheta^I}{\Delta t} \mathbb{M}^L \bar{\boldsymbol{\gamma}}^{n+1} + \varepsilon \mathbb{K}_\gamma(\bar{\mathbf{w}}^{n+1}) \bar{\boldsymbol{\gamma}}^{n+1} + \boldsymbol{\Phi}(\bar{\mathbf{w}}^{n+1}, \bar{\boldsymbol{\gamma}}^{n+1}, \bar{\mathbf{d}}_s^{n+1}) = \frac{1}{\Delta t} \mathbb{M}^L \bar{\boldsymbol{\gamma}}^I, \quad (2.24)$$

and

$$\begin{cases} \mathbb{J}_{\mathcal{A},k}^{n+1} \delta \bar{\mathbf{w}}_{k+1}^{n+1} + \mathbb{J}_{\mathcal{A},k}^{n+1} \delta \bar{\boldsymbol{\gamma}}_{k+1}^{n+1} + \mathbb{J}_{\mathcal{A},\mathcal{M},k}^{n+1} \delta \bar{\mathbf{d}}_{s,k+1}^{n+1} = -\mathbf{r}_{\mathcal{A},k}^{n+1}, \\ \bar{\boldsymbol{\gamma}}_{k+1}^{n+1} = \bar{\boldsymbol{\gamma}}_k^{n+1} + \delta \bar{\boldsymbol{\gamma}}_{k+1}^{n+1}. \end{cases} \quad (2.25)$$

where

$$\begin{aligned} \mathbb{J}_{\mathcal{A},k}^{n+1} &= \varepsilon \partial_{\mathbf{w}} \mathbb{K}_\gamma(\bar{\mathbf{w}}_k^{n+1}, \bar{\boldsymbol{\gamma}}_k^{n+1}) + \partial_{\mathbf{w}} \boldsymbol{\Phi}(\bar{\mathbf{w}}_k^{n+1}, \bar{\boldsymbol{\gamma}}_k^{n+1}, \bar{\mathbf{d}}_{s,k}^{n+1}), \\ \mathbb{J}_{\mathcal{A},k}^{n+1} &= \frac{\vartheta^I}{\Delta t} \mathbb{M}^L + \varepsilon \mathbb{K}_\gamma(\bar{\mathbf{w}}_k^{n+1}) + \partial_{\boldsymbol{\gamma}} \boldsymbol{\Phi}(\bar{\mathbf{w}}_k^{n+1}, \bar{\boldsymbol{\gamma}}_k^{n+1}, \bar{\mathbf{d}}_{s,k}^{n+1}), \\ \mathbb{J}_{\mathcal{A},\mathcal{M},k}^{n+1} &= \partial_{\mathbf{d}_s} \boldsymbol{\Phi}(\bar{\mathbf{w}}_k^{n+1}, \bar{\boldsymbol{\gamma}}_k^{n+1}, \bar{\mathbf{d}}_{s,k}^{n+1}), \\ \mathbf{r}_{\mathcal{A},k}^{n+1} &= \frac{\vartheta^I}{\Delta t} \mathbb{M}^L \bar{\boldsymbol{\gamma}}_k^{n+1} + \varepsilon \mathbb{K}_\gamma(\bar{\mathbf{w}}_k^{n+1}) \bar{\boldsymbol{\gamma}}_k^{n+1} + \boldsymbol{\Phi}(\bar{\mathbf{w}}_k^{n+1}, \bar{\boldsymbol{\gamma}}_k^{n+1}, \bar{\mathbf{d}}_{s,h}^{n+1}) - \frac{1}{\Delta t} \mathbb{M}^L \bar{\boldsymbol{\gamma}}^I, \end{aligned}$$

and

$$\begin{aligned} (\partial_{\mathbf{w}} \mathbb{K}_\gamma)_{ij}(\bar{\mathbf{w}}, \bar{\boldsymbol{\gamma}}) &= - \int_{\Omega_0^s} \frac{\varepsilon}{\mu_A(\widehat{w_h^l})^3} \nabla_0 \psi_j \cdot \nabla_0 \psi_i \, d\Omega_0^s, \\ (\partial_{\mathbf{w}} \boldsymbol{\Phi})_{ij}(\bar{\mathbf{w}}, \bar{\boldsymbol{\gamma}}, \bar{\mathbf{d}}_s) &= \int_{\Omega_0^s} \frac{\partial \Phi(\mathbf{w}_h, \gamma_h, \mathbf{d}_{s,h})}{\partial \mathbf{w}_h} \psi_{s,j} \psi_{s,i} \, d\Omega_0^s, \\ (\partial_{\boldsymbol{\gamma}} \boldsymbol{\Phi})_{ij}(\bar{\mathbf{w}}, \bar{\boldsymbol{\gamma}}, \bar{\mathbf{d}}_s) &= \int_{\Omega_0^s} \frac{\partial \Phi(\mathbf{w}_h, \gamma_h, \mathbf{d}_{s,h})}{\partial \gamma_h} \psi_{s,j} \psi_{s,i} \, d\Omega_0^s, \\ (\partial_{\mathbf{d}_s} \boldsymbol{\Phi})_{ij}(\bar{\mathbf{w}}, \bar{\boldsymbol{\gamma}}, \bar{\mathbf{d}}_s) &= \int_{\Omega_0^s} \left( \frac{\partial \Phi(\mathbf{w}_h, \gamma_h, \mathbf{d}_{s,h})}{\partial \mathbf{F}_h} : \nabla_0 \boldsymbol{\psi}_{s,j} \right) \psi_{s,i} \, d\Omega_0^s. \end{aligned}$$

In this case, the semi-implicit scheme is obtained from Eq. (2.24) by extrapolating the  $\bar{\gamma}$  variable and reads

$$\left( \frac{\vartheta^I}{\Delta t} \mathbb{M}^L + \varepsilon \mathbb{K}_\gamma(\bar{\mathbf{w}}^*) + \Phi_\gamma(\bar{\mathbf{w}}^*, \bar{\gamma}^*, \bar{\mathbf{d}}_s^*) \right) \bar{\gamma}_k^{n+1} = \frac{1}{\Delta t} \mathbb{M}^L \bar{\gamma}^I + \tilde{\Phi}(\bar{\mathbf{w}}^*, \bar{\gamma}^*, \bar{\mathbf{d}}_s^*). \quad (2.26)$$

The definition of the terms in Eq. (2.25), (2.26) is reported in Appendix B.3.

### Mechanics

As already mentioned, the implicit scheme only is used for the mechanics problem because no stable semi-implicit were found to be stable for the problem under consideration, unless unreasonably small timesteps were employed. We conjecture that this is due to the peculiar form of the first Piola-Kirchhoff stress tensor, which features exponential and logarithmic nonlinearities as well as a strong anisotropy. This accounts to an accentuated sensibility of the values taken by the stress tensor  $\mathbf{P}$  on the displacement: for this reason, the extrapolated variable  $\mathbf{d}_s^*$  is not sufficiently close to  $\mathbf{d}_s^{n+1}$  to ensure that  $\mathbf{P}(\mathbf{d}_s^*)$  is a close approximation of  $\mathbf{P}(\mathbf{d}_s^{n+1})$ .

The implicit scheme for the mechanics problem reads

$$\left( \rho_s \frac{\vartheta^{II}}{\Delta t^2} \mathbb{M}_3^s + \frac{\vartheta^I}{\Delta t} \mathbb{F} + \mathbb{G} \right) \bar{\mathbf{d}}_s^{n+1} + \mathbf{S}(\bar{\mathbf{d}}_s^{n+1}, \bar{\gamma}^{n+1}) = \rho_s \frac{1}{\Delta t^2} \mathbb{M}_3^s \bar{\mathbf{d}}_s^{II} + \frac{1}{\Delta t} \mathbb{F} \bar{\mathbf{d}}_s^I + \boldsymbol{\rho}^{n+1},$$

and the Newton method

$$\begin{cases} \mathbb{J}_{\mathcal{M},k}^{n+1} \delta \bar{\gamma}_{k+1}^{n+1} + \mathbb{J}_{\mathcal{M},k}^{n+1} \delta \bar{\mathbf{d}}_{s,k+1}^{n+1} = -\mathbf{r}_{\mathcal{M},k}^{n+1}, \\ \bar{\mathbf{d}}_{s,k+1}^{n+1} = \bar{\mathbf{d}}_{s,k}^{n+1} + \delta \bar{\mathbf{d}}_{s,k+1}^{n+1}, \end{cases} \quad (2.27)$$

where

$$\begin{aligned} \mathbb{J}_{\mathcal{M},k}^{n+1} &= \partial_\gamma \mathbf{S}(\bar{\mathbf{d}}_{s,k}^{n+1}, \bar{\gamma}_k^{n+1}), \\ \mathbb{J}_{\mathcal{M},k}^{n+1} &= \left( \rho_s \frac{\vartheta^{II}}{\Delta t^2} \mathbb{M}_3^s + \frac{\vartheta^I}{\Delta t} \mathbb{F} + \mathbb{G} \right) + \partial_{\mathbf{d}_s} \mathbf{S}(\bar{\mathbf{d}}_{s,k}^{n+1}, \bar{\gamma}_k^{n+1}), \\ \mathbf{r}_{\mathcal{M},k}^{n+1} &= \left( \rho_s \frac{\vartheta^{II}}{\Delta t^2} \mathbb{M}_3^s + \frac{\vartheta^I}{\Delta t} \mathbb{F} + \mathbb{G} \right) \bar{\mathbf{d}}_{s,k}^{n+1} + \mathbf{S}(\bar{\mathbf{d}}_{s,k}^{n+1}, \bar{\gamma}_k^{n+1}) \\ &\quad - \rho_s \frac{1}{\Delta t^2} \mathbb{M}_3^s \bar{\mathbf{d}}_s^{II} - \frac{1}{\Delta t} \mathbb{F} \bar{\mathbf{d}}_s^I - \boldsymbol{\rho}_k^{n+1}. \end{aligned} \quad (2.28)$$

The calculation of terms of the Jacobian matrix in Eq. (2.28) is a complex task which requires knowledge of matrix and tensor calculus. The differentiation of the (second order) stress tensor  $\mathbf{P}_E$  with respect to the (second order) deformation tensor  $\mathbf{F}$  gives

## Chapter 2. Numerical approximation

---

rise to a fourth order tensor; the latter is then subsequently contracted with the (second order) deformation gradient tensor of the basis function  $\psi_{s,j}$ , that is

$$\begin{aligned}\partial_\gamma \mathbf{S}(\bar{\mathbf{d}}_s, \bar{\gamma}) &= \int_{\Omega_0^s} \left( \mathbf{P}_E \frac{\partial \mathbf{F}_A^{-1}}{\partial \gamma_h} \psi_{s,j} \right) : \nabla_0 \psi_{s,i} \, d\Omega_0^s, \\ \partial_{\mathbf{d}_s} \mathbf{S}(\bar{\mathbf{d}}_s, \bar{\gamma}) &= \int_{\Omega_0^s} \left( \frac{\partial \mathbf{P}_E}{\partial \mathbf{F}_h} \right) [\nabla_0 \psi_{s,j}] \mathbf{F}_A^{-1} : \nabla_0 \psi_{s,i} \, d\Omega_0^s,\end{aligned}$$

where - with an abuse of notation - we used the same symbol introduced for the contraction of a third with a second order tensor, to denote the contraction of a fourth with a second order tensor. We report in Appendix A the minimal set of rules which is required to perform the differentiation of  $\mathbf{P}_E$ ; the latter is then carried out in Appendix B.4.

We recall that, as explained in detail in Section 2.1.4, if the full 3D Navier-Stokes equations are solved together with the mechanics we have  $\rho_k^{n+1} = \rho(\bar{\boldsymbol{\lambda}}_k^{n+1}) = \boldsymbol{\Pi}_s^f \bar{\boldsymbol{\lambda}}_k^{n+1}$ . As such, we add the term  $\mathbb{J}_{\mathcal{M}_{\mathcal{L}},k}^{n+1} \bar{\boldsymbol{\lambda}}_k^{n+1}$  to the first of Eq. (2.27), where  $\mathbb{J}_{\mathcal{M}_{\mathcal{L}},k}^{n+1} = \boldsymbol{\Pi}_s^f$ .

### Fluid

We write the implicit scheme for the fluid velocity and pressure, the fluid geometry, and the Lagrange multipliers in a single system since, as previously stated, in this thesis the corresponding equations are always solved simultaneously together with the mechanics:

$$\begin{aligned}\tilde{\mathbb{K}}_G \bar{\mathbf{d}}_f^{n+1} - \boldsymbol{\Pi}_f^s \bar{\mathbf{d}}_s^{n+1} &= \mathbf{0}, \\ \left( \rho_f \frac{\vartheta^I}{\Delta t} \mathbb{M}_3^f + \mu_f \mathbb{A} + \rho_f \mathbb{C}(\bar{\mathbf{u}}^{n+1} - \dot{\bar{\mathbf{d}}}_f^{n+1}) \right) \bar{\mathbf{u}}^{n+1} + \mathbb{B}^T \bar{\mathbf{p}}^{n+1} \\ &\quad + \boldsymbol{\Pi}_f^T \bar{\boldsymbol{\lambda}}^{n+1} + \mathbf{S}_M^{SUPG}(\bar{\mathbf{u}}^{n+1}, \bar{\mathbf{p}}^{n+1}) = \rho_f \frac{1}{\Delta t} \mathbb{M}_3^f \bar{\mathbf{u}}^I, \\ \mathbb{B} \bar{\mathbf{u}}^{n+1} + \mathbf{S}_C^{SUPG}(\bar{\mathbf{u}}^{n+1}, \bar{\mathbf{p}}^{n+1}) &= \mathbf{0}, \\ - \frac{\vartheta^I}{\Delta t} \boldsymbol{\Pi}_f^s \bar{\mathbf{d}}_s^{n+1} + \boldsymbol{\Pi}_f^f \bar{\mathbf{u}}^{n+1} &= - \frac{1}{\Delta t} \boldsymbol{\Pi}_f^s \bar{\mathbf{d}}_s^I,\end{aligned}\tag{2.29}$$

where we set  $\dot{\bar{\mathbf{d}}}_f^{n+1} = \frac{1}{\Delta t} (\vartheta^I \bar{\mathbf{d}}_f^{n+1} - \bar{\mathbf{d}}_f^I)$ , the approximation of the fluid geometry displacement time derivative given by the BDF. The Newton method for the solution of the

nonlinear Eq. (2.29) reads:

$$\begin{cases} \mathbb{J}_{\mathcal{F}_{11},k}^{n+1} \delta \bar{\mathbf{u}}_{k+1}^{n+1} + \mathbb{J}_{\mathcal{F}_{12},k}^{n+1} \delta \bar{\mathbf{p}}_{k+1}^{n+1} + \mathbb{J}_{\mathcal{F}_{\mathcal{L}},k}^{n+1} \delta \bar{\boldsymbol{\lambda}}_{k+1}^{n+1} = -\mathbf{r}_{\mathcal{F}_1,k}^{n+1}, \\ \mathbb{J}_{\mathcal{F}_{21},k}^{n+1} \delta \bar{\mathbf{u}}_{k+1}^{n+1} + \mathbb{J}_{\mathcal{F}_{22},k}^{n+1} \delta \bar{\mathbf{p}}_{k+1}^{n+1} = -\mathbf{r}_{\mathcal{F}_2,k}^{n+1}, \\ \mathbb{J}_{\mathcal{G},k}^{n+1} \delta \bar{\mathbf{d}}_{f,k+1}^{n+1} = -\mathbf{r}_{\mathcal{G},k}^{n+1}, \\ \mathbb{J}_{\mathcal{L}_{\mathcal{M}},k}^{n+1} \delta \bar{\mathbf{d}}_{s,k+1}^{n+1} + \mathbb{J}_{\mathcal{L}_{\mathcal{F}},k}^{n+1} \delta \bar{\mathbf{u}}_{k+1}^{n+1} = -\mathbf{r}_{\mathcal{L},k}^{n+1}, \\ \bar{\mathbf{u}}_{k+1}^{n+1} = \bar{\mathbf{u}}_k^{n+1} + \delta \bar{\mathbf{u}}_{k+1}^{n+1}, \\ \bar{\mathbf{p}}_{k+1}^{n+1} = \bar{\mathbf{p}}_k^{n+1} + \delta \bar{\mathbf{p}}_{k+1}^{n+1}, \\ \bar{\mathbf{d}}_{f,k+1}^{n+1} = \bar{\mathbf{d}}_{f,k}^{n+1} + \delta \bar{\mathbf{d}}_{f,k+1}^{n+1}, \\ \bar{\boldsymbol{\lambda}}_{k+1}^{n+1} = \bar{\boldsymbol{\lambda}}_k^{n+1} + \delta \bar{\boldsymbol{\lambda}}_{k+1}^{n+1}, \end{cases}$$

where

$$\begin{aligned} \mathbb{J}_{\mathcal{F}_{11},k}^{n+1} &= \rho_f \frac{\vartheta^I}{\Delta t} \mathbb{M}_3^f + \mu_f \mathbb{A} + \rho_f \partial_u \mathbb{C}(\bar{\mathbf{u}}_k^{n+1}, \dot{\bar{\mathbf{d}}}_{f,k}^{n+1}) + \partial_u \mathbf{S}_M^{SUPG}(\bar{\mathbf{u}}_k^{n+1}, \bar{\mathbf{p}}_k^{n+1}), \\ \mathbb{J}_{\mathcal{F}_{12},k}^{n+1} &= \mathbb{B}^T + \partial_p \mathbf{S}_M^{SUPG}(\bar{\mathbf{u}}_k^{n+1}, \bar{\mathbf{p}}_k^{n+1}), \\ \mathbb{J}_{\mathcal{F}_{21},k}^{n+1} &= \mathbb{B} + \partial_u \mathbf{S}_C^{SUPG}(\bar{\mathbf{u}}_k^{n+1}, \bar{\mathbf{p}}_k^{n+1}), \\ \mathbb{J}_{\mathcal{F}_{22},k}^{n+1} &= \partial_p \mathbf{S}_C^{SUPG}(\bar{\mathbf{u}}_k^{n+1}, \bar{\mathbf{p}}_k^{n+1}), \\ \mathbb{J}_{\mathcal{F}_{\mathcal{L}},k}^{n+1} &= \boldsymbol{\Pi}_{\Gamma}^{fT}, \\ \mathbb{J}_{\mathcal{G},k}^{n+1} &= \tilde{\mathbb{K}}_G, \\ \mathbb{J}_{\mathcal{L}_{\mathcal{M}},k}^{n+1} &= -\frac{\vartheta^I}{\Delta t} \boldsymbol{\Pi}_{\Gamma}^s, \\ \mathbb{J}_{\mathcal{L}_{\mathcal{F}},k}^{n+1} &= \boldsymbol{\Pi}_{\Gamma}^f, \\ \mathbf{r}_{\mathcal{F}_1,k}^{n+1} &= \left( \rho_f \frac{\vartheta^I}{\Delta t} \mathbb{M}_3^f + \mu_f \mathbb{A} + \rho_f \mathbb{C}(\bar{\mathbf{u}}_k^{n+1} - \dot{\bar{\mathbf{d}}}_f^{n+1}) \right) \bar{\mathbf{u}}_k^{n+1} + \mathbb{B}^T \bar{\mathbf{p}}_k^{n+1} + \boldsymbol{\Pi}_{\Gamma}^{fT} \bar{\boldsymbol{\lambda}}_k^{n+1} \\ &\quad + \mathbf{S}_M^{SUPG}(\bar{\mathbf{u}}_k^{n+1}, \bar{\mathbf{p}}_k^{n+1}) - \rho_f \frac{1}{\Delta t} \mathbb{M}_3^f \bar{\mathbf{u}}_k^I, \\ \mathbf{r}_{\mathcal{F}_2,k}^{n+1} &= \mathbb{B} \bar{\mathbf{u}}_k^{n+1} + \mathbf{S}_C^{SUPG}(\bar{\mathbf{u}}_k^{n+1}, \bar{\mathbf{p}}_k^{n+1}), \\ \mathbf{r}_{\mathcal{G},k}^{n+1} &= \tilde{\mathbb{K}}_G \bar{\mathbf{d}}_f^{n+1} - \boldsymbol{\Pi}_f^s \bar{\mathbf{d}}_s^{n+1}, \\ \mathbf{r}_{\mathcal{L},k}^{n+1} &= -\frac{\vartheta^I}{\Delta t} \boldsymbol{\Pi}_{\Gamma}^s \bar{\mathbf{d}}_s^{n+1} + \boldsymbol{\Pi}_{\Gamma}^f \bar{\mathbf{u}}_k^{n+1} + \frac{1}{\Delta t} \boldsymbol{\Pi}_{\Gamma}^s \bar{\mathbf{d}}_s^I, \end{aligned}$$

and in particular

$$\partial_u \mathbb{C}(\bar{\mathbf{u}}, \dot{\bar{\mathbf{d}}}_f) = \int_{\Omega_t^f} \left( ((\mathbf{u}_h - \dot{\mathbf{d}}_{f,h}) \cdot \nabla) \boldsymbol{\psi}_{f,j} \cdot \boldsymbol{\psi}_{f,i} + (\boldsymbol{\psi}_{f,j} \cdot \nabla) \mathbf{u}_h \cdot \boldsymbol{\psi}_{f,i} \right) d\Omega_t^f.$$

We remark that we are here neglecting the shape derivatives terms (i.e. the Jacobian of  $\mathbb{C}$  differentiated with respect to  $\bar{\mathbf{d}}_f$ ), thus in this case the method employed is in fact an inexact Newton method. For the sake of readability, we do not report the Jacobian

terms corresponding to the SUPG stabilization.

### 2.2.2 Discretization of the 0D fluid model

We evaluate the volume  $V^{endo}(t)$  at time  $t^n$  by exploiting the formula

$$V^{endo,n} = V^{endo}(\bar{\mathbf{d}}_h^n) = \int_{\Gamma_0^{endo}} J(\mathbf{d}_h^n) \boldsymbol{\xi} \cdot \mathbf{F}_h^{-T}(\mathbf{d}_h^n) \mathbf{N}_s d\Gamma_0, \quad (2.30)$$

which is rigorously derived in [Rossi, 2014] and where  $\boldsymbol{\xi}$  is a vector directed as the normal to the plane of the LV base. We then model the endocardial pressure  $p^{endo}(t)$  with different 0D models, following [Eriksson et al., 2013, Rossi, 2014, Usyk et al., 2002], for each of the aforementioned phases (in the following, we drop the “endo” superscript for simplicity).

1. *Isovolumic contraction*: Isovolumic contraction: we use the Newton method to solve Eq. (1.26) by iteratively updating the pressure as

$$p_{k+1}^{n+1} = p_k^{n+1} - \left( \frac{\partial V}{\partial p}(p_k^{n+1}) \right)^{-1} (V_k^{n+1} - V^n),$$

for  $k = 0, 1, \dots$ , with  $p_0^{n+1} = p^n$  and  $V_0^{n+1} = V^n$ . By dimensional arguments, we approximate  $\frac{\partial V}{\partial p}(p_k^{n+1})$  as  $-\frac{\Delta t}{\zeta} \left[ \frac{mm^4 s^2}{g} \right]$ . At each iteration,  $p_{k+1}^{n+1}$  is used to solve the electromechanics problem thus obtaining  $V_{k+1}^{n+1}$  with (2.30); the procedure is repeated until the condition  $\frac{|V_{k+1}^{n+1} - V^n|}{\Delta t} < \varepsilon$  is satisfied. The parameter  $\zeta < 0$  has to be “sufficiently” small in order for the fixed point algorithm to converge;

2. *Ejection*: the two elements Windkessel model (1.27) is solved in the pressure variable with a BDF scheme of order  $\sigma = 1$ :

$$C \frac{p^{n+1} - p^n}{\Delta t} = -\frac{p^{n+1}}{R} - \frac{V^n - V^{n-1}}{\Delta t}.$$

3. *Isovolumic relaxation*: modeled as the first isovolumic contraction phase.
4. *Filling*: the pressure is simply updated as:

$$p^{n+1} = p^n + \Delta t \varsigma.$$

## 3 Preprocessing

We discuss in this chapter the set of procedures to be performed, after the numerical discretization has been completed, before it is possible to execute simulations in the framework that we established. First, we describe how to obtain the mesh approximating the domains  $\Omega_0^s$  and  $\Omega_0^f$ , whether they represent an idealized geometry or a subject-specific Magnetic Resonance Imaging (MRI) fitted LV. Then, we recall a simple algorithm for the generation of the fibers, the sheets, and the normal fields on the nodes of the myocardium mesh. Finally, we outline the algorithm implemented to solve the prestress problem. After these elements have been obtained, they can be used as the input for the electromechanics and electrofluidmechanics problems in the following chapters.

### 3.1 Mesh generation

In this section we describe the three different cases that were dealt with for the generation of the meshes used in this work. While we aim at simulating the LV function using subject-specific meshes, the extraction of a real LV geometry from medical images is often a time consuming task; moreover, the mesh thus obtained feature a large number of degrees of freedom – which is required to ensure a fine description of the geometry – making their use in the development and testing phases impractical. Therefore, it is convenient to use at first a mesh approximating an idealized, simple, geometry, for which the number of tetrahedra can be controlled. Besides these two scenarios, we will also consider the case in which the geometry is given in the form of a set of non conforming surfaces.

In general, dealing with surface and/or volume meshes is a complex task. A large number of files and formats exists, to begin with; among the most popular we used the *Visualization Toolkit*<sup>1</sup> (.vtk) 2D format [Schroeder et al., 2004], introduced in the homonymous C++ library, the *STereo Lithography* (.stl) 2D format [Béchet et al., 2002],

---

<sup>1</sup><https://www.vtk.org>

one of the most commonly used in Computer-Aided Design (CAD) software and in the context of 3D printing, and the *INRIA Medit* (.mesh) 3D format [Frey, 2001], which is the standard one for the LifeV library. Moreover, a multitude of both commercial and academic software has been developed for the generation, the manipulation and the repairing of meshes. The ones exploited in this work are:

- 3D Slicer<sup>2</sup>: an open source software platform for medical image informatics, image processing, and three-dimensional visualization [Fedorov et al., 2012], which was used to manage and segment the *Digital Imaging and COmmunications in Medicine* (DICOM) sets [Mildenberger et al., 2002] of cardiac MRI.
- ParaView<sup>3</sup>: an open source data analysis and visualization application [Ahrens et al., 2005], for both the preprocessing of the meshes and the postprocessing of the data.
- MeshLab<sup>4</sup>: an open source system for the processing and the editing of 3D triangular meshes [Cignoni et al., 2008], for the manipulation and application of filters to the meshes.
- NetFabb<sup>®</sup>: a commercial software for additive manufacturing and design developed by Autodesk<sup>®</sup>, which is however free for academic and educational use, for the fine tuning of the meshes.
- GMSH<sup>5</sup>: an open source three-dimensional finite element mesh generator [Geuzaine and Remacle, 2009] using the Delauney triangulation algorithm [Lee and Schachter, 1980], for the generation of the 3D meshes.

We cite, among others, the *Vascular Modeling Toolkit* (VMTK), a collection of libraries and tools for 3D reconstruction, geometric analysis, mesh generation and surface data analysis oriented towards the modeling of blood vessels and based on VTK [Antiga et al., 2008]. Indeed, even if it was not directly used for the simulations included in this work, it has proven to be a valuable tool for the generation of blood vessels from medical images [Colciago, 2014, Deparis et al., 2016b, Masci et al., 2017, Faggiano et al., 2013].

### 3.1.1 Idealized geometry

In the field of 2D and 3D cardiac modeling, it is common in the literature the adoption of a *prolate* geometry [Eriksson et al., 2013, Guccione and McCulloch, 1991, Guccione et al., 1995, Rossi, 2014, Wang et al., 2013], also known as Auckland heart model [LeGrice et al.,

---

<sup>2</sup><https://www.slicer.org>

<sup>3</sup><https://www.paraview.org>

<sup>4</sup><http://www.meshlab.net>

<sup>5</sup><https://www.gmsh.info>



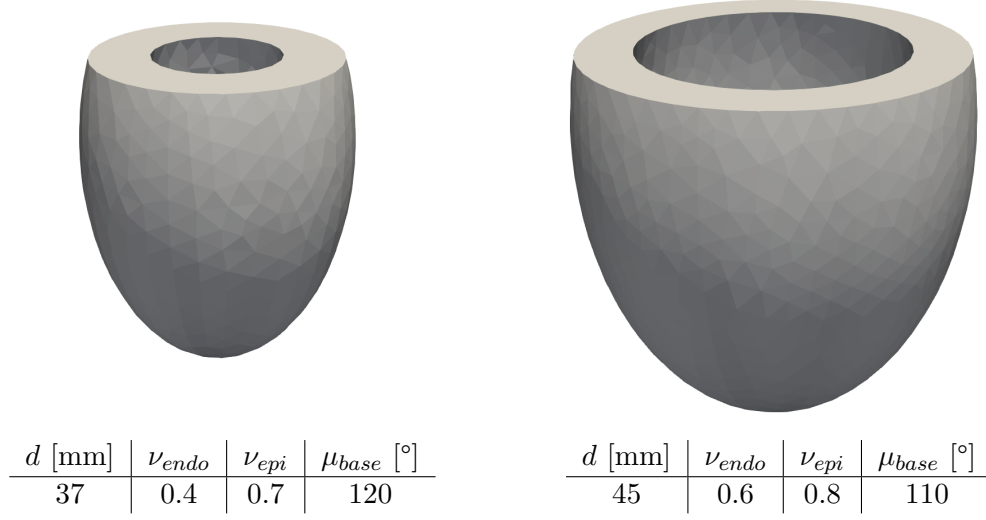


Figure 3.1 – Prolate ellipsoid geometries for two distinct sets of parameters, representing a canine LV (left) as in [Guccione et al., 1995], and a human LV (right) as in [Wang et al., 2013].

2001]. The name is due the fact that it is described in a reference prolate spheroidal coordinate system:

$$\begin{cases} x &= d \sinh(\nu) \sin(\mu) \cos(\theta), \\ y &= d \sinh(\nu) \sin(\mu) \sin(\theta), \\ z &= d \sinh(\nu) \cosh(\mu), \end{cases}$$

where  $d$  is the focal length,  $\nu \geq 0$ , and  $\mu, \theta \in (0, 2\pi]$  [Pezzuto, 2013]. The geometry is then the region of space defined as

$$\Omega_0^s = \{(\nu, \mu, \theta) : \nu_{endo} < \nu < \nu_{epi}, \mu_{base} < \mu < 0, 0 \leq \theta < 2\pi\}.$$

In Figure 3.1 we show two different prolate geometries and the corresponding parameters used to define them.

The GMSH software is used to define surfaces and volumes described by analytic functions and parametrization, and was used to generate the three dimensional mesh and to set different flags at the boundaries, namely the endocardium, the epicardium, and the base. Setting the flags is a mandatory step which will allow the finite element library to assign the boundary conditions on the correct boundaries. The geometry on the right side of Figure 3.1 is the one which was considered in this thesis, obtained by using the parameters indicated therein. From it, we generate a base coarse mesh featuring 1'827 nodes and 6'500 tetrahedra, and subsequently refine it by edge halvening to obtain four increasingly finer meshes. The base prolate mesh and the first two refinements are reported, together with the fibers and the sheets field, in Figure 3.7.



Figure 3.2 – An overview of the 3D MRI images along three orthogonal slices, as given by the 3D Slicer software. The pulmonary artery is clearly visible in the central slice, while the LV with the sinus of Valsalva and the aorta can be seen in the right slice.

### 3.1.2 Image processing and segmentation

Image segmentation is the process of locating regions of interest (ROI) in the form of a subset of pixels [Haralick and Shapiro, 1985] which, in the context of 3D imaging, are volumetric pixels (voxels) [Chen et al., 2012]. In biomedical applications, this amounts to assign different flags to regions containing different types of tissues and/or fluids. This result, depending on the properties of the biological material which is to be segmented, can often be achieved through semi-automatic or automatic procedures (see e.g. [Fedele et al., 2015, Isgum et al., 2009, Trentin et al., 2015] for arteries and blood vessels and [Bordas et al., 2010, Vergara et al., 2014] for the Purkinje network), exploiting a large set of different techniques. However, since the development of algorithms for the segmentation of the chambers of the heart [Peters et al., 2007, Zheng et al., 2007, Zhuang et al., 2010] is beyond the scope of this work, we used a manual procedure based on the brightness of the pixels of 3D MRIs. The MRI images that we used were provided by Prof. J. Schwitter (Chief physician at the Centre Hospitalier Universitaire Vaudois CHUV, Lausanne) and Dr. P. Masci in the framework of the collaboration CMCS@EPFL-CHUV hospital.

The procedure used to create the subject-specific mesh can be outlined as follows. The MRI is first imported in 3D Slicer as in Figure 3.2 and subsequently cropped to the region of interest, that is the smallest rectangular box containing the LV. The same software features a set of modules aimed to identify the subregions where the different tissues lie, both manually by selecting sets of adjacent voxels, and semi-automatically with filters based on the brightness of the voxels. We use in particular a filter exploiting the GrowCut algorithm [Vezhnevets and Konouchine, 2005] which, after different samples characterizing different tissues are given as input, tries to expand such samples coherently with the brightness to fill the whole region of interest. After this procedure has been

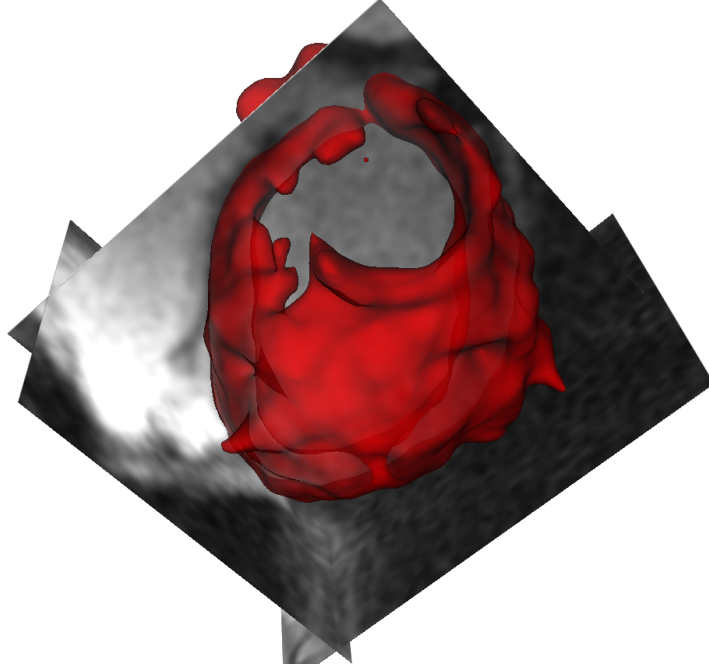


Figure 3.3 – The segmented LV after several smoothing steps, overlaid on three slices of a subset of the MRI shown in Figure 3.2.

fulfilled, several Gaussian smoothing steps [Wink and Roerdink, 2004] are performed to improve the overall quality of the mesh, which would otherwise feature a very rough surface, and isolated not connected regions are discarded. The result, shown in Figure 3.3, represents the first stage of the mesh and is exported in .vtk format.

Before it is actually possible to use the (still only surface at this stage) subject-specific mesh, we perform the following steps: we clip the vtk triangulation with respect to a plane orthogonal to the ventricle centerline with ParaView, disregarding the region close to the aortic and the mitral valves; then, further local smoothing is carried out with MeshLab, and filters to fill the holes and clean the mesh are applied; finally, a fine tuning and repairing is performed with NetFabb<sup>®</sup> to fix mismatched vertices and edges. The .stl mesh thus obtained can be used to generate a labelled 3D .mesh with GMSH as previously done for the prolate geometry.

In the case of the geometry of Figures 3.2-3.3, the MRI image from which it was segmented was taken at the end of the diastolic phase, that is when the LV reaches its maximum enlargement. The internal volume of the subject-specific myocardium at this stage of the heartbeat measures approximately 95 ml. The mesh is reported, together with the fibers and the sheets field, in Figure 3.8.

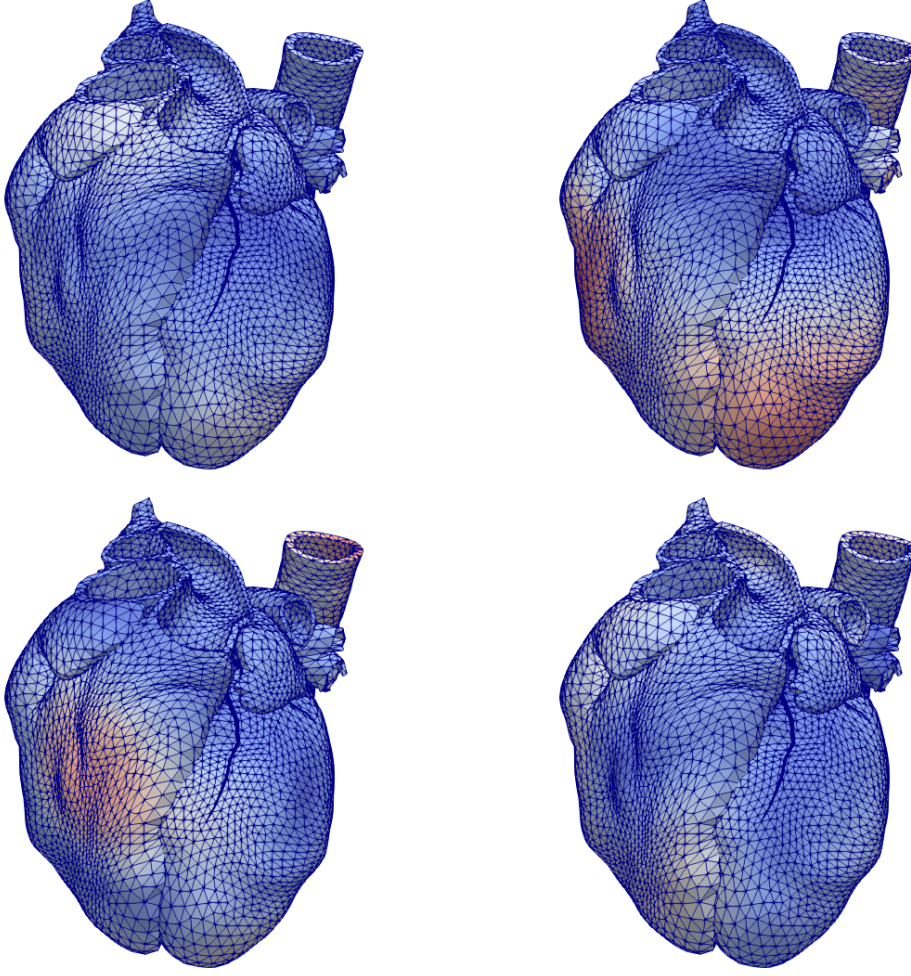


Figure 3.4 – The full-heart cardiac atlas colored by the first four modes obtained from the PCA analysis of the shape of the cardiac components of multiple subjects [Hoogendoorn et al., 2013]. From this perspective, the LV is located at the bottom right corner of each image.

### 3.1.3 Cardiac atlas

The last mesh generation case reported in this section concerns the generation of both the  $\Omega_0^s$  and the  $\Omega_0^f$  domains for the electrofluidmechanics model. Since the level of detail of the MRI of Section 3.1.2 was not sufficient to ensure that the myocardium in the region close to the valves and the aorta were accurately reproduced, we decided to use instead the cardiac atlas data provided in [Hoogendoorn et al., 2013]. The latter represents a cardiac geometry split into 13 components, obtained as the average of 134 subject-specific geometries. In the same work, a principal component analysis is carried on, and the obtained modes of variation are included in the data shown in Figure 3.4.

The data is provided as a .vtk file and the surface geometry features a relatively small

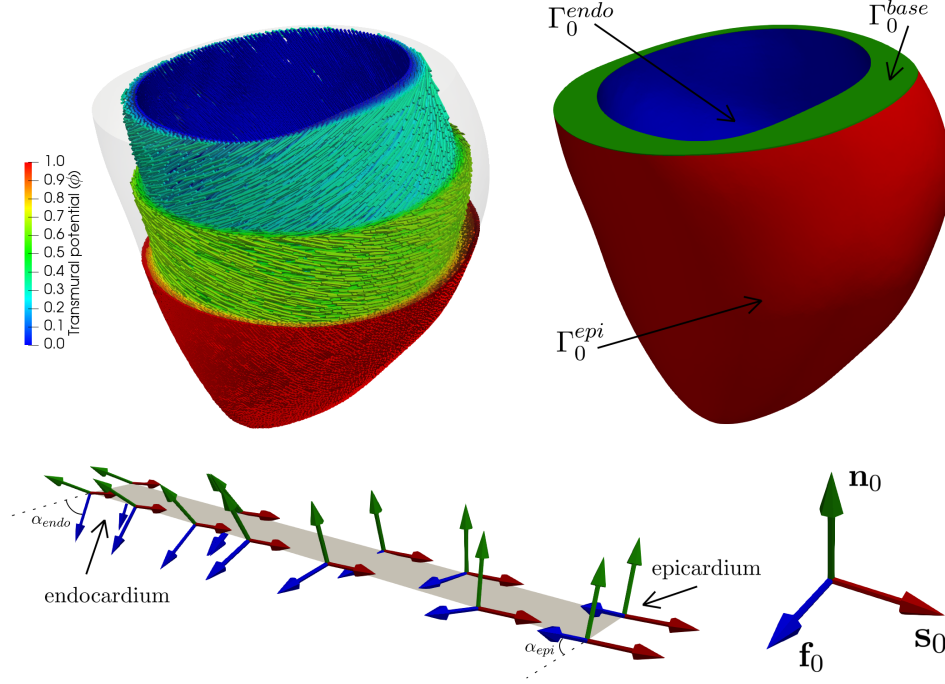


Figure 3.5 – Fibers field (top left) generated for the subject-specific mesh, and the mesh boundaries (top right), together with a close-up of a transmural slice of the myocardium with fibers, sheets and normals (bottom). Angles  $\alpha_{endo}$  and  $\alpha_{epi}$  are highlighted at the endocardium and epicardium, respectively.

number of triangles, which allows it to use for the testing of the electrofluidmechanics solvers. A procedure similar to the one outlined in Section 3.1.2 was performed, however in this case we clipped the fluid domain instead of the structure one, as soon as it bifurcates towards the aorta and the left atrium, respectively. The myocardium and the blood meshes thus obtained are reported, together with the fibers and the sheets field, in Figure 3.9.

### 3.2 Fibers and sheets distribution

In Chapter 1, we introduced the fibers, the sheets, and the (fibers-sheets) normals as vector fields defined on  $\Omega_0^s$  influencing the electrical and mechanical properties of the tissue in an anisotropic manner. In this section, we report a common rule-based algorithm for the generation of these three fields on the mesh approximating  $\Omega_0^s$ , which assumes that fibers are arranged in a helical fashion and their orientation varies transmurally from the epicardium to the endocardium, while sheets are directed transmurally [Rossi et al., 2014, Rossi, 2014].

Unlike the geometry, the fibers and the sheets fields in the myocardium may not be



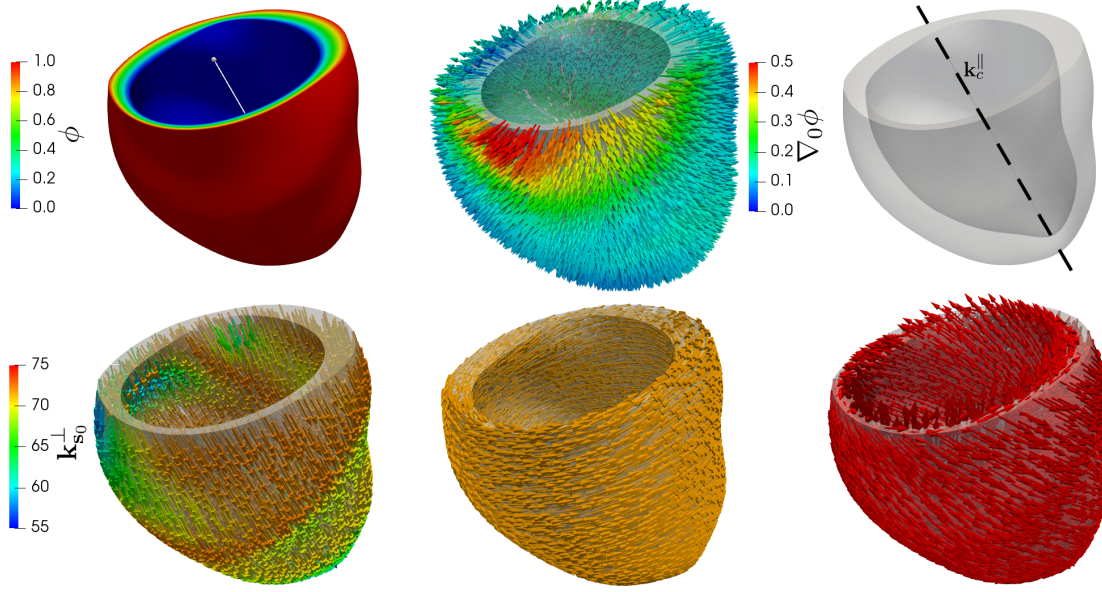


Figure 3.6 – Stages of the fibers generation rule algorithm, for the subject specific geometry. In the top row, we show the scalar potential  $\Phi$  (top left), its gradient  $\nabla_0\Phi$  before normalization (top), and the centerline direction  $\mathbf{k}_c^{\parallel}$  (top right). In the second row, the field  $\mathbf{k}_{s_0}^{\perp}$  (bottom left), the unrotated fiber field  $\tilde{\mathbf{f}}_0$  (bottom), and the final result  $\mathbf{f}_0$  (bottom right).

extracted from medical images unless special procedures are applied [Reese et al., 1995], such as Diffusion Tensor Imaging (DTI), which provides three orthotropic axes for every voxel in an imaged heart data set [Hsu et al., 1998, Scollan et al., 1998]. For this reason, several mathematically rule-based definitions of the fields have been used in literature [Göktepe and Kuhl, 2010, LeGrice et al., 2001, Nickerson et al., 2005, Rossi et al., 2012], which try to approximate their orientation. A more involved approach for the generation of the fibers in biventricle geometries of both the left and the right ventricles known as Laplace-Dirichlet Rule-Based (LDRB) was proposed in [Bayer et al., 2012].

In this work we assume that, at the epicardium and at the endocardium, the fiber direction is tangential to the boundary, while the sheet direction belongs to the plane identified by the normal and the ventricle centerline; in the most general case, angles  $\alpha_{endo}$ ,  $\alpha_{epi}$ ,  $\beta_{endo}$ , and  $\beta_{epi}$ , representing the inclination of the fibers and the sheets with respect to the base plane, are assigned. In order to determine the direction of fibers and sheets inside the myocardium, we solve a Laplace problem imposing a transmurally linear mapping of the fibers angle. A first study of the influence of the angles on both the conductivity and the deformation was carried out in [Eriksson et al., 2013]. Since this kind of analysis goes beyond the scope of this work, we will consider for all the geometries employed the algorithm and parameters proposed in [Wong and Kuhl, 2014] and further developed in [Rossi, 2014], therefore setting  $\alpha_{endo} = -60^\circ$ ,  $\alpha_{epi} = +60^\circ$ ,

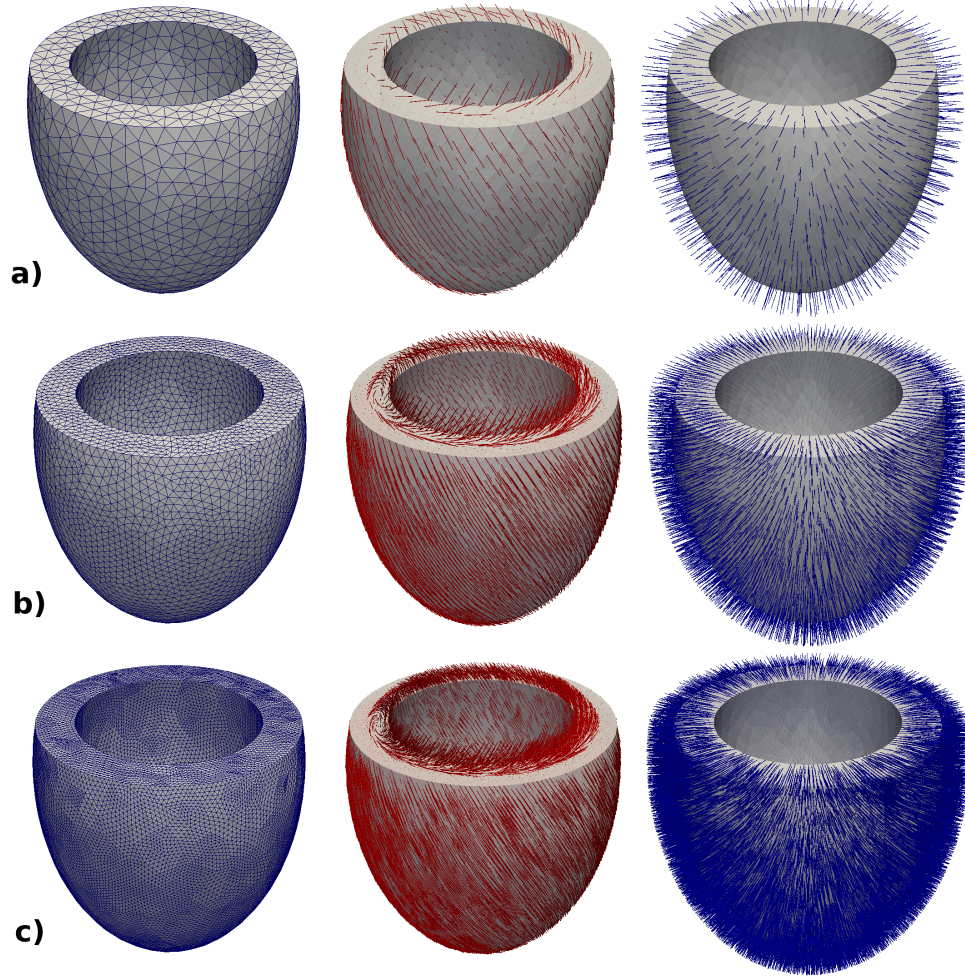


Figure 3.7 – Mesh of the idealized prolate LV geometry (top left), together with the fibers (top) and the sheets (top right) fields. The finer meshes (b) and (c) are obtained by hierarchical refinement of the coarsest mesh (a).

$\beta_{endo} = \beta_{epi} = 0^\circ$  (see Figure 3.5).

The algorithm implemented to generate the fibers can be formulated as follows. It is first assumed that the sheets vector field  $\mathbf{s}_0$  is irrotational, and hence there exists a scalar potential  $\phi$  which fully determines it up to an additive constant:

$$\nabla_0 \times \mathbf{s}_0 \Rightarrow \mathbf{s}_0 = \nabla_0 \phi.$$

Therefore, since the sheets are oriented along the direction going from the epicardium to the endocardium, we impose that the potential  $\phi$  varies transmurally; in order to do so,

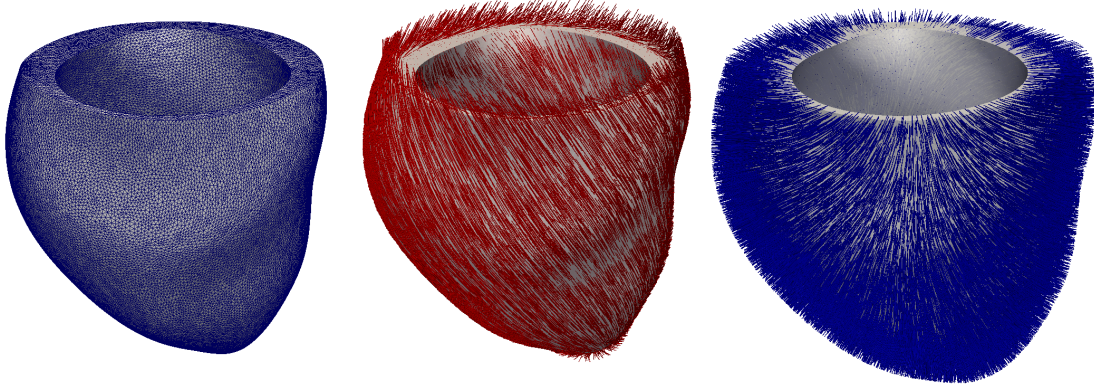


Figure 3.8 – Mesh of the patient-specific geometry (left), together with the fibers (center) and the sheets (right) fields.

we define it as the solution of the Laplace problem

$$\begin{cases} -\Delta_0 \phi = 0, & \text{in } \Omega_0^s, \\ \phi = 0, & \text{on } \Gamma_0^{endo}, \\ \phi = 1, & \text{on } \Gamma_0^{epi}, \\ \nabla_0 \phi \cdot \mathbf{N}_s = 0, & \text{on } \Gamma_0^{base}. \end{cases} \quad (3.1)$$

After (3.1) has been solved, a gradient recovering technique [Zienkiewicz and Zhu, 1992] is used to obtain  $\nabla_0 \phi$  and hence  $\mathbf{s}_0$  by normalization:

$$\mathbf{s}_0 = \frac{\nabla_0 \phi}{\|\nabla_0 \phi\|_2}.$$

Let now be  $\mathbf{k}_c^\parallel$  a vector oriented as the LV centerline; we then define  $\mathbf{k}_{s_0}^\perp$  as the projection of  $\mathbf{k}_c^\parallel$  on the plane orthogonal to  $\mathbf{s}_0$ :

$$\mathbf{k}_{s_0}^\perp = \mathbf{k}_c^\parallel - (\mathbf{k}_c^\parallel \cdot \mathbf{s}_0) \mathbf{s}_0,$$

then, a first approximation of the fibers field (with zero component in the centerline direction) is obtained by setting

$$\tilde{\mathbf{f}}_0 = \mathbf{s}_0 \times \frac{\mathbf{k}_{s_0}^\perp}{\|\mathbf{k}_{s_0}^\perp\|_2}.$$

The last step consists in the definition of the matrix  $\mathbb{R}_{s_0}(\phi)$ , which describes the local rotation of a single fiber around the  $\mathbf{s}_0$  axis. Assuming a bijective relation between the rotation angle and the potential  $\phi$ , we set

$$\mathbb{R}_{s_0}(\phi) = \mathbf{I} + \sin(\theta)[\mathbf{s}_0]_\times + 2\sin^2(\theta)[\mathbf{s}_0 \otimes \mathbf{s}_0 - \mathbf{I}],$$



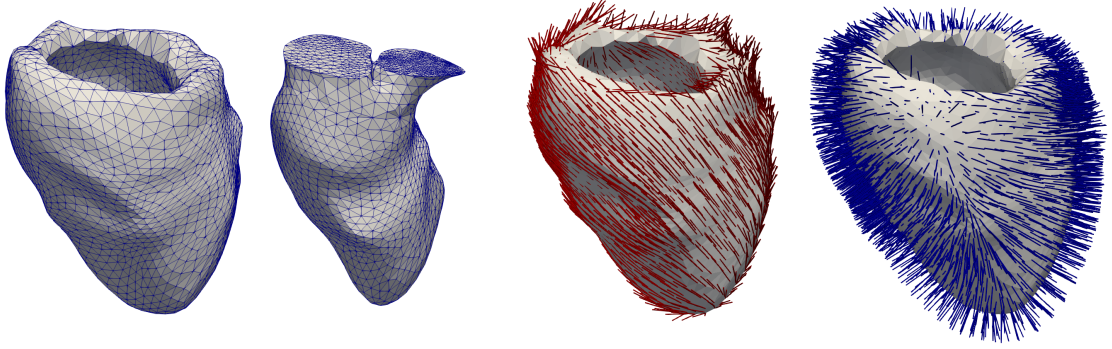


Figure 3.9 – Meshes of the cardiac atlas myocardium and blood geometries (left), together with the fibers (center) and the sheets (right) fields.

where

$$[\mathbf{s}_0]_{\times} = \begin{bmatrix} 0 & -s_{0,x} & s_{0,y} \\ s_{0,z} & 0 & -s_{0,x} \\ -s_{0,y} & s_{0,x} & 0 \end{bmatrix}, \quad \mathbf{s}_0 = [s_{0,x} \ s_{0,y} \ s_{0,z}]^T.$$

Finally, the fibers field  $\mathbf{f}_0$  are obtained by setting

$$\mathbf{f}_0 = \mathbb{R}_{\mathbf{s}_0}(\phi)\tilde{\mathbf{f}}_0.$$

We remark that, for simplicity, the normals field  $\mathbf{n}_0$  is not generated and saved, but rather computed once at simulation runtime as  $\mathbf{n}_0 = \mathbf{f}_0 \times \mathbf{s}_0$ .

In Figures 3.7, 3.8, and 3.9, we show the fields obtained by applying the algorithm to the prolate, the subject specific, and the atlas meshes, respectively. The algorithm herein described is implemented in LifeV and the result is saved into a Hierarchical Data Format (HDF5) file [Folk et al., 1999, Folk et al., 2011], a format designed to store and organize large amounts and high volume of data with efficient parallel I/O, thus making its use convenient in a HPC framework.

### 3.3 Prestress

In Section 2.1.4 we discretized in space the equations for the prestress, which we recall they take the form:

$$\mathbb{G}\hat{\mathbf{d}}_{s,0} + \mathbf{S}(\hat{\mathbf{d}}_{s,0}) = \bar{\mathbf{p}}^{endo} - \mathbf{S}_0, \quad (3.2)$$

where in particular

$$\mathbf{S}_{0,i} = \int_{\Gamma_0^{endo}} \mathbf{P}_0 : \nabla_0 \psi_{s,i} d\Omega_0^s, \quad (3.3)$$

---

**Algorithm 1** Prestress computation

---

```

function PRESTRESS( $S, \bar{p}, \varepsilon^{pre}, \mathbf{P}_{0,0}$ )
  for  $k = 1, \dots, S$  do
    set  $m = 1, \mathbf{P}_{0,k}^m = \mathbf{P}_{0,k-1}$ ;
    repeat
      solving problem (1.17) by means of the Newton method with
       $p = p_k = \frac{k}{S}\bar{p}$  and  $\mathbf{P}_0 = \mathbf{P}_{0,k}^m$ , thus obtaining  $\mathbf{d}_k^{m+1}$ ;
      update  $\mathbf{P}_{0,k}^{m+1} = \mathbf{P}_{0,k}^m + \mathbf{P}(\mathbf{d}_k^{m+1}, \mathbf{I})$  by means of Eq. (B.1);
      set  $m = m + 1$ ;
    until  $\frac{\|\mathbf{P}(\mathbf{d}_k^m, \mathbf{I})\|_\infty}{\|\mathbf{P}_{0,k}^m\|_\infty} < \varepsilon^{pre}$ 
    set  $\mathbf{P}_{0,k} = \mathbf{P}_{0,k}^m$ ;
  end for
return  $\mathbf{P}_{0,S}$ 
end function

```

---

for  $i = 1, \dots, 3N_{s,r}^{\text{dof}}$ .

In Eq. (3.2), both  $\hat{\mathbf{d}}_{s,0}$  and  $\mathbf{P}_0$  (and hence  $\mathbf{S}_0$ ) have to be determined. However, since it is equivalent to a system of 3 non linear equations in 12 unknowns (3 for the displacement, 9 for the prestress tensor), Eq. (3.2) is underdetermined. We solve it by using a numerical continuation method [Meyn, 1983, Chen and Yamamoto, 1994, Chen and Womersley, 2006, Allgower and Georg, 2012], which given an initial guess will produce an increasingly accurate approximation of a pair  $(\hat{\mathbf{d}}_{s,0}, \mathbf{P}_0)$  satisfying Eq. (3.2) by exploiting a fixed point scheme.

We first set

$$p_k = \frac{k}{S}\bar{p}^{endo}, \quad k = 1, \dots, S, \quad (3.4)$$

where  $S \in \mathbb{N}$  is the number of steps of the continuation method exploited to gradually increase the endocardial pressure value. Then, given  $S, \bar{p}^{endo}$ , a tolerance  $\varepsilon^{pre}$ , and an initial guess  $\mathbf{P}_{0,0}$ , the fixed point Algorithm 1 is applied to obtain the tensor  $\mathbf{P}_0 = \text{PRESTRESS}(S, \varepsilon^{pre}, \bar{p}^{endo}, \mathbf{P}_{0,0})$ . At each fixed point iteration, the Newton method is used to solve Eq. (3.2).

We empirically observe that the best results in terms of accuracy/efficiency ratio is obtained when Algorithm 1 is applied twice: a first approximation  $\tilde{\mathbf{P}}_0$  is computed by

### 3.4. A critical discussion on the preprocess pipeline

setting  $S = S_1$ ,  $\varepsilon^{pre} = \varepsilon_1^{pre}$  and  $\mathbf{P}_{0,0} = \mathbf{0}$ , and then used to re-initialize Algorithm 1 with  $S = 1$ ,  $\varepsilon^{pre} = \varepsilon_2^{pre} \ll \varepsilon_1^{pre}$ , and  $\mathbf{P}_{0,0} = \tilde{\mathbf{P}}_0$ . The additional step is performed to require a smaller tolerance when Algorithm 1 has already reached a closer value of the tensor  $\tilde{\mathbf{P}}_0$  to the target. Typical value used for the tolerances are  $\varepsilon_1^{pre} = 10^{-2}$ ,  $\varepsilon_2^{pre} = 10^{-7}$ , while the number of steps  $S_1$  has to be large enough to ensure the convergence of the continuation method, however its value is proportional to the computational cost of Algorithm 1 and depends on the value of  $\bar{p}^{endo}$ . Setting  $S_1 = 100$  proved to be sufficient in all the cases with the considered meshes and values of  $\bar{p}^{endo}$  ranging from 5 to 15 mmHg. We nonetheless observe that, while  $\frac{\|\mathbf{P}(\mathbf{d}_k^m, \mathbf{I})\|_\infty}{\|\mathbf{P}_{0,k}^m\|_\infty} \rightarrow 0$  for  $m \rightarrow +\infty$  according to the fixed point method, the displacement  $\mathbf{d}_k^{m+1}$  does not converge to  $\mathbf{0}$  but to a vector which we denote by  $\hat{\mathbf{d}}$ . However, we observe that the  $\hat{\mathbf{d}}$  accounts mostly to a rigid translation of the domain, and that this initial displacement ensures that the prestress is in equilibrium with the pressure at the epicardium. Therefore, we decide to set  $\mathbf{d}_{s,0} = \hat{\mathbf{d}}_{s,0}$  in (1.15).

Algorithm 1 is implemented in LifeV, and the solution is saved again in a HDF5 format file. However, in order to keep the implementation as simple as possible, and since we only need the prestress in the form of the vector  $\mathbf{S}_0$  defined in Eq. (3.3), we save the latter instead of the original tensor field  $\mathbf{P}_0$ .

### 3.4 A critical discussion on the preprocess pipeline

In this chapter, we outlined the pipeline for the preprocessing to be followed before the methods presented in Chapter 2 can be fully exploited; the pipeline is summarized in Figure 3.10.

We highlight that all the procedures described, with the notable exception of the mesh generation, can be fully automatized once the mesh and the LV centerline are given. The latter could be estimated from the medical images [De Vito and Qian, 1995, Bauer and Bischof, 2008, Xu et al., 2007] but, since the extensive test of multiple real geometries goes beyond the scope of this work, was manually measured. Nonetheless, we chose to complete each stage of the pipeline individually, instead of performing them automatically before the simulations. This choice was made for efficiency reasons. Indeed, even if the generation of fibers and sheets requires a negligible computational cost with respect to the integrated simulations, the prestress computation took several hours for the finest meshes considered. It was hence more convenient at this stage to compute the latter once before the simulations, instead of recomputing it each time.

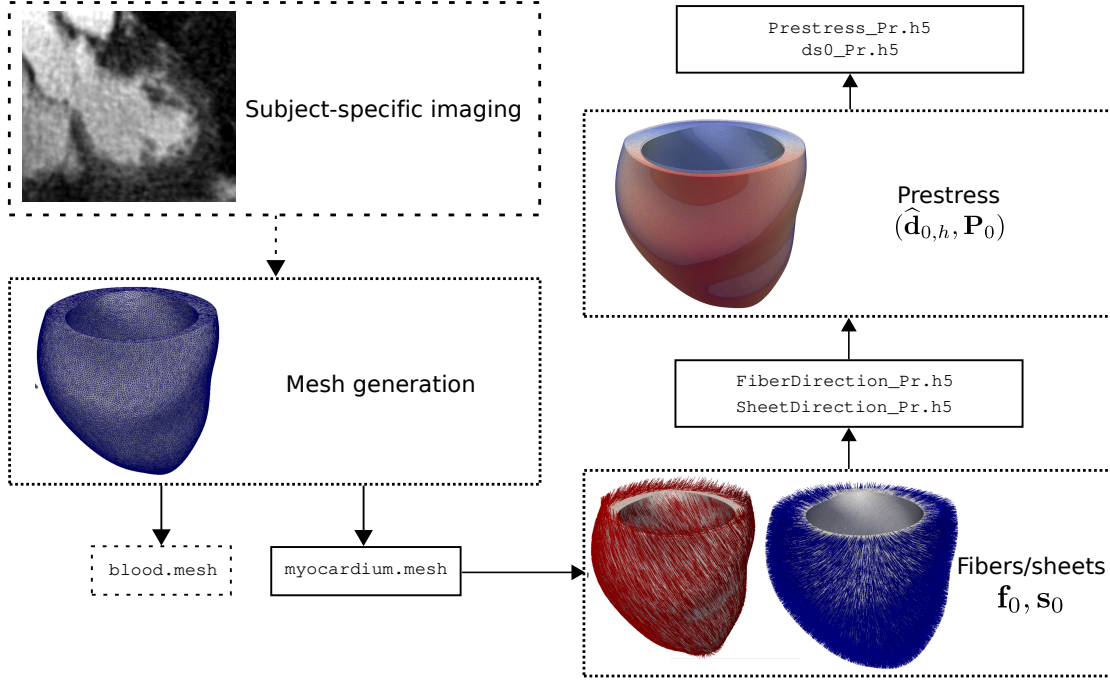


Figure 3.10 – The preprocess pipeline aiming at collecting the data required for the simulations. From the top left corner, counter-clockwise: the generation of the mesh, preceded by the segmentation of medical images in case of subject-specific geometries, produces the myocardium mesh file (and the blood one in the electrofluidmechanics case); the fibers and the sheets fields are defined in the nodes (depending on the FEM polynomial order  $r$ ) of the myocardium mesh; the mesh and the fields are used to generate the prestress and the initial displacement.

Automatizing the pipeline would also simplify the managing of the simulations. With the current setting, the user is required to provide the following 10 input files:

1. `myocardium.mesh` and `blood.mesh`;
2. `FiberDirection_Pr.xmf,.h5` (fibers  $\mathbf{f}_0$  field);
3. `SheetDirection_Pr.xmf,.h5` (sheet  $\mathbf{s}_0$  field);
4. `Prestress_Pr.xmf,.h5` (prestress  $\mathbf{P}_0$ );
5. `ds0_Pr.xmf,.h5` (initial displacement  $\hat{\mathbf{d}}_{s,0}$ ),

besides an additional file for the setting of the simulation parameters. This approach tends to be error prone and disk space demanding; we remark however that at a “release” stage an automatic pipeline can be implemented.

### 3.4. A critical discussion on the preprocess pipeline

---

| Mesh               | Figure | Vertices  | Tetrahedra | Edge [mm] |
|--------------------|--------|-----------|------------|-----------|
| Ideal              | 3.7a   | 1'827     | 6'500      | 5.85      |
| Refined Ideal      | 3.7b   | 11'658    | 52'000     | 2.93      |
| 2x Refined Ideal   | 3.7c   | 81'335    | 416'000    | 1.46      |
| 3x Refined Ideal   | -      | 602'749   | 3'328'000  | 0.73      |
| 4x Refined Ideal   | -      | 4'629'817 | 26'624'000 | 0.36      |
| Subject-specific   | 3.8    | 126'031   | 637'379    | 1.00      |
| Atlas (myocardium) | 3.9    | 4'126     | 15'543     | 4.55      |
| Atlas (fluid)      | 3.9    | 3'443     | 14'254     | 4.43      |

Table 3.1 – List of meshes used in this thesis, with their number of vertices, tetrahedra, and average edge length.

We conclude the chapter by reporting in Table 3.1 the meshes considered in the thesis with their number of vertices and tetrahedra and average edge length.



# Electromechanics Part II





## 4 Algorithms for the EM of the LV

The second part of this thesis is dedicated to the proposal of several algorithms for the solution of the electromechanics problem, which are based on the discretization of the single core models described in Chapter 2. As previously explained, the interaction of the myocardium with the fluid is taken into account only in the form of the endocardial pressure  $p^{endo}(t)$ , which in this chapter will be considered as given. Moreover, without loss of generality, we consider the monodomain equation for the remainder of this chapter for the sake of readability.

### 4.1 Fully monolithic strategy $(\mathcal{I}_I \mathcal{E}_I \mathcal{A}_I \mathcal{M}_I)$

We use the implicit scheme (2.14) for the time discretization of each core model and we assemble the integrated problem in a monolithic fashion, thus considering a “strong” coupling among the fully discretized core models; see [Gerbi et al., 2017]. This accounts to solve, for  $n = \sigma, \dots, N_T - 1$ , the following system of size  $8N_{s,r}^{\text{dof}}$ :

$$(\mathcal{I}_I \mathcal{E}_I \mathcal{A}_I \mathcal{M}_I) : \begin{cases} \left( \frac{\vartheta_0^I}{\Delta t} + \mathbb{U}(\bar{\mathbf{v}}^{n+1}) \right) \bar{\mathbf{w}}^{n+1} - \mathbf{Q}(\bar{\mathbf{v}}^{n+1}) = \frac{1}{\Delta t} \bar{\mathbf{w}}^I, \\ \left( \frac{\vartheta_0^I}{\Delta t} \mathbb{M} + \mathbb{K}(\bar{\mathbf{d}}_s^{n+1}) \right) \bar{\mathbf{v}}^{n+1} + \mathbf{I}^{ion}(\bar{\mathbf{v}}^{n+1}, \bar{\mathbf{w}}^{n+1}) = \frac{1}{\Delta t} \mathbb{M} \bar{\mathbf{v}}^I + \mathbb{M} \mathbf{I}^{app}(t^{n+1}), \\ \left( \frac{\vartheta_0^I}{\Delta t} \mathbb{M} + \varepsilon \mathbb{K}(\bar{\mathbf{w}}^{n+1}) \right) \bar{\gamma}_f^{n+1} + \Phi(\bar{\mathbf{w}}^{n+1}, \bar{\gamma}_f^{n+1}, \bar{\mathbf{d}}_s^{n+1}) = \frac{1}{\Delta t} \mathbb{M} \bar{\gamma}_f^I, \\ \left( \rho_s \frac{\vartheta_0^{\text{II}}}{(\Delta t)^2} \mathbb{M}_3 + \frac{\vartheta_0^I}{\Delta t} \mathbb{F} + \mathbb{G} \right) \bar{\mathbf{d}}_s^{n+1} + \mathbf{S}(\bar{\mathbf{d}}_s^{n+1}, \bar{\gamma}_f^{n+1}) \\ = \rho_s \frac{1}{(\Delta t)^2} \mathbb{M}_3 \bar{\mathbf{d}}_s^{\text{II}} + \frac{1}{\Delta t} \mathbb{F} \bar{\mathbf{d}}_s^I + \mathbf{p}^{endo}(t^{n+1}) - \mathbf{S}_0, \end{cases} \quad (4.1)$$

## Chapter 4. Algorithms for the EM of the LV

which we indicate as  $(\mathcal{I}_I \mathcal{E}_I \mathcal{A}_I \mathcal{M}_I)$ , where I stands for the implicit solver, and compactly rewrite in algebraic form as

$$\mathbf{A}_{EM}^{n+1}(\mathbf{z}^{n+1}) = \mathbf{b}_{EM}^{n+1}, \quad (4.2)$$

with notation being understood. We then apply, at each timestep, the Newton method [Quarteroni et al., 2010] to approximate the solution of the nonlinear problem (4.2) by iteratively solving the linear system

$$\begin{cases} \mathbb{J}_{EM}(\mathbf{z}_{k+1}^{n+1}) \delta \mathbf{z}_{k+1}^{n+1} = -\mathbf{r}_k^{n+1} \\ \mathbf{z}_{k+1}^{n+1} = \mathbf{z}_k^{n+1} + \delta \mathbf{z}_{k+1}^{n+1}, \end{cases} \quad (4.3)$$

for  $k = 0, \dots$ , until  $\|\mathbf{r}_k^{n+1}\|_{L^2} < \varepsilon_{tol}^N$ , where  $\varepsilon_{tol}^N$  is a given tolerance.  $\mathbb{J}_{EM}$  is the Jacobian matrix of (4.2), evaluated in  $\mathbf{z}_k^{n+1}$ :

$$\mathbb{J}_{EM}(\mathbf{z}) = \begin{bmatrix} \frac{\vartheta^I}{\Delta t} \mathbb{I} + \mathbb{U}(\bar{\mathbf{v}}) & \partial_v \mathbb{U}(\bar{\mathbf{v}}) - \partial_v \mathbf{Q}(\bar{\mathbf{v}}) & 0 & 0 \\ \partial_{\mathbf{w}} \mathbf{I}^{ion}(\bar{\mathbf{v}}, \bar{\mathbf{w}}) & \frac{\vartheta^I}{\Delta t} \mathbb{M}^L + \mathbb{K}_M(\bar{\mathbf{d}}_s) & 0 & \partial_{\mathbf{d}_s} \mathbb{K}_M(\bar{\mathbf{d}}_s, \bar{\mathbf{v}}) \\ & + \partial_v \mathbf{I}^{ion}(\bar{\mathbf{v}}, \bar{\mathbf{w}}) & & \\ \varepsilon \partial_{\mathbf{w}} \mathbb{K}_\gamma(\bar{\mathbf{w}}, \bar{\gamma}) & 0 & \frac{\vartheta^I}{\Delta t} \mathbb{M}^L + \varepsilon \mathbb{K}_\gamma(\bar{\mathbf{w}}) & \partial_{\mathbf{d}_s} \Phi(\bar{\mathbf{w}}, \bar{\gamma}, \bar{\mathbf{d}}_s) \\ + \partial_{\mathbf{w}} \Phi(\bar{\mathbf{w}}, \bar{\gamma}, \bar{\mathbf{d}}_s) & & + \partial_\gamma \Phi(\bar{\mathbf{w}}, \bar{\gamma}, \bar{\mathbf{d}}_s) & \\ 0 & 0 & \partial_\gamma \mathbf{S}(\bar{\mathbf{d}}_s, \bar{\gamma}) & \rho_s \frac{\vartheta^{II}}{\Delta t^2} \mathbb{M}_3^s + \frac{\vartheta^I}{\Delta t} \mathbb{F} + \mathbb{G} \\ & & & + \partial_{\mathbf{d}_s} \mathbf{S}(\bar{\mathbf{d}}_s, \bar{\gamma}) \end{bmatrix},$$

while the residual is defined as  $\mathbf{r}_k^{n+1} = \mathbf{b}_{EM}^{n+1} - \mathbf{A}_{EM}^{n+1}(\mathbf{z}_k^{n+1})$ . We highlight the block structure of  $\mathbb{J}_{EM}$ :

$$\mathbb{J}_{EM} = \begin{bmatrix} \boxed{J_{11} \ J_{12}} & 0 & 0 \\ \boxed{J_{21} \ J_{22}} & 0 & J_{24} \\ J_{31} & 0 & \boxed{J_{33}} & J_{34} \\ 0 & 0 & J_{43} & \boxed{J_{44}} \end{bmatrix}, \quad (4.4)$$

where we pointed out the diagonal blocks corresponding to the electrophysiology, the mechanical activation, and the mechanics, respectively.

While  $(\mathcal{I}_I \mathcal{E}_I \mathcal{A}_I \mathcal{M}_I)$  is “numerically” stable and convergent as long as the initial guess  $\mathbf{z}_0^{n+1}$  in (4.3) is, at each time, sufficiently close to the solution, it also requires to use the same timestep for the time discretization of each core model. Hence, even if the electrophysiology and the mechanics are characterized by very different time scales, the former dictates our choice for the timestep of the fully monolithic problem.

### 4.1.1 Preconditioning the monolithic problem

We rewrite, for the sake of readability, the linear system associated to a single Newton iteration for the implicit scheme (4.3) in the following form:

$$\mathbb{J}_{EM} \delta \mathbf{z} = -\mathbf{r}. \quad (4.5)$$

We use the GMRES method [Saad, 2003] for the solution of the linear problem (4.5) as  $\mathbb{J}_{EM}$  is non-symmetric and the distribution of the eigenvalues of its spectrum is not known a priori.

The choice of the preconditioner is critical in order to ensure the convergence of the linear solver; while this is true in general, it is even more relevant in the case of monolithic multiphysics problems [Keyes et al., 2013]. Indeed, using a black-box algebraic preconditioner for problem (4.5) the information related to each differential problem associated to a single core model would be neglected; we instead consider a strategy exploiting such information at the block level, that is we create a preconditioner that exploits the “physics” of the coupled problem at the level of the block structure. Following [Deparis et al., 2016a, Deparis et al., 2016b, Forti et al., 2016] for FSI problems, we propose a block Gauss-Seidel preconditioner  $\mathcal{P}_{EM}$  obtained by dropping the upper triangular blocks of matrix  $\mathbb{J}_{EM}$ , i.e. the off-diagonal blocks, thus obtaining:

$$\mathcal{P}_{EM} = \begin{bmatrix} J_{11} & 0 & 0 & 0 \\ J_{21} & J_{22} & 0 & 0 \\ J_{31} & 0 & J_{33} & 0 \\ 0 & 0 & J_{43} & J_{44} \end{bmatrix}.$$

$\mathcal{P}_{EM}$  can then be factorized into four model-specific nonsingular matrices, namely  $\mathcal{P}_{ion}$ ,  $\mathcal{P}_{pot}$ ,  $\mathcal{P}_{act}$ , and  $\mathcal{P}_{mec}$  corresponding to the ionic, the potential, the activation, and the mechanics single core models, respectively:

$$\mathcal{P}_{EM} = \underbrace{\begin{bmatrix} J_{11} & 0 & 0 & 0 \\ 0 & I & 0 & 0 \\ 0 & 0 & I & 0 \\ 0 & 0 & 0 & I \end{bmatrix}}_{\mathcal{P}_1 = \mathcal{P}_{ion}} \underbrace{\begin{bmatrix} I & 0 & 0 & 0 \\ J_{21} & J_{22} & 0 & 0 \\ 0 & 0 & I & 0 \\ 0 & 0 & 0 & I \end{bmatrix}}_{\mathcal{P}_2 = \mathcal{P}_{pot}} \underbrace{\begin{bmatrix} I & 0 & 0 & 0 \\ 0 & I & 0 & 0 \\ J_{31} & 0 & J_{33} & 0 \\ 0 & 0 & 0 & I \end{bmatrix}}_{\mathcal{P}_3 = \mathcal{P}_{act}} \underbrace{\begin{bmatrix} I & 0 & 0 & 0 \\ 0 & I & 0 & 0 \\ 0 & 0 & I & 0 \\ 0 & 0 & J_{43} & J_{44} \end{bmatrix}}_{\mathcal{P}_4 = \mathcal{P}_{mec}}.$$

This decomposition can also be interpreted as an inexact factorization of matrix  $\mathbb{J}_{EM}$ . The preconditioned version of problem (4.5) then reads:

$$\begin{cases} \mathbb{J}_{EM} \mathcal{P}_{EM}^{-1} \mathbf{y} = -\mathbf{r} \\ \mathcal{P}_{EM} \delta \mathbf{z} = \mathbf{y}. \end{cases} \quad (4.6)$$

Since each diagonal block  $J_{ii}$  appears in a distinct factor  $\mathcal{P}_i$ , for  $i = 1, \dots, 4$ , then

physics-specific ad-hoc preconditioners can be efficiently used to approximate its inverse. Indeed, we define the symbolic operation  $\delta \mathbf{z} = \mathcal{P}_{EM}^{-1} \mathbf{y}$  in (4.6) as the application of the following sequential steps

$$\begin{cases} \delta \mathbf{z}_w &= J_{11}^{-1} \mathbf{y}_w, \\ \delta \mathbf{z}_V &= J_{22}^{-1} (\mathbf{y}_V - J_{21} \delta \mathbf{z}_w), \\ \delta \mathbf{z}_d &= J_{33}^{-1} (\mathbf{y}_d - J_{31} \delta \mathbf{z}_w), \\ \delta \mathbf{z}_\gamma &= J_{44}^{-1} (\mathbf{y}_\gamma - J_{43} \delta \mathbf{z}_d); \end{cases} \quad (4.7)$$

the solution of each linear system in (4.7) is carried out by using again the GMRES method and by exploiting Algebraic Multigrid (AMG) [Briggs et al., 2000] and Additive Schwarz (AS) [Quarteroni and Valli, 1996] preconditioners. The preconditioner  $\mathcal{P}_{EM}$  can be regarded as a generalization of the FaCSI preconditioner for FSI problems proposed in [Deparis et al., 2016b] (see also [Deparis et al., 2016a, Forti et al., 2016]).

## 4.2 Segregated schemes

Even though the monolithic strategy  $(\mathcal{I}_I \mathcal{E}_I \mathcal{A}_I \mathcal{M}_I)$  presented in Section 4.1 is stable, it has two main practical drawbacks. First, the time advancement of Eq. (4.1) must be carried out using the same timestep size  $\Delta t$  for all the core models involved: as a consequence, the the small timestep size required by the electrophysiology must be used for the mechanics too, thus solving the latter more often than “necessary”. Second, the large size of the Jacobian matrix  $\mathbb{J}_{EM}$  requires a relatively large amount of memory to be stored, and of processing units for its assembly. In order to overcome these issues, we propose three segregated algorithms exploiting the Godunov splitting scheme [Godunov, 1959]. The latter consists in solving Eq. (4.1) in two consecutive steps at each timestep, by properly uncoupling the core problems. However, as we will show, the scheme introduces a first order error on the solution.

The block structure of  $\mathbb{J}_{EM}$ , and the different characteristic time scales for the electrophysiology and for the mechanics, suggest a first splitting between the latter models, and we choose to keep the mechanical activation core problem coupled with the electrophysiology. To this aim, the dependence of the monodomain/bidomain equations and of the mechanical activation on the displacement  $\mathbf{d}_s^{n+1}$  is realized by evaluating them in  $\mathbf{d}_s^*$  instead. We show that this operation introduces a first order error on the following model problem:

$$\begin{cases} \frac{d\mathbf{u}}{dt} = L\mathbf{u} + \mathbf{f}, & t \in (0, T], \\ \mathbf{u}(0) = \mathbf{u}_0, \end{cases} \quad (4.8)$$

where

$$L = \begin{bmatrix} L_{vv} & L_{vd} \\ L_{dv} & L_{dd} \end{bmatrix}, \quad \mathbf{u} = \begin{bmatrix} v \\ d \end{bmatrix}, \quad \mathbf{f} = \begin{bmatrix} f_v \\ f_d \end{bmatrix}.$$

Here,  $v$  and  $d$  synthetically represent the variables associated to the electrophysiology and to the mechanics, respectively. To this aim, let us first prove the following result relative to the error introduced on a single timestep:

**Theorem 1.** *Consider Eq. (4.8) with  $T = \Delta t$  and the uncoupled problem*

$$\begin{cases} \frac{d\mathbf{w}}{dt} = L_1\mathbf{w} + L_2\mathbf{w}_0 + \mathbf{f}, & t \in (0, \Delta t], \\ \mathbf{w}(0) = \mathbf{w}_0 = \mathbf{u}_0, \end{cases} \quad (4.9)$$

where

$$L = L_1 + L_2 = \begin{bmatrix} L_{vv} & 0 \\ L_{dv} & L_{dd} \end{bmatrix} + \begin{bmatrix} 0 & L_{vd} \\ 0 & 0 \end{bmatrix}.$$

Then, it holds:

$$e(\Delta t) = \|\mathbf{u}(\Delta t) - \mathbf{w}(\Delta t)\| \leq C_1 \Delta t^2$$

for a positive constant  $C_1$ .

*Proof.* We first write  $\mathbf{u}$  and  $\mathbf{w}$  at time  $t = \Delta t$  in terms of their Taylor expansion around time  $t = 0$ :

$$\begin{aligned} \mathbf{u}(\Delta t) &= \mathbf{u}_0 + \Delta t \frac{\partial \mathbf{u}}{\partial t} \Big|_0 + \frac{\Delta t^2}{2} \frac{\partial^2 \mathbf{u}}{\partial t^2} \Big|_0 + O(\Delta t^3) \\ &= \mathbf{u}_0 + \Delta t (L\mathbf{u}_0 + \mathbf{f}(0)) + \frac{\Delta t^2}{2} \left( L(L\mathbf{u}_0 + \mathbf{f}(0)) + \frac{\partial \mathbf{f}}{\partial t}(0) \right) + O(\Delta t^3) \\ &= \mathbf{u}_0 + \Delta t (L\mathbf{u}_0 + \mathbf{f}(0)) + \frac{\Delta t^2}{2} (L^2\mathbf{u}_0 + L\mathbf{f}(0) + \frac{\partial \mathbf{f}}{\partial t}(0)) + O(\Delta t^3), \end{aligned}$$

and

$$\begin{aligned}
\mathbf{w}(\Delta t) &= \mathbf{w}_0 + \Delta t \left. \frac{\partial \mathbf{w}}{\partial t} \right|_0 + \frac{\Delta t^2}{2} \left. \frac{\partial^2 \mathbf{w}}{\partial t^2} \right|_0 + O(\Delta t^3) \\
&= \mathbf{w}_0 + \Delta t (L_1 \mathbf{w} + L_2 \mathbf{w}_0 + \mathbf{f}) \Big|_0 + \frac{\Delta t^2}{2} \frac{\partial}{\partial t} (L_1 \mathbf{w} + L_2 \mathbf{w}_0 + \mathbf{f}) \Big|_0 + O(\Delta t^3) \\
&= \mathbf{w}_0 + \Delta t (L_1 \mathbf{w}_0 + L_2 \mathbf{w}_0 + \mathbf{f}(0)) + \frac{\Delta t^2}{2} \left( L_1 (L_1 \mathbf{w}_0 + L_2 \mathbf{w}_0 + \mathbf{f}(0)) + \frac{\partial \mathbf{f}}{\partial t}(0) \right) + O(\Delta t^3) \\
&= \mathbf{u}_0 + \Delta t (L \mathbf{u}_0 + \mathbf{f}(0)) + \frac{\Delta t^2}{2} \left( (L_1^2 \mathbf{u}_0 + L_1 L_2 \mathbf{u}_0 + L_1 \mathbf{f}(0)) + \frac{\partial \mathbf{f}}{\partial t}(0) \right) + O(\Delta t^3).
\end{aligned}$$

Then, we evaluate the difference between  $\mathbf{u}(\Delta t)$  and  $\mathbf{w}(\Delta t)$ :

$$\begin{aligned}
\mathbf{u}(\Delta t) - \mathbf{w}(\Delta t) &= \frac{\Delta t^2}{2} (L^2 \mathbf{u}_0 + L \mathbf{f}(0) - L_1^2 \mathbf{u}_0 - L_1 L_2 \mathbf{u}_0 - L_1 \mathbf{f}(0)) + O(\Delta t^3) \\
&= \frac{\Delta t^2}{2} \left( (L^2 - L_1^2 - L_1 L_2) \mathbf{u}_0 + (L - L_1) \mathbf{f}(0) \right) + O(\Delta t^3) \\
&= \frac{\Delta t^2}{2} \left( (L_2^2 + L_2 L_1) \mathbf{u}_0 + L_2 \mathbf{f}(0) \right) + O(\Delta t^3) \\
&= \frac{\Delta t^2}{2} L_2 (L \mathbf{u}_0 + \mathbf{f}(0)) + O(\Delta t^3) \\
&= \frac{\Delta t^2}{2} L_2 \left. \frac{\partial \mathbf{w}}{\partial t} \right|_0 + O(\Delta t^3).
\end{aligned}$$

The result follows then from the definition of  $e(\Delta t)$ . □

We have hence proven that a second order error is introduced when solving a single timestep of the uncoupled problem. Considering now the error at the final time  $e(T)$ , we have

$$e(T) \approx N_T e(\Delta t) \leq \frac{T}{\Delta t} C_1 \Delta t^2 \leq C_2(T) \Delta t.$$

Thus, the solution of the uncoupled problem converges to the solution of the coupled problem linearly with respect to  $\Delta t$ . We now take advantage of this result to formulate three different segregated (and possibly staggered) strategies.

#### 4.2.1 Partially segregated strategy $(\mathcal{I}_I \mathcal{E}_I \mathcal{A}_I) - (\mathcal{M}_I)$

As anticipated, we first break the strong coupling between the electrophysiology and the mechanical activation  $(\mathcal{I}_I \mathcal{E}_I \mathcal{A}_I)$  and the tissue mechanics  $(\mathcal{M}_I)$ . We hence evaluate the terms  $\mathbb{K}(\bar{\mathbf{d}}^{n+1})$  and  $\Phi(\bar{\mathbf{w}}^{n+1}, \bar{\gamma}^{n+1}, \bar{\mathbf{d}}^{n+1})$  of Eq. (4.1) in the extrapolated variable  $\bar{\mathbf{d}}^*$  instead of  $\bar{\mathbf{d}}^{n+1}$ , thus obtaining two separated problems which are solved in a segregated fashion. We notice that the  $(\mathcal{I}_I \mathcal{E}_I \mathcal{A}_I)$  problem is still fully coupled, while it is decoupled

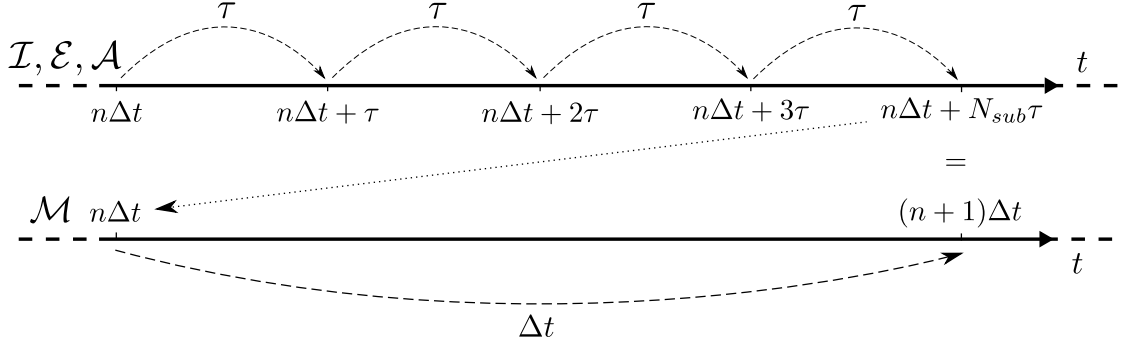


Figure 4.1 – Graphical representation of the time advancement for the  $(\mathcal{I}_I \mathcal{E}_I \mathcal{A}_I) - (\mathcal{M}_I)$  and the  $(\mathcal{I}_{SI} \mathcal{E}_{SI} \mathcal{A}_{SI}) - (\mathcal{M}_I)$  schemes.

from the  $(\mathcal{M}_I)$  block, hence the denomination  $(\mathcal{I}_I \mathcal{E}_I \mathcal{A}_I) - (\mathcal{M}_I)$ .

This approach allows to use a smaller timestep for the  $(\mathcal{I}_I \mathcal{E}_I \mathcal{A}_I)$  problem, which we denote by  $\tau$ , with respect to the one used for the mechanics  $(\mathcal{M}_I)$ . In such a case, we speak of a *staggered* strategy. For our purposes, we set in particular

$$\tau = \frac{\Delta t}{N_{sub}},$$

where  $N_{sub} \in \mathbb{N}$  is the number of intermediate substeps;  $\tau$  is the timestep size of  $(\mathcal{I}_I \mathcal{E}_I \mathcal{A}_I)$  and  $\Delta t$  that of  $(\mathcal{M}_I)$ . This implies that  $\tau \leq \Delta t$  and  $t^{n+\frac{m}{N_{sub}}} = t^n + m\tau$  for  $m = 1, \dots, N_{sub}$ .  $N_{sub}$  can also be regarded as the ratio of the timestep lengths used for the mechanics, and for the electrophysiology and activation. The overall time advancement is represented in Figure 4.1. Another clear advantage of this approach is that, in the isovolumic phases, only the mechanics problem needs to be solved, contrarily to the fully monolithic one where Eq. (4.1) has to be solved at each subiteration. Problem  $(\mathcal{I}_I \mathcal{E}_I \mathcal{A}_I)$  from  $t^n$  to  $t^{n+1}$  reads:

$$(\mathcal{I}_I \mathcal{E}_I \mathcal{A}_I) : \begin{cases} \left( \frac{\vartheta_0^I}{\tau} + \mathbb{U}(\bar{\mathbf{v}}^{n+\frac{m}{N_{sub}}}) \right) \bar{\mathbf{w}}^{n+\frac{m}{N_{sub}}} - \mathbf{Q}(\bar{\mathbf{v}}^{n+\frac{m}{N_{sub}}}) = \frac{1}{\tau} \bar{\mathbf{w}}^I, \\ \left( \frac{\vartheta_0^I}{\tau} \mathbb{M} + \mathbb{K}(\bar{\mathbf{d}}^*) \right) \bar{\mathbf{v}}^{n+\frac{m}{N_{sub}}} + \mathbf{I}^{ion}(\bar{\mathbf{v}}^{n+\frac{m}{N_{sub}}}, \bar{\mathbf{w}}^{n+\frac{m}{N_{sub}}}) = \frac{1}{\tau} \mathbb{M} \bar{\mathbf{v}}^I + \mathbb{M} \mathbf{I}^{app}(t^{n+\frac{m}{N_{sub}}}), \\ \left( \frac{\vartheta_0^I}{\tau} \mathbb{M} + \varepsilon \mathbb{K}(\bar{\mathbf{w}}^{n+\frac{m}{N_{sub}}}) \right) \bar{\gamma}^{n+\frac{m}{N_{sub}}} + \Phi(\bar{\mathbf{w}}^{n+\frac{m}{N_{sub}}}, \bar{\gamma}^{n+\frac{m}{N_{sub}}}, \bar{\mathbf{d}}^*) = \frac{1}{\tau} \mathbb{M} \bar{\gamma}^I, \end{cases} \quad (4.10)$$

for  $m = 1, \dots, N_{sub}$ , where the terms  $\bar{\mathbf{w}}^I$ ,  $\bar{\mathbf{v}}^I$ , and  $\bar{\gamma}^I$  (defined in Eq. (2.13)) are evaluated by using the variables at times  $t^n, t^n - \tau, \dots, t^n - (\sigma - 1)\tau$ . As in the case of the implicit electromechanics, we use the Newton method to solve problem (4.10), and the block

structure of the correspondent Jacobian matrix  $\mathbb{J}_{EA}$  is:

$$\mathbb{J}_{EA} = \begin{bmatrix} \boxed{J_{11} \ J_{12}} & 0 \\ J_{21} \ J_{22} & 0 \\ J_{31} \ 0 & \boxed{J_{33}} \end{bmatrix} \quad (4.11)$$

We exploit the same preconditioning technique that was outlined in Section 4.1 for the  $(\mathcal{I}_I \mathcal{E}_I \mathcal{A}_I \mathcal{M}_I)$  strategy, only restricted to the block  $(\mathcal{I}_I \mathcal{E}_I \mathcal{A}_I)$ . After solving Eq. (4.10) for  $N_{sub}$  steps, we solve at  $t^{n+1}$  the implicit mechanics problem  $(\mathcal{M}_I)$ :

$$\begin{aligned} (\mathcal{M}_I) : \quad & \left( \rho_s \frac{\vartheta_0^{\text{II}}}{(\Delta t)^2} \mathbb{M}_3 + \frac{\vartheta_0'}{\Delta t} \mathbb{F} + \mathbb{G} \right) \bar{\mathbf{d}}^{n+1} + \mathbf{S}(\bar{\mathbf{d}}^{n+1}, \bar{\boldsymbol{\gamma}}^{n+1}) \\ & = \rho_s \frac{1}{(\Delta t)^2} \mathbb{M}_3 \bar{\mathbf{d}}^{\text{II}} + \frac{1}{\Delta t} \mathbb{F} \bar{\mathbf{d}}^{\text{I}} + \mathbf{p}^{endo}(t^{n+1}) - \mathbf{S}_0, \end{aligned} \quad (4.12)$$

by means of the Newton method. We highlight that the vector  $\bar{\boldsymbol{\gamma}}^{n+1}$  in Eq. (4.12) is already known, since it is given after the last step of Eq. (4.10) (i.e. for  $m = N_{sub}$ ).

#### 4.2.2 Partially segregated strategy $(\mathcal{I}_{SI} \mathcal{E}_{SI} \mathcal{A}_{SI}) - (\mathcal{M}_I)$

By considering now the semi-implicit scheme for the time discretization, the  $(\mathcal{I}_{SI} \mathcal{E}_{SI} \mathcal{A}_{SI})$  problem reads:

$$(\mathcal{I}_{SI} \mathcal{E}_{SI} \mathcal{A}_{SI}) : \quad \begin{cases} \left( \frac{\vartheta_0^{\text{I}}}{\Delta t} + \mathbb{U}(\bar{\mathbf{v}}^*) \right) \bar{\mathbf{w}}^{n+\frac{m}{N_{sub}}} = \frac{1}{\tau} \bar{\mathbf{w}}^{\text{I}} + \mathbf{Q}(\bar{\mathbf{v}}^*), \\ \left( \frac{\vartheta_0^{\text{I}}}{\Delta t} \mathbb{M} + \mathbb{K}(\bar{\mathbf{d}}^*) + \mathbb{I}_v^{ion}(\bar{\mathbf{v}}^*, \bar{\mathbf{w}}^*) \right) \bar{\mathbf{v}}^{n+\frac{m}{N_{sub}}} + \mathbb{I}_{\mathbf{w}}^{ion}(\bar{\mathbf{v}}^*, \bar{\mathbf{w}}^*) \bar{\mathbf{w}}^{n+\frac{m}{N_{sub}}} \\ \quad = \frac{1}{\tau} \mathbb{M} \bar{\mathbf{v}}^{\text{I}} + \tilde{\mathbf{I}}^{ion}(\bar{\mathbf{v}}^*, \bar{\mathbf{w}}^*) + \mathbb{M} \mathbf{I}^{app}(t^{n+\frac{m}{N_{sub}}}), \\ \left( \frac{\vartheta_0^{\text{I}}}{\tau} \mathbb{M} + \varepsilon \mathbb{K}(\bar{\mathbf{w}}^*) + \mathbb{P}_{\gamma_f}(\bar{\mathbf{w}}^*, \bar{\boldsymbol{\gamma}}^*, \bar{\mathbf{d}}^*) \right) \bar{\boldsymbol{\gamma}}^{n+\frac{m}{N_{sub}}} = \frac{1}{\tau} \mathbb{M} \bar{\boldsymbol{\gamma}}^{\text{I}} + \tilde{\boldsymbol{\Phi}}(\bar{\mathbf{w}}^*, \bar{\boldsymbol{\gamma}}^*, \bar{\mathbf{d}}^*), \end{cases} \quad (4.13)$$

for  $m = 1, \dots, N_{sub}$ . In this case, the block pattern of the matrix  $\mathbb{A}_{EA}$ , stemming from the linear system (4.13), is:

$$\mathbb{A}_{EA} = \begin{bmatrix} \boxed{A_{11} \ 0} & 0 \\ A_{21} \ A_{22} & 0 \\ 0 \ 0 & \boxed{A_{33}} \end{bmatrix}. \quad (4.14)$$



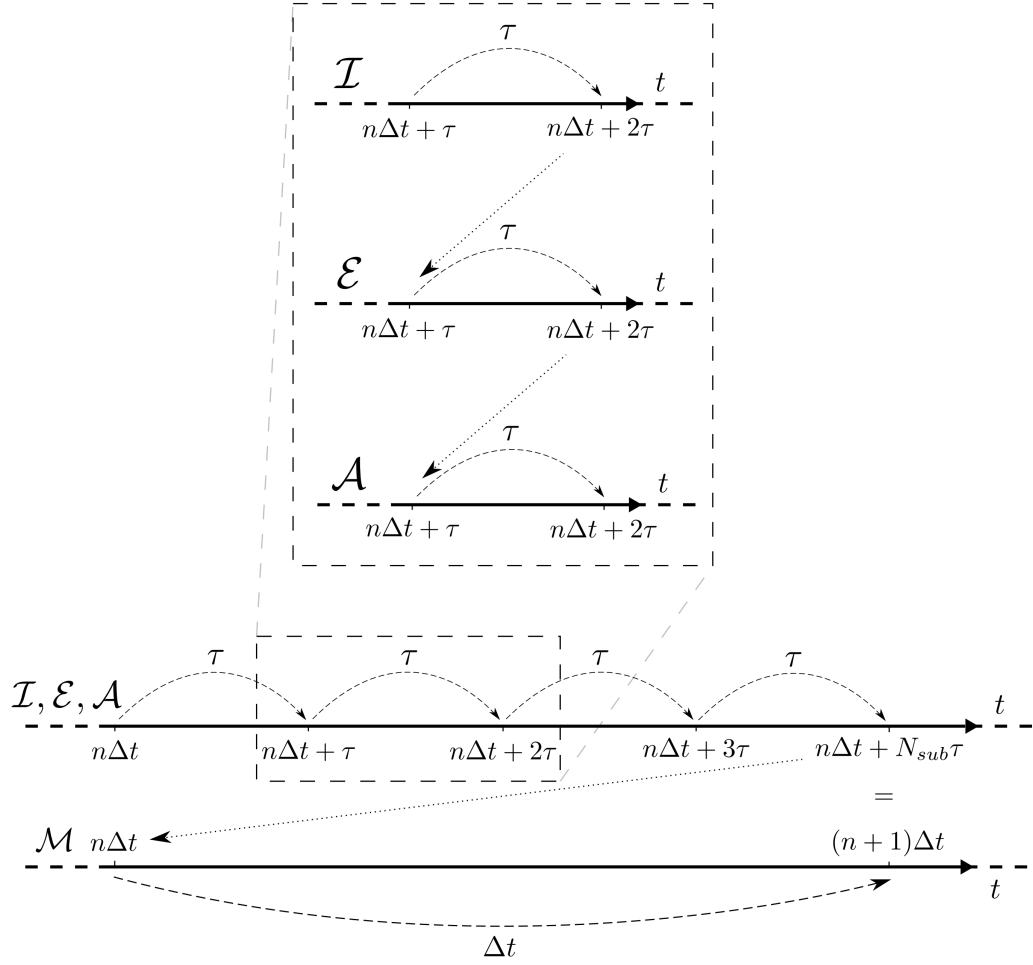


Figure 4.2 – Graphical representation of the time advancement for the  $(\mathcal{I}_{\text{SI}})-(\mathcal{E}_{\text{SI}})-(\mathcal{A}_{\text{SI}})-(\mathcal{M}_{\text{I}})$  scheme.

As in the case of the  $(\mathcal{I}_{\text{I}}\mathcal{E}_{\text{I}}\mathcal{A}_{\text{I}})$  strategy, after solving Eq. (4.13) for  $N_{\text{sub}}$  steps, we solve the implicit mechanics problem  $(\mathcal{M}_{\text{I}})$  (4.12).

### 4.2.3 Fully segregated strategy $(\mathcal{I}_{\text{SI}})-(\mathcal{E}_{\text{SI}})-(\mathcal{A}_{\text{SI}})-(\mathcal{M}_{\text{I}})$

Finally, we further segregate the  $(\mathcal{I}_{\text{SI}}\mathcal{E}_{\text{SI}}\mathcal{A}_{\text{SI}})$  block, that is instead of solving  $(\mathcal{I}_{\text{SI}}\mathcal{E}_{\text{SI}}\mathcal{A}_{\text{SI}})$  (4.13) in a monolithic fashion, we solve the three subproblems sequentially. In Figure 4.2 we show a representation of the time advancement in this case. At each time  $t^n$ , the algorithm amounts to perform, for  $m = 1, \dots, N_{\text{sub}}$ , the following steps, in order:

1. find  $\bar{\mathbf{w}}^{n+\frac{m}{N_{sub}}}$  by solving:

$$(\mathcal{I}_{SI}) : \quad \left( \frac{\vartheta_0^I}{\Delta t} + \mathbb{U}(\bar{\mathbf{v}}^*) \right) \bar{\mathbf{w}}^{n+\frac{m}{N_{sub}}} = \frac{1}{\tau} \bar{\mathbf{w}}^I + \mathbf{Q}(\bar{\mathbf{v}}^*); \quad (4.15)$$

2. use  $\bar{\mathbf{w}}^{n+\frac{m}{N_{sub}}}$ , obtained with Eq. (4.15), to find  $\bar{\mathbf{v}}^{n+\frac{m}{N_{sub}}}$  by solving:

$$(\mathcal{E}_{SI}) : \quad \left( \frac{\vartheta_0^I}{\Delta t} \mathbb{M} + \mathbb{K}(\bar{\mathbf{d}}^*) + \mathbb{I}_v^{ion}(\bar{\mathbf{v}}^*, \bar{\mathbf{w}}^{n+\frac{m}{N_{sub}}}) \right) \bar{\mathbf{v}}^{n+\frac{m}{N_{sub}}} = \frac{1}{\tau} \mathbb{M} \bar{\mathbf{v}}^I \\ + \tilde{\mathbf{I}}^{ion}(\bar{\mathbf{v}}^*, \bar{\mathbf{w}}^{n+\frac{m}{N_{sub}}}) - \mathbb{I}_{\mathbf{w}}^{ion}(\bar{\mathbf{v}}^*, \bar{\mathbf{w}}^{n+\frac{m}{N_{sub}}}) \bar{\mathbf{w}}^{n+\frac{m}{N_{sub}}} + \mathbb{M} \mathbf{I}^{app}(t^{n+\frac{m}{N_{sub}}}); \quad (4.16)$$

3. use  $\bar{\mathbf{w}}^{n+\frac{m}{N_{sub}}}$  and  $\bar{\mathbf{v}}^{n+\frac{m}{N_{sub}}}$ , obtained with Eq. (4.15) and Eq. (4.16), to find  $\bar{\boldsymbol{\gamma}}^{n+\frac{m}{N_{sub}}}$  by solving:

$$(\mathcal{A}_{SI}) : \quad \left( \frac{\vartheta_0^I}{\tau} \mathbb{M} + \varepsilon \mathbb{K}(\bar{\mathbf{w}}^{n+\frac{m}{N_{sub}}}) + \mathbb{P}^\gamma(\bar{\mathbf{w}}^{n+\frac{m}{N_{sub}}}, \bar{\boldsymbol{\gamma}}^*, \bar{\mathbf{d}}^*) \right) \bar{\boldsymbol{\gamma}}^{n+\frac{m}{N_{sub}}} \\ = \frac{1}{\tau} \mathbb{M} \bar{\boldsymbol{\gamma}}^I + \tilde{\boldsymbol{\Phi}}(\bar{\mathbf{w}}^{n+\frac{m}{N_{sub}}}, \bar{\boldsymbol{\gamma}}^*, \bar{\mathbf{d}}^*). \quad (4.17)$$

After  $N_{sub}$  steps, we once again solve problem (4.12) and finally obtain  $\bar{\mathbf{d}}^{n+1}$ .

## 5 Numerical simulations

In this chapter we show the results obtained with the simulation of different scenarios with the strategies proposed in Chapter 4. In the first part, we setup a benchmark in which the ventricle is stimulated with a current and let contract freely while a constant pressure is applied at the endocardial wall. The strategies proposed in the previous chapter are tested in this setting and the results compared in terms of accuracy and efficiency. In the second part, the same strategies are used for a subject-specific simulation (in healthy conditions), with the MRI-segmented geometry showed in Chapter 3. In this case, a full heartbeat is simulated, and the heartbeat pressure-volume (pV) loops obtained are also reported. Finally, after having introduced an ad hoc methodology for the electrophysiology and the mechanics modeling of infarcted tissue, we detail an application of the electromechanics solvers for the simulation of an ischemic heart.

### 5.1 Free contraction benchmark

We use the coarse idealized prolate mesh of Figure 3.7 for the free contraction benchmark. The monodomain and the Bueno-Orovio [Bueno-Orovio et al., 2008] models are used for the electrophysiology, and the parameters used for each core model are reported in Appendix B. Finite elements of order  $r = 1$  are employed for the space discretization to keep the computational cost low, while BDF of order  $\sigma = 1, 2$  are employed for the time discretization to ensure A-stability while maximizing the convergence order [Quarteroni et al., 2010]. The simulation is started by applying an external current, represented by  $I^{app}$ , in three points located on the endocardium; the current then triggers the electrical activity in the idealized LV which drives the fibers shortening and hence the contraction. The final time of the simulation is set to  $T = 100$  ms, during which time the endocardial pressure is kept at the constant value  $p_{EDP}^{endo} = 10$  mmHg. With these settings, the ventricular volume halves going from approximately 136 ml at  $t = 0$  to around 68 ml at the end of the simulation thus approximately reproducing the physiological shrinking of the LV during the systole.

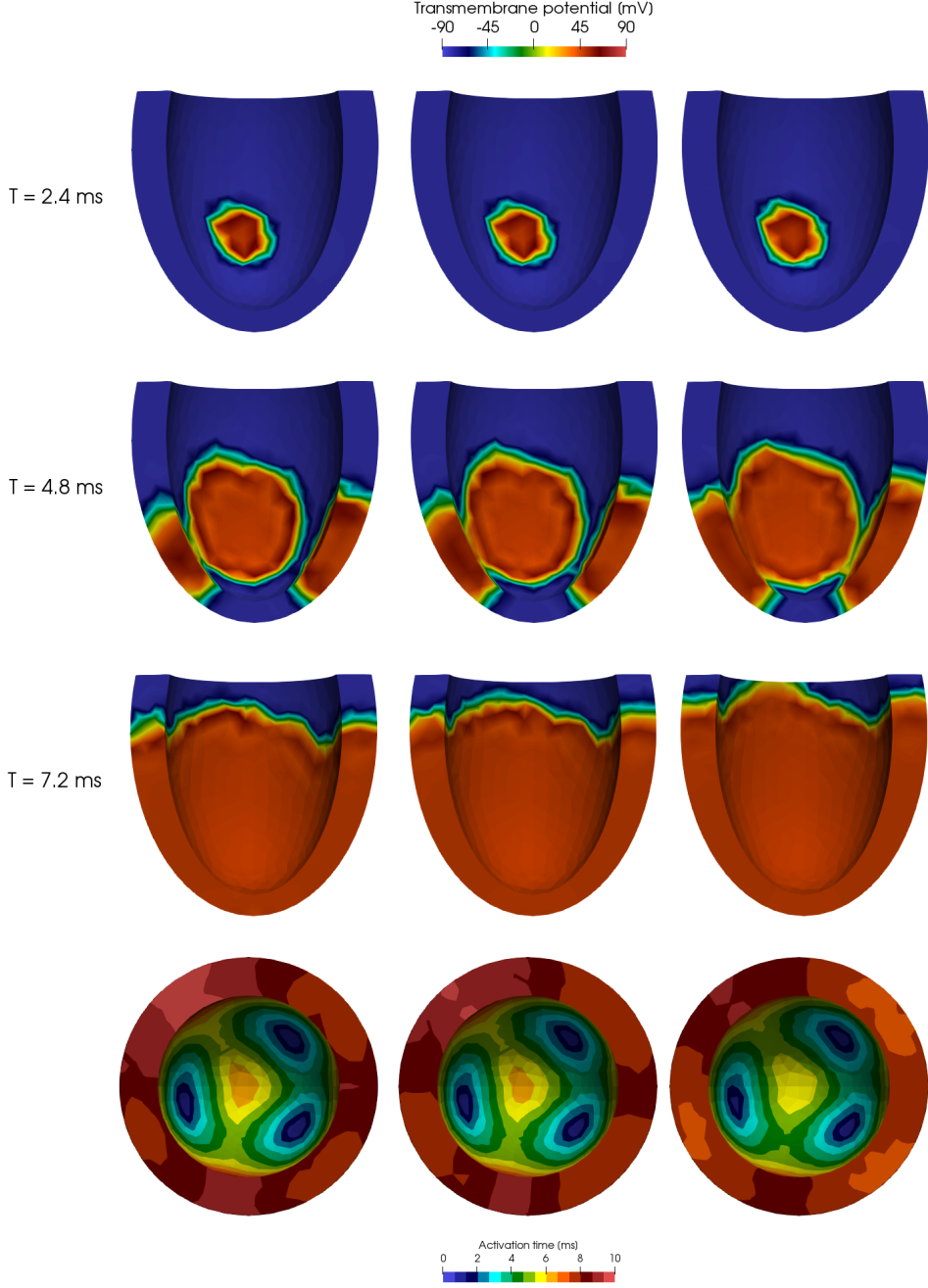


Figure 5.1 – Transmembrane potential  $v$  at times  $T = 2.4$  ms (first row),  $T = 4.8$  ms (second row),  $T = 7.2$  ms (third row), and AT (fourth row) obtained with the  $(\mathcal{I}_I \mathcal{E}_I \mathcal{A}_I \mathcal{M}_I)$  strategy and timesteps  $\tau = 8 \times 10^{-5}$  s (left),  $\tau = 16 \times 10^{-5}$  s (center), and  $\tau = 24 \times 10^{-5}$  s (right).

Before quantitatively comparing the four strategies, we discuss the results of the benchmark test obtained by using the  $(\mathcal{I}_I \mathcal{E}_I \mathcal{A}_I \mathcal{M}_I)$  strategy. In Figure 5.1 we show the transmembrane potential  $v$  in the prolate LV at the three distinct times  $T = 2.4$  ms,

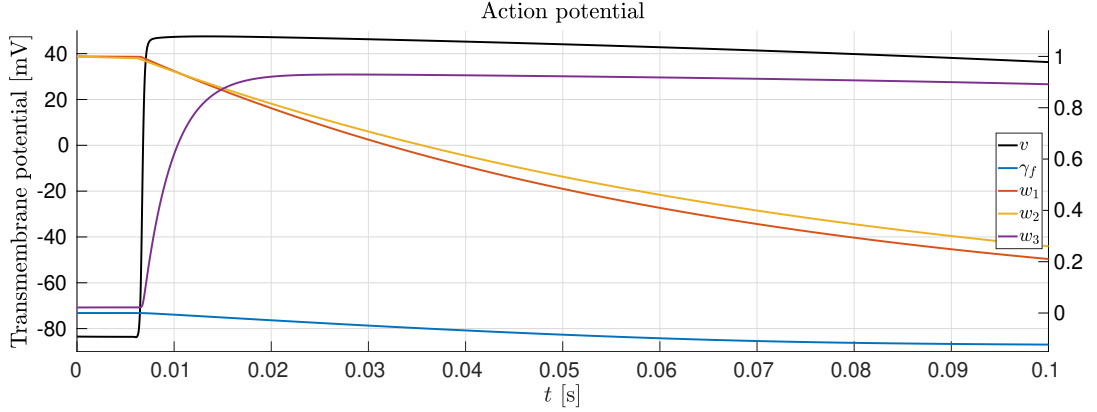


Figure 5.2 – Evolution of the transmembrane potential  $v$  (left y-axis), the fibers shortening  $\gamma_f$ , and the ionic variables  $w_1$ ,  $w_2$ ,  $w_3$  (right y-axis) in a point located on the apex, during the free contraction benchmark.

$T = 4.8$  ms, and  $T = 7.2$  ms, before the ventricle is fully depolarized. In the same figure, the activation time (AT) is displayed: the latter is defined, in each point, as the time at which the electric potential reaches a threshold value  $v^{thr}$  (we set in particular  $v^{thr} = 10$  mV) [Pagani, 2017, Usyk and McCulloch, 2003]. The results shown are obtained by using the timesteps  $\tau = 8 \times 10^{-5}$  s,  $\tau = 16 \times 10^{-5}$  s, and  $\tau = 24 \times 10^{-5}$  s. We recall that in this case, because of the monolithic nature of the strategy, it holds  $\Delta t = \tau$  and hence we conventionally set  $N_{sub} = 1$ . We also report in Figure 5.2 the values of the transmembrane potential  $v$ , of the fibers shortening  $\gamma_f$ , and of the ionic variables  $w_1$ ,  $w_2$ ,  $w_3$  in the external apical point of the LV, obtained with  $(\mathcal{I}_1 \mathcal{E}_1 \mathcal{A}_1 \mathcal{M}_1)$  and  $\tau = 8 \times 10^{-5}$ . The depolarization wave reaches the apical point in around 5 ms, thus triggering the action potential. The transmembrane potential enters then the plateau phase [Rudy, 2008], followed by the repolarization which is not reached in Figure 5.2 since the final time falls within the plateau phase.

We highlight that the conduction velocity, that is the velocity at which the potential wave propagates in the myocardium, is overestimated – and conversely the AT is underestimated – with respect to physiological values. This is a known numerical issue [Pezzuto et al., 2016] which arises when using the monodomain or the bidomain equations with meshes featuring tetrahedra with diameter  $h \gtrsim 0.1$  mm [Rossi, 2014]. Nonetheless, we use the coarsest idealized meshes in order to keep the computational costs reasonable since we want to extensively test the proposed strategy for varying  $\tau$  and  $N_{sub}$ . This will not represent an issue for this benchmark: indeed, since no exact solution to the electromechanics problem is available, the analysis of the convergence with respect to the timesteps will be carried out by using a reference solution on the same mesh, effectively disregarding the error in space. The estimated conduction velocities are also influenced by the timestep employed, as detailed in [Rossi, 2014]. It can indeed be observed from Figure 5.1 that a larger timestep corresponds to an overestimation of the conduction velocities. Finally, a

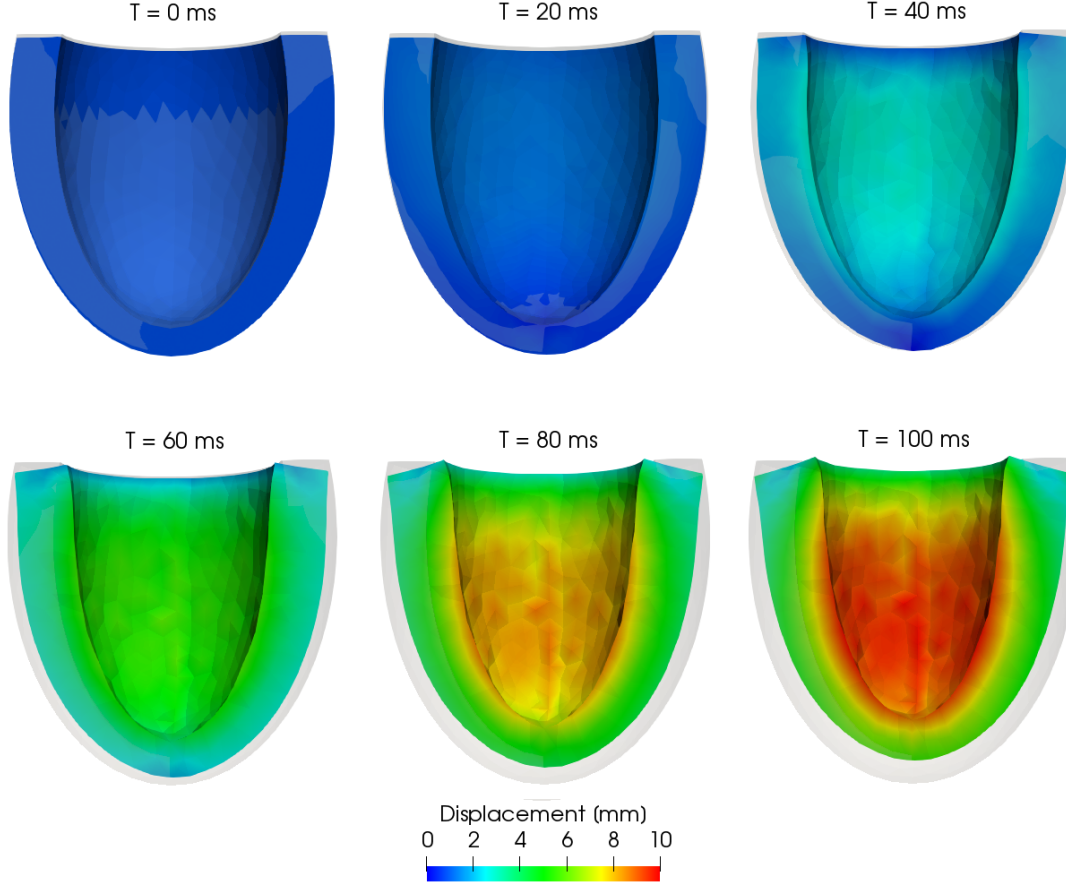


Figure 5.3 – Deformed myocardium at six different times during the free contraction benchmark, coloured by the displacement magnitude  $\|\mathbf{d}_{s,h}\|_2$  and compared with the reference domain  $\Omega_0^s$ .

factor contributing to the underestimation of the propagation speed is to be identified in the use of mass lumping for the monodomain equation (see Section 2.1.2) with large elements size [Pathmanathan et al., 2012], as is the case with these simulations. A more in-depth analysis of these numerical issues is carried out, among other works, in [Niederer et al., 2011, Pezzuto et al., 2016, Rossi, 2014].

In Figure 5.3 the deformed myocardium is shown at different times with the displacement magnitude  $\|\mathbf{d}_{s,h}\|_2$  (where  $\|\cdot\|_2$  denotes the Euclidean norm), and compared with the reference domain  $\Omega_0^s$ . A significant thickening of the LV walls takes place, which is in accordance with experimental observations [Quinn and Kohl, 2013] and with the nearly incompressible formulation employed. The model, with the set of parameters used, fails however to produce a significant rotation of the LV: a recent work [Pezzuto and Ambrosi, 2014] suggests that this behavior is related to the choice of the volumetric strain energy, the bulk modulus  $B$  magnitude, and the boundary conditions, but this issue is not further investigated in this work.

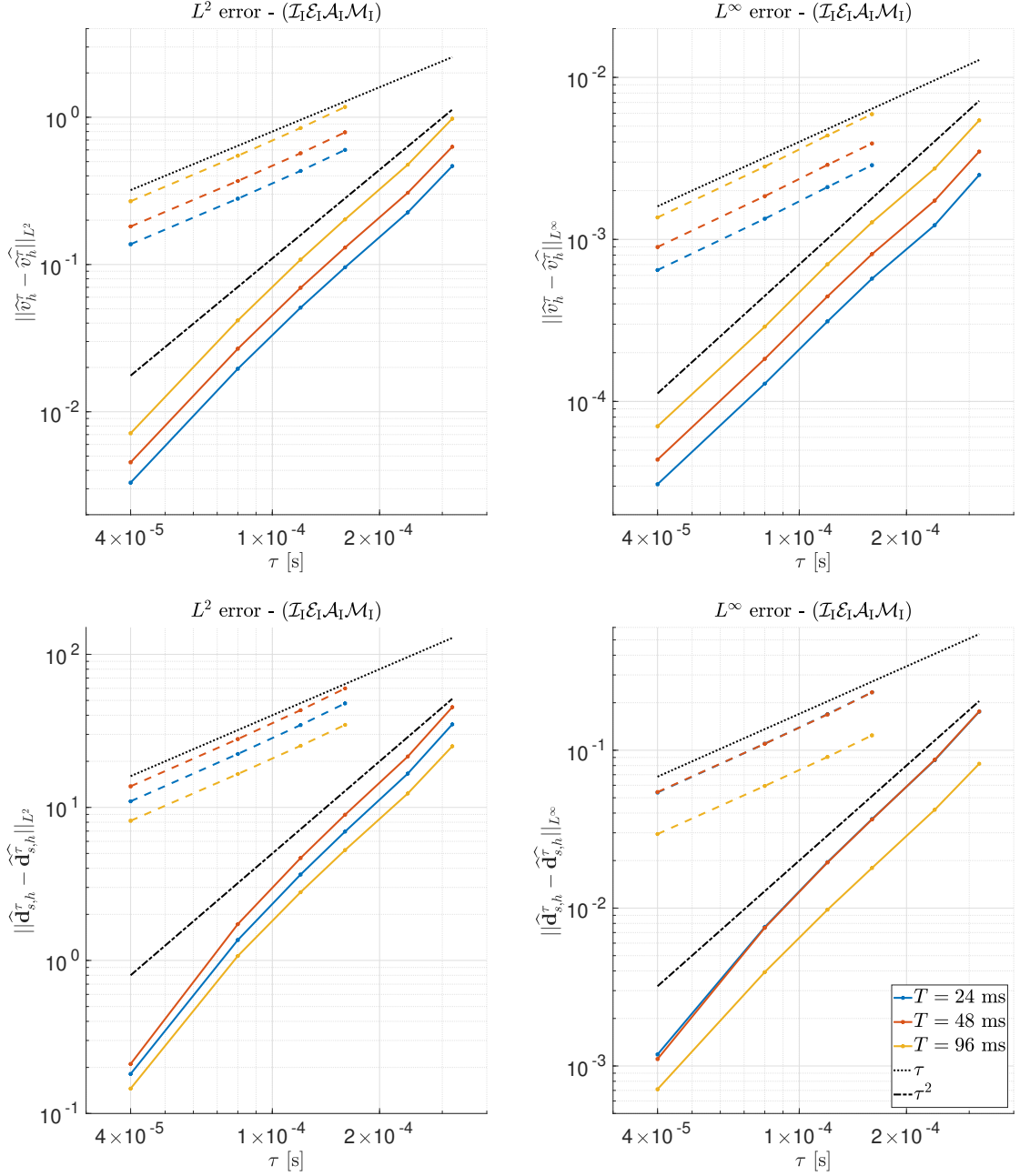


Figure 5.4 – Errors in  $L^2(\Omega_0^s)$  (left) and  $L^\infty(\Omega_0^s)$  (right) norms of the potentials  $\hat{v}_h^\tau$  (top) and of the displacements  $\hat{\mathbf{d}}_{s,h}^\tau$  (bottom) obtained using  $(\mathcal{I}_1\mathcal{E}_1\mathcal{A}_1\mathcal{M}_1)$  with timestep  $\tau$ , at times  $T = 24$  ms (blue),  $T = 48$  ms (green) and  $T = 96$  ms (red) in logarithmic scale. The errors for both BDF1 (dashed lines) and BDF2 (solid lines) are reported, together with linear and quadratic reference slopes.

### 5.1.1 Convergence with respect to time discretization

In order to assess the properties of the proposed strategies and to evaluate their behavior for different timestep lengths, we set  $\tau = 1, 2, 4, 8, 12, 16, 24, 32 \times 10^{-5}$  s and

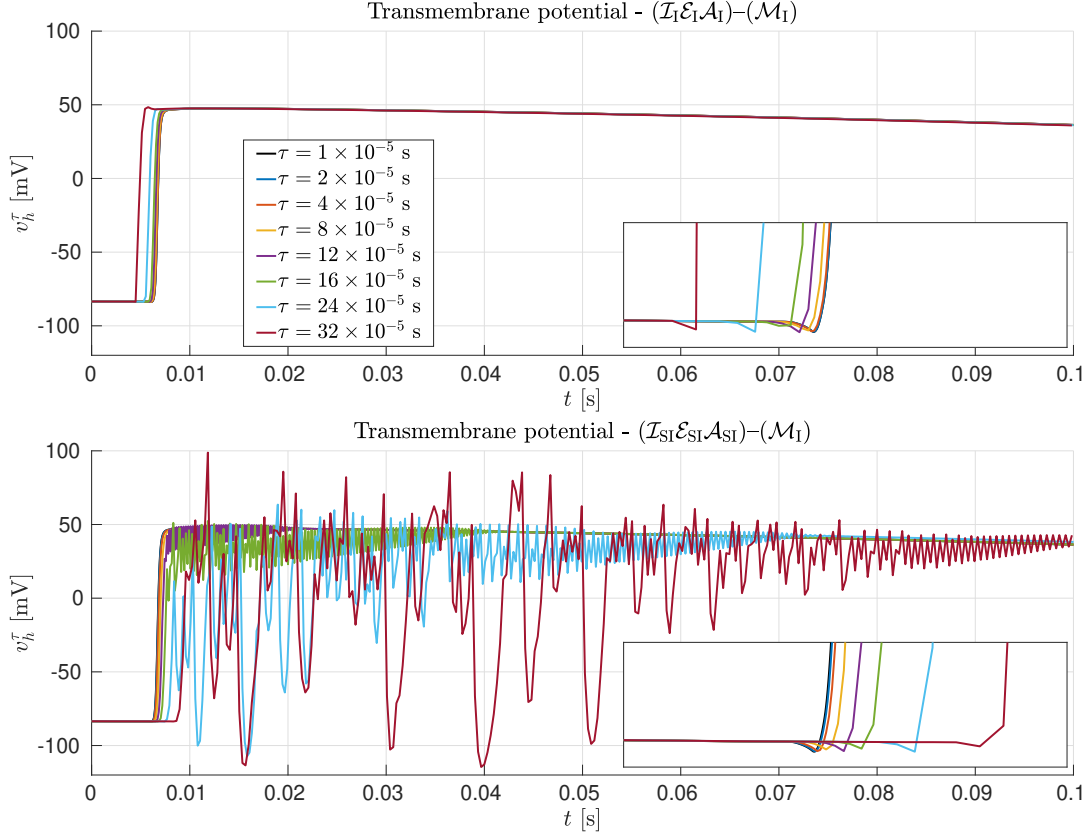


Figure 5.5 – Evolution of the transmembrane potential  $v_h^\tau$  in the apex obtained using  $(\mathcal{I}_I \mathcal{E}_I \mathcal{A}_I) - (\mathcal{M}_I)$  (top) and  $(\mathcal{I}_{SI} \mathcal{E}_{SI} \mathcal{A}_{SI}) - (\mathcal{M}_I)$  (bottom) for different  $\tau$  and  $N_{sub} = 1$  (and hence  $\Delta t = \tau$ ). The close-ups highlight the instant in which the depolarization wave reaches the apex.

$N_{sub} = 1, 2, 4, 8, 16$  for the segregated strategies, while  $\Delta t = \tau$  (as previously done) for the monolithic strategy. The absolute tolerances for the Newton method and the GMRES solver are set to  $\varepsilon^N = 10^{-4}$  and  $\varepsilon^G = 10^{-8}$ , respectively. For all the numerical simulations of this benchmark, 6 cpus are used. As already noted, we use the solution obtained by using  $(\mathcal{I}_I \mathcal{E}_I \mathcal{A}_I \mathcal{M}_I)$  with the smallest timestep as a reference one (a manufactured “exact” solution). Indeed, with  $(\mathcal{I}_I \mathcal{E}_I \mathcal{A}_I \mathcal{M}_I)$ , we are forced to use the smallest timestep for the electrophysiology, the mechanical activation, and the mechanics, and all the coupling conditions between the core models are enforced in the extradiagonal blocks of the monolithic system matrix. However, as we will show, this accuracy comes at a high computational cost.

In the following, we denote by  $\hat{v}_h^\tau$  and  $\hat{\mathbf{d}}_{s,h}^\tau$  the potential and the displacement solutions, respectively, obtained with  $(\mathcal{I}_I \mathcal{E}_I \mathcal{A}_I \mathcal{M}_I)$  and timestep  $\tau$  while  $\hat{\tau} = 10^{-5}$  s is the smallest timestep considered. We first verify numerically that in the  $(\mathcal{I}_I \mathcal{E}_I \mathcal{A}_I \mathcal{M}_I)$  case the errors in  $L^2(\Omega_0^s)$  and  $L^\infty(\Omega_0^s)$  norms of the potential and of the displacement magnitude decay as  $\tau$  and  $\tau^2$  when using BDF with  $\sigma = 1$  (i.e. Backward Euler) and  $\sigma = 2$ , respectively.



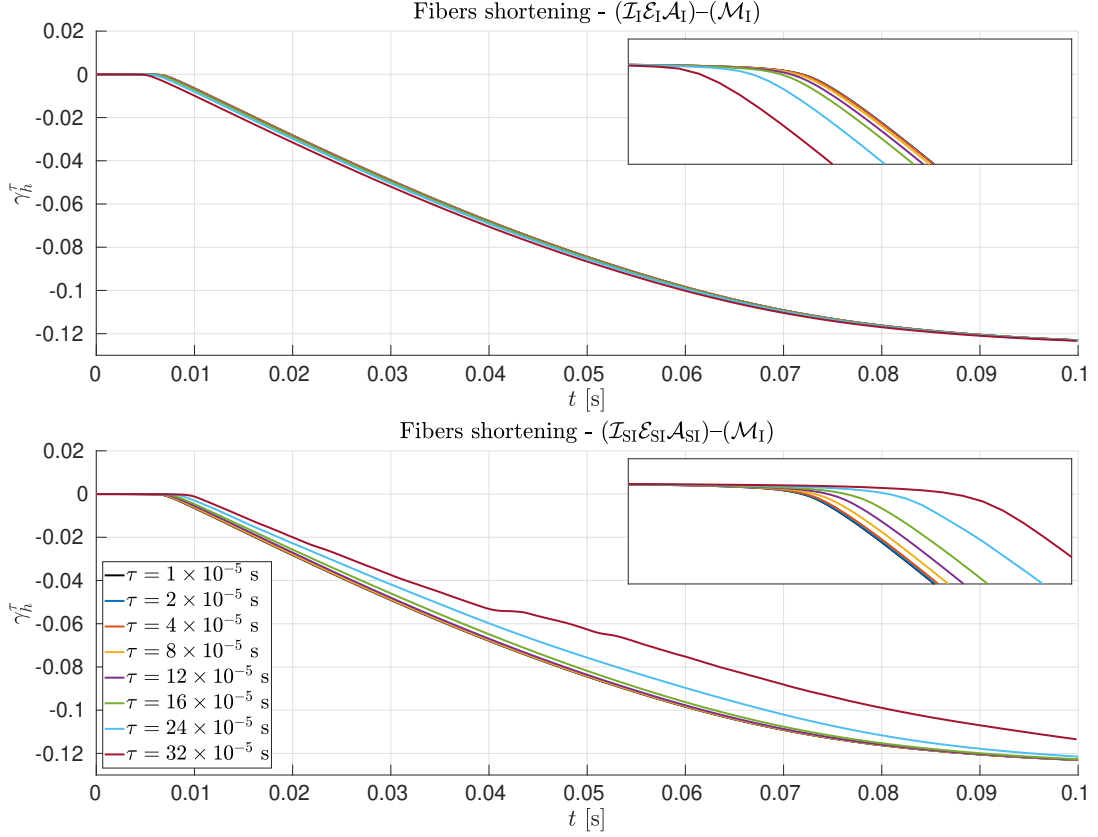


Figure 5.6 – Evolution of the fibers shortening  $\gamma_h^\tau$  in the apex obtained using  $(\mathcal{I}_1\mathcal{E}_1\mathcal{A}_1)-(\mathcal{M}_1)$  (top) and  $(\mathcal{I}_{S1}\mathcal{E}_{S1}\mathcal{A}_{S1})-(\mathcal{M}_1)$  (bottom) for different  $\tau$  and  $N_{sub} = 1$  (and hence  $\Delta t = \tau$ ). The close-ups highlight the instant in which the calcium concentration reaches the threshold and  $\gamma_h^\tau$  starts to decrease.

To this aim, we display in Figure 5.4 the errors  $\|\hat{v}_h^\tau - \hat{v}_h^\tau\|$ , and  $\|\hat{\mathbf{d}}_{s,h}^\tau - \hat{\mathbf{d}}_{s,h}^\tau\|$  against the timestep length  $\tau$ . The converge rate is indeed coherent with the order  $\sigma$  of the BDF scheme under use.

We begin the analysis of the results given by the strategies by inspecting the evolution of several variables in the apex of the LV against the time for different choices of  $\tau$ . First, in Figure 5.5, the transmembrane potential  $v_h^\tau$  given by  $(\mathcal{I}_1\mathcal{E}_1\mathcal{A}_1)-(\mathcal{M}_1)$  and  $(\mathcal{I}_{S1}\mathcal{E}_{S1}\mathcal{A}_{S1})-(\mathcal{M}_1)$  is reported. We observe that, while in both cases  $v_h^\tau$  converges to  $\hat{v}_h^\tau$  as  $\tau \rightarrow \hat{\tau}$ , numerical instabilities take place when a timestep larger than  $\tau = 8 \times 10^{-5}$  is used with the  $(\mathcal{I}_{S1}\mathcal{E}_{S1}\mathcal{A}_{S1})-(\mathcal{M}_1)$  strategy, and the value of  $v_h^\tau$  increasingly oscillates for increasing  $\tau$ . A similar effect, though less pronounced, is observable also in  $\mathbf{w}_h^\tau$  for  $\tau \geq 24 \times 10^{-5}$  (not reported). Nonetheless such instabilities appear to be “non-destructive”, meaning that the evolution of  $\gamma_h^\tau$  is reasonably close to that obtained with smaller timesteps even when using the largest one (see Figure 5.6). This is due to the diffusive term in Eq. (1.20) which regularizes the solution  $\gamma_h^\tau$ . We also deduce from the close-ups of  $v_h^\tau$  in Figures 5.5-5.6 that in the implicit case the conduction velocity is

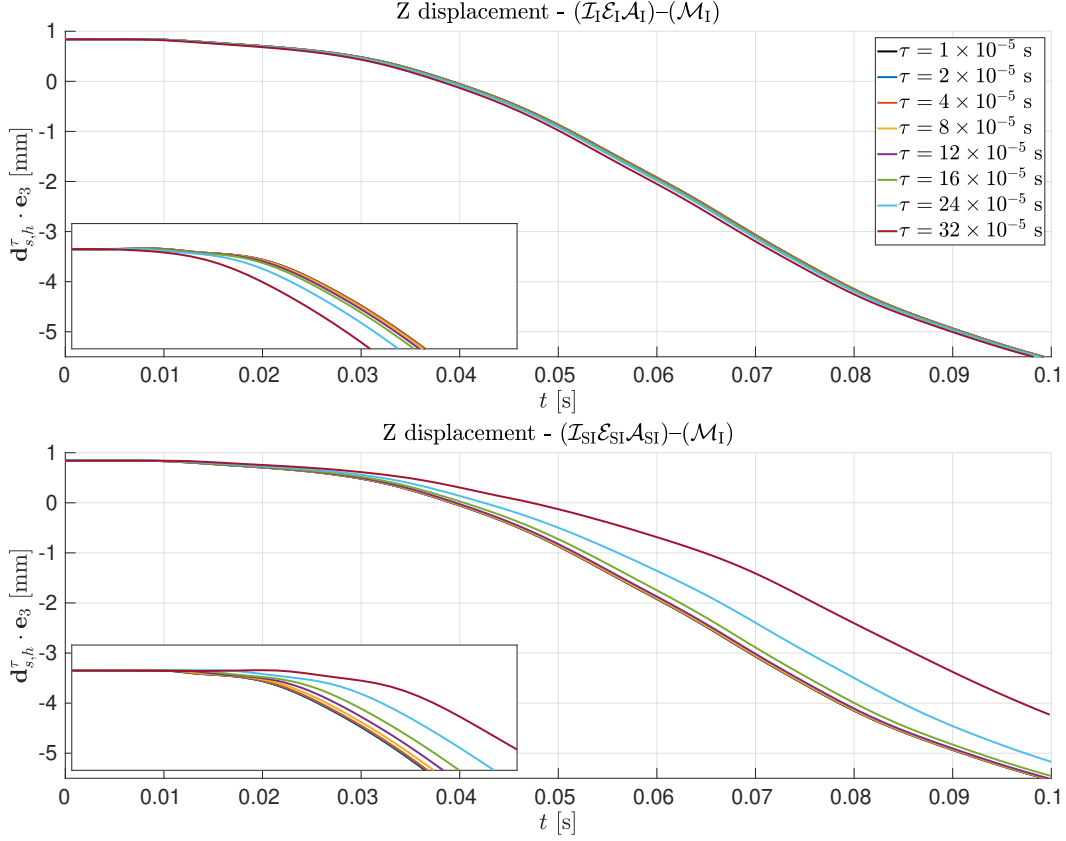


Figure 5.7 – Evolution of the displacement in the Z direction  $\mathbf{d}_{s,h}^\tau \cdot \mathbf{e}_3$  in the apex obtained using  $(\mathcal{I}_I \mathcal{E}_I \mathcal{A}_I) - (\mathcal{M}_I)$  (top) and  $(\mathcal{I}_{SI} \mathcal{E}_{SI} \mathcal{A}_{SI}) - (\mathcal{M}_I)$  (bottom) for different  $\tau$  and  $N_{sub} = 1$  (and hence  $\Delta t = \tau$ ). The close-ups highlight the instant in which the apex starts moving.

overestimated, and hence the action potential is triggered earlier with respect to the reference solution; on the other hand, in the semi-implicit case, the conduction velocity is underestimated and the dynamics is in turn delayed. This behavior is expected and in accordance with the results reported in [Whiteley, 2006], and we speculate that this is due to the additional dependence on the variables obtained at the previous timesteps introduced in the linearization of the ionic currents terms.

In this benchmark, the boundary conditions do not depend on time and hence the displacement of the LV is fully determined by the evolution in time of  $\gamma_h^\tau$ . Indeed the early/late activation in the  $(\mathcal{I}_I \mathcal{E}_I \mathcal{A}_I) - (\mathcal{M}_I) / (\mathcal{I}_{SI} \mathcal{E}_{SI} \mathcal{A}_{SI}) - (\mathcal{M}_I)$  case drives an anticipated/delayed deformation of the myocardium, as shown in Figure 5.7 where the displacement of the apex in the Z direction is reported. The latter is oriented as the LV centerline, in the base-apex direction: thus, the displacement decreases as the LV contracts (see Figure 5.3). As in the previous cases, the approximation given by  $(\mathcal{I}_I \mathcal{E}_I \mathcal{A}_I) - (\mathcal{M}_I)$  is more accurate with respect to that given by  $(\mathcal{I}_{SI} \mathcal{E}_{SI} \mathcal{A}_{SI}) - (\mathcal{M}_I)$  for equal timestep length. In the latter case, using the largest timestep length  $\tau = 32 \times 10^{-5}$  s causes an underestimation up to

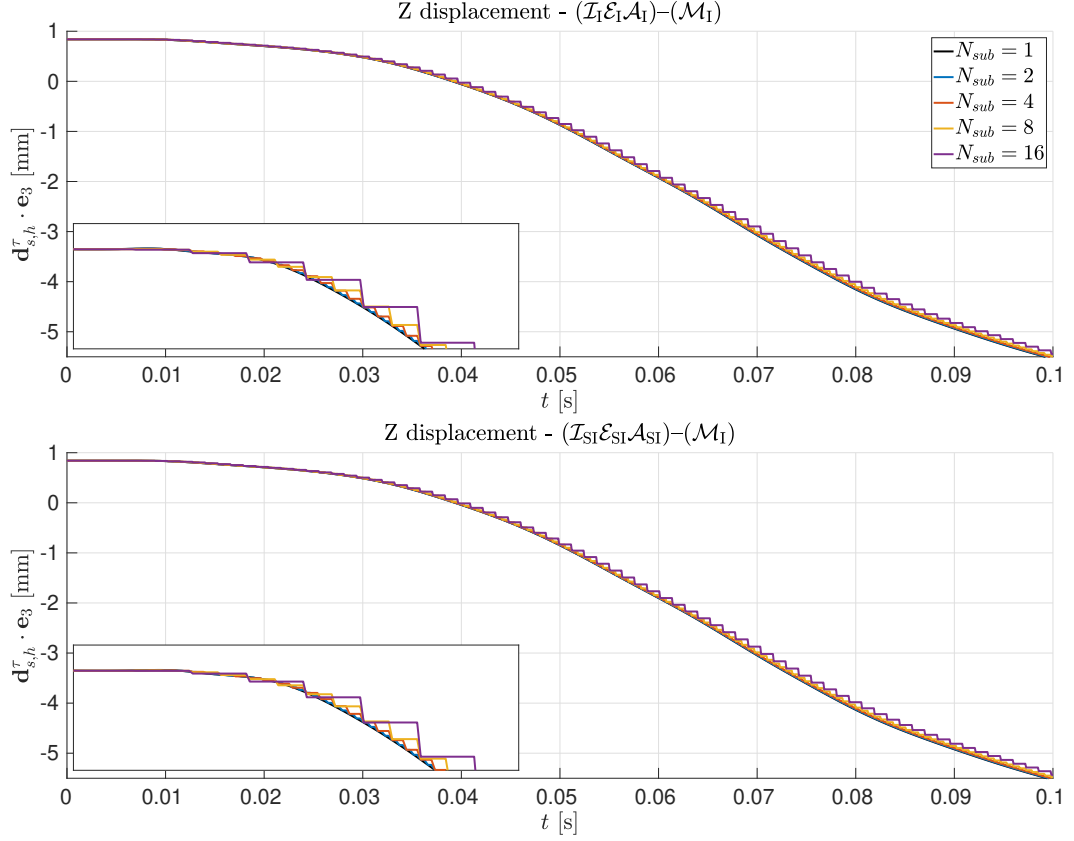


Figure 5.8 – Evolution of the displacement in the Z direction  $\mathbf{d}_{s,h}^\tau \cdot \mathbf{e}_3$  in the apex obtained using  $(\mathcal{I}_I \mathcal{E}_I \mathcal{A}_I) - (\mathcal{M}_I)$  (top) and  $(\mathcal{I}_{SI} \mathcal{E}_{SI} \mathcal{A}_{SI}) - (\mathcal{M}_I)$  (bottom) for different  $N_{sub}$  and  $\tau = \hat{\tau}$  (and hence  $\Delta t = N_{sub} \hat{\tau}$ ). The close-ups highlight the instant in which the apex starts moving.

100% of the displacement.

We also investigate how the displacement is influenced by using different  $N_{sub}$  while keeping  $\tau = \hat{\tau}$ , which is reported in Figure 5.8. In this case the displacements obtained with large  $N_{sub}$  (and consequently large  $\Delta t$ ) appear as staircase functions. This is due to the fact that the displacement is not updated during the  $N_{sub}$  steps of electrophysiology and mechanical activation which are performed between two consecutive mechanics timesteps. Nonetheless we observe that, when a time corresponding to the solution of the mechanics problem is reached, the displacement is updated and the deviation of the volume from the reference solution drops. The reason why this happens is due to our choice of solving the mechanical activation together with the electrophysiology. Indeed, since the displacement is driven by the active shortening of the fibers, the more accurate is the approximation of  $\gamma_f$  (i.e. the one obtained with a smaller timestep), the more accurate is the approximation of  $\mathbf{d}_s$ . From this macroscopic perspective we speculate that, if the goal is that of reducing the computational cost of the simulation, increasing  $N_{sub}$

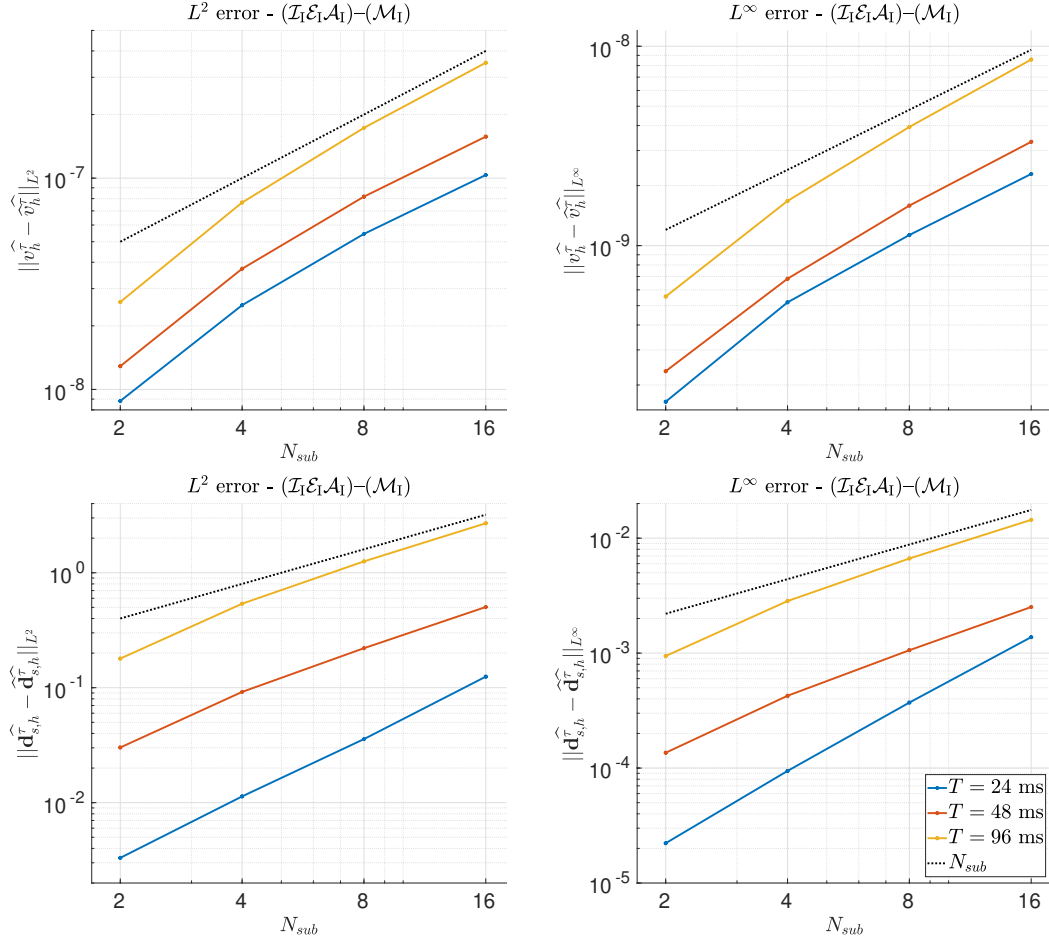


Figure 5.9 – Errors in  $L^2(\Omega_0)$  (left) and  $L^\infty(\Omega_0)$  (right) norms of the potentials  $\hat{v}_h^\tau$  (top) and of the displacements  $\hat{\mathbf{d}}_{s,h}^\tau$  (bottom) at times  $T = 24$  ms (blue),  $T = 48$  ms (green) and  $T = 96$  ms (red) obtained by solving the problem with  $(\mathcal{I}_1\mathcal{E}_1\mathcal{A}_1)-(\mathcal{M}_1)$  and timestep  $\tau$ , in logarithmic scale against  $N_{sub}$ .

represents a better alternative to increasing  $\tau$  in terms of accuracy – with the advantage of avoiding the electrophysiology instabilities for large timesteps. This approach is also coherent with the multiphysics nature of the problem under study: with a larger  $N_{sub}$  we impose a stronger separation of the time scales of the electrophysiology and the mechanics, and each problem can be solved with a timestep proportional to its own time scale.

After having qualitatively discussed the results of the benchmark test for different strategies and parameters, we quantitatively study the convergence of the errors for the segregated strategies as was done for  $(\mathcal{I}_1\mathcal{E}_1\mathcal{A}_1\mathcal{M}_1)$  in Figure 5.4. The first step that we take in the analysis of the convergence is that of weighting the influence of the splitting scheme on the mechanical feedback in the monodomain equation, which is realized by the dependence of the diffusion tensor on the deformation gradient  $\mathbf{F}$  and of the mechanical

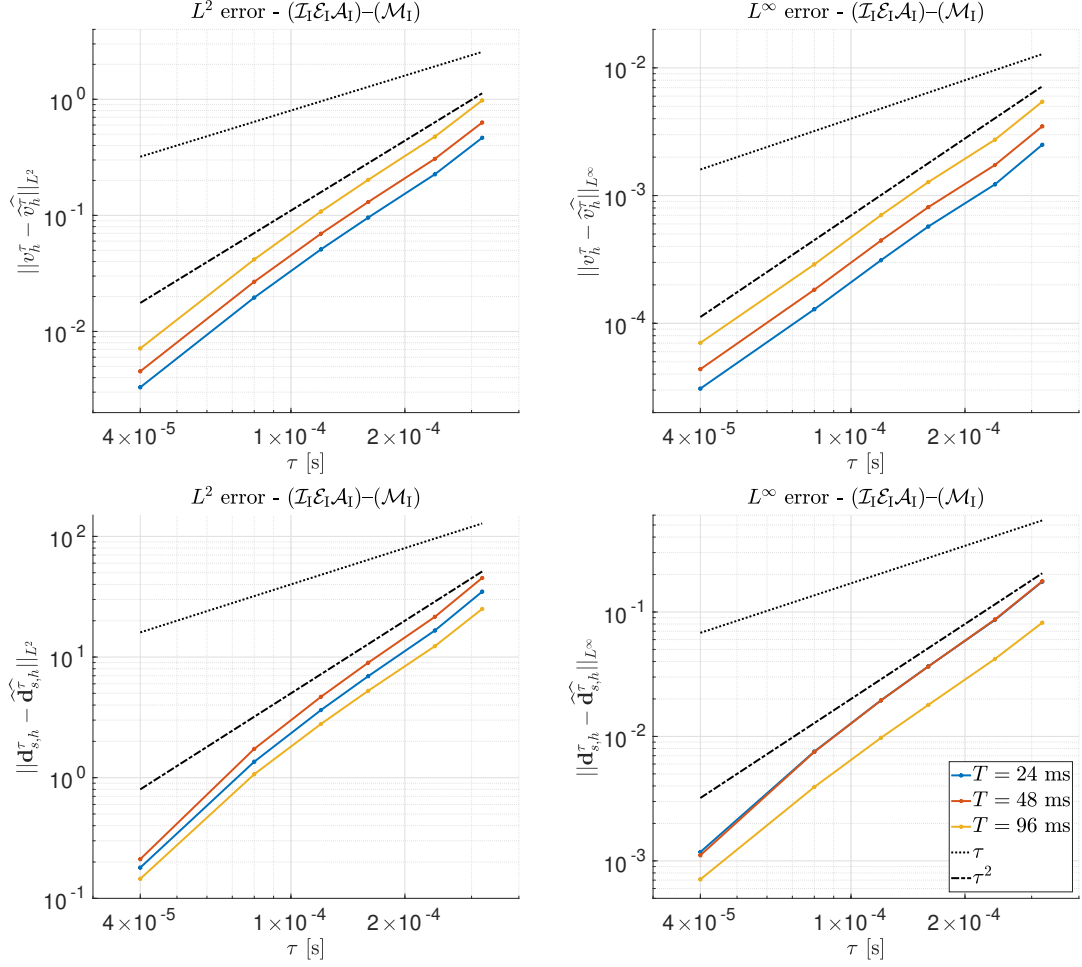


Figure 5.10 – Errors in  $L^2(\Omega_0^s)$  (left) and  $L^\infty(\Omega_0^s)$  (right) norms of the potentials  $v_h^\tau$  (top) and of the displacements  $\mathbf{d}_{s,h}^\tau$  (bottom) obtained using  $(\mathcal{I}_I \mathcal{E}_I \mathcal{A}_I) - (\mathcal{M}_I)$  with timestep  $\tau$  and  $N_{sub} = 1$ , at times  $T = 24, 48, 96$  ms in logarithmic scale.

activation equation on  $I_{4f}$ . To this aim, we display in Figure 5.9 the errors made when using  $(\mathcal{I}_I \mathcal{E}_I \mathcal{A}_I) - (\mathcal{M}_I)$  with  $\hat{\tau}$  at times  $T = 24, 48, 96$  ms against  $N_{sub}$ . In this way, we use the smallest timestep length for the electrophysiology and the activation – the same used to obtain the reference solution – while using different timestep sizes for the mechanics. We first observe that the convergence rate is linear with respect to  $N_{sub}$  (equivalently, with respect to  $\Delta t$  since  $\Delta t = N_{sub}\tau$ ) in all cases; this behavior is expected since the employed Godunov splitting scheme introduces a first order error in time. Furthermore, while the magnitude of the error of the potential  $\hat{v}_h^\tau$  is negligible when compared to the errors in Figure 5.4, the same does not hold for the displacement  $\hat{\mathbf{d}}_h^\tau$ . This is also largely expected since in Figure 5.9 the value of  $\tau$  is fixed while that of  $\Delta t$  is not: nonetheless it clearly shows that the splitting error introduced on the potential is several orders of magnitude smaller than the one introduced when using a larger  $\tau$ .

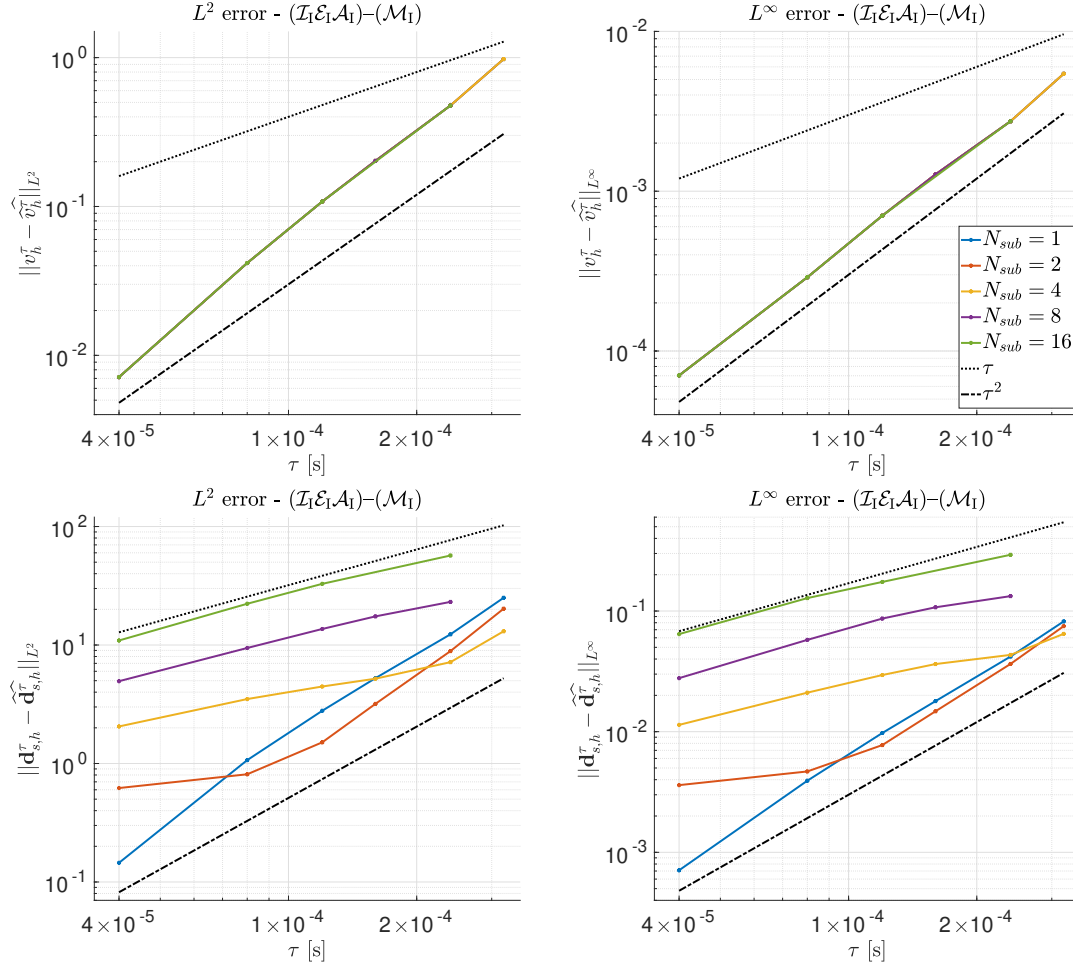


Figure 5.11 – Errors in  $L^2(\Omega_0^s)$  (left) and  $L^\infty(\Omega_0^s)$  (right) norms of the potentials  $v_h^\tau$  (top) and of the displacements  $\mathbf{d}_{s,h}^\tau$  (bottom) obtained using  $(\mathcal{I}_I \mathcal{E}_I \mathcal{A}_I) - (\mathcal{M}_I)$  with timestep  $\tau$  and  $N_{sub} = 1, 2, 4, 8, 16$ , at time  $T = 96$  ms in logarithmic scale.

We then analyze the errors made when using the  $(\mathcal{I}_I \mathcal{E}_I \mathcal{A}_I) - (\mathcal{M}_I)$  for varying  $\tau$ . By observing Figure 5.10, we assess that the errors for  $v_h^\tau$  and  $\mathbf{d}_{s,h}^\tau$  with  $N_{sub} = 1$  decay quadratically even if the splitting scheme is of the first order. Indeed, even if a first order only convergence rate is granted, as previously mentioned, the errors are superconvergent. The dependence of the convergence rate on the parameter  $N_{sub}$  is further investigated by considering the errors at time  $T = 96$  ms for different choices of  $N_{sub}$ , which we report in Figure 5.11. We deduce from it that the potential  $v_h^\tau$  is superconvergent for any choice of  $N_{sub}$ , while the same holds for the displacement  $\mathbf{d}_{s,h}^\tau$  in the  $N_{sub} = 1, 2$  cases only. On the other hand, when larger  $N_{sub}$  (and hence larger mechanics timestep  $\Delta t$ ) are employed, the splitting error magnitude becomes significant and we therefore observe a linear convergence.

We then report in Figure 5.12 the errors for the  $(\mathcal{I}_{SI} \mathcal{E}_{SI} \mathcal{A}_{SI}) - (\mathcal{M}_I)$  and the

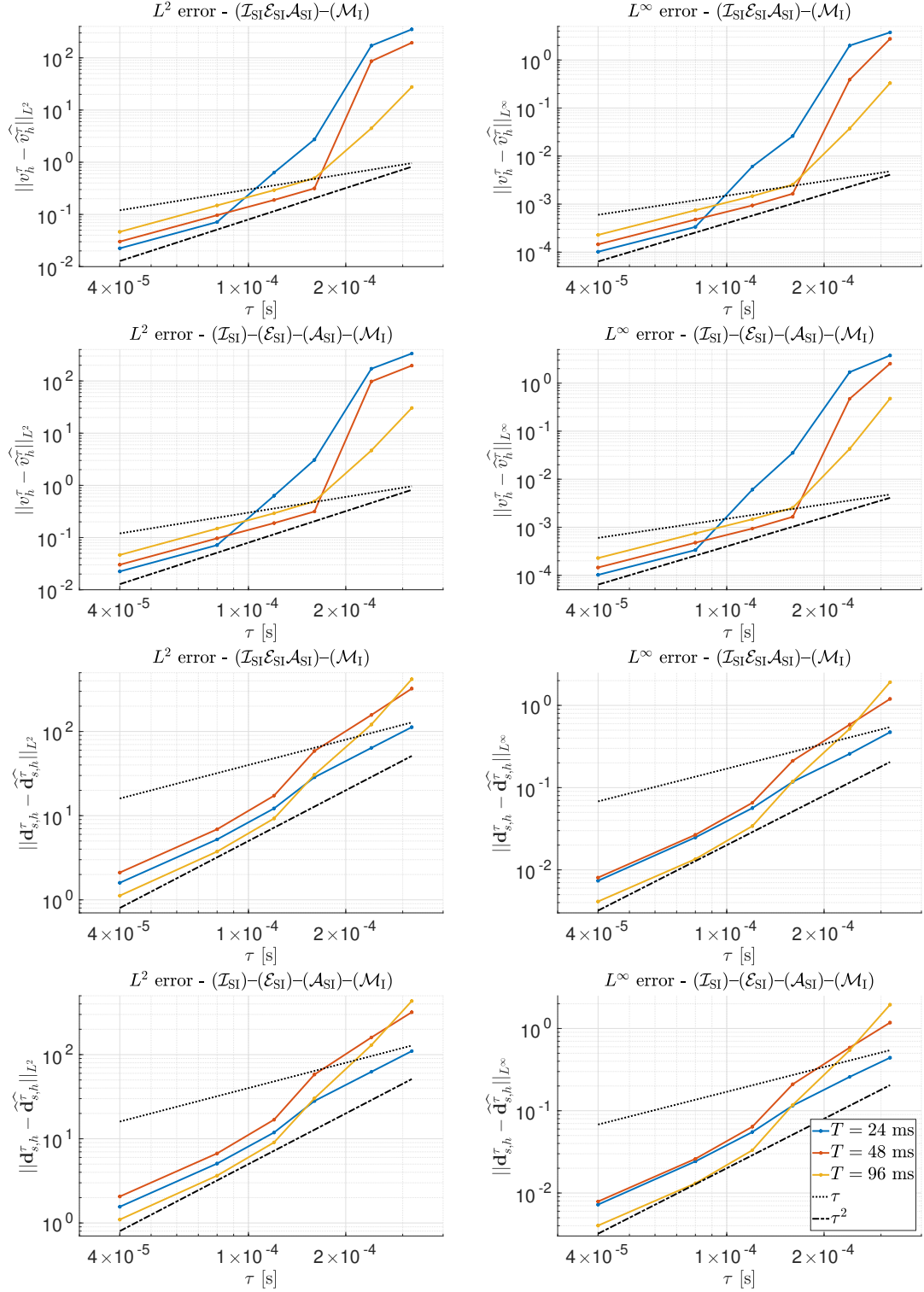


Figure 5.12 – Errors in  $L^2(\Omega_0^s)$  (left) and  $L^\infty(\Omega_0^s)$  (right) norms of the potentials  $v_h^\tau$  and of the displacements  $\mathbf{d}_{s,h}^\tau$  obtained using  $(\mathcal{I}_{\text{Sl}}\mathcal{E}_{\text{Sl}}\mathcal{A}_{\text{Sl}})-(\mathcal{M}_{\text{I}})$  (first and third rows) and  $(\mathcal{I}_{\text{Sl}})-(\mathcal{E}_{\text{Sl}})-(\mathcal{A}_{\text{Sl}})-(\mathcal{M}_{\text{I}})$  (second and fourth rows) with timestep  $\tau$  and  $N_{\text{sub}} = 1$ , at times  $T = 24, 48, 96$  ms in logarithmic scale.

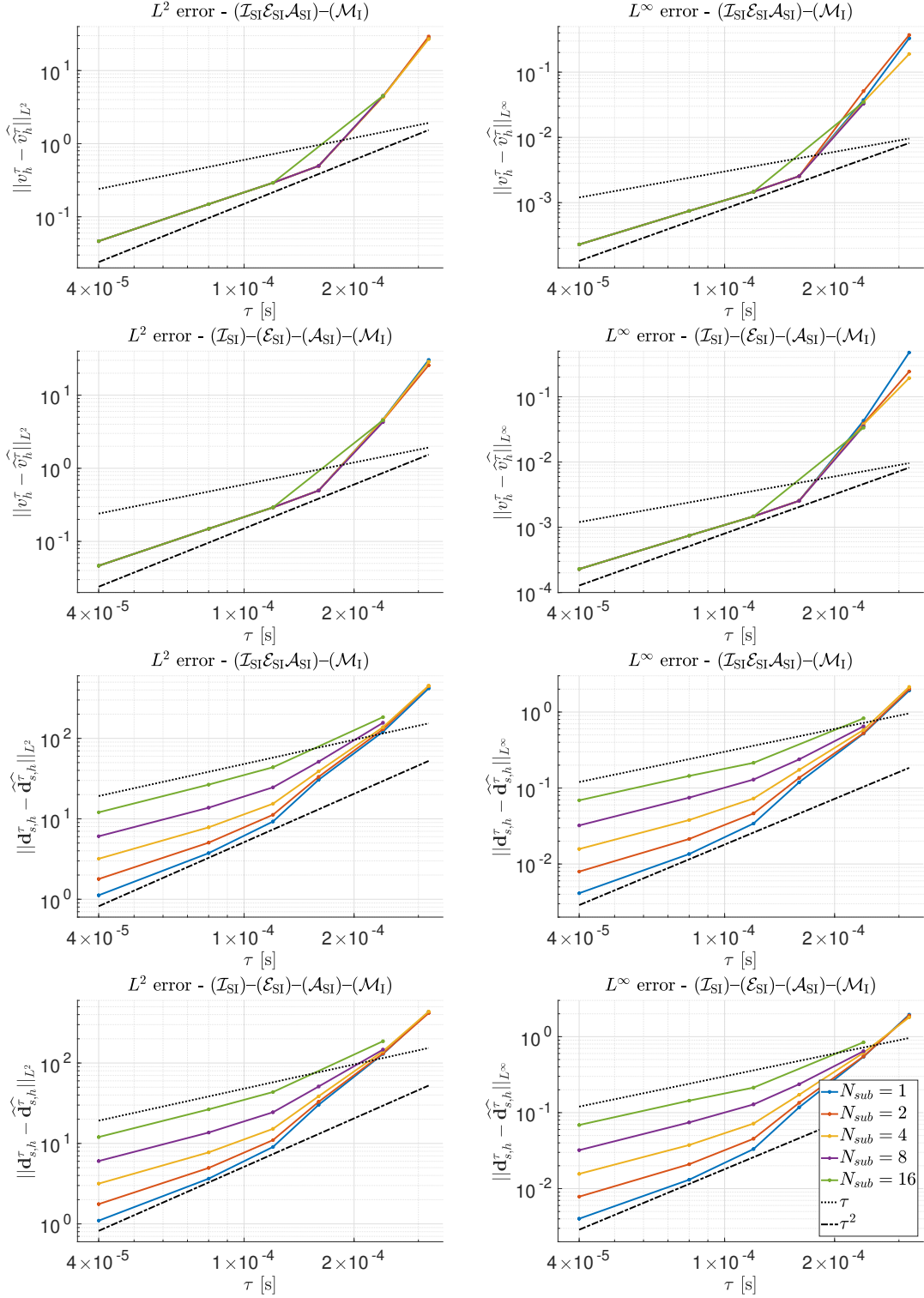


Figure 5.13 – Errors in  $L^2(\Omega_0^s)$  (left) and  $L^\infty(\Omega_0^s)$  (right) norms of the potentials  $v_h^\tau$  (top) and of the displacements  $\mathbf{d}_{s,h}^\tau$  (bottom) obtained using  $(\mathcal{I}_{\text{SI}}\mathcal{E}_{\text{SI}}\mathcal{A}_{\text{SI}})-(\mathcal{M}_I)$  (first and third rows) and  $(\mathcal{I}_{\text{SI}})-(\mathcal{E}_{\text{SI}})-(\mathcal{A}_{\text{SI}})-(\mathcal{M}_I)$  (second and fourth rows) with timestep  $\tau$  and  $N_{\text{sub}} = 1, 2, 4, 8, 16$ , at time  $T = 96$  ms in logarithmic scale.



## 5.1. Free contraction benchmark

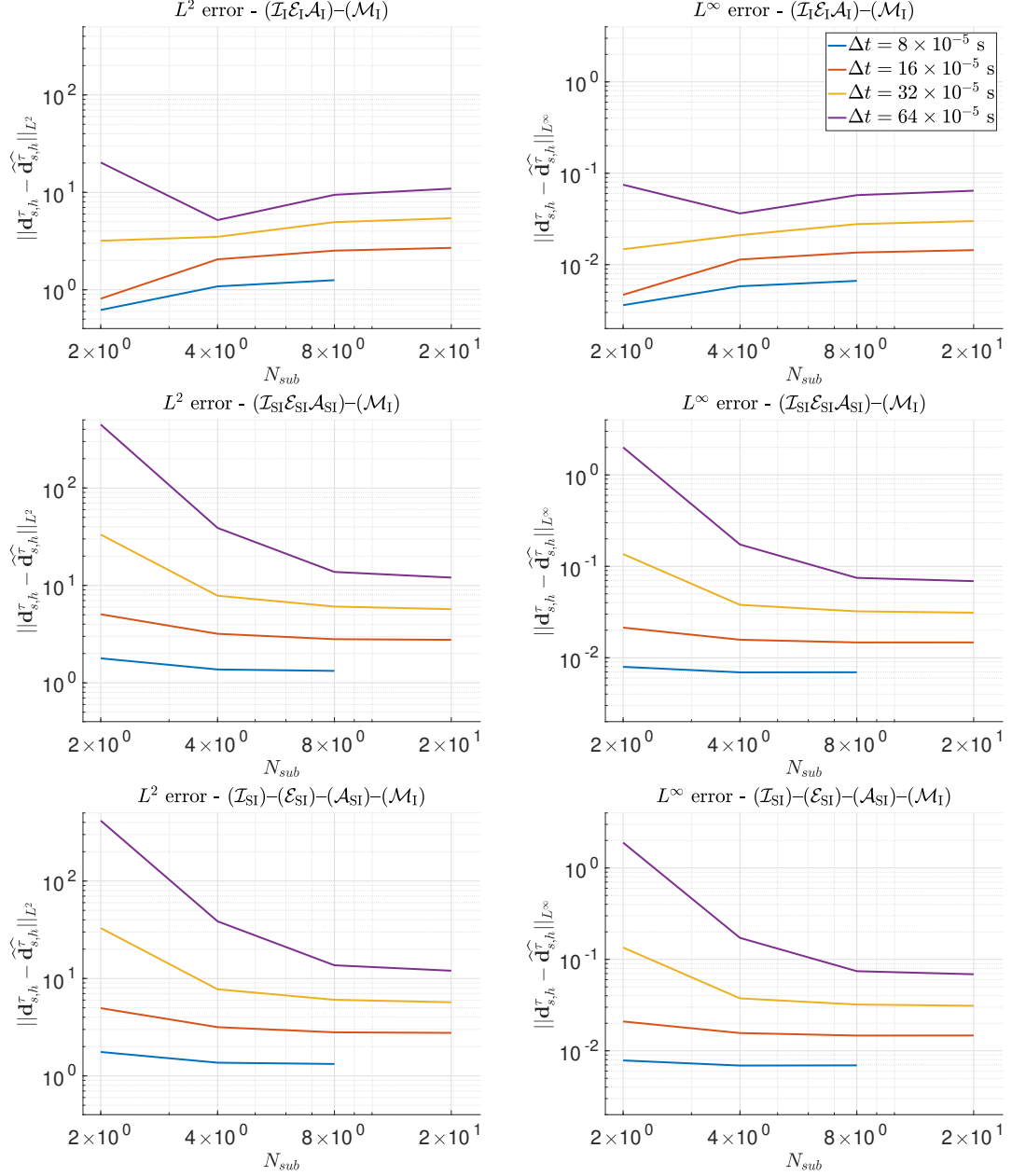


Figure 5.14 – Errors in  $L^2(\Omega_0^s)$  (left) and  $L^\infty(\Omega_0^s)$  (right) norms of the displacements  $\mathbf{d}_{s,h}^\tau$  obtained using  $(\mathcal{I}_I \mathcal{E}_I \mathcal{A}_I) - (\mathcal{M}_I)$  (first row),  $(\mathcal{I}_{SI} \mathcal{E}_{SI} \mathcal{A}_{SI}) - (\mathcal{M}_I)$  (second row), and  $(\mathcal{I}_{SI}) - (\mathcal{E}_{SI}) - (\mathcal{A}_{SI}) - (\mathcal{M}_I)$  (third row) with fixed mechanics timestep  $\Delta t = N_{sub} \tau$  at time  $T = 96$  ms, in logarithmic scale against  $N_{sub}$ .

$(\mathcal{I}_{SI}) - (\mathcal{E}_{SI}) - (\mathcal{A}_{SI}) - (\mathcal{M}_I)$  strategies at the times  $T = 24, 48, 96$  ms against  $\tau$ . We highlight that the difference in the error between the two strategies is negligible: the only difference between the two strategies – up to the GMRES tolerance – is due to the fact that the variable  $\bar{\mathbf{w}}_h^{n+m\tau}$  is used instead of  $\bar{\mathbf{w}}_h^*$  when evaluating the terms in Eqs. (4.16)-(4.17).

|                       | $(\mathcal{I}_I \mathcal{E}_I \mathcal{A}_I \mathcal{M}_I)$ |             |       |
|-----------------------|---|-------------|-------|
| $\tau (= \Delta t)$   | $\bar{N}^N$   | $\bar{N}^G$ | $T^W$ |
| $10^{-5}$ s           | 2.1   | 8.5         | 363'  |
| $2 \times 10^{-5}$ s  | 2.4   | 8.1         | 188'  |
| $4 \times 10^{-5}$ s  | 3.0   | 7.8         | 101'  |
| $8 \times 10^{-5}$ s  | 3.5   | 7.7         | 54'   |
| $12 \times 10^{-5}$ s | 3.6   | 7.9         | 36'   |
| $16 \times 10^{-5}$ s | 4.0   | 7.6         | 28'   |
| $24 \times 10^{-5}$ s | 4.7   | 7.9         | 22'   |
| $32 \times 10^{-5}$ s | 5.2   | 9.2         | 18'   |

Table 5.1 – The average number of Newton ( $\bar{N}^N$ ) and GMRES ( $\bar{N}^G$ ) iterations for the solution of the monolithic problem  $(\mathcal{I}_I \mathcal{E}_I \mathcal{A}_I \mathcal{M}_I)$ , and the total wall time ( $T^W$ , in minutes) for the benchmark simulations, for each  $\tau (= \Delta t)$  considered.

As was observed in Figure 5.5, numerical instabilities cause the potential to oscillate for  $\tau > \bar{\tau} = 8 \times 10^{-5}$  s. Indeed, for this reason, the errors in Figure 5.12 become significantly larger when the timestep is larger than  $\bar{\tau}$ : the effect of these oscillations is however less pronounced in the error of the displacement. Moreover, similarly to the  $(\mathcal{I}_I \mathcal{E}_I \mathcal{A}_I) - (\mathcal{M}_I)$  case, we observe from Figure 5.13 that, for  $\tau \leq 12 \times 10^{-5}$ , the convergence rate of the errors is at least linear while the error on the potential is superconvergent.

We conclude the convergence analysis by reporting in Figure 5.14 the errors obtained with the three segregated strategies when keeping the mechanics timestep  $\Delta t$  fixed, while letting  $N_{sub}$  vary. In this way, we can verify how increasing the number of electrophysiology and mechanical activation steps between two consecutive mechanics steps influences the error once  $\Delta t$  is chosen. We observe that in the  $(\mathcal{I}_I \mathcal{E}_I \mathcal{A}_I) - (\mathcal{M}_I)$  case the error is not significantly affected by using different  $N_{sub}$ , while in the  $(\mathcal{I}_{SI} \mathcal{E}_{SI} \mathcal{A}_{SI}) - (\mathcal{M}_I)$  and  $(\mathcal{I}_{SI}) - (\mathcal{E}_{SI}) - (\mathcal{A}_{SI}) - (\mathcal{M}_I)$  cases a significant error reduction is obtained when increasing  $N_{sub}$ , if  $\Delta t$  is large enough. This is the case when we want to use a large mechanics timestep in order to reduce the computational cost: with the semi-implicit strategies it is particularly convenient to choose  $N_{sub}$  so that it holds  $\tau \leq \bar{\tau}$ , thus avoiding the numerical instabilities for the electrophysiology.

Finally, we discuss the efficiency of the considered strategies for the benchmark test. In Table 5.1, the average number of Newton ( $\bar{N}^N$ ) and GMRES ( $\bar{N}^G$ ) iterations, and the total wall time  $T^W$  are reported for the  $(\mathcal{I}_I \mathcal{E}_I \mathcal{A}_I \mathcal{M}_I)$  case, for each employed timestep  $\tau$ . As expected, for increasing  $\tau$ ,  $\bar{N}^N$  becomes larger while  $T^W$  drops significantly. The average number of GMRES iterations  $\bar{N}^G$  required to solve the linear system with the proposed monolithic preconditioner is on the other hand not significantly affected by the choice of  $\tau$ . In Table 5.2 we report the same quantities for the  $(\mathcal{I}_I \mathcal{E}_I \mathcal{A}_I) - (\mathcal{M}_I)$ , the  $(\mathcal{I}_{SI} \mathcal{E}_{SI} \mathcal{A}_{SI}) - (\mathcal{M}_I)$ , and the  $(\mathcal{I}_{SI}) - (\mathcal{E}_{SI}) - (\mathcal{A}_{SI}) - (\mathcal{M}_I)$  strategies, when varying both  $\tau$  and

### 5.1. Free contraction benchmark

|        | $(\mathcal{I}_1 \mathcal{E}_1 \mathcal{A}_1) - (\mathcal{M}_1)$ |                  |       |                  |                  |       |                  |                  |       |                  |                  |       |                  |                  |       |
|--------|---|------------------|-------|------------------|------------------|-------|------------------|------------------|-------|------------------|------------------|-------|------------------|------------------|-------|
|        | $N_{sub} = 1$   |                  |       | $N_{sub} = 2$    |                  |       | $N_{sub} = 4$    |                  |       | $N_{sub} = 8$    |                  |       | $N_{sub} = 16$   |                  |       |
| $\tau$ | $\overline{N}^N$  | $\overline{N}^G$ | $T^W$ | $\overline{N}^N$ | $\overline{N}^G$ | $T^W$ | $\overline{N}^N$ | $\overline{N}^G$ | $T^W$ | $\overline{N}^N$ | $\overline{N}^G$ | $T^W$ | $\overline{N}^N$ | $\overline{N}^G$ | $T^W$ |
| 1      | 2.5   | 4.4              | 300'  | 2.7              | 4.7              | 221'  | 2.8              | 5.6              | 178'  | 3.3              | 5.4              | 156'  | 3.6              | 7.0              | 144'  |
| 2      | 2.7   | 4.7              | 144'  | 2.8              | 5.6              | 101'  | 3.3              | 5.4              | 81'   | 3.6              | 7.0              | 69'   | 4.1              | 10.3             | 63'   |
| 4      | 2.8   | 5.6              | 70'   | 3.3              | 5.4              | 50'   | 3.6              | 7.0              | 38'   | 4.1              | 10.2             | 32'   | 4.5              | 14.5             | 29'   |
| 8      | 3.3   | 5.4              | 38'   | 3.6              | 7.0              | 26'   | 4.1              | 10.3             | 20'   | 4.4              | 14.6             | 16'   | 5.2              | 18.7             | 15'   |
| 12     | 3.4   | 6.2              | 26'   | 3.8              | 8.8              | 18'   | 4.4              | 12.6             | 13'   | 4.8              | 17.2             | 11'   | 5.4              | 21.9             | 10'   |
| 16     | 3.6   | 7.0              | 20'   | 4.2              | 10.2             | 14'   | 4.4              | 14.6             | 10'   | 5.2              | 18.7             | 9'    | 5.5              | 24.7             | 8'    |
| 24     | 3.8   | 8.9              | 15'   | 4.4              | 12.6             | 10'   | 4.8              | 17.2             | 8'    | 5.4              | 21.9             | 6'    | 6.0              | 28.8             | 6'    |
| 32     | 4.2   | 10.3             | 12'   | 4.5              | 14.6             | 8'    | 5.3              | 18.7             | 6'    | 5.5              | 24.8             | 5'    | 6.0              | 33.2             | 5'    |

|        | $(\mathcal{I}_{\text{SI}}\mathcal{E}_{\text{SI}}\mathcal{A}_{\text{SI}})-(\mathcal{M}_{\text{I}})$ |                  |       |                  |                  |       |                  |                  |       |                  |                  |       |                  |                  |       |
|--------|--|------------------|-------|------------------|------------------|-------|------------------|------------------|-------|------------------|------------------|-------|------------------|------------------|-------|
|        | $N_{sub}=1$  |                  |       | $N_{sub}=2$      |                  |       | $N_{sub}=4$      |                  |       | $N_{sub}=8$      |                  |       | $N_{sub}=16$     |                  |       |
| $\tau$ | $\overline{N}^N$   | $\overline{N}^G$ | $T^W$ | $\overline{N}^N$ | $\overline{N}^G$ | $T^W$ | $\overline{N}^N$ | $\overline{N}^G$ | $T^W$ | $\overline{N}^N$ | $\overline{N}^G$ | $T^W$ | $\overline{N}^N$ | $\overline{N}^G$ | $T^W$ |
| 1      | 2.5  | 4.4              | 258'  | 2.7              | 4.7              | 179'  | 2.8              | 5.6              | 137'  | 3.3              | 5.4              | 115'  | 3.6              | 7.0              | 107'  |
| 2      | 2.7  | 4.7              | 123'  | 2.8              | 5.6              | 81'   | 3.3              | 5.4              | 59'   | 3.6              | 7.0              | 48'   | 4.1              | 10.2             | 42'   |
| 4      | 2.8  | 5.6              | 60'   | 3.3              | 5.4              | 39'   | 3.6              | 7.0              | 27'   | 4.2              | 10.2             | 21'   | 4.5              | 14.5             | 18'   |
| 8      | 3.3  | 5.4              | 32'   | 3.6              | 7.0              | 20'   | 4.1              | 10.2             | 14'   | 4.5              | 14.5             | 10'   | 5.2              | 18.6             | 8'    |
| 12     | 3.4  | 6.2              | 22'   | 3.9              | 8.8              | 13'   | 4.4              | 12.5             | 9'    | 4.8              | 17.1             | 7'    | 5.4              | 21.8             | 5'    |
| 16     | 3.5  | 7.0              | 16'   | 4.1              | 10.2             | 10'   | 4.4              | 14.5             | 7'    | 5.2              | 18.6             | 5'    | 5.5              | 24.6             | 4'    |
| 24     | 3.7  | 8.7              | 11'   | 4.3              | 12.3             | 7'    | 4.7              | 16.9             | 4'    | 5.3              | 21.5             | 3'    | 6.0              | 28.4             | 2'    |
| 32     | 3.8  | 9.9              | 8'    | 4.3              | 13.9             | 5'    | 4.8              | 18.5             | 3'    | 5.3              | 23.9             | 2'    | 10.6             | 23.9             | 2'    |

|        | $(\mathcal{I}_{\text{SI}}) - (\mathcal{E}_{\text{SI}}) - (\mathcal{A}_{\text{SI}}) - (\mathcal{M}_{\text{I}})$ |                  |       |                      |                  |       |                      |                  |       |                      |                  |       |                       |                  |       |
|--------|--|------------------|-------|----------------------|------------------|-------|----------------------|------------------|-------|----------------------|------------------|-------|-----------------------|------------------|-------|
|        | $N_{\text{sub}} = 1$   |                  |       | $N_{\text{sub}} = 2$ |                  |       | $N_{\text{sub}} = 4$ |                  |       | $N_{\text{sub}} = 8$ |                  |       | $N_{\text{sub}} = 16$ |                  |       |
| $\tau$ | $\overline{N}^N$   | $\overline{N}^G$ | $T^W$ | $\overline{N}^N$     | $\overline{N}^G$ | $T^W$ | $\overline{N}^N$     | $\overline{N}^G$ | $T^W$ | $\overline{N}^N$     | $\overline{N}^G$ | $T^W$ | $\overline{N}^N$      | $\overline{N}^G$ | $T^W$ |
| 1      | 2.5  | 3.2              | 242'  | 2.7                  | 3.6              | 159'  | 2.8                  | 4.4              | 118'  | 3.3                  | 4.4              | 97'   | 3.6                   | 5.8              | 84'   |
| 2      | 2.7  | 3.6              | 114'  | 2.8                  | 4.5              | 71'   | 3.3                  | 4.5              | 50'   | 3.6                  | 5.8              | 38'   | 4.1                   | 8.5              | 32'   |
| 4      | 2.8  | 4.5              | 57'   | 3.3                  | 4.5              | 36'   | 3.6                  | 5.8              | 24'   | 4.2                  | 8.5              | 18'   | 4.5                   | 12.2             | 14'   |
| 8      | 3.3  | 4.5              | 31'   | 3.6                  | 5.9              | 18'   | 4.2                  | 8.6              | 12'   | 4.5                  | 12.2             | 8'    | 5.2                   | 15.9             | 7'    |
| 12     | 3.4  | 6.0              | 21'   | 3.8                  | 8.0              | 13'   | 4.4                  | 11.1             | 8'    | 4.8                  | 15.2             | 6'    | 5.4                   | 19.6             | 4'    |
| 16     | 3.5  | 7.0              | 16'   | 4.1                  | 10.1             | 10'   | 4.4                  | 14.3             | 6'    | 5.2                  | 18.3             | 4'    | 5.5                   | 24.3             | 3'    |
| 24     | 3.7  | 8.2              | 11'   | 4.3                  | 11.6             | 6'    | 4.6                  | 15.7             | 4'    | 5.4                  | 20.2             | 3'    | 6.0                   | 26.7             | 2'    |
| 32     | 3.8  | 8.5              | 8'    | 4.3                  | 12.0             | 5'    | 4.8                  | 15.9             | 3'    | 5.4                  | 20.5             | 2'    | 9.8                   | 28.7             | 1'    |

Table 5.2 – The average number of Newton ( $\bar{N}^N$ ) and GMRES ( $\bar{N}^G$ ) iterations for the solution of the mechanics problem and the total wall time ( $T^W$ , in minutes) for the benchmark simulations, for each segregated strategy,  $\tau$  (in  $10^{-5}$  s), and  $N_{sub}$  considered.

$N_{sub}$ . In this case, however, the number of iterations  $\bar{N}^G$  and  $\bar{N}^N$  account for the solution of the mechanics problem only: we choose to do so since the solution of the mechanics problem is the clear computational bottleneck of the simulation, and because it is the one which is mostly affected by the choice of  $N_{sub}$ .

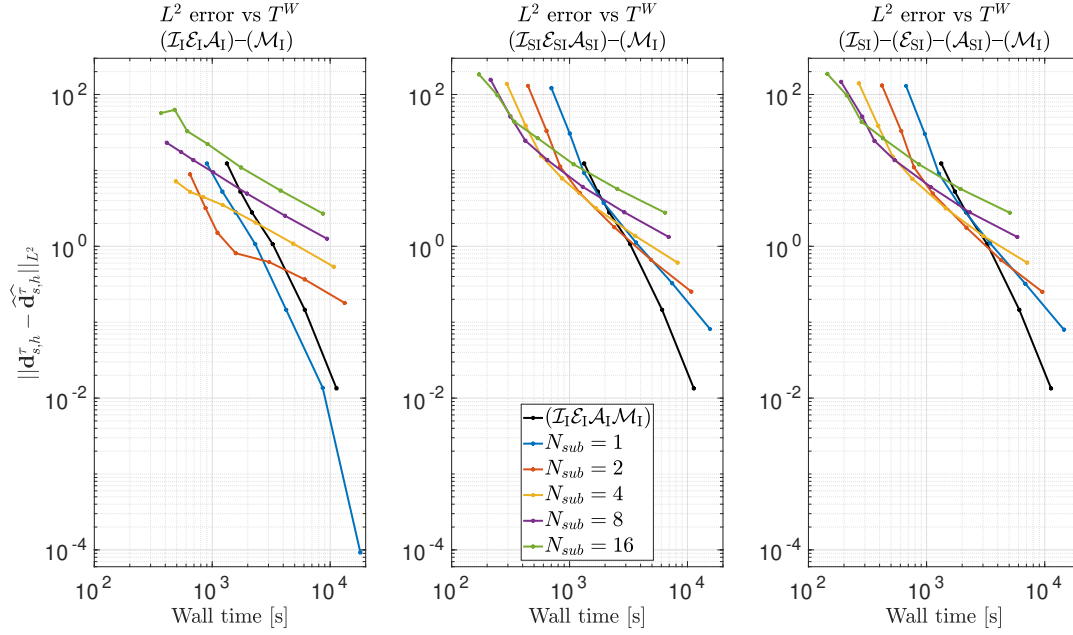


Figure 5.15 – Errors in  $L^2(\Omega_0^s)$  norm of the displacements  $\mathbf{d}_{s,h}^\tau$  obtained with  $(\mathcal{I}_I \mathcal{E}_I \mathcal{A}_I) - (\mathcal{M}_I)$  (left),  $(\mathcal{I}_{SI} \mathcal{E}_{SI} \mathcal{A}_{SI}) - (\mathcal{M}_I)$  (center) and  $(\mathcal{I}_{SI}) - (\mathcal{E}_{SI}) - (\mathcal{A}_{SI}) - (\mathcal{M}_I)$  (right) at time  $T = 96$  ms, for every  $\tau$  and  $N_{sub}$  considered, in logarithmic scale against the wall time. The errors obtained with  $(\mathcal{I}_I \mathcal{E}_I \mathcal{A}_I \mathcal{M}_I)$  are also reported in each figure.

By analyzing the data in Table 5.2 we observe that, in constrast with the  $(\mathcal{I}_I \mathcal{E}_I \mathcal{A}_I \mathcal{M}_I)$  strategy, the number of GMRES iterations  $\overline{N}^G$  gets larger for increasing values of both  $\tau$  and  $N_{sub}$ . Nonetheless, the wall time  $T^W$  drops dramatically accounting for a speed-up of more than  $300\times$  times when using  $(\mathcal{I}_{SI}) - (\mathcal{E}_{SI}) - (\mathcal{A}_{SI}) - (\mathcal{M}_I)$ , timestep  $\tau = 32 \times 10^{-5}$ , and  $N_{sub} = 16$ , compared to using  $(\mathcal{I}_I \mathcal{E}_I \mathcal{A}_I \mathcal{M}_I)$  and timestep  $\tau = 1 \times 10^{-5}$ . If the stability of the electrophysiology must be ensured, one can use e.g.  $(\mathcal{I}_I \mathcal{E}_I \mathcal{A}_I) - (\mathcal{M}_I)$  with the same parameters with a  $72\times$  speed-up, or  $(\mathcal{I}_{SI}) - (\mathcal{E}_{SI}) - (\mathcal{A}_{SI}) - (\mathcal{M}_I)$  with  $\tau = 8 \times 10^{-5}$  and  $N_{sub} = 16$  with a  $52\times$  speed-up.

However, by comparing the wall time, we are neglecting the information on the accuracy. We hence conclude this section by gathering together the values of  $T^W$  and the errors on the displacement at the time  $T = 96$  ms for all the cases considered. We then verify the balance between the accuracy and the efficiency of each strategy by reporting in Figure 5.15 the errors against  $T^W$ . In this way, given a tolerance representing the maximum admissible error on the displacement, we can verify which strategy and parameters allow to attain such error in the shortest time. We first observe that the  $(\mathcal{I}_I \mathcal{E}_I \mathcal{A}_I) - (\mathcal{M}_I)$  strategy with  $N_{sub} = 1$  is always more convenient with respect to  $(\mathcal{I}_I \mathcal{E}_I \mathcal{A}_I \mathcal{M}_I)$ , meaning that the same accuracy can be obtained with a shorter wall time. This is in agreement with our previous observations on the magnitude of the splitting error introduced by using the  $(\mathcal{I}_I \mathcal{E}_I \mathcal{A}_I) - (\mathcal{M}_I)$  strategy. Moreover, the errors in the  $(\mathcal{I}_{SI}) - (\mathcal{E}_{SI}) - (\mathcal{A}_{SI}) - (\mathcal{M}_I)$  case are the same as those in the  $(\mathcal{I}_{SI} \mathcal{E}_{SI} \mathcal{A}_{SI}) - (\mathcal{M}_I)$  case; the latter, however, requires a shorter wall

time, as reported also in Table 5.2. The  $(\mathcal{I}_{\text{SI}})-(\mathcal{E}_{\text{SI}})-(\mathcal{A}_{\text{SI}})-(\mathcal{M}_1)$  strategy is hence always more convenient with respect to  $(\mathcal{I}_{\text{SI}}\mathcal{E}_{\text{SI}}\mathcal{A}_{\text{SI}})-(\mathcal{M}_1)$ .

We observe that, in general, the proposed segregated strategies represent a better alternative with respect to the monolithic one if a relatively large error on the displacement is acceptable. We conclude that the choice of the strategy should depend on the requirements on the efficiency of the simulation and the accuracy of the approximated solution. If the goal is that of reducing the computational cost,  $(\mathcal{I}_{\text{SI}})-(\mathcal{E}_{\text{SI}})-(\mathcal{A}_{\text{SI}})-(\mathcal{M}_1)$  should be used, although its accuracy drops for larger timesteps. On the other hand, if accuracy is the driving factor in the choice,  $(\mathcal{I}_1\mathcal{E}_1\mathcal{A}_1)-(\mathcal{M}_1)$  can be used instead of  $(\mathcal{I}_1\mathcal{E}_1\mathcal{A}_1\mathcal{M}_1)$  with little to no compromise on the precision, thus avoiding the extremely long wall times needed by the latter.

### 5.1.2 Scalability test and $h$ -refinement

After having assessed the accuracy and the efficiency of the proposed strategies on the coarsest idealized mesh, we now focus on increasing the size of the discretized electromechanics problem by using the refined meshes indicated in Table 3.1. We want indeed to verify the scalability – i.e. the effectiveness of increasing the number of processors – of our solvers, with a particular focus on the mechanics solver and preconditioner for the segregated strategies. The solution of the mechanical core problem, indeed, is the computational bottleneck of the simulations. To this aim, we perform several simulations to study the weak and the strong scalability [Grama, 2003]. These are defined as the capability of the algorithm to cut down the solution time when increasing the number of CPUs, and to keep the solution time constant while increasing the problem size (i.e. the number of DoFs), provided that the ratio between the latter and the number of CPUs employed is kept constant, respectively. All the computations were carried out using Piz Daint, a Cray XC50/XC40 supercomputer installed at the Swiss National Supercomputing Center (CSCS)<sup>1</sup>.

We begin by performing a strong scalability test for the  $(\mathcal{I}_1\mathcal{E}_1\mathcal{A}_1\mathcal{M}_1)$  strategy with the finest idealized mesh, which features 4’629’817 vertices. We set  $\Delta t = 2 \times 10^{-4}$  s and solve 100 timesteps – i.e. we set  $T = 10^{-2}$  s. For this set of simulations, we use an Additive Schwarz preconditioner (Ifpack [Sala and Heroux, 2005]) for the preconditioning of the mechanics core block: indeed, it is known to be more scalable compared with Algebraic Multigrid [Forti, 2016]. We use 800, 1’600, and 3’200 cpus: since with this mesh the total number of DoFs of the monolithic system amounts to 37’038’536, the number of DoFs per CPU is around 46’298, 23’149, and 11’574, respectively. We did not perform a simulation with less CPUs because of memory limitations preventing us from using more DoFs per CPU. Nonetheless, it must be noted that, in the application of the preconditioner, we effectively solve the core problems when “inverting” the diagonal

---

<sup>1</sup><http://www.cscs.ch>

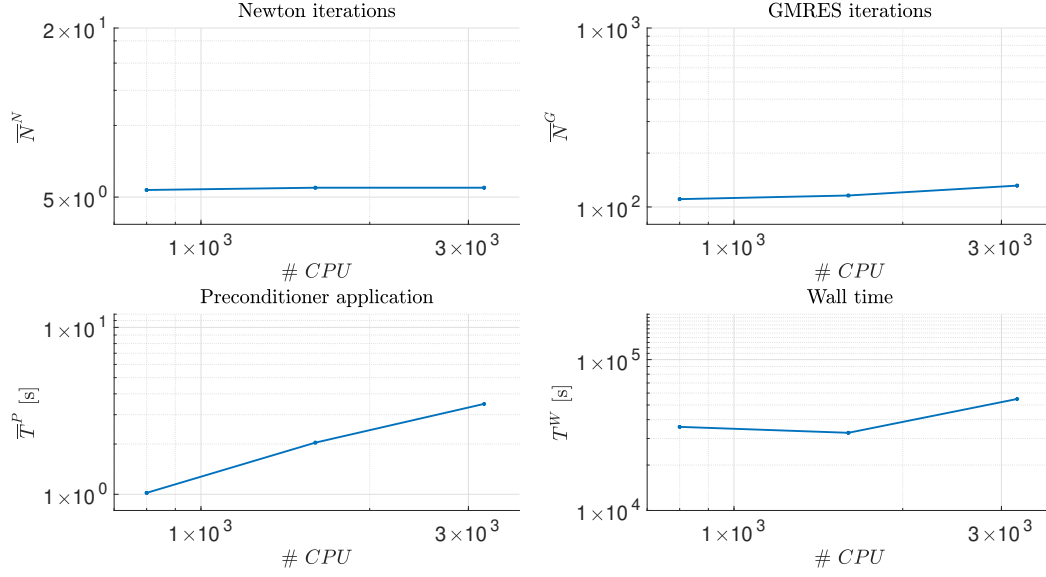


Figure 5.16 – Strong scalability for  $(\mathcal{I}_1\mathcal{E}_1\mathcal{A}_1\mathcal{M}_1)$ : the average number of Newton iterations  $\overline{N}^N$  (top left) and GMRES iterations  $\overline{N}^G$  (top right), the average time spent for the assembly and application of the preconditioner  $\overline{T}^P$  (bottom left), and the total wall time  $T^W$  (bottom right). The total number of DoFs amounts to 37'038'536.

blocks of the monolithic matrix: this operation is carried out with 5'787, 2'894, and 1'447 DoFs per CPU, respectively. In Figure 5.16 we report the number of Newton and GMRES iterations  $\overline{N}^N$  and  $\overline{N}^G$  in the first row, while the time required for the simulation  $T^W$  and the average preconditioner assembly and application time  $\overline{T}^P$  in the second row. We observe that, while  $\overline{N}^N$  and  $\overline{N}^G$  are kept almost constant, the wall time does not scale. Indeed, when using 1'600 CPUs, the speedup with respect to the simulation with 800 CPUs is only around 10%; when using 3'200 CPUs the wall time  $T^W$  even significantly increases. This is due to the fact that, when using a small number of DoFs per CPU when solving the core problems, the communication between the CPUs becomes the computational bottleneck of the simulation. We conclude that, even if the number of Newton and GMRES iterations does not significantly vary when increasing the number of CPUs, there exist strong lower and upper constraints on the number of DoFs per CPU (due to the communication bottleneck and to the large size of the monolithic problem, respectively). Indeed, the increment in the average time required for the application of the preconditioner  $\overline{T}^P$  for an increasing number of CPUs (see Figure 5.16) is responsible for this behavior.

In order to analyze the behavior of the mechanics solver, we choose to study the strong and the weak scalability for the  $(\mathcal{I}_{SI})-(\mathcal{E}_{SI})-(\mathcal{A}_{SI})-(\mathcal{M}_I)$  strategy with  $\tau = 8 \times 10^{-5}$  s and  $T = 100$  ms. This choice was shown to provide a reasonable balance between accuracy and efficiency in Section 5.1.1. In Table 5.3 we report the number of CPUs used for the

### 5.1. Free contraction benchmark

| CPUs | Vertices/CPUs | DoFs/CPUs |
|------|---------------|-----------|
| 400  | 11'575        | 34'725    |
| 800  | 5'787         | 17'361    |
| 1600 | 2'894         | 8'682     |

Table 5.3 – Strong scalability for  $(\mathcal{I}_{SI})-(\mathcal{E}_{SI})-(\mathcal{A}_{SI})-(\mathcal{M}_I)$ : the number of CPUs, the Vertices/CPUs ratio, and the DoFs/CPUs ratio for the mechanics problem.

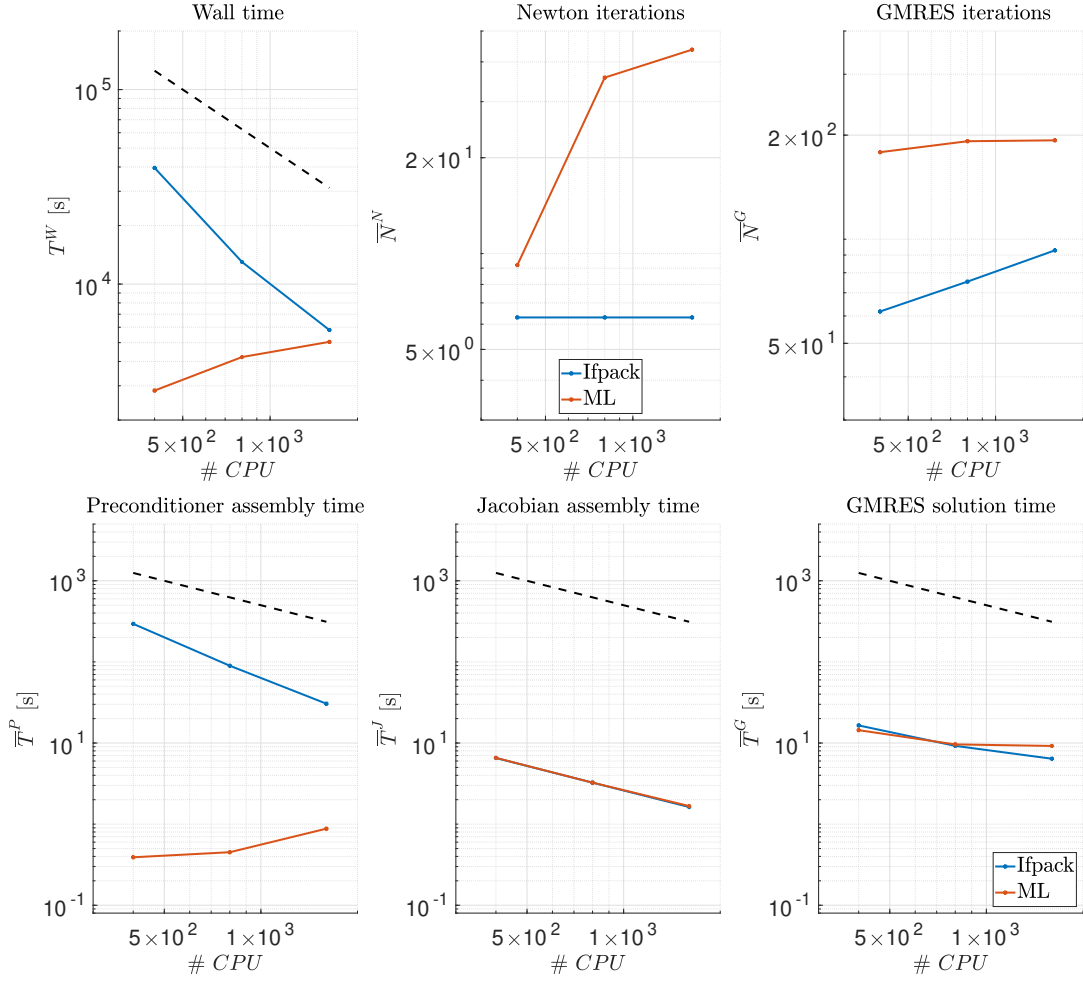


Figure 5.17 – Strong scalability for  $(\mathcal{I}_{SI})-(\mathcal{E}_{SI})-(\mathcal{A}_{SI})-(\mathcal{M}_I)$ : the total wall time  $T^W$  (top left), the average number of Newton iterations  $\bar{N}^N$  (top) and GMRES iterations  $\bar{N}^G$  (top right), the average assembly time for the preconditioner  $\bar{T}^P$  (bottom left) and the Jacobian matrix (bottom), and the GMRES average time  $\bar{T}^G$  for the solution of the mechanics problem (bottom right).

strong scalability test with the finest idealized mesh, while in Figure 5.17 the results are displayed. In this case we employ both Algebraic Multigrid (ML [Gee et al., 2006])

## Chapter 5. Numerical simulations

| Refinement | Vertices  | Tetrahedra | CPUs | Vertices/CPUs | DoFs/CPUs |
|------------|-----------|------------|------|---------------|-----------|
| 2×         | 81'335    | 416'000    | 14   | 5'809         | 17'427    |
| 3×         | 602'749   | 3'328'000  | 104  | 5'796         | 17'388    |
| 4×         | 4'629'817 | 26'624'000 | 800  | 5'787         | 17'361    |

Table 5.4 – Weak scalability for  $(\mathcal{I}_{SI})-(\mathcal{E}_{SI})-(\mathcal{A}_{SI})-(\mathcal{M}_I)$ : the level of hierarchical refinement, the number of vertices and tetrahedra for each idealized mesh, the number of CPUs, the Vertices/CPUs ratio, and the DoFs/CPUs ratio for the mechanics problem.

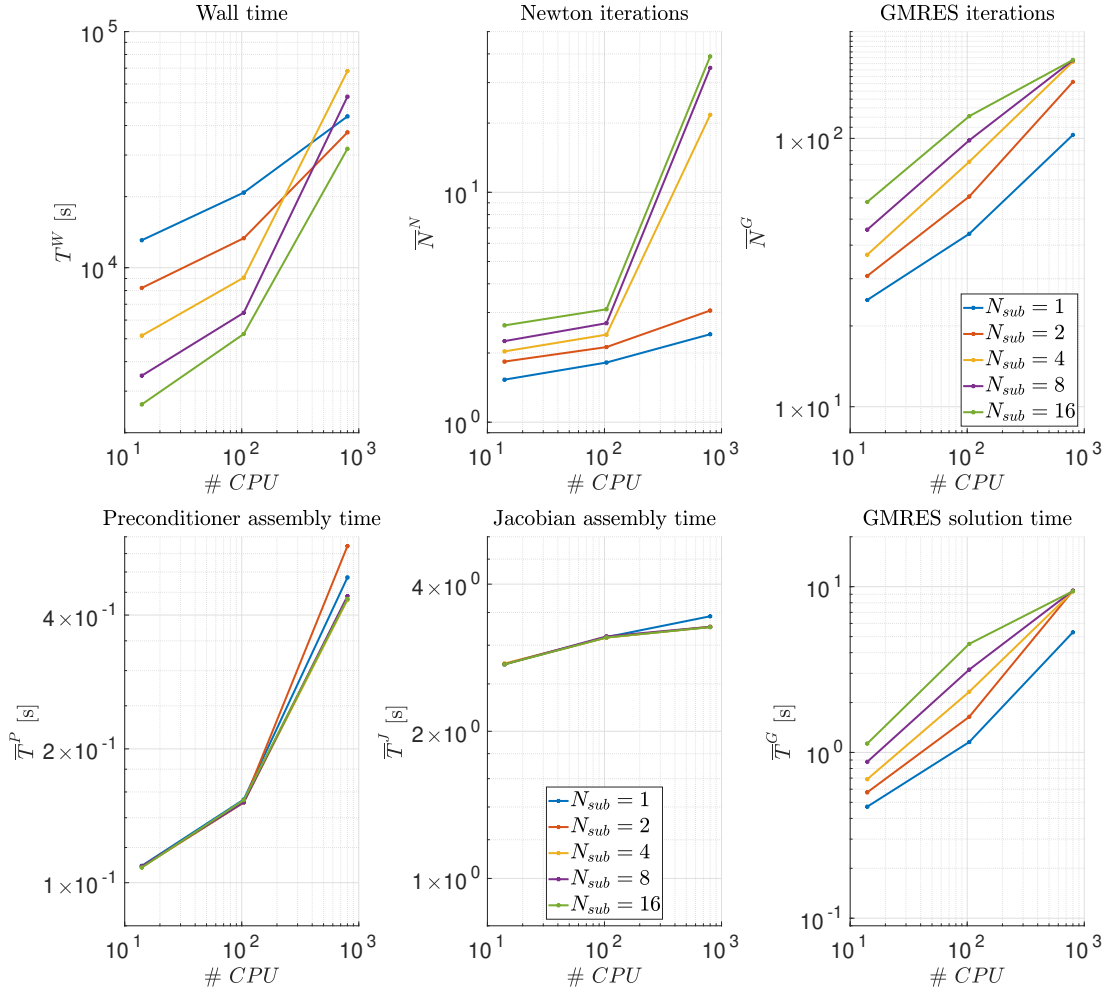


Figure 5.18 – Weak scalability for  $(\mathcal{I}_{SI})-(\mathcal{E}_{SI})-(\mathcal{A}_{SI})-(\mathcal{M}_I)$ : the total wall time  $T^W$  (top left), the average number of Newton iterations  $\bar{N}^N$  (top) and GMRES iterations  $\bar{N}^G$  (top right), the average assembly time for the preconditioner  $\bar{T}^P$  (bottom left) and the Jacobian matrix (bottom), and the GMRES average time  $\bar{T}^G$  for the solution of the mechanics problem (bottom right).



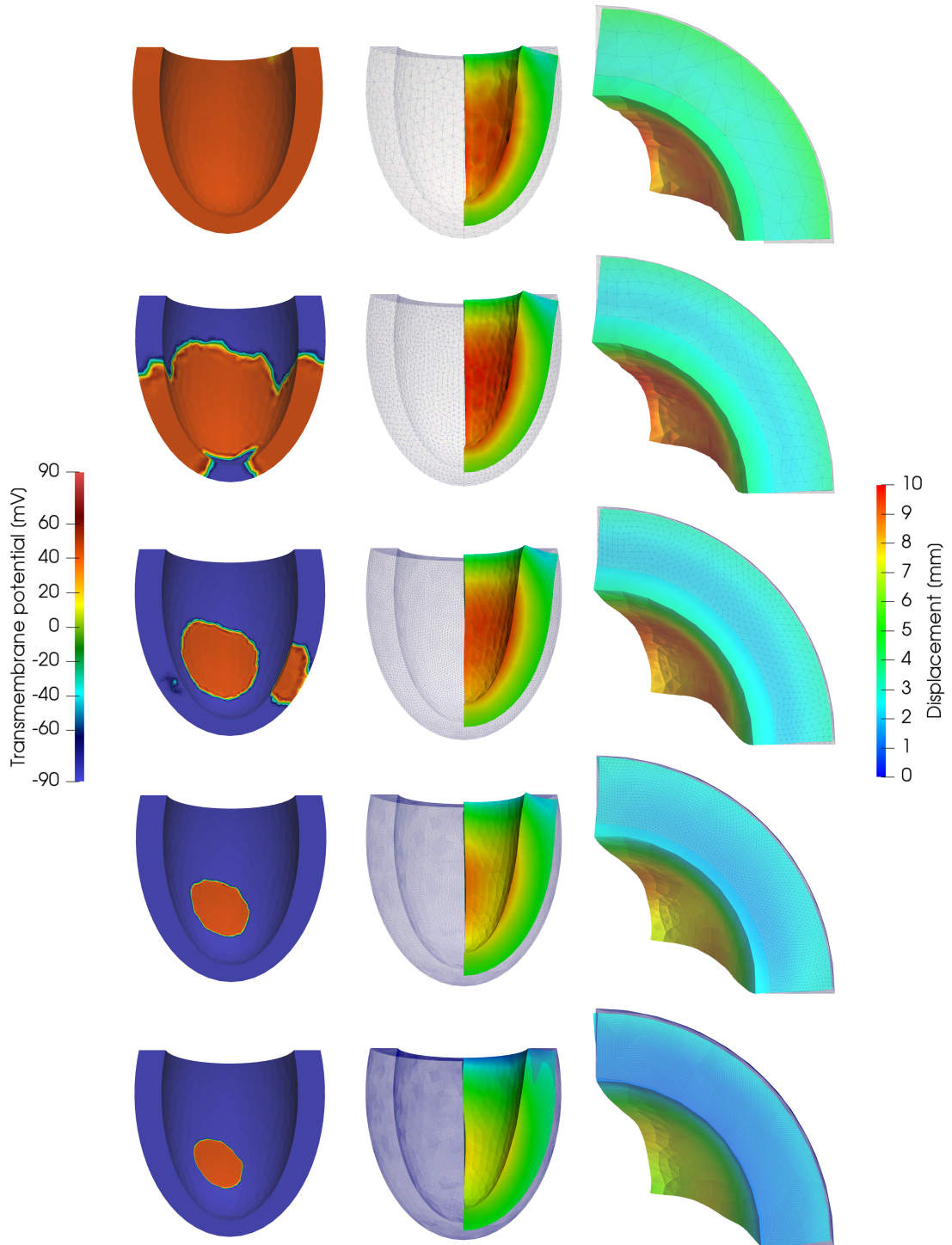


Figure 5.19 – Transmembrane potential at time  $T=10$  ms (left) and displacement magnitude (center and right) at time  $T=100$  ms obtained by using the  $(\mathcal{I}_{\text{SI}})-(\mathcal{E}_{\text{SI}})-(\mathcal{A}_{\text{SI}})-(\mathcal{M}_{\text{I}})$  strategy for each of the five idealized meshes indicated in Table 3.1.

and Additive Schwarz (Ipack) preconditioners and we set  $N_{sub} = 8$ . The first clear conclusion that can be drawn by observing the wall time  $T^W$  plot is that the Ipack preconditioner is strongly scalable while the ML preconditioner is not; nonetheless, the latter allows to solve the problem in a shorter time, in particular when using a large number of DoFs per CPU. The improved scalability of the Ipack preconditioner is mostly due to the significantly lower average number of GMRES iterations  $\bar{N}^G$  and, in particular, of Newton iterations  $\bar{N}^N$ . Indeed, a larger  $\bar{N}^G$  for ML does not imply a longer GMRES solution time  $\bar{T}^G$  with respect to Ipack since the assembly of the former is much faster than that of the latter; however, the poor performances of ML are confirmed from the fact that  $\bar{N}^G$  is almost equal to the maximum number of GMRES iterations (which was set to 200), thus determining a number of Newton iterations  $\bar{N}^N$  almost an order of magnitude larger than in the Ipack case.

Regarding now the weak scalability, we report in Table 5.4 the information related to the meshes and the number of CPUs used for the weak scalability simulations. We use in this case the ML preconditioner since it ensures a shorter  $T^W$  with the chosen number of DoFs per CPU (see Figure 5.17). The simulations are performed for  $N_{sub} = 1, 2, 4, 8, 16$ , and the results reported in Figure 5.18. We observe that, similarly to the strong scalability case,  $\bar{N}^G$  significantly grows with the number of CPUs confirming the non-optimal performances when using ML. On the other hand, in contrast with the strong scalability case,  $\bar{T}^G$  grows accordingly to the number of GMRES iterations. The increment of  $\bar{N}^G$  is notable in particular for  $N_{sub} > 2$ ; nonetheless, for  $N_{sub} = 16$ , the time saved by using a larger  $N_{sub}$  ( $\Delta t$ ) balances the effect on the total wall time in all cases.

We conclude our discussion on the topic by showing in Figure 5.19 the potential at time  $T=10$  ms and the displacement at time  $T=100$  ms for the five idealized meshes of Table 3.1. We observe that, in the coarsest cases, the activation time is highly underestimated for reasons which were discussed in Section 5.1. On the other hand, the displacement magnitude is overestimated up to around 30% with respect to the finest mesh.

## 5.2 Subject-specific LV: the full heartbeat

In this section, we use the four strategies to simulate a full heartbeat with the subject-specific mesh (see Figure 3.8). The heartbeat is reproduced by coupling the electromechanics solver with the 0D model for the endocardial pressure. The final time (i.e. the heartbeat duration) is set to  $T = 0.8$  s. Finite elements of order  $r = 1$  are employed, thus obtaining a system of size  $M = 8 \times N_1^{dof} = 1'008'248$  in the monolithic case, together with BDF of order  $\sigma = 2$ . The timestep size is set to  $\tau = 5 \times 10^{-5}$  s while  $N_{sub} = 1, 5, 10$ . For these set of simulations, 72 CPUs are used in all cases.

As in the previous tests, a current is applied at the endocardium in three distinct points for

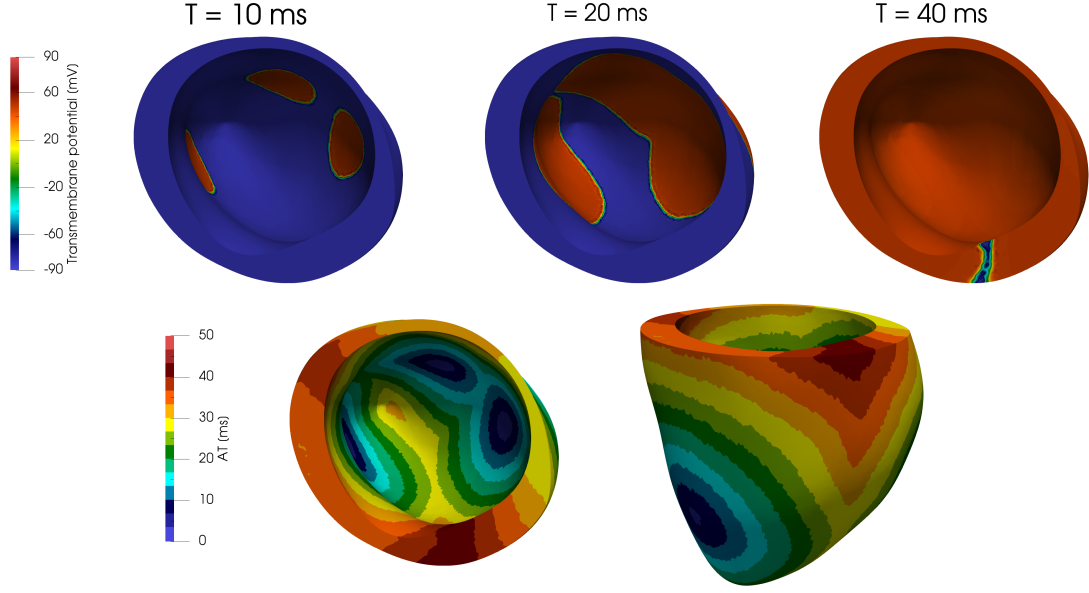


Figure 5.20 – Transmembrane potential at different times (top row) and activation time (bottom row) for the subject-specific simulation.

3 ms to trigger the heartbeat. We show the results obtained with  $(\mathcal{I}_{\text{SI}})-(\mathcal{E}_{\text{SI}})-(\mathcal{A}_{\text{SI}})-(\mathcal{M}_{\text{I}})$  in Figure 5.20, where the transmembrane potential at times  $T = 10, 20, 40$  ms is depicted together with the activation time. The latter is defined, in each point, as the time at which the electric potential reaches a threshold value  $v^{thr}$  (we set in particular  $v^{thr} = 10$  mV) [Pagani, 2017, Usyk and McCulloch, 2003]. Taking around 40 ms for the complete activation of the myocardium, the activation time is in agreement with experimental data obtained from healthy patients [Cassidy et al., 1984, Vassallo et al., 1986].

In Figure 5.21 we show the displacement magnitude on the deformed myocardium, with the reference geometry  $\Omega_0^s$ , during the full heartbeat. The isovolumic contraction phase is characterized by a displacement of the base towards the apex; then, during the ejection phase, the base and the apex move towards the center of the LV which remains essentially steady; finally, during the isovolumic relaxation and filling phases, the LV quickly returns to the initial configuration. Compared with the in vivo results in [Codreanu et al., 2010], the results given by our integrated model correctly reproduce the longitudinal movement of the LV. Moreover, as in the idealized geometry case, a significant thickening takes place while the rotation of the LV is underestimated [Codreanu et al., 2010].

In order to better appreciate the behavior of the employed model, we also estimate the components of the stress tensor in the fibers and sheets direction  $\sigma_{ff} = (\mathbf{P}\mathbf{f}_0)\mathbf{f}$  and  $\sigma_{ss} = (\mathbf{P}\mathbf{s}_0)\mathbf{s}$ . With this aim, we solve the following  $L^2$ -projection problem: find  $\sigma_{ff}$

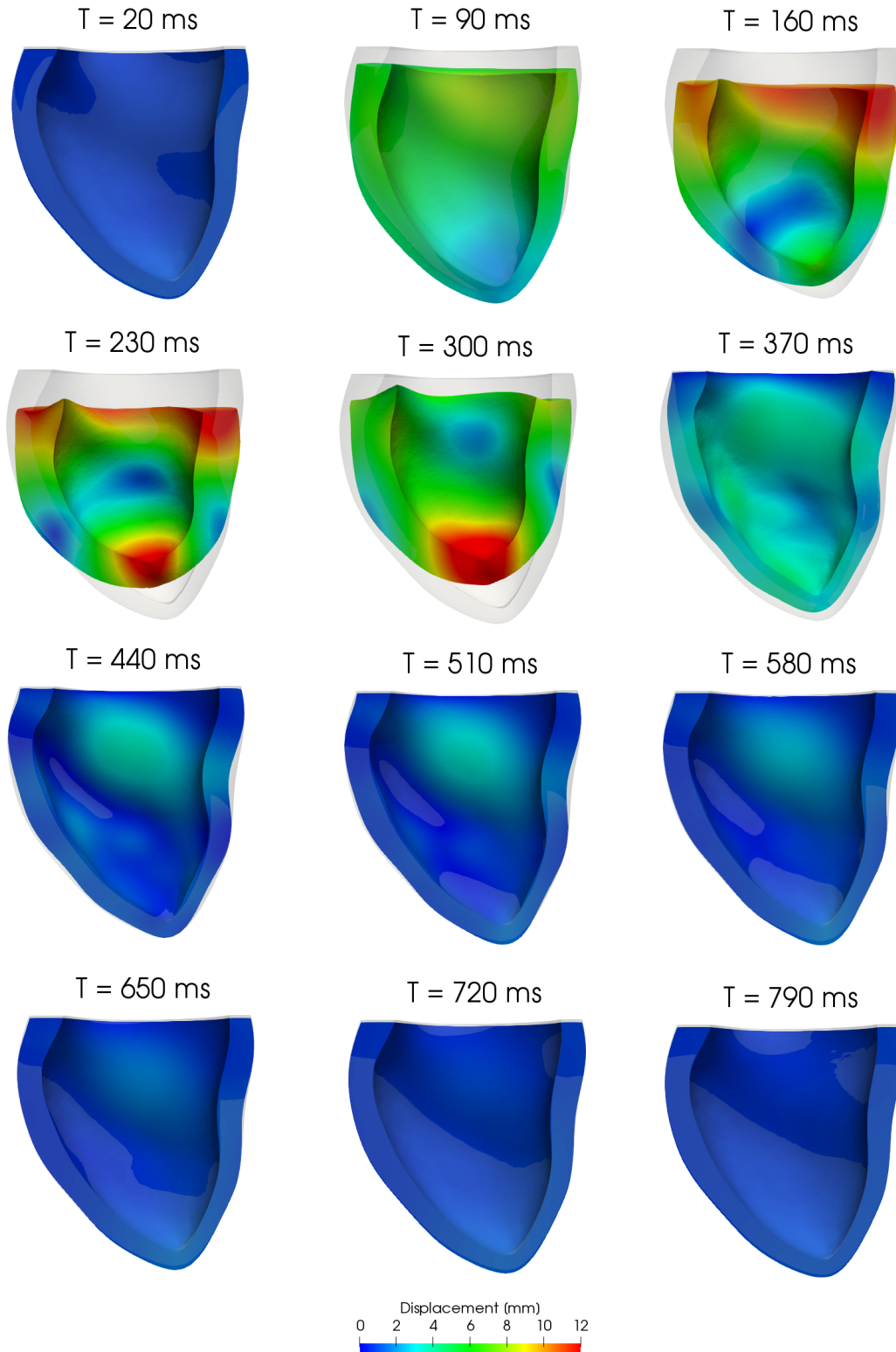


Figure 5.21 – Deformed subject-specific geometry and displacement field at different times, compared with the reference domain  $\Omega_0$ , for the full heartbeat simulation.

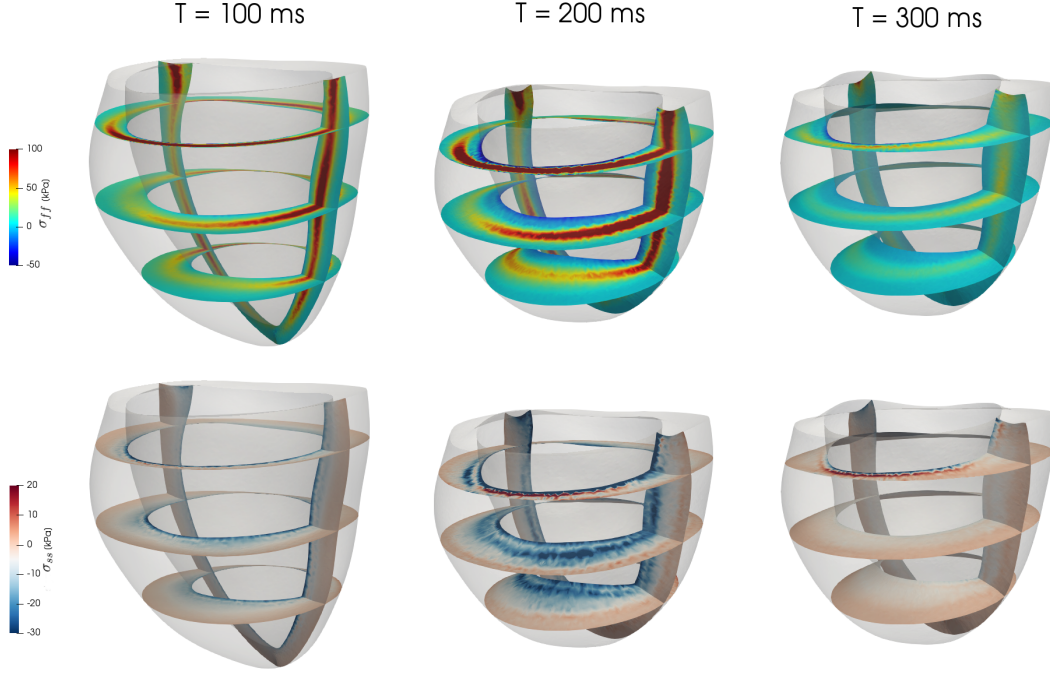


Figure 5.22 – Stress components  $\sigma_{ss}$  (left) and  $\sigma_{ff}$  (right) depicted on three slices of the deformed domain at different times.

such that

$$\int_{\Omega_0^s} \sigma_{ff} \psi_i \, d\Omega_0^s = \int_{\Omega_0^s} (\mathbf{P}\mathbf{f}_0) \mathbf{f} \psi_i \, d\Omega_0^s,$$

for  $i, \dots, N_1^{\text{dof}}$ , and analogously for  $\sigma_{ss}$ . In Figure 5.22 we show the two fields obtained at times  $T = 100, 200, 300$  ms; we highlight that  $T = 200$  ms corresponds approximately to the time at which the LV pressure attains its maximum (around 120 mmHg). The values assumed by  $\sigma_{ss}$  mostly fall in the physiological range [Holzapfel and Ogden, 2009, Streeter et al., 1970, Wong and Rautaharju, 1968, Yin et al., 1987] and match the pressure value at the endocardium. Nonetheless the stress value peaks in the region close to the myocardium base; we believe that this is due to the thickness of the septum wall which, in this subject-specific geometry, was reconstructed as particularly thin. Regarding the stress  $\sigma_{ff}$ , the model reproduces much larger values with respect to those indicated in [Barbarotta et al., 2017, Holzapfel and Ogden, 2009, Yin et al., 1987], thus overestimating them by almost an order of magnitude especially where the myocardium wall is (much) thinner. We remark, however, that the available medical data used in [Holzapfel and Ogden, 2009] to fit the strain energy function is obtained with in vitro loading tests, hence accounting only for the passive component of the stress.

Finally, we compare in Figure 5.23 the pressure-volume (pV) loops obtained with the

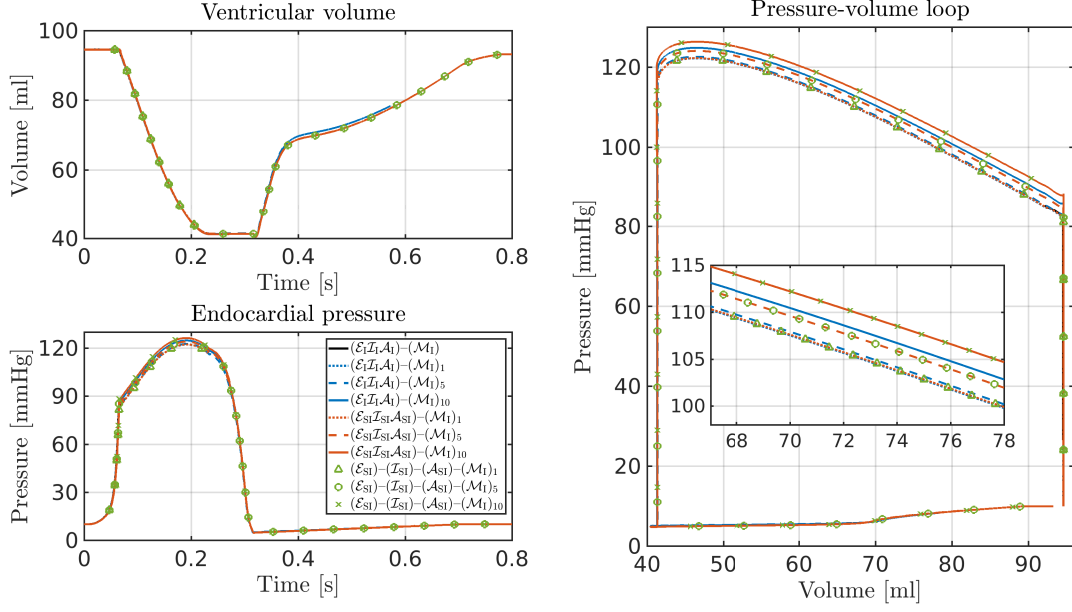


Figure 5.23 – LV internal volumes (top left) and endocardial pressures (bottom left) versus time, with pV loops (right) for the subject-specific simulations with all the strategies considered (the parameter  $N_{sub}$  used is indicated in legend with a subscript).

different numerical coupling strategies. A close up of the pV loops in the ejection phase is also reported to better assess the differences among them. We observe that, as in the benchmark test, the difference between the results obtained with  $(\mathcal{I}_{SI}\mathcal{E}_{SI}\mathcal{A}_{SI})-(\mathcal{M}_I)$  and those obtained with  $(\mathcal{I}_{SI})-(\mathcal{E}_{SI})-(\mathcal{A}_{SI})-(\mathcal{M}_I)$  is negligible. We conclude that the main deviation among the pV loops is caused by the choice of different timestep lengths  $\Delta t = N_{sub}\tau$  for the mechanical model. Specifically, during the last part of the first isovolumic phase, the endocardial pressure increases very rapidly, while the change of the phase (as detailed in Section 1.4.2) takes place when the condition  $p^{endo} \geq p^{ao}$  is satisfied. Hence, when using a large mechanics timestep  $\Delta t$ , the value of the pressure is higher when the ejection phase begins.

We conclude the analysis of this set of simulations by reporting in Table 5.5 the values of  $\overline{N}^N$ ,  $\overline{N}^G$ , and  $T^W$ , for the simulation of the heartbeat with final time set to  $T = 0.073$  s (the maximum final time attainable using  $(\mathcal{I}_1\mathcal{E}_1\mathcal{A}_1\mathcal{M}_1)$ , because of the 24 hours limit for jobs on Piz Daint) for all the strategies used. We observe that, even if in this case the number of Newton and GMRES iterations is larger with respect to the benchmark case, the segregated schemes, and in particular the staggered schemes, allow to greatly reduce the computational costs for the subject-specific simulations too. Indeed, a speed-up of up to  $16\times$  is obtained when using the  $(\mathcal{I}_{SI})-(\mathcal{E}_{SI})-(\mathcal{A}_{SI})-(\mathcal{M}_I)$  strategy with  $N_{sub} = 10$ , compared to  $(\mathcal{I}_1\mathcal{E}_1\mathcal{A}_1\mathcal{M}_1)$  used with the same timestep length  $\tau$ .



### 5.3. Application to a pathological scenario: LV with ischemic necrosis

| Strategy   | $N_{sub}$ | $\Delta t$ | $\overline{N}^N$ | $\overline{N}^G$ | $T^W$ |
|--|-----------|------------|------------------|------------------|-------|
| $(\mathcal{I}_I \mathcal{E}_I \mathcal{A}_I \mathcal{M}_I)$                      | -         | 5          | 3.3              | 18.7             | 1440' |
| $(\mathcal{I}_I \mathcal{E}_I \mathcal{A}_I) - (\mathcal{M}_I)$                  | 1         | 10         | 4.4              | 40.8             | 723'  |
| $(\mathcal{I}_I \mathcal{E}_I \mathcal{A}_I) - (\mathcal{M}_I)$                  | 5         | 25         | 5.1              | 71.8             | 284'  |
| $(\mathcal{I}_I \mathcal{E}_I \mathcal{A}_I) - (\mathcal{M}_I)$                  | 10        | 50         | 5.8              | 93.6             | 259'  |
| $(\mathcal{I}_{SI} \mathcal{E}_{SI} \mathcal{A}_{SI}) - (\mathcal{M}_I)$         | 1         | 10         | 4.4              | 40.8             | 543'  |
| $(\mathcal{I}_{SI} \mathcal{E}_{SI} \mathcal{A}_{SI}) - (\mathcal{M}_I)$         | 5         | 25         | 5.0              | 72.1             | 136'  |
| $(\mathcal{I}_{SI} \mathcal{E}_{SI} \mathcal{A}_{SI}) - (\mathcal{M}_I)$         | 10        | 50         | 5.7              | 93.7             | 130'  |
| $(\mathcal{I}_{SI}) - (\mathcal{E}_{SI}) - (\mathcal{A}_{SI}) - (\mathcal{M}_I)$ | 1         | 10         | 4.4              | 37.7             | 582'  |
| $(\mathcal{I}_{SI}) - (\mathcal{E}_{SI}) - (\mathcal{A}_{SI}) - (\mathcal{M}_I)$ | 5         | 25         | 5.1              | 66.1             | 148'  |
| $(\mathcal{I}_{SI}) - (\mathcal{E}_{SI}) - (\mathcal{A}_{SI}) - (\mathcal{M}_I)$ | 10        | 50         | 5.7              | 86.4             | 93'   |

Table 5.5 – The mechanics timestep  $\Delta t$  (in  $10^{-5}$  s), the average number of Newton ( $\overline{N}^N$ ) and GMRES ( $\overline{N}^G$ ) iterations, and the total wall time ( $T^W$ , in minutes) for the simulation of the heartbeat with final time  $T = 0.073$  s with the subject-specific mesh, using the four strategies considered and  $N_{sub} = 1, 5, 10$ .

### 5.3 Application to a pathological scenario: LV with ischemic necrosis

Cardiac ischemia is a pathological condition characterized by a reduction in the blood supply to the myocardial tissues [Griffin et al., 2008] which causes a shortage in the oxygen supply required for the cellular metabolism. In the most severe cases, it leads to the death of the cells of the affected portion of tissue: in this case the pathology is called *ischemic necrosis*. Regarding the electrophysiology, the cells in a necrotic region are characterized by a reduced excitability and altered ionic currents [Rozanski et al., 1998]; on the other hand, the contractibility of the affected tissue and its surrounding is strongly inhibited, thus determining a reduction in the *stroke volume* (the volume of blood pumped from the left ventricle per beat) [Gaudron et al., 1993, Shimkunov et al., 2013]. Nonetheless a complex remodeling process takes place in the weeks after the infarct episode [Mitchell et al., 1992, Pinto and Boyden, 1999], by which the necrotic region undergoes a marked thickening (hypertrophy) [Rozanski et al., 1998] while the LV cavity is persistently enlarged. The enlargement of the cavity tends to restore the stroke volume, despite a depressed *ejection fraction* (the ratio between the stroke volume and the end diastolic volume of the LV) [Pfeffer and Braunwald, 1990].

We propose here a method developed to model the electromechanics of the LV with a region of the myocardium affected by ischemic necrosis. In such a region cells behave as passive conductors, preventing the depolarization of the tissue [Pagani, 2017]. We model this behavior by “switching off” the ionic currents and the mechanical activation equations in the DoFs belonging to the necrotic region. A more complex technique at

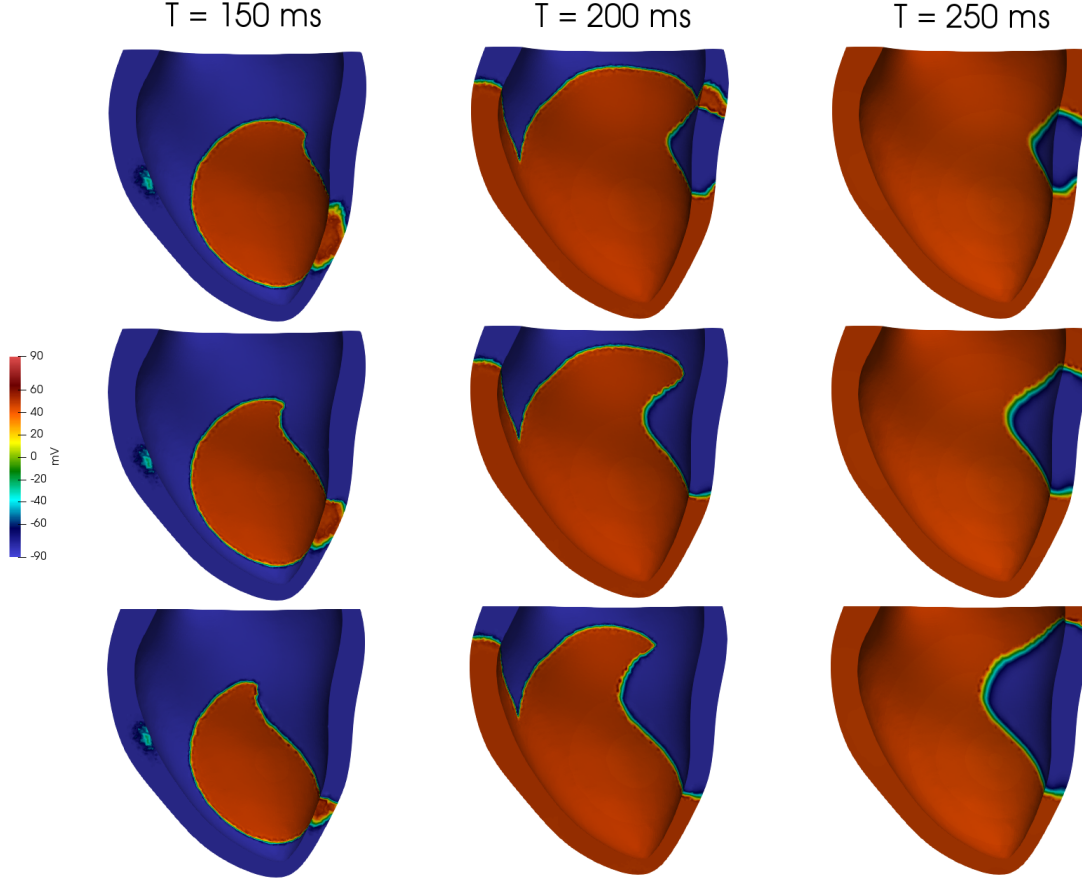


Figure 5.24 – Transmembrane potential at times  $T = 150, 200, 250$  ms for the small (top row), medium (middle row), and large (bottom row) necrotic regions for the simulations using the monodomain equation.

the cellular level have been proposed, e.g., in [Shaw and Rudy, 1997]. For our purposes, we proceed as follows: we first define a subset of the reference domain  $\Omega_{0,isc}^s \subset \Omega_0^s$  representing the region affected by the necrosis. Then, we define the subset of DoFs, say  $\Upsilon \subset (1, \dots, N_{s,r}^{\text{dof}})$ , such that  $\mathbf{X}_i \in \Omega_{0,isc}^s$  if  $i \in \Upsilon$  and we set  $\mathbf{I}_{w,i}^{\text{ion}} = \mathbf{I}_{v,i}^{\text{ion}} = \tilde{\mathbf{I}}_i^{\text{ion}} = 0$  for every  $i \in \Upsilon$  in Eq. (2.21) (or in Eq. (2.23)), and  $\Phi_{\gamma,i} = \tilde{\Phi}_i = 0$  in Eq. (2.26).

We analytically define the necrotic region as

$$\Omega_{0,isc}^s = \left\{ \mathbf{X} = (x, y, z) : (x - x_0)^4 + (y - y_0)^4 + (z - z_0)^4 < R^4 \right\},$$

and  $R > 0$  determines the extension of the necrotic region. We consider the values  $R = 5, 10, 15$  to model small, medium, and large regions, and we choose the point  $(x_0, y_0, z_0)$ , in a way such that it is located inside the myocardium and the points in which the external current is applied fall outside of  $\Omega_{0,isc}^s$ .



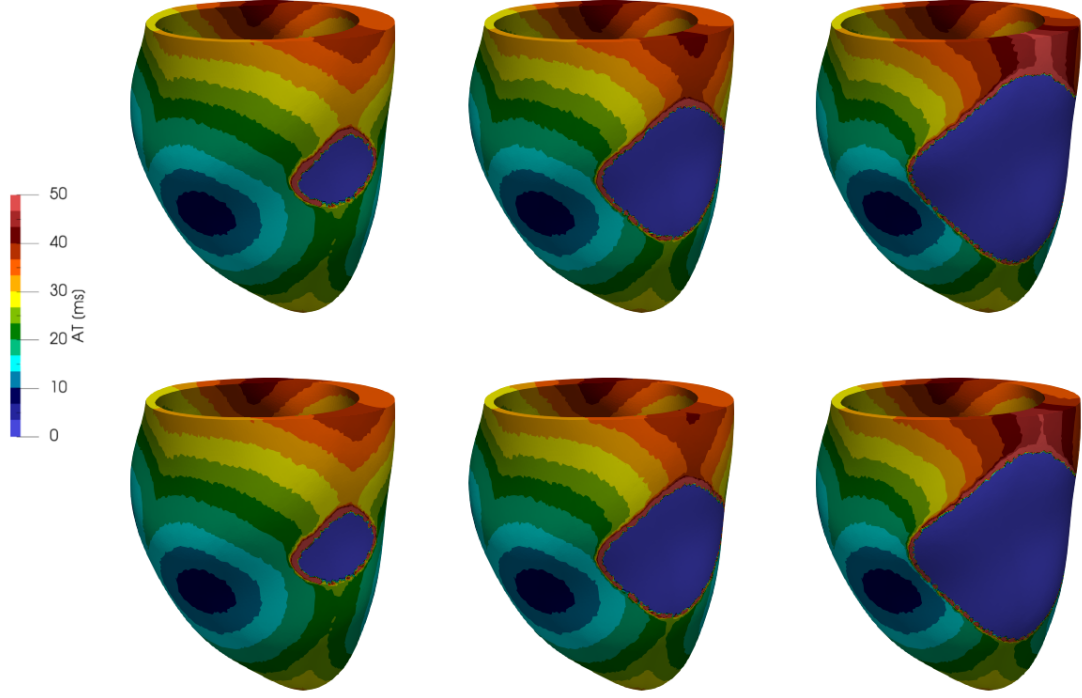


Figure 5.25 – AT for the simulations with the small (left), medium (center), and large (right) necrotic regions. The results obtained by using the bidomain equations (top row) and the monodomain equation (bottom row) are both reported.

For the simulations of this section, we use the same setting considered in Section 5.2 for the healthy case; we hence use in particular the  $(\mathcal{I}_{\text{SI}})-(\mathcal{E}_{\text{SI}})-(\mathcal{A}_{\text{SI}})-(\mathcal{M}_{\text{I}})$  strategy with  $\tau = 5 \times 10^{-5}$ , while we set  $N_{\text{sub}} = 5$ . We use both the monodomain equation, with conductivities

$$\sigma_l = 1.2042 \times 10^2 \text{ mm}^2\text{s}^{-1}, \quad \sigma_t = 0.1761 \times 10^2 \text{ mm}^2\text{s}^{-1},$$

and the bidomain equations with conductivities

$$\begin{aligned} \sigma_{E,l} &= 1.2042 \times 10^2 \text{ mm}^2\text{s}^{-1}, & \sigma_{E,t} &= 0.7044 \times 10^2 \text{ mm}^2\text{s}^{-1}, \\ \sigma_{I,l} &= 2.4084 \times 10^2 \text{ mm}^2\text{s}^{-1}, & \sigma_{I,t} &= 0.3522 \times 10^2 \text{ mm}^2\text{s}^{-1}, \end{aligned}$$

since we want to verify if important phenomena arise [Roth, 1997] when the intra/extracellular conduction anisotropy ratios are different, that is when

$$\frac{\sigma_{E,l}}{\sigma_{E,t}} \neq \frac{\sigma_{I,l}}{\sigma_{I,t}}.$$

However, as we will show, the difference between the transmembrane potentials obtained by using the two models is essentially negligible.

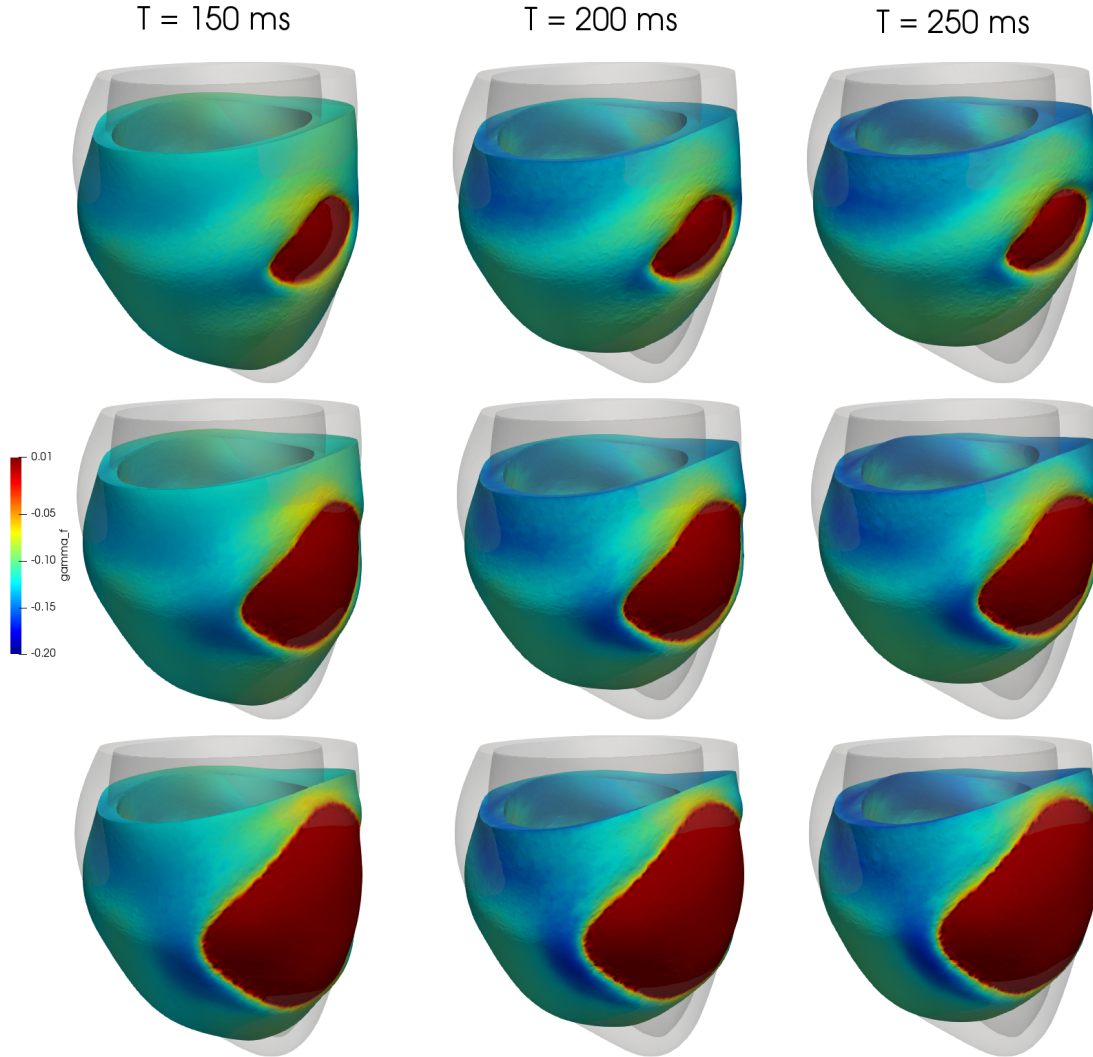


Figure 5.26 – Fibers shortening at times  $T = 150, 200, 250 \text{ ms}$  for the small (top row), medium (middle row), and large (bottom row) necrotic regions.

In Figure 5.24 we show the transmembrane potential at times  $T = 20, 40, 60 \text{ ms}$  in the three considered cases. The necrotic regions act as an obstacle in the transmission of the depolarization wave, and therein the transmembrane potential remains at its resting value of  $85 \text{ mV}$  for the full heartbeat. More detailed information on the electrical activation of the LV can be gathered from Figure 5.25, where the AT for the three cases is reported for both the monodomain and the bidomain. We observe that the size of the necrosis significantly influences the conduction velocities also in the regions close to it. Specifically, the conduction velocity is reduced in the points laying close to the necrosis, since the diffusion terms of Eq. (1.5) and Eq. (1.7) imply a dependence on the potential value inside the necrosis. Moreover, we observe the solution obtained by using the monodomain or the bidomain equation is essentially the same in the two cases, and

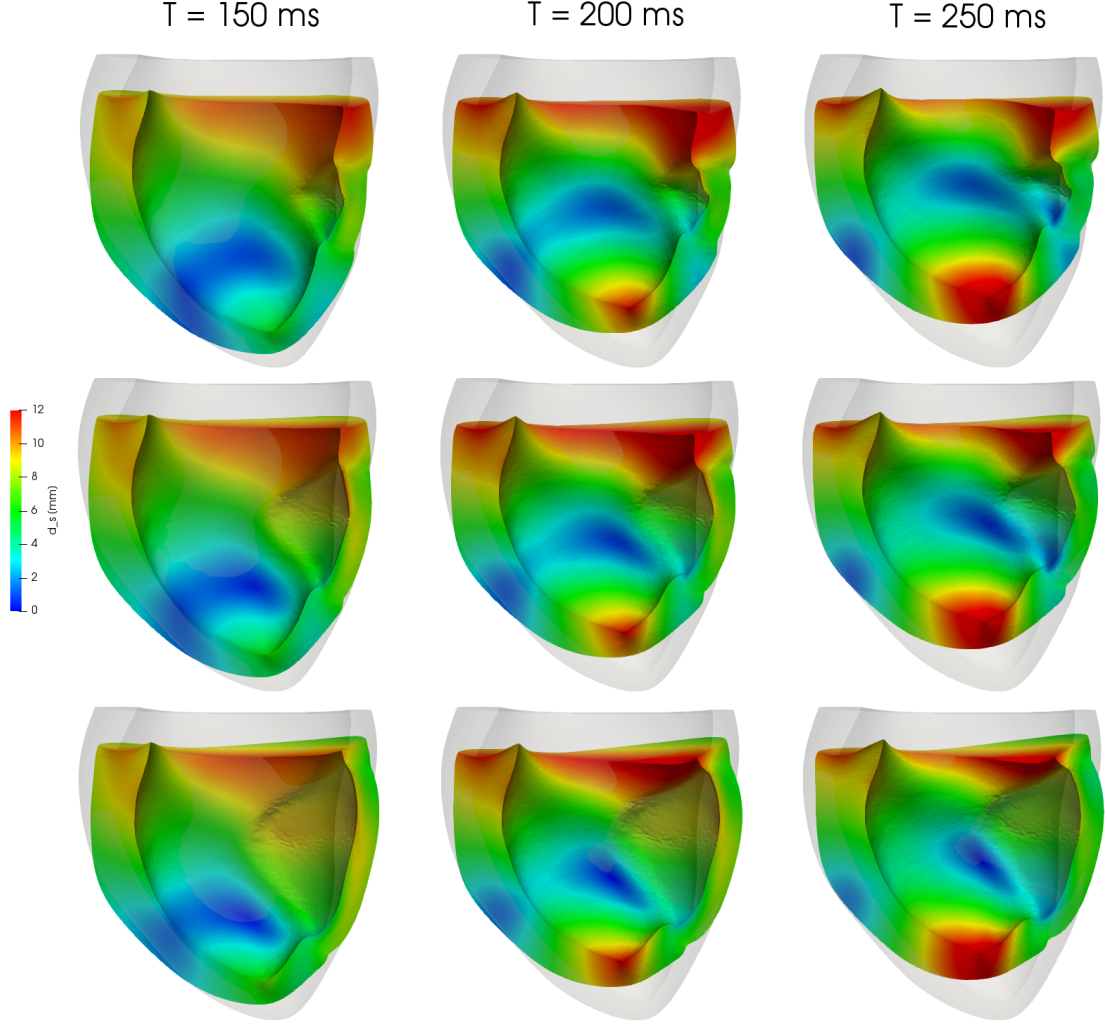


Figure 5.27 – Deformed subject-specific geometry and displacement field at times  $T = 150, 200, 250$  ms for the small (top row), medium (middle row), and large (bottom row) necrotic regions.

we speculate that this is due to the simple pacing strategy adopted which prevents the formation of reentry spiral waves [Bueno-Orovio et al., 2008, Roth, 1997].

In Figures 5.26, 5.27, and 5.28 we show the fibers shortening, the displacement, and the stress component  $\sigma_{ff}$ , respectively, at three times around the instant at which the maximum contraction is attained ( $T = 200$  ms). Coherently with the approach that we used to model the necrosis as a completely passive tissue, the fibers do not shorten in the affected region since therein  $\gamma_f = 0$ . Indeed, contrarily to the healthy tissue, in Figure 5.27 the necrosis does not thicken throughout the heartbeat and, since the internal pressure is not balanced by the contraction, the myocardium is inflated. The stress along the fibers direction  $\sigma_{ff}$  reported in Figure 5.28, compared at time  $T = 200$  ms with that

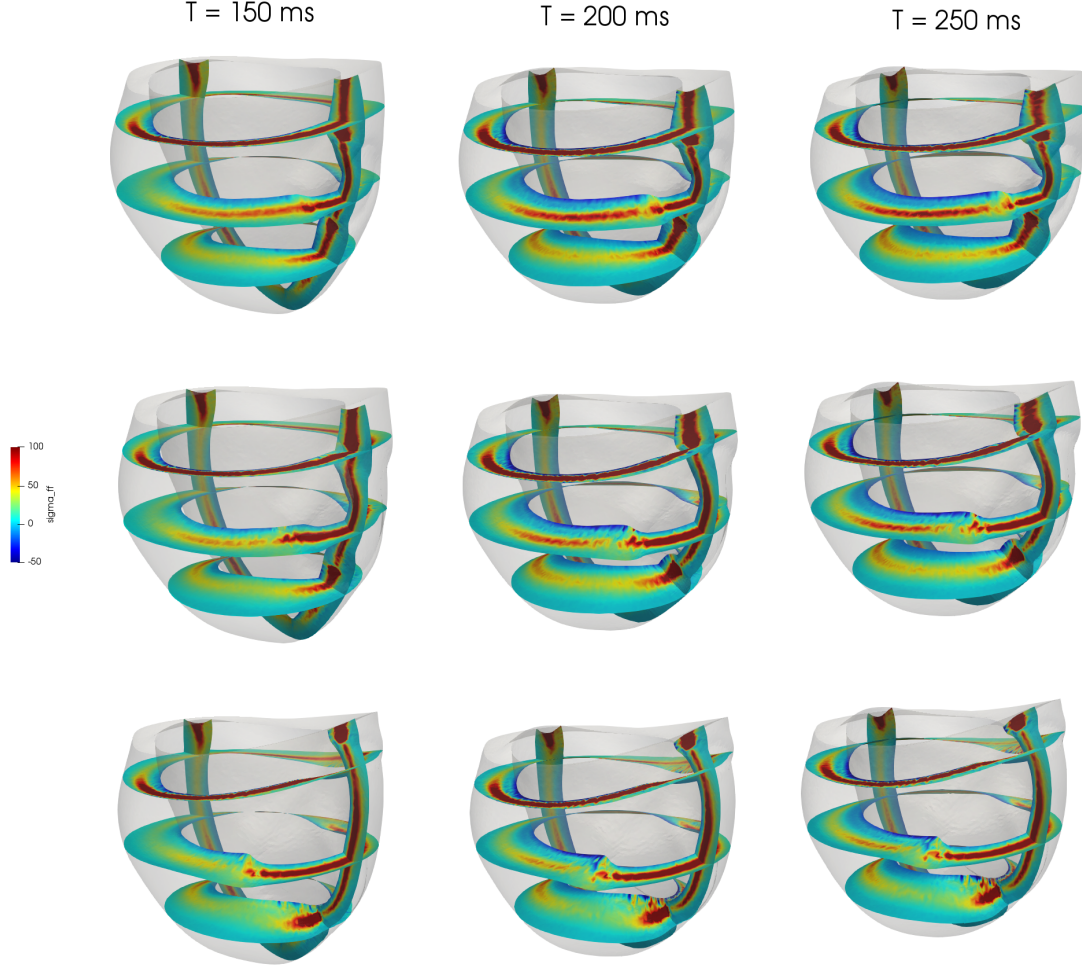


Figure 5.28 – Stress component  $\sigma_{ff}$  at times  $T = 150, 200, 250 \text{ ms}$  for the small (top row), medium (middle row), and large (bottom row) necrotic regions.

of Figure 5.22, is not significantly different with respect to the healthy case. Nonetheless, the distribution of  $\sigma_{ff}$  is less regular in the pathologic case.

In Figure 5.29 we then report the LV internal volume, the endocardial pressure, and the pV loops corresponding to the healthy and to the three pathological cases. We observe that the End Systolic Volume (ESV), i.e. the value of  $V^{endo}$  at the end of the systole, which is also the minimal value  $V^{endo}$ , increases as we increase the size of the necrotic region. This result is qualitatively in good agreement with experimental data [Pfeffer and Braunwald, 1990]: this behavior is due to the fact that the muscle in the necrotic region does not contract (or, in less severe cases, its contraction is reduced), a smaller overall force is applied when the LV pushes the blood during systole. Indeed, the maximum pressure decreases as the necrotic region size increases. We highlight that the ESV is considered a major determinant of the patient's prognosis after infarction [White et al.,

### 5.3. Application to a pathological scenario: LV with ischemic necrosis

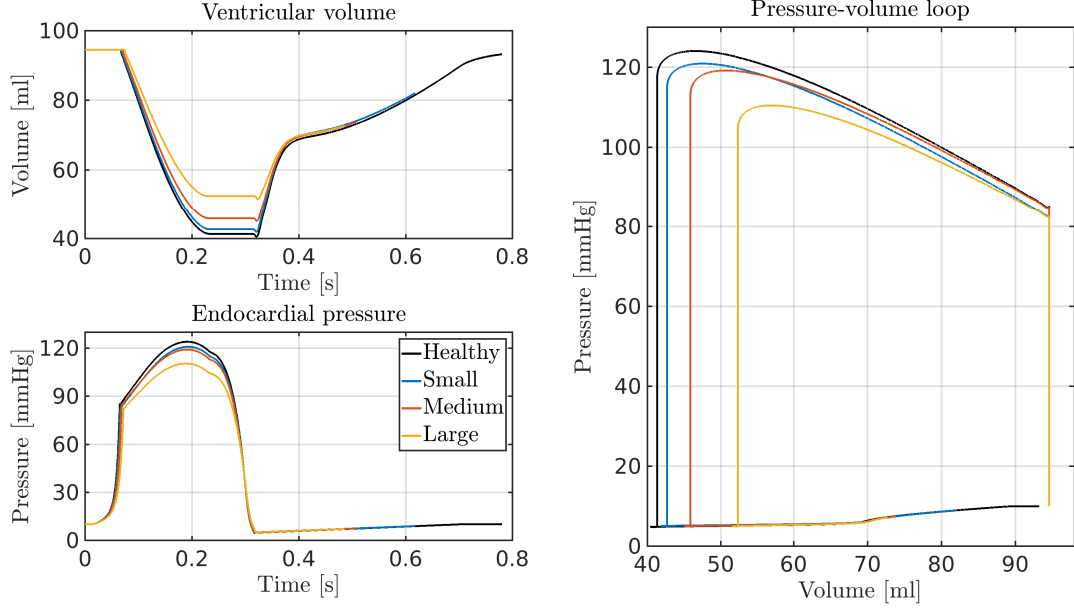


Figure 5.29 – LV internal volumes (top left) and endocardial pressures (bottom left) versus time, with pV loops (right) for the

1987]. In the clinical practice, the ESV and the End Diastolic Volume (EDV) values, are typically used to calculate the Stroke Volume (SV) and the (Left Ventricular) Ejection Fraction (LVEF) according to the following formulas:

$$SV = EDV - ESV, \quad LVEF = \frac{SV}{EDV}. \quad (5.1)$$

It has been established that the LVEF is reduced when large portion of the myocardial tissue are damaged [Burns et al., 2002]: the latter is indeed one of the most used measure of the pumping efficiency of the LV.

Another commonly considered quantity is the End Systolic Pressure-Volume Relationship (ESPVR), representing the so called *inotropic* state, which is a measure of the contractility of the LV. It is defined as the ratio between the ventricular pressure and volume at the end of the systole, and is easily evaluated as the slope of the tangent in the upper left corner of the pV loop. In Figure 5.30 we report the pV loops together with the value of ESPVR: the latter is indeed significantly lower in the pathological cases thus signaling a reduced contractility. In Table 5.6 we summarize the value of the introduced quantities for all the considered cases.

In this work we do not take into account the previously mentioned remodeling process; the latter takes place over a relatively long time (weeks/months) by permanently modifying the myocardium morphology, and ultimately produces an enlargement of the LV with hence larger EDV values [Fletcher et al., 1981, Pfeffer and Braunwald, 1990]. This has



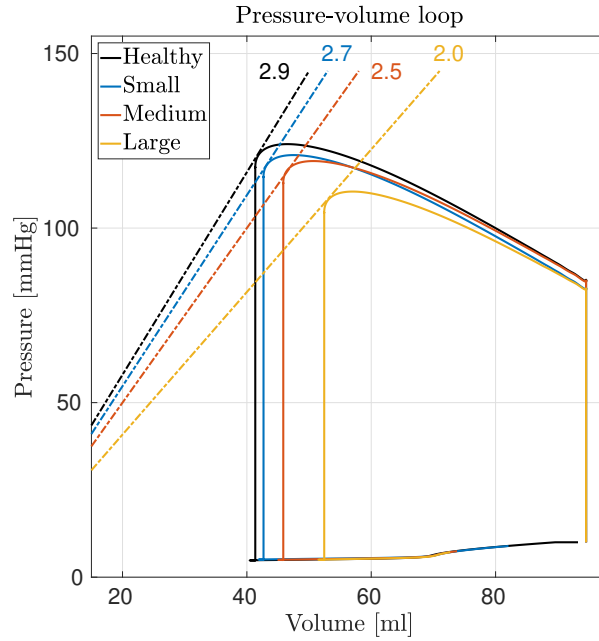


Figure 5.30 – The pV loops and the ESPVR for the healthy and the three pathological cases.

|                 | Healthy | Small | Medium | Large |
|-----------------|---------|-------|--------|-------|
| EDV [ml]        | 95      | 95    | 95     | 95    |
| ESV [ml]        | 41      | 43    | 46     | 52    |
| SV [ml]         | 54      | 52    | 49     | 43    |
| LVEF            | 57%     | 55%   | 52%    | 45%   |
| ESPVR [mmHg/ml] | 2.9     | 2.7   | 2.5    | 2.0   |

Table 5.6 – EDV, ESV, SV, LVEF, and ESPVR for the healthy and the pathological cases.

the effect of restoring physiological values for the SV however the LVEF, as is trivial from its definition Eq. (5.1), remains low thus indicating a permanent lowered effectiveness of the LV pumping of the blood into the systemic circulation.

# Electrofluidmechanics **Part III**





## 6 Algorithms for the EFM of the LV

In this chapter, we briefly extend the four strategies described in Chapter 4 to the electrofluidmechanics case. For the monolithic strategy this amounts to solve an even larger system with respect to  $(\mathcal{I}_1\mathcal{E}_1\mathcal{A}_1\mathcal{M}_1)$ , which in this case we coherently denote as  $(\mathcal{I}_1\mathcal{E}_1\mathcal{A}_1\mathcal{M}_1\mathcal{G}_1\mathcal{F}_1)$  – where we recall that  $\mathcal{G}$  and  $\mathcal{F}$  refer to the models for the deformation of the fluid geometry, and to the Navier-Stokes equations, respectively. Indeed, we use here the ALE framework ([Donea et al., 1982, Forti, 2016, Hu et al., 2001]) for which modeling the fluid domain displacement is necessary. Conveniently, since no direct interaction between the fluid and the electrophysiology is taken into account, the coupling conditions between the FSI and the electrophysiology subproblems are unchanged with respect to the electromechanics problem.

### 6.1 The FSI problem

Extensive work has been carried out in the past on the development of algorithms for the solution of time dependent FSI problems; we cite [Badia et al., 2008, Bazilevs et al., 2008, Crosetto et al., 2011b, Deparis et al., 2006, Gerbeau and Vidrascu, 2003, Nobile et al., 2013, Quaini, 2009] just to name a few. Generally speaking, two main approaches can be found in literature for its solution, namely, the segregated and the monolithic ones. In the first case, the segregated problem is solved by exploiting Steklov-Poincaré operators [Deparis et al., 2006], inexact factorizations [Quaini, 2009], or Newton-like methods [Gerbeau and Vidrascu, 2003]. On the other hand, the monolithic approach has been widely studied e.g. in [Forti, 2016, Gee et al., 2011, Küttler et al., 2010, Tezduyar et al., 2006].

According to [Tricerri et al., 2015], the monolithic approach leads to a more accurate and robust time discretization of the FSI problem, compared to the segregated one. Moreover, as already discussed in Chapter 2, the monolithic approach allows to avoid the added mass effect [Bathe et al., 1999, Causin et al., 2005, Le Tallec and Mouro,

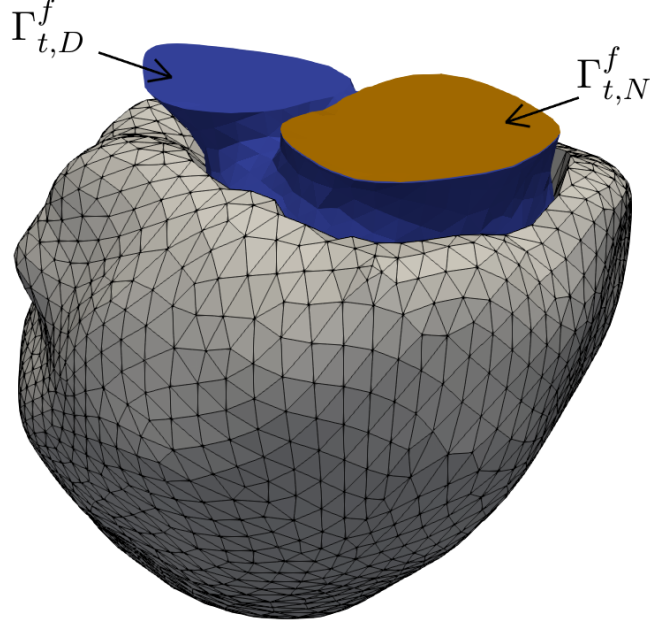


Figure 6.1 – The boundaries  $\Gamma_{t,D}^f$  and  $\Gamma_{t,N}^f$  on which we impose the essential (“Dirichlet”) condition for the continuity of the domain and the fluid velocities, and the natural (“Neumann”) condition.

2001, Nobile, 2001, Van Brummelen, 2009], which is a peculiarity in biomechanics where the similar density of the fluid and the structure, combined with incompressible flows, leads to increased numerical effort. This observations motivate our choice of a monolithic approach to solve the FSI, with a fully implicit time scheme, necessary to ensure the converge of the mechanics part of the problem.

The solution of the monolithic FSI problem is a computationally expensive task. The choice of an effective preconditioner is hence critical in order for the linear solver to reach convergence in a reasonable time. We opt for the recently proposed FaCSI preconditioner [Deparis et al., 2016a, Deparis et al., 2016b, Forti et al., 2016], which has been shown to provide good performances when used in haemodynamics applications, and is scalable up to thousands of cores.

We remark that, with respect to the FSI problems considered in [Forti, 2016] (on which our formulation is based), we strongly impose an additional coupling between the fluid domain velocity and the fluid velocity on  $\Gamma_{t,D}^f$ , depicted in Figure 6.1. This is motivated by the need of imposing the no-slip condition for the fluid on  $\Gamma_{t,D}^f$ , representing the blood wall in the region between the myocardium base and the aortic and mitral valves, and the surface corresponding to the mitral valve which we model as always closed, since the systolic phase only is simulated. Hence, while on the interface  $\Gamma^{endo}$  we set  $\mathbf{u} = \mathbf{d}_s$ , on

$\Gamma_{t,D}^f$  we must set  $\mathbf{u} = \dot{\mathbf{d}}_f$ . At the discrete level, this is obtained by imposing:

$$-\frac{\vartheta^I}{\Delta t} \mathbf{\Pi}_{\Gamma_{t,D}^f}^f \bar{\mathbf{d}}_f^{n+1} + \mathbf{\Pi}_{\Gamma_{t,D}^f}^f \bar{\mathbf{u}}^{n+1} = -\frac{1}{\Delta t} \mathbf{\Pi}_{\Gamma_{t,D}^f}^f \bar{\mathbf{d}}_f^I, \quad (6.1)$$

for the DoFs belonging to  $\Gamma_{t,D}^f$  by modifying the fluid momentum equation, as will be cleared out in Section 6.2.

## 6.2 Fully monolithic strategy $(\mathcal{I}_I \mathcal{E}_I \mathcal{A}_I \mathcal{M}_I \mathcal{G}_I \mathcal{F}_I)$

Recalling that  $N_{s,r}^{\text{dof}}$ ,  $N_{f,r}^{\text{dof}}$ , and  $N_{\Gamma,r}^{\text{dof}}$  represent the size of the (scalar) finite element spaces  $\mathcal{X}_{s,h}^r$ ,  $\mathcal{X}_{f,h}^r$ ,  $\mathcal{X}_{\Gamma,h}^r$  – equivalently, the size of a scalar core problem defined in  $\Omega_0^s$ ,  $\Omega_0^f$ ,  $\Gamma_0^{\text{endo}}$  – the fully implicit monolithic  $(\mathcal{I}_I \mathcal{E}_I \mathcal{A}_I \mathcal{M}_I \mathcal{G}_I \mathcal{F}_I)$  accounts to solve, for  $n = \sigma, \dots, N_T - 1$ , the following system of size  $8 \times N_{s,r}^{\text{dof}} + 7 \times N_{f,r}^{\text{dof}} + 3 \times N_{\Gamma,r}^{\text{dof}}$ :

$$(\mathcal{I}_I \mathcal{E}_I \mathcal{A}_I \mathcal{M}_I \mathcal{G}_I \mathcal{F}_I) : \left\{ \begin{array}{l} \left( \frac{\vartheta_0^I}{\Delta t} + \mathbb{U}(\bar{\mathbf{v}}^{n+1}) \right) \bar{\mathbf{w}}^{n+1} - \mathbf{Q}(\bar{\mathbf{v}}^{n+1}) = \frac{1}{\Delta t} \bar{\mathbf{w}}^I, \\ \left( \frac{\vartheta_0^I}{\Delta t} \mathbb{M} + \mathbb{K}(\bar{\mathbf{d}}_s^{n+1}) \right) \bar{\mathbf{v}}^{n+1} + \mathbf{I}^{ion}(\bar{\mathbf{v}}^{n+1}, \bar{\mathbf{w}}^{n+1}) = \frac{1}{\Delta t} \mathbb{M} \bar{\mathbf{v}}^I + \mathbb{M} \mathbf{I}^{app}(t^{n+1}), \\ \left( \frac{\vartheta_0^I}{\Delta t} \mathbb{M} + \varepsilon \mathbb{K}(\bar{\mathbf{w}}^{n+1}) \right) \bar{\gamma}_f^{n+1} + \mathbf{\Phi}(\bar{\mathbf{w}}^{n+1}, \bar{\gamma}_f^{n+1}, \bar{\mathbf{d}}_s^{n+1}) = \frac{1}{\Delta t} \mathbb{M} \bar{\gamma}_f^I, \\ \left( \rho_s \frac{\vartheta_0^{\text{II}}}{(\Delta t)^2} \mathbb{M}_3 + \frac{\vartheta_0^I}{\Delta t} \mathbb{F} + \mathbb{G} \right) \bar{\mathbf{d}}_s^{n+1} + \mathbf{S}(\bar{\mathbf{d}}_s^{n+1}, \bar{\gamma}_f^{n+1}) - \mathbf{\Pi}_{\Gamma}^s \bar{\lambda}^{n+1} \\ = \rho_s \frac{1}{(\Delta t)^2} \mathbb{M}_3 \bar{\mathbf{d}}_s^{\text{II}} + \frac{1}{\Delta t} \mathbb{F} \bar{\mathbf{d}}_s^I - \mathbf{S}_0, \\ \tilde{\mathbb{K}}_G \bar{\mathbf{d}}_f^{n+1} - \mathbf{\Pi}_f^s \bar{\mathbf{d}}_s^{n+1} = \mathbf{0}, \\ \left( \rho_f \frac{\vartheta^I}{\Delta t} \mathbb{M}_3^f + \mu_f \mathbb{A} + \rho_f \mathbf{C}(\bar{\mathbf{u}}^{n+1} - \dot{\bar{\mathbf{d}}}_f^{n+1}) \right) \bar{\mathbf{u}}^{n+1} + \mathbb{B}^T \bar{\mathbf{p}}^{n+1} \\ + \mathbf{\Pi}_{\Gamma}^{fT} \bar{\lambda}^{n+1} + \mathbf{S}_M^{SUPG}(\bar{\mathbf{u}}^{n+1}, \bar{\mathbf{p}}^{n+1}) = \rho_f \frac{1}{\Delta t} \mathbb{M}_3^f \bar{\mathbf{u}}^I, \\ \mathbb{B} \bar{\mathbf{u}}^{n+1} + \mathbf{S}_C^{SUPG}(\bar{\mathbf{u}}^{n+1}, \bar{\mathbf{p}}^{n+1}) = \mathbf{0}, \\ -\frac{\vartheta^I}{\Delta t} \mathbf{\Pi}_{\Gamma}^f \bar{\mathbf{d}}_s^{n+1} + \mathbf{\Pi}_{\Gamma}^f \bar{\mathbf{u}}^{n+1} = -\frac{1}{\Delta t} \mathbf{\Pi}_{\Gamma}^f \bar{\mathbf{d}}_s^I. \end{array} \right.$$

The Jacobian  $\mathbb{J}_{EFM}$  corresponding to the tangent problem arising from the application of the Newton method to  $(\mathcal{I}_I \mathcal{E}_I \mathcal{A}_I \mathcal{M}_I \mathcal{G}_I \mathcal{F}_I)$  is reported in the next page with landscape orientation for the sake of readability.

In the definition of  $\mathbb{J}_{EFM}$  we stress the presence of the additional extradiagonal block  $-\frac{\vartheta^I}{\Delta t} \mathbf{\Pi}_{\Gamma_{t,D}^f}^f$ , arising from the imposition of Eq. (6.1) in the rows corresponding to the fluid momentum equation; it is understood that the other blocks on the same rows have to be

$$\mathbb{J}_{EFM} = \begin{bmatrix}
 \frac{\vartheta^I}{\Delta t} \mathbb{I} + \mathbb{U}(\bar{\mathbf{v}}) & \partial_u \mathbb{U}(\bar{\mathbf{v}}) - \partial_u \mathbf{Q}(\bar{\mathbf{v}}) & 0 & 0 & 0 & 0 & 0 \\
 \partial_{\mathbf{w}} \mathbf{I}^{ion}(\bar{\mathbf{v}}, \bar{\mathbf{w}}) & \frac{\vartheta^I}{\Delta t} \mathbb{M}^L + \mathbb{K}_M(\bar{\mathbf{d}}_s) & 0 & \partial_{\mathbf{d}_s} \mathbb{K}_M(\bar{\mathbf{d}}_s, \bar{\mathbf{v}}) & 0 & 0 & 0 \\
 \varepsilon \partial_{\mathbf{w}} \mathbb{K}_\gamma(\bar{\mathbf{w}}, \bar{\gamma}) & 0 & \frac{\vartheta^I}{\Delta t} \mathbb{M}^L + \varepsilon \mathbb{K}_\gamma(\bar{\mathbf{w}}) & \partial_{\mathbf{d}_s} \Phi(\bar{\mathbf{w}}, \bar{\gamma}, \bar{\mathbf{d}}_s) & 0 & 0 & 0 \\
 + \partial_{\mathbf{w}} \Phi(\bar{\mathbf{w}}, \bar{\gamma}, \bar{\mathbf{d}}_s) & & + \partial_\gamma \Phi(\bar{\mathbf{w}}, \bar{\gamma}, \bar{\mathbf{d}}_s) & & & & \\
 0 & 0 & \partial_\gamma \mathbf{S}(\bar{\mathbf{d}}_s, \bar{\gamma}) & \rho_s \frac{\vartheta^{II}}{\Delta t^2} \mathbb{M}_3^s + \frac{\vartheta^I}{\Delta t} \mathbb{F} & 0 & 0 & -\Pi_{\Gamma}^{sT} \\
 & & & + \mathbb{G} + \partial_{\mathbf{d}_s} \mathbf{S}(\bar{\mathbf{d}}_s, \bar{\gamma}) & & & \\
 0 & 0 & 0 & -\Pi_f^s & \tilde{\mathbb{K}}_G & 0 & 0 \\
 0 & 0 & 0 & & & & \\
 0 & 0 & 0 & & & \rho_f \frac{\vartheta^I}{\Delta t} \mathbb{M}_3^f + \mu_f \mathbb{A} & \Pi_{\Gamma}^{fT} \\
 & & & & & + \rho_f \partial_u \mathbb{C}(\bar{\mathbf{u}}, \dot{\bar{\mathbf{d}}}_f) & + \partial_p \mathbf{S}_M^{SUPG}(\bar{\mathbf{u}}, \bar{\mathbf{p}}) \\
 & & & & & + \partial_u \mathbf{S}_M^{SUPG}(\bar{\mathbf{u}}, \bar{\mathbf{p}}) & \\
 0 & 0 & 0 & & & \mathbb{B} & \partial_p \mathbf{S}_C^{SUPG}(\bar{\mathbf{u}}, \bar{\mathbf{p}}) & 0 \\
 & & & & & + \partial_u \mathbf{S}_C^{SUPG}(\bar{\mathbf{u}}, \bar{\mathbf{p}}) & \\
 0 & 0 & 0 & -\frac{\vartheta^I}{\Delta t} \Pi_{\Gamma}^s & 0 & \Pi_{\Gamma}^f & 0 & 0
 \end{bmatrix}$$

modified accordingly to Eq. (6.1). The block pattern of  $\mathbb{J}_{EFM}$  is then:

$$\mathbb{J}_{EFM} = \begin{bmatrix} \boxed{J_{11} & J_{12}} & 0 & 0 & 0 & 0 & 0 & 0 \\ J_{21} & J_{22} & 0 & J_{24} & 0 & 0 & 0 & 0 \\ J_{31} & 0 & \boxed{J_{33}} & J_{34} & 0 & 0 & 0 & 0 \\ 0 & 0 & J_{43} & \boxed{J_{44}} & 0 & 0 & 0 & J_{48} \\ 0 & 0 & 0 & J_{54} & \boxed{J_{55}} & 0 & 0 & 0 \\ 0 & 0 & 0 & 0 & J_{65} & \boxed{J_{66} & J_{67} & J_{68}} \\ 0 & 0 & 0 & 0 & 0 & J_{76} & J_{77} & 0 \\ 0 & 0 & 0 & J_{84} & 0 & J_{86} & 0 & 0 \end{bmatrix}, \quad (6.2)$$

with boxed blocks corresponding to the electrophysiology ( $\mathcal{IE}$ ), the mechanical activation ( $\mathcal{A}$ ), the mechanics ( $\mathcal{M}$ ), the fluid geometry ( $\mathcal{G}$ ), and the fluid dynamics ( $\mathcal{F}$ ), respectively, the latter with additional constraints given by the Lagrange multipliers.

### 6.2.1 Preconditioning the monolithic problem

The same preconditioning strategy described in Section 4.1.1 is now extended to the monolithic preconditioner  $\mathcal{P}_{EFM}$  for  $(\mathcal{I}_I \mathcal{E}_I \mathcal{A}_I \mathcal{M}_I \mathcal{G}_I \mathcal{F}_I)$ . To this aim, we first define the block pattern of  $\mathcal{P}_{EFM}$ , which is again obtained by discarding the upper triangular extradiagonal blocks of  $\mathbb{J}_{EFM}$  as follows:

$$\mathcal{P}_{EFM} = \begin{bmatrix} J_{11} & 0 & 0 & 0 & 0 & 0 & 0 & 0 \\ J_{21} & J_{22} & 0 & 0 & 0 & 0 & 0 & 0 \\ J_{31} & 0 & J_{33} & 0 & 0 & 0 & 0 & 0 \\ 0 & 0 & J_{43} & J_{44} & 0 & 0 & 0 & 0 \\ 0 & 0 & 0 & J_{54} & J_{55} & 0 & 0 & 0 \\ 0 & 0 & 0 & 0 & J_{65} & J_{66} & J_{67} & J_{68} \\ 0 & 0 & 0 & 0 & 0 & J_{76} & J_{77} & 0 \\ 0 & 0 & 0 & J_{84} & 0 & J_{86} & 0 & 0 \end{bmatrix},$$

where the submatrix

$$\tilde{\mathcal{P}}_{fl} = \begin{bmatrix} J_{66} & J_{67} & J_{68} \\ J_{76} & J_{77} & 0 \\ J_{86} & 0 & 0 \end{bmatrix},$$

corresponding to the stabilized Navier-Stokes and the Lagrange multipliers equations, is here treated as an individual block. As was done in Section 4.1.1,  $\mathcal{P}_{EFM}$  is then factorized as:

$$\mathcal{P}_{EFM} = \mathcal{P}_{ion} \mathcal{P}_{pot} \mathcal{P}_{act} \mathcal{P}_{mec} \mathcal{P}_{geo} \mathcal{P}_{fl},$$

where:

$$\begin{aligned}
 \mathcal{P}_{ion} &= \begin{bmatrix} J_{11} & 0 & 0 & 0 & 0 & 0 & 0 & 0 \\ 0 & I & 0 & 0 & 0 & 0 & 0 & 0 \\ 0 & 0 & I & 0 & 0 & 0 & 0 & 0 \\ 0 & 0 & 0 & I & 0 & 0 & 0 & 0 \\ 0 & 0 & 0 & 0 & I & 0 & 0 & 0 \\ 0 & 0 & 0 & 0 & 0 & I & 0 & 0 \\ 0 & 0 & 0 & 0 & 0 & 0 & I & 0 \\ 0 & 0 & 0 & 0 & 0 & 0 & 0 & I \end{bmatrix}, \quad \mathcal{P}_{pot} = \begin{bmatrix} I & 0 & 0 & 0 & 0 & 0 & 0 & 0 \\ J_{21} & J_{22} & 0 & 0 & 0 & 0 & 0 & 0 \\ 0 & 0 & I & 0 & 0 & 0 & 0 & 0 \\ 0 & 0 & 0 & I & 0 & 0 & 0 & 0 \\ 0 & 0 & 0 & 0 & I & 0 & 0 & 0 \\ 0 & 0 & 0 & 0 & 0 & I & 0 & 0 \\ 0 & 0 & 0 & 0 & 0 & 0 & I & 0 \\ 0 & 0 & 0 & 0 & 0 & 0 & 0 & I \end{bmatrix}, \\
 \mathcal{P}_{act} &= \begin{bmatrix} I & 0 & 0 & 0 & 0 & 0 & 0 & 0 \\ 0 & I & 0 & 0 & 0 & 0 & 0 & 0 \\ J_{31} & 0 & J_{33} & 0 & 0 & 0 & 0 & 0 \\ 0 & 0 & 0 & I & 0 & 0 & 0 & 0 \\ 0 & 0 & 0 & 0 & I & 0 & 0 & 0 \\ 0 & 0 & 0 & 0 & 0 & I & 0 & 0 \\ 0 & 0 & 0 & 0 & 0 & 0 & I & 0 \\ 0 & 0 & 0 & 0 & 0 & 0 & 0 & I \end{bmatrix}, \quad \mathcal{P}_{mec} = \begin{bmatrix} I & 0 & 0 & 0 & 0 & 0 & 0 & 0 \\ 0 & I & 0 & 0 & 0 & 0 & 0 & 0 \\ 0 & 0 & I & 0 & 0 & 0 & 0 & 0 \\ 0 & 0 & J_{43} & J_{44} & 0 & 0 & 0 & 0 \\ 0 & 0 & 0 & 0 & I & 0 & 0 & 0 \\ 0 & 0 & 0 & 0 & 0 & I & 0 & 0 \\ 0 & 0 & 0 & 0 & 0 & 0 & I & 0 \\ 0 & 0 & 0 & 0 & 0 & 0 & 0 & I \end{bmatrix}, \\
 \mathcal{P}_{geo} &= \begin{bmatrix} I & 0 & 0 & 0 & 0 & 0 & 0 & 0 \\ 0 & I & 0 & 0 & 0 & 0 & 0 & 0 \\ 0 & 0 & I & 0 & 0 & 0 & 0 & 0 \\ 0 & 0 & 0 & I & 0 & 0 & 0 & 0 \\ 0 & 0 & 0 & J_{54} & J_{55} & 0 & 0 & 0 \\ 0 & 0 & 0 & 0 & 0 & I & 0 & 0 \\ 0 & 0 & 0 & 0 & 0 & 0 & I & 0 \\ 0 & 0 & 0 & 0 & 0 & 0 & 0 & I \end{bmatrix}, \quad \mathcal{P}_{fl} = \begin{bmatrix} I & 0 & 0 & 0 & 0 & 0 & 0 & 0 \\ 0 & I & 0 & 0 & 0 & 0 & 0 & 0 \\ 0 & 0 & I & 0 & 0 & 0 & 0 & 0 \\ 0 & 0 & 0 & I & 0 & 0 & 0 & 0 \\ 0 & 0 & 0 & 0 & I & 0 & 0 & 0 \\ 0 & 0 & 0 & 0 & J_{56} & J_{66} & J_{67} & J_{68} \\ 0 & 0 & 0 & 0 & 0 & J_{76} & J_{77} & 0 \\ 0 & 0 & 0 & J_{84} & 0 & J_{86} & 0 & 0 \end{bmatrix}.
 \end{aligned}$$

Following [Forti, 2016],  $\mathcal{P}_{fl}$  can be further factorized in order to isolate the block  $\tilde{\mathcal{P}}_{fl}$ . The latter is then reduced by operating a static condensation on the interface fluid variables at the level of the fluid preconditioner (for another approach consisting in the removal of the interface variables from the unknowns set of the FSI problem see [Gee et al., 2011, Mayr et al., 2015]). Regarding the preconditioner for the reduced fluid block, we use the SIMPLE preconditioner [Elman et al., 2008, Patankar and Spalding, 1972]. The FSI part of the  $\mathcal{P}_{EFM}$  preconditioner coincides with the FaCSI preconditioner: we refer the reader to [Deparis et al., 2016b, Forti, 2016] for more details on its definition.

### 6.3 Segregated strategies

As already pointed out, the extension of the segregated strategies introduced in Section 4.2 to the electrofluidmechanics case is straightforward. Indeed, it only accounts to replace

the last step (i.e. the solution of the  $(\mathcal{M}_I)$  mechanics problem) with the solution of the following FSI problem:

$$(\mathcal{M}_I \mathcal{G}_I \mathcal{F}_I) : \begin{cases} \left( \rho_s \frac{\vartheta_0^{\text{II}}}{(\Delta t)^2} \mathbb{M}_3 + \frac{\vartheta_0^{\text{I}}}{\Delta t} \mathbb{F} + \mathbb{G} \right) \bar{\mathbf{d}}_s^{n+1} + \mathbf{S}(\bar{\mathbf{d}}_s^{n+1}, \bar{\gamma}_f^*) - \boldsymbol{\Pi}_\Gamma^s \bar{\boldsymbol{\lambda}}^{n+1} \\ \quad = \rho_s \frac{1}{(\Delta t)^2} \mathbb{M}_3 \bar{\mathbf{d}}_s^{\text{II}} + \frac{1}{\Delta t} \mathbb{F} \bar{\mathbf{d}}_s^{\text{I}} - \mathbf{S}_0, \\ \tilde{\mathbb{K}}_G \bar{\mathbf{d}}_f^{n+1} - \boldsymbol{\Pi}_f^s \bar{\mathbf{d}}_s^{n+1} = \mathbf{0}, \\ \left( \rho_f \frac{\vartheta^{\text{I}}}{\Delta t} \mathbb{M}_3^f + \mu_f \mathbb{A} + \rho_f \mathbb{C}(\bar{\mathbf{u}}^{n+1} - \dot{\bar{\mathbf{d}}}_f^{n+1}) \right) \bar{\mathbf{u}}^{n+1} + \mathbb{B}^T \bar{\mathbf{p}}^{n+1} \\ \quad + \boldsymbol{\Pi}_\Gamma^f \bar{\boldsymbol{\lambda}}^{n+1} + \mathbf{S}_M^{\text{SUPG}}(\bar{\mathbf{u}}^{n+1}, \bar{\mathbf{p}}^{n+1}) = \rho_f \frac{1}{\Delta t} \mathbb{M}_3^f \bar{\mathbf{u}}^{\text{I}}, \\ \mathbb{B} \bar{\mathbf{u}}^{n+1} + \mathbf{S}_C^{\text{SUPG}}(\bar{\mathbf{u}}^{n+1}, \bar{\mathbf{p}}^{n+1}) = \mathbf{0}, \\ - \frac{\vartheta^{\text{I}}}{\Delta t} \boldsymbol{\Pi}_\Gamma^s \bar{\mathbf{d}}_s^{n+1} + \boldsymbol{\Pi}_\Gamma^f \bar{\mathbf{u}}^{n+1} = - \frac{1}{\Delta t} \boldsymbol{\Pi}_\Gamma^s \bar{\mathbf{d}}_s^{\text{I}}. \end{cases}$$

We will refer to the strategies thus obtained as  $(\mathcal{I}_I \mathcal{E}_I \mathcal{A}_I) - (\mathcal{M}_I \mathcal{G}_I \mathcal{F}_I)$ ,  $(\mathcal{I}_{\text{SI}} \mathcal{E}_{\text{SI}} \mathcal{A}_{\text{SI}}) - (\mathcal{M}_I \mathcal{G}_I \mathcal{F}_I)$ , and  $(\mathcal{I}_{\text{SI}}) - (\mathcal{E}_{\text{SI}}) - (\mathcal{A}_{\text{SI}}) - (\mathcal{M}_I \mathcal{G}_I \mathcal{F}_I)$ .

We remark that solving the coupled problem  $(\mathcal{M}_I \mathcal{G}_I \mathcal{F}_I)$  is significantly more “expensive” than solving the  $(\mathcal{M}_I)$  problem only. In these respect, we expect an even more substantial speedup when using the staggered strategies compared to the monolithic  $(\mathcal{I}_I \mathcal{E}_I \mathcal{A}_I \mathcal{M}_I \mathcal{G}_I \mathcal{F}_I)$ , since they ultimately allow to reduce the number of times that the FSI problem is solved. On the other hand, since the bottleneck of the electrofluidmechanics simulation is represented by the solution of  $(\mathcal{M}_I \mathcal{G}_I \mathcal{F}_I)$ , the further speedup given by  $(\mathcal{I}_{\text{SI}} \mathcal{E}_{\text{SI}} \mathcal{A}_{\text{SI}}) - (\mathcal{M}_I \mathcal{G}_I \mathcal{F}_I)$  and  $(\mathcal{I}_{\text{SI}}) - (\mathcal{E}_{\text{SI}}) - (\mathcal{A}_{\text{SI}}) - (\mathcal{M}_I \mathcal{G}_I \mathcal{F}_I)$  with respect to  $(\mathcal{I}_I \mathcal{E}_I \mathcal{A}_I \mathcal{M}_I \mathcal{G}_I \mathcal{F}_I)$  is limited, compared to the electromechanics case.





## 7 Numerical simulations

In this chapter we use the numerical strategies introduced in Chapter 6 to simulate the electrofluidmechanics of the human LV. As already mentioned, we simulate the systolic phase only due to the complexity of simulating the full heartbeat. Hence, we assume the mitral valve to be always closed and we impose an essential no-slip condition correspondingly. Regarding the aortic valve, which is located in the sinus of Valsalva outside the outflow of our geometry (the boundary  $\Gamma_{t,N}^f$  in Figure 6.1), we use a natural resistance (or defective) condition [Bazilevs et al., 2008, Bazilevs et al., 2009] to obtain meaningful blood flows and to account for the downstream circulation in the aorta [Tagliabue et al., 2017]. In order to impose the resistance condition, we first recall the definition of the flowrate through the  $\Gamma_{t,N}^f$  surface:

$$Q^{ao} = \int_{\Gamma_{t,N}^f} \mathbf{u} \cdot \mathbf{n}_f \, d\Gamma_{t,N}^f. \quad (7.1)$$

By recalling now Eq. (1.22), the boundary condition reads:

$$\boldsymbol{\sigma}_f \mathbf{n}_f = \mathbf{g}_N \quad \text{where} \quad \mathbf{g}_N = g_N \mathbf{n}_f \quad \text{and} \quad g_N = -(C_{out} Q^{ao} + p_V);$$

$C_{out}$  is a resistance constant to be tuned and  $p_V$  a physiologically realistic pressure, which we set to  $p_V \approx 80$  mmHg, approximately the value measured at the root of aorta when the aortic valve is closed [Chen et al., 1997]. We choose to impose the resistance condition in an explicit way, for simplicity, by evaluating  $Q^{ao}$  in Eq. (7.1) with the velocity  $\mathbf{u}^n$ , when solving the problem at time  $t^{n+1}$ .

We highlight that numerical instabilities may occur on  $\Gamma_{t,N}^f$  when using the resistance boundary condition for the fluid [Tagliabue et al., 2017]. These instabilities are associated to nonphysical reflow at the valve, and could be avoided by considering additional stabilizing terms to the boundary condition [Moghadam et al., 2011]. Nonetheless, the model is able to reproduce physiological results even in presence of such instabilities.

|  |          |            |       |           |
|--|----------|------------|-------|-----------|
|  |          | Myocardium | Fluid | Interface |
|  | Vertices | 4'126      | 3'443 | 1'283     |

|      |               |               |               |               |               |               |
|------|---------------|---------------|---------------|---------------|---------------|---------------|
|      | $\mathcal{I}$ | $\mathcal{E}$ | $\mathcal{A}$ | $\mathcal{M}$ | $\mathcal{G}$ | $\mathcal{F}$ |
| DoFs | 12'378        | 4'126         | 4'126         | 12'378        | 10'329        | 13'772        |

|                         |                   |                   |                      |
|-------------------------|-------------------|-------------------|----------------------|
|                         | $(\mathcal{IEA})$ | $(\mathcal{MGF})$ | $(\mathcal{IEAMGF})$ |
| DoFs                    | 20'630            | 40'328            | 60'958               |
| DoFs / CPU <sub>s</sub> | 3'438             | 6'721             | 10'160               |

Table 7.1 – Top table: the number of vertices for the myocardium, the fluid, and the common interface meshes. Middle table: the number of DoFs for each single core problem. Bottom table: the number of DoFs and DoFs per CPU for the  $(\mathcal{IEA})$  (electrophysiology + mechanical activation),  $(\mathcal{MGF})$  (FSI), and  $(\mathcal{IEAMGF})$  (electrofluidmechanics) problems.

## 7.1 Realistic LV: systolic phase

For the simulations of this chapter we use the “Atlas” geometry shown in Figure 3.9; in Table 7.1 we report the number of vertices for the myocardium, the fluid, and the common interface, together with the number of DoFs for each single core problem, and for the integrated problems  $(\mathcal{IEA})$ ,  $(\mathcal{MGF})$ , and  $(\mathcal{IEAMGF})$ . The first is monolithically solved when using the  $(\mathcal{I}_I\mathcal{E}_I\mathcal{A}_I)-(\mathcal{M}_I\mathcal{G}_I\mathcal{F}_I)$  or the  $(\mathcal{I}_{SI}\mathcal{E}_{SI}\mathcal{A}_{SI})-(\mathcal{M}_I\mathcal{G}_I\mathcal{F}_I)$  strategies, the second when using any of the segregated strategies, and the third when using the  $(\mathcal{I}_I\mathcal{E}_I\mathcal{A}_I\mathcal{M}_I\mathcal{G}_I\mathcal{F}_I)$  strategy. Finite elements of order  $r = 1$  and BDF of order  $\sigma = 2$  are employed, while 6 CPUs are used for all the simulations. We report in Table 7.1 the number of DoFs per CPU for the  $(\mathcal{IEA})$ ,  $(\mathcal{MGF})$ , and  $(\mathcal{IEAMGF})$  problems.

We set the final time to  $T = 0.25$  s and, as previously done in Chapter 5, the simulation is started by applying an external current at three points located on the endocardium. We show in Figure 7.1 the transmembrane potential and the activation time obtained by using the  $(\mathcal{I}_{SI})-(\mathcal{E}_{SI})-(\mathcal{A}_{SI})-(\mathcal{M}_I\mathcal{G}_I\mathcal{F}_I)$  strategy, with timestep size  $\tau = 8 \times 10^{-5}$  s and  $N_{sub} = 8$  (and hence  $\Delta t = N_{sub}\tau = 64 \times 10^{-5}$  s). Coherently with the discussion on the conduction velocities carried out in Chapter 5, the conduction velocity is significantly reduced in this case with respect to Figure 5.1 since the mesh employed features a smaller mesh size  $h$  (see Table 3.1).

We then show in Figure 7.2 the fiber shortening on the deformed myocardium, and the displacement magnitude for both domains, compared with the reference ones at different times. While for clarity in the representation the two domains are reported separately, the continuity of the displacements at the common interface is evident. According with the results reported in Chapter 5 (see in particular Figure 5.21) for the electromechanics model, the contraction in the early systole takes place mostly in the base-apex longitudinal

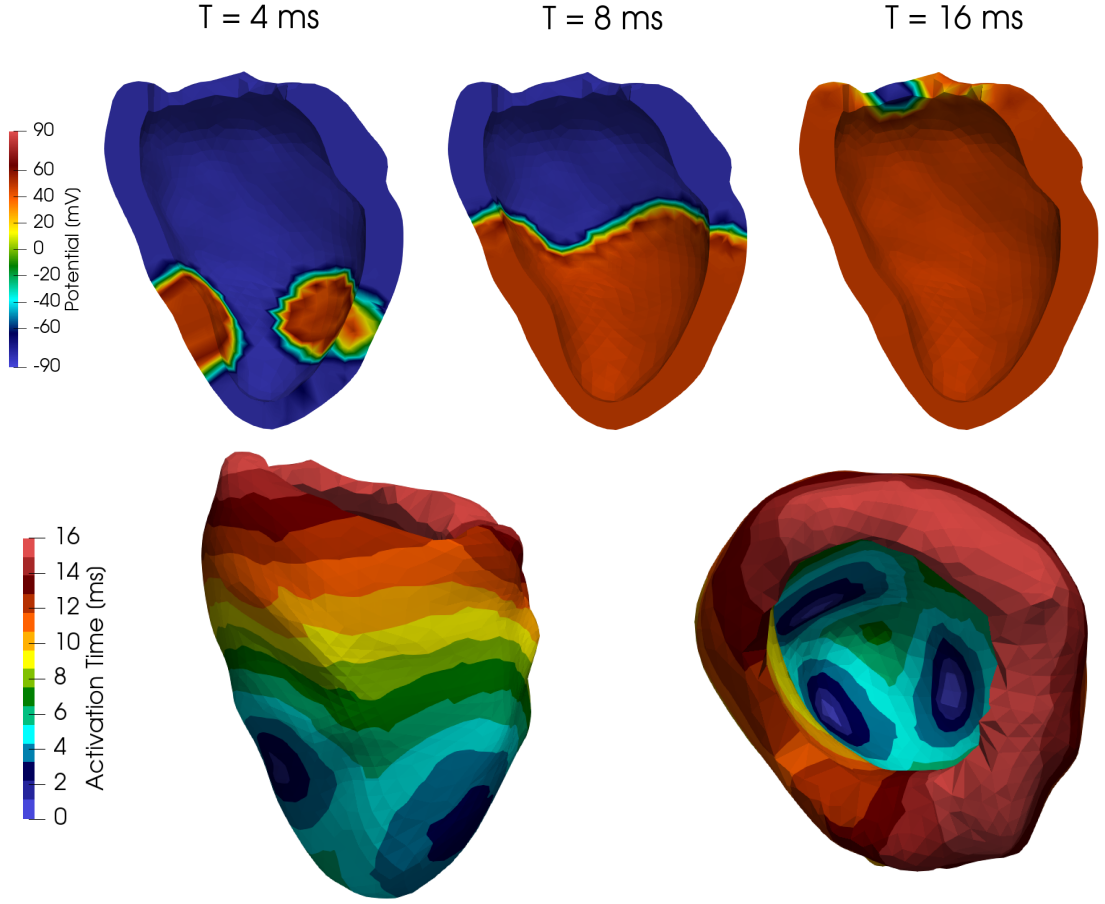


Figure 7.1 – Transmembrane potential (top row) at three different times and activation time (bottom row) from different viewpoints.

direction, in a way such that the longitudinal displacement is comparable at the base and at the endocardium. Then, in the late systole, the largest displacement occurs in the region close to the apex.

We verify that the volume of the LV and the average pressure  $p^{endo}$  inside it are compatible with the results obtained by simulating the electromechanics only. With this aim, anticipated, we consider the subregion obtained by clipping the fluid domain as depicted in Figure 7.3. We use this procedure mainly for two reasons: first, the subdomain thus obtained approximately represents the same region filled in by the blood in the subject-specific mesh of Figure 3.8, hence making it possible to compare the results obtained with the electromechanics simulation reported in Figure 5.23; second, by using the same subdomain to calculate the average pressure, we neglect the region close to the aortic valve in which the pressure oscillates for the numerical instabilities discussed at the beginning of this chapter.

The results reported in Figure 7.4 show that, even if the maximal values of both the volume

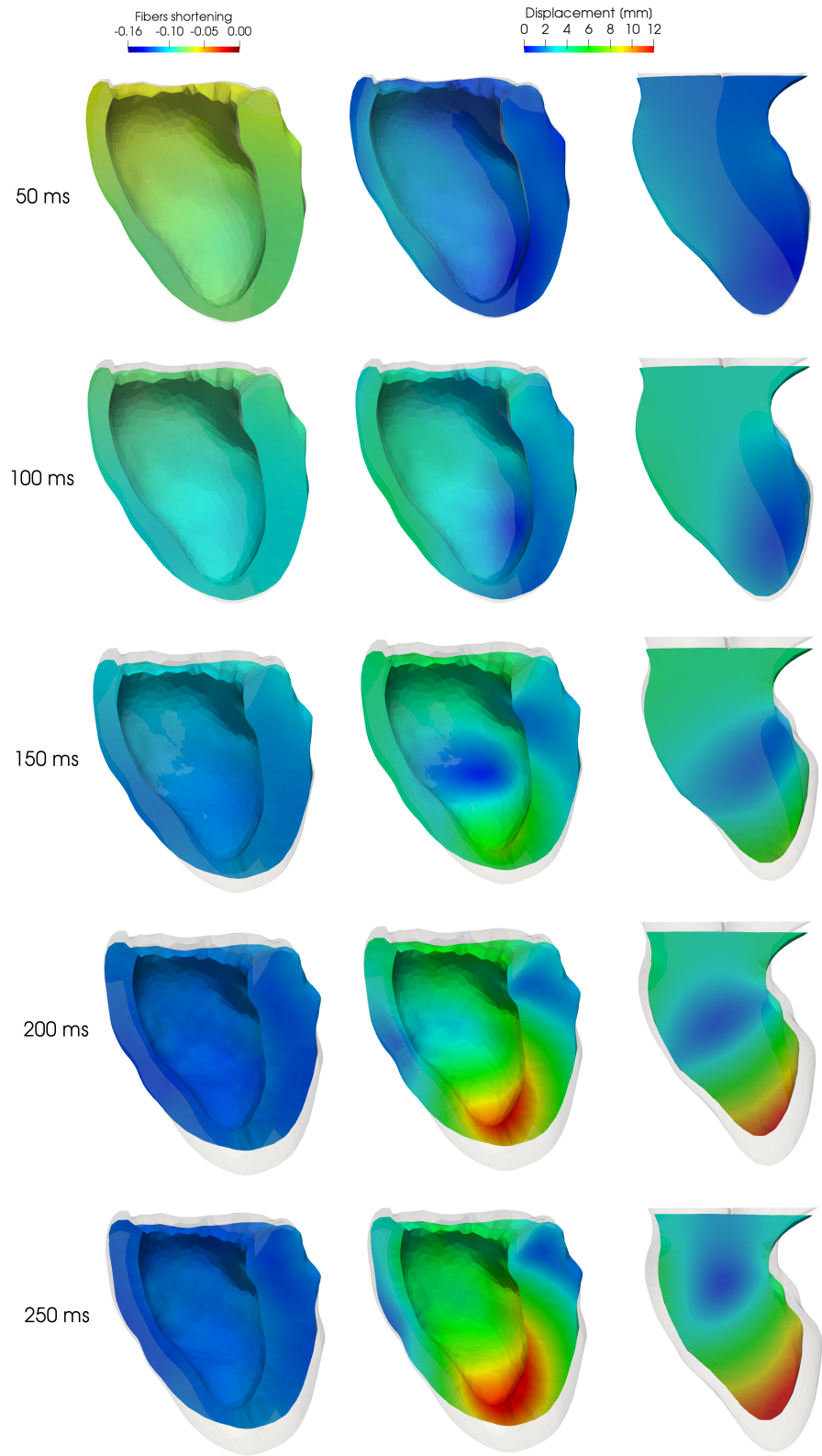


Figure 7.2 – Fibers shortening (left) and displacement magnitude of the deformed myocardium (center) and blood (right) domains.

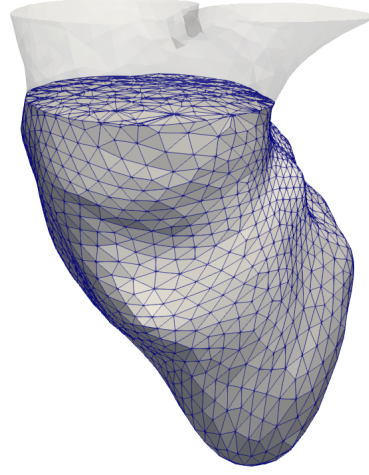


Figure 7.3 – The fluid subregion considered to calculate the ventricular volume and the averaged pressure, obtained by clipping the fluid domain in correspondance of the myocardium base.

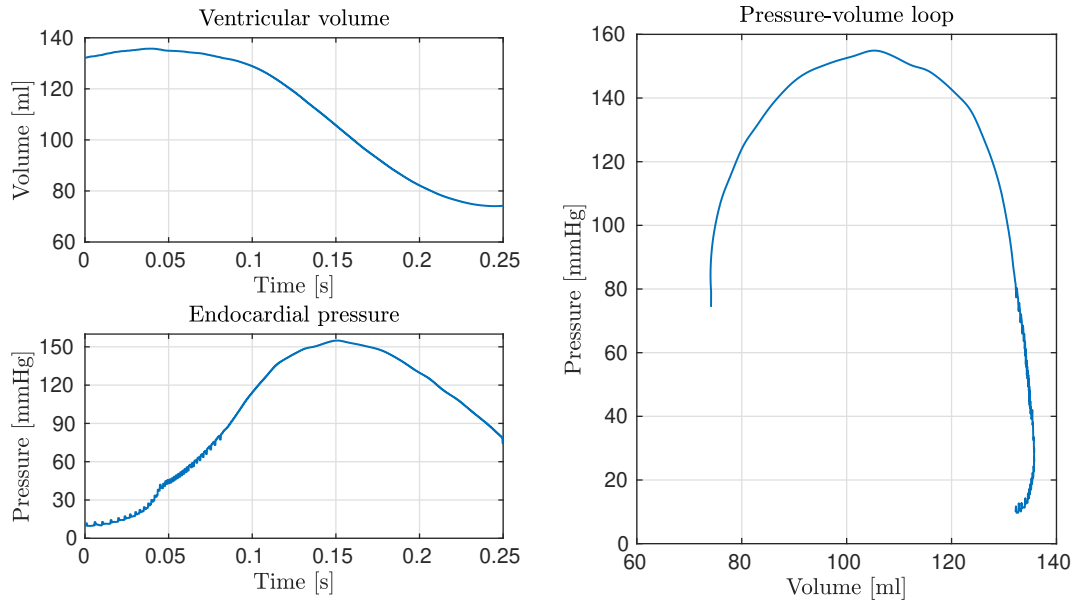


Figure 7.4 – The volume (top left) and the averaged pressure (bottom left) in the same subregion over time and the partial pV loop (right).

and the pressure are 10-20% larger with respect to those reported for the electromechanics model in Figure 5.23, the results are qualitatively in agreement. We remark that the numerical instabilities occurring when using the resistance condition are responsible for the “small” oscillations on the pressure in the first part of the systole.

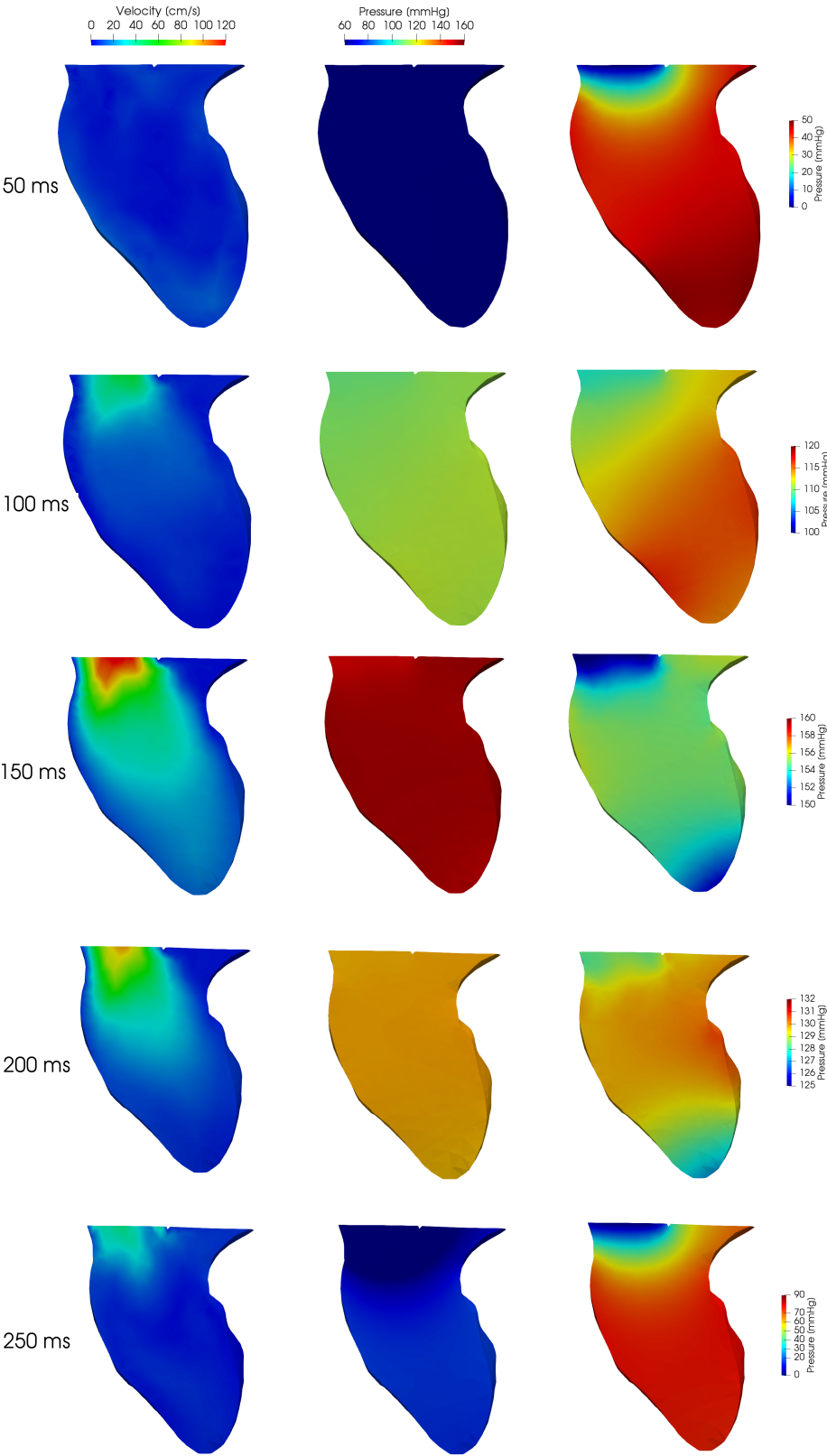


Figure 7.5 – Blood velocity magnitude (left) and pressure field with fixed (center) and variable (right) scales on a slice of the fluid domain.

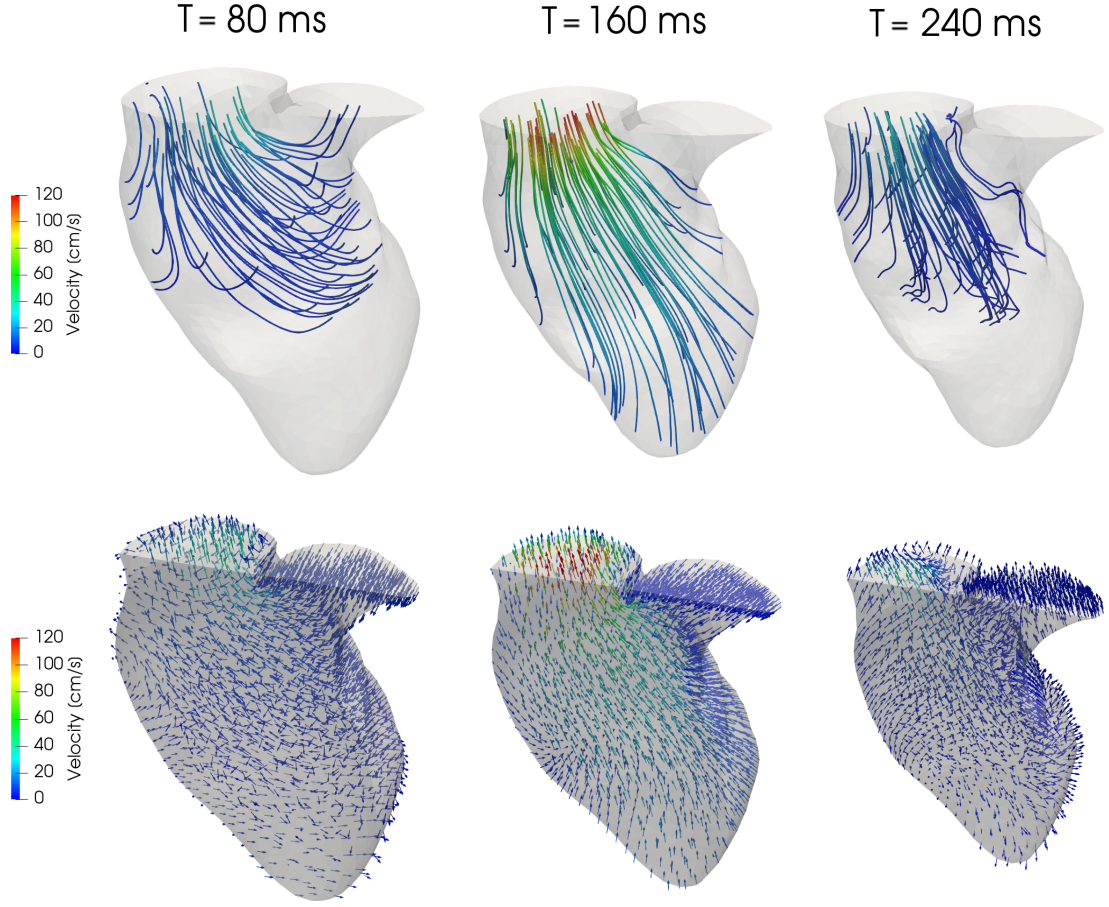


Figure 7.6 – Streamlines (top row) and velocity vector field (bottom row) on the blood deformed domain, at three different times.

We then analyze more in detail the behavior of the blood inside the LV. In Figure 7.5, the pressure and the velocity magnitude on a slice of the fluid domain are shown. We observe that at all the three instants reported the pressure is spatially homogeneous far from the outflow, and in agreement with the data reported in Figure 7.3. Moreover, while the peak value of the pressure ( $\approx 150 \text{ mmHg}$ ) is around 20% larger with respect to physiological data [Wallace et al., 1963], the peak velocity ( $\approx 120 \text{ cm/s}$ ) is in agreement with values measured in healthy individuals [Sabbah et al., 1986]. The distribution is also in agreement with our observations on the displacement of the myocardium: indeed, during the early systole, the contraction in the longitudinal direction determines a pressure gradient along the same direction, while in mid systole the thickening of the myocardium induces a somehow larger pressure in the central region of the domain.

Finally, we report in Figure 7.6 the (backwards) streamlines calculated starting from the outflow  $\Gamma_{t,N}^f$ , and the velocity vector field. The streamlines shed light on the dynamics of the blood inside the ventricle: the results show that in the early and in the late systole

| $(\mathcal{I}_I \mathcal{E}_I \mathcal{A}_I \mathcal{M}_I \mathcal{G}_I \mathcal{F}_I)$ |                  |                  |       |
|---|------------------|------------------|-------|
| $\tau (= \Delta t)$   | $\overline{N}^N$ | $\overline{N}^G$ | $T^W$ |
| $8 \times 10^{-5}$ s  | 4.5              | 98.1             | 911'  |
| $16 \times 10^{-5}$ s   | 5.8              | 71.8             | 474'  |
| $24 \times 10^{-5}$ s   | 6.8              | 59.3             | 325'  |

Table 7.2 – The average number of Newton ( $\overline{N}^N$ ) and GMRES ( $\overline{N}^G$ ) iterations for the solution of the monolithic problem  $(\mathcal{I}_I \mathcal{E}_I \mathcal{A}_I \mathcal{M}_I \mathcal{G}_I \mathcal{F}_I)$ , and the total wall time ( $T^W$ , in minutes) for the electrofluidmechanics simulations, for each  $\tau (= \Delta t)$  considered.

the blood ejected in the aorta comes from the region close to the aortic and mitral valves, while in the mid systole the streamlines and the velocity vector field indicate a laminar flow involving the blood in the whole ventricle. As in the electromechanics case, in Figure 7.2 we do not observe an appreciable rotation of the myocardium; nonetheless, we highlight that the fluid close to the endocardium (see the velocity vector field in Figure 7.6) still exhibits an angular momentum with respect to the longitudinal direction, due to the contraction along the fibers direction and the continuity of the velocities.

## 7.2 Comparison of computational costs

We now investigate and discuss the computational costs associated to the monolithic and the three segregated strategies introduced in Chapter 6 for the electrofluidmechanics. Nonetheless, since as we will show the former are dramatically larger in this case with respect to the electromechanics case, we repeat the simulation of Section 7.1 with  $T = 0.1$  and we investigate a smaller set of parameter  $\tau$ ,  $N_{sub}$ , and  $\Delta t$  with respect to the one used in Section 5.1. Starting with the monolithic  $(\mathcal{I}_I \mathcal{E}_I \mathcal{A}_I \mathcal{M}_I \mathcal{G}_I \mathcal{F}_I)$  strategy, we  $\tau = \Delta t = 8, 16, 24 \times 10^{-5}$  s; while smaller timestep lengths are avoided to ensure an acceptable total wall time, we observe that larger values prevent the convergence of the Newton method because the initial guess is not close enough to the solution. In Table 7.2 we report  $\overline{N}^N$ ,  $\overline{N}^G$ , and  $T^W$  obtained in the three cases. Coherently with the results of Table 5.1, the average number of Newton iterations  $\overline{N}^N$  gets larger for increasing  $\tau$ , while  $\overline{N}^G$  and  $T^W$  are significantly reduced. We remark that, compared with  $(\mathcal{I}_I \mathcal{E}_I \mathcal{A}_I \mathcal{M}_I)$ , the wall time  $T^W$  is almost 17 times larger for  $\tau = 8 \times 10^{-5}$  s and almost 15 times larger for  $\tau = 24 \times 10^{-5}$  s.

Regarding the segregated strategy, we choose to set  $\tau = 8 \times 10^{-5}$  s and  $N_{sub} = 4, 8, 16$ ; we report the results relative to the solution of the FSI problem and the wall time in Table 7.3. First of all we notice that the number of Newton iterations remains constant among the three strategies, while the number of GMRES iterations increases, in particular in the  $(\mathcal{I}_{SI})-(\mathcal{E}_{SI})-(\mathcal{A}_{SI})-(\mathcal{M}_I \mathcal{G}_I \mathcal{F}_I)$  case. We also observe that, while  $\overline{N}^G$  is kept relatively small in all cases,  $\overline{N}^N$  significantly increases. By comparing the results in Table 7.2



## 7.2. Comparison of computational costs

| $(\mathcal{I}_I \mathcal{E}_I \mathcal{A}_I) - (\mathcal{M}_I \mathcal{G}_I \mathcal{F}_I)$ |                        |             |             |       |
|---|------------------------|-------------|-------------|-------|
| $N_{sub}$   | $\Delta t$             | $\bar{N}^N$ | $\bar{N}^G$ | $T^W$ |
| 4   | $32 \times 10^{-5}$ s  | 8.0         | 29.2        | 217'  |
| 8   | $64 \times 10^{-5}$ s  | 13.4        | 21.1        | 146'  |
| 16  | $128 \times 10^{-5}$ s | 26.2        | 17.1        | 115'  |

| $(\mathcal{I}_{SI} \mathcal{E}_{SI} \mathcal{A}_{SI}) - (\mathcal{M}_I \mathcal{G}_I \mathcal{F}_I)$ |                        |             |             |       |
|--|------------------------|-------------|-------------|-------|
| $N_{sub}$  | $\Delta t$             | $\bar{N}^N$ | $\bar{N}^G$ | $T^W$ |
| 4  | $32 \times 10^{-5}$ s  | 8.0         | 34.2        | 200'  |
| 8  | $64 \times 10^{-5}$ s  | 13.5        | 24.7        | 129'  |
| 16   | $128 \times 10^{-5}$ s | 27.1        | 19.7        | 97'   |

| $(\mathcal{I}_{SI}) - (\mathcal{E}_{SI}) - (\mathcal{A}_{SI}) - (\mathcal{M}_I \mathcal{G}_I \mathcal{F}_I)$ |                        |             |             |       |
|--|------------------------|-------------|-------------|-------|
| $N_{sub}$  | $\Delta t$             | $\bar{N}^N$ | $\bar{N}^G$ | $T^W$ |
| 4  | $32 \times 10^{-5}$ s  | 8.0         | 51.5        | 199'  |
| 8  | $64 \times 10^{-5}$ s  | 13.5        | 40.6        | 126'  |
| 16   | $128 \times 10^{-5}$ s | 27.1        | 34.1        | 95'   |

Table 7.3 – The average number of Newton ( $\bar{N}^N$ ) and GMRES ( $\bar{N}^G$ ) iterations for the solution of the mechanics problem and the total wall time ( $T^W$ , in minutes) for the electrofluidmechanics simulations, for each segregated strategy, and  $N_{sub}$  considered and  $\tau = 8 \times 10^{-5}$  s.

with those in Table 7.3 we conclude that, in the monolithic case too, the FSI part of the problem is the principal responsible for the monotonic increment (decrement) of  $\bar{N}^N$  ( $\bar{N}^G$ ) with respect to  $\Delta t$ . We believe however that, as with the electromechanics model, the mechanics core model is the main responsible for this behavior also in the FSI case. Finally, we compare the wall times  $T^W$  with those reported in Table 5.2. In the electrofluidmechanics case, the latter is from 10 to 14 times larger with respect to the electromechanics case, while the maximum difference among the different strategies is around 15% between  $(\mathcal{I}_I \mathcal{E}_I \mathcal{A}_I) - (\mathcal{M}_I \mathcal{G}_I \mathcal{F}_I)$  and  $(\mathcal{I}_{SI} \mathcal{E}_{SI} \mathcal{A}_{SI}) - (\mathcal{M}_I \mathcal{G}_I \mathcal{F}_I)$ . Significant differences are not noticeable between  $(\mathcal{I}_{SI} \mathcal{E}_{SI} \mathcal{A}_{SI}) - (\mathcal{M}_I \mathcal{G}_I \mathcal{F}_I)$  and  $(\mathcal{I}_{SI}) - (\mathcal{E}_{SI}) - (\mathcal{A}_{SI}) - (\mathcal{M}_I \mathcal{G}_I \mathcal{F}_I)$ . In conclusion, the computational cost in terms of  $T^W$  is even more significantly reduced in the electrofluidmechanics case by using staggered strategies, compared to the electromechanics one. Indeed, we obtained a speedup of more than  $8\times$  by simply using the  $(\mathcal{I}_I \mathcal{E}_I \mathcal{A}_I) - (\mathcal{M}_I \mathcal{G}_I \mathcal{F}_I)$  strategy with  $N_{sub} = 16$  instead of  $(\mathcal{I}_I \mathcal{E}_I \mathcal{A}_I \mathcal{M}_I \mathcal{G}_I \mathcal{F}_I)$ , while keeping  $\tau = 8 \times 10^{-5}$  s fixed. Moreover, since the bottleneck of the simulation is definitely represented by the solution of the FSI problem, which is in turn much more “expensive” than the mechanics alone, the wall time among the segregated strategies for given values of  $\tau$  and  $N_{sub}$  is almost the same. As a comparison, the same sets of parameters determined a speedup of less than  $3\times$  in the electromechanics case. Hence, if saving

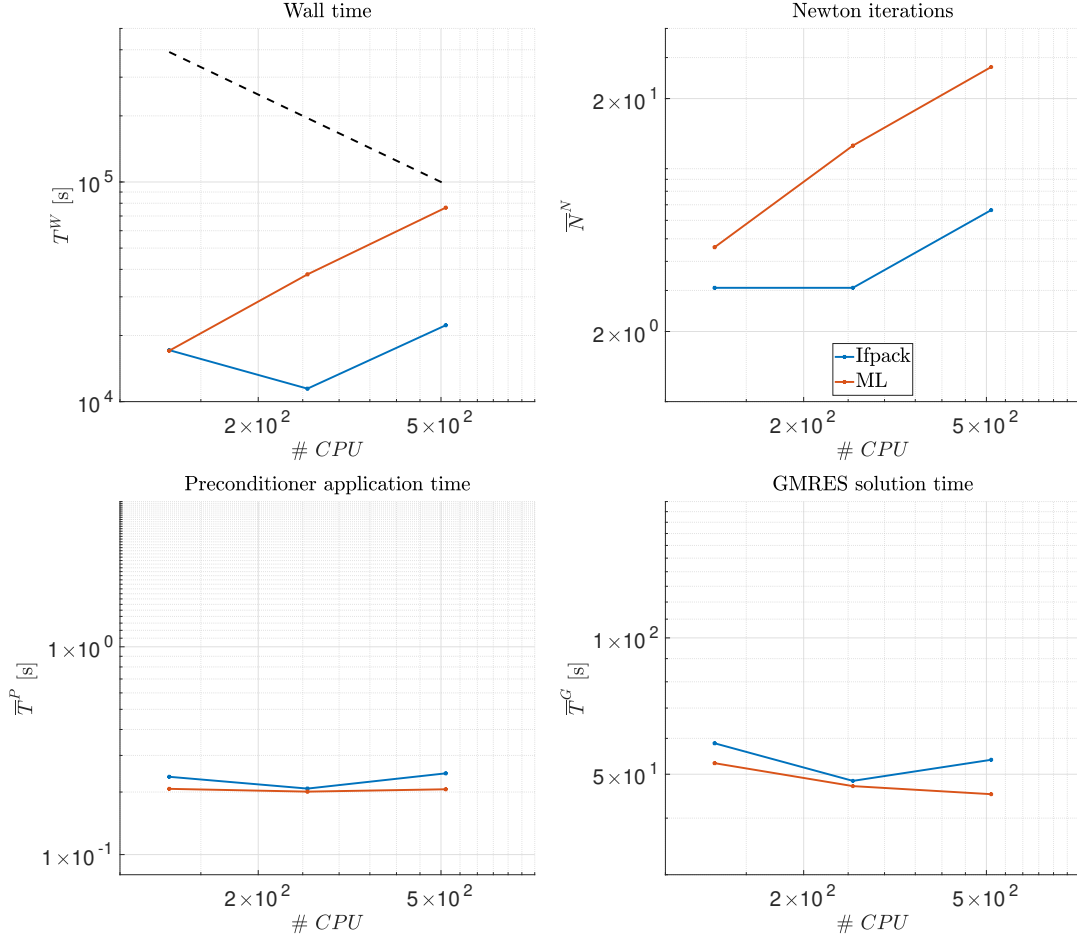


Figure 7.7 – Strong scalability for  $(\mathcal{I}_I \mathcal{E}_I \mathcal{A}_I \mathcal{M}_I \mathcal{G}_I \mathcal{F}_I)$ : the total wall time  $T^W$  (top left), the average number of Newton iterations  $\bar{N}^N$  (top right), the average assembly time for the preconditioner  $\bar{T}^P$  (bottom left), and the average GMRES solution time  $\bar{T}^G$  (bottom right).

computational resource is a critical issue, the  $(\mathcal{I}_I \mathcal{E}_I \mathcal{A}_I) - (\mathcal{M}_I \mathcal{G}_I \mathcal{F}_I)$  should be used instead of  $(\mathcal{I}_I \mathcal{E}_I \mathcal{A}_I \mathcal{M}_I \mathcal{G}_I \mathcal{F}_I)$ . The further speedup obtained by using  $(\mathcal{I}_{SI} \mathcal{E}_{SI} \mathcal{A}_{SI}) - (\mathcal{M}_I \mathcal{G}_I \mathcal{F}_I)$  and  $(\mathcal{I}_{SI}) - (\mathcal{E}_{SI}) - (\mathcal{A}_{SI}) - (\mathcal{M}_I \mathcal{G}_I \mathcal{F}_I)$ , which we recall that are not stable for “relatively” large values of  $\tau$ , is minimal.

We conclude this chapter by reporting in Figure 7.7 the strong scalability results for  $(\mathcal{I}_I \mathcal{E}_I \mathcal{A}_I \mathcal{M}_I \mathcal{G}_I \mathcal{F}_I)$ . These were obtained by solving the electrofluidmechanics problem using a refined mesh featuring 558’890 vertices for the structure, 409’585 vertices for the fluid, and 99’123 vertices for the interface. The total number of DoFs for this simulations is 7’076’694, while 128, 256, and 512 CPUs were employed. The results obtained show that the problem is indeed strongly scalable when using the Ifpack preconditioner for the

## 7.2. Comparison of computational costs

---

mechanics, with up to 256 CPUs, while it is not when using the ML preconditioner. We remark that these results are coherent with the strong scalability in the electromechanics case.



# Conclusions

In this thesis, we proposed and analyzed several strategies for the solution of the electromechanics and electrofluidmechanics problems for the LV in the human heart. We first described the physical processes at play in the LV during the heartbeat, that is the electrophysiology, the passive and active mechanics, and the fluid dynamics, and discussed the single core models used in this work for their individual mathematical description. We considered in particular: the monodomain and the bidomain equations, together with the minimal ionic model, for the electrophysiology; the Holzapfel-Ogden model and a model for the fibers shortening for the passive and the active mechanics, respectively, in the active strain framework with a new transmurally variable orthotropic activation; the incompressible Navier-Stokes equations in ALE formulation for the fluid dynamics. Then, we discretized in space the continuous core models by means of the FEM and in time by using BDFs with implicit and semi-implicit schemes. The fully discretized core models thus obtained were then exploited to define our electromechanics model, by considering both monolithic and segregated strategies for the solution of the integrated problem. The same strategies were then extended to the electrofluidmechanics case. We carried out several numerical simulations using the proposed strategies both in idealized settings to assess the accuracy, the efficiency, and the scalability of the strategies, and in subject-specific settings. In the latter case, a comparison with physiological experimental data, where available in literature, showed that the behavior of the LV is at least qualitatively correctly reproduced.

We report herein the main scientific contributions of this thesis.

- We proposed strategies for the electromechanics and the electrofluidmechanics of the LV with state-of-the-art models for the description of the myocardium active and passive mechanics using in particular the active strain framework and a model for the heterogeneous thickening of the myocardium. The complexity of the mechanical model allows to obtain results in agreement with experimental data over the whole heartbeat, however it requires a significant amount of computational resources to be solved at the discrete level. We then formulated two preconditioners for the monolithic algorithms, one for each integrated problem considered, based on the inexact factorization of the Jacobian of the nonlinear monolithic system. This

approach, which exploits the block structure of the Jacobian matrix, allows to precondition the individual blocks arising from the discretizations of the single core model with black-box preconditioners tailored on the specific physics represented by the core model. Even if the wall time required for the solution of the problem using the monolithic strategy resulted to be large, we showed that the monolithic preconditioner for the electromechanics is strongly scalable when using meshes up to several millions of vertices and several thousands of CPUs.

- We proposed three novel segregated strategies, obtained by uncoupling the core models in the monolithic problems with a Godunov splitting scheme, by exploiting both implicit and semi-implicit time schemes for the electrophysiology and the mechanical activation. The segregated strategies are also generalized to staggered strategies, where different timestep sizes can be used for the uncoupled problems. We then carried out a rigorous and thorough numerical study of the accuracy of the proposed monolithic and staggered strategies in the electromechanics case, by studying the convergence rate with respect to a manufactured “exact” solution obtained using a fine time discretization. The errors introduced with the Godunov splitting used for the segregated strategies were theoretically and numerically verified to be at least of the first order in time. The efficiency of the monolithic and of the staggered strategies was assessed by comparing the errors and the wall times for several choices of the timestep sizes. The dramatic reduction in the wall time obtained by using the segregated strategies is such that, even if they feature a lower accuracy, the latter are often more efficient than the monolithic strategy. The staggered strategies, both in the electromechanics and the electrofluidmechanics cases, are employed for large scale simulations in an HPC framework.
- The electromechanics model was used to simulate an ischemic necrosis in the myocardium tissue over a full heartbeat. The results obtained are in agreement with several clinical indicators commonly used by medical doctors to assess the residual contractility of the ventricle.
- The formulation and simulation of a full 3D electrofluidmechanics problem for the LV, with rigorously justified models and methods, represents a novelty itself. Even if the systolic phase only was considered, and a resistance boundary condition was used to model the aortic valve in a simplified way, the extension to the whole heartbeat can be obtained by properly modeling the valves behavior.
- We established a preprocess pipeline, including in particular algorithms for the generation of fibers and sheets and for the calculation of the prestress, that is the stresses in the myocardium for a given “initial” endocardial pressure. The preprocess pipeline was used generate the data required to initialize the simulations for idealized, realistic, and subject-specific myocardium meshes, thus proving its robustness.

---

Several future development and perspectives arise from the work carried out in this thesis. We identify the following fields that should be better investigated.

- **Mathematical models**

Several improvements to the mathematical models employed in this thesis are possible. For instance, a more sophisticated ionic model, which would in general feature a much larger number of equations, could be employed; in this work, the choice of a simple ionic model was driven by the goal of simulating the LV function with meshes featuring a large number of vertices, hence ultimately by the need of reducing the computational cost. Moreover, the model for the mechanical activation here employed was developed for the systolic phase only: indeed, in order to correctly represent the diastolic phase when simulating the whole heartbeat, we modified the model by changing the  $\mu_A$  parameter depending on the heartbeat phase. This choice was motivated by empirical observations on the contraction of the LV in the diastolic phase, nonetheless a physically motivated such as the one proposed in [Regazzoni et al., 2017] should be employed if the increased complexity of the model is acceptable.

- **Numerical methods**

Here, for simplicity, we only developed first order (Godunov) splitting schemes. The accuracy of the proposed strategies could however be improved by using second order (Strang) splitting schemes [McLachlan and Quispel, 2002]. More in general, different segregating strategies could be employed, namely by uncoupling the core models for the FSI in the electrofluidmechanics case. Moreover, a staggered approach could be used for the space discretization, that is by using different meshes for the electrophysiology and the mechanics/FSI. In particular, by using a finer mesh for the electrophysiology only, as is done e.g. in [Rossi, 2014] by using Radial Basis Functions (RBF) [Deparis et al., 2014] for the interpolation of the solutions between two different and possibly nonconforming meshes, the conduction velocities in the myocardium would be better estimated.

- **Further couplings and cardiovascular processes**

Additional feedbacks from the mechanics to the electrophysiology (such as the stretch activated currents) could be added to the integrated models [Colli Franzone et al., 2016b]. Indeed, different conclusions on the efficiency of the strategies might be drawn by verifying whether the splitting error in the segregated cases is influenced by different mechanical feedbacks. The electrofluidmechanics model, moreover, could be enriched with a model for each of the two valves, firstly with a reduced model [Mynard et al., 2012], and secondly with a full FSI model [De Hart et al., 2003]; a one dimensional model for the blood [Lamponi, 2004], coupled with the inflow and the outflow, would then allow to simulate the full blood cycle in the circulatory system.

- **Efficiency improvement of the methods**

The prestress technique developed for our simulations, which is based on a continuation method, requires a significant wall time to reach convergence. In this thesis, since the prestress is computed “offline” once for each given geometry, mechanics parameters, and endocardial pressure, we did not focus on improving the efficiency of the prestress computation algorithm. Nonetheless, a more efficient algorithm would allow to remove the need for the offline preprocessing phase. Regarding the integrated solvers, significant improvements could be obtained by exploiting time adaptation techniques, namely by using different timestep sizes depending on the phase of the heartbeat. Furthermore, encouraging results have been obtained by avoiding the (computationally expensive) update the Jacobian matrix of the mechanics problem at each timestep [McCormick et al., 2013]. Finally, if one is interested in reproducing the myocardium mechanics only for the whole heartbeat, the electrophysiology could be “switched off” during the diastolic phase, where it plays a smaller role in determining the displacement compared to the systolic phase.

- **Subject- and patient-specific simulations**

Since we showed that the model is capable to reproduce physiological data, a natural step forward in this direction would be that of estimating the models parameters with uncertainty quantification techniques [Manzoni et al., 2016, Pagani, 2017]; in this way, it would also be possible to simulate (eventually pathological) subject-specific scenarios to compare the results with data measured from the same subject for which the parameters have been tuned. The subject-specific simulations could then provide a useful predictive tool for clinicians.



# A Matrix calculus

We summarize in this Appendix several matrix calculus rules, useful for the computation of the Jacobian matrices for the discrete mono/bidomain and momentum mechanics equations, carried out in Appendix B. The following identities were taken in part from [Petersen et al., 2008].

Let now  $\mathbf{X} \in \mathbb{R}^{3 \times 3}$  with entries  $X_{ij}$ , and  $\mathbf{a}_0, \mathbf{b}_0 \in \mathbb{R}^3$  two vectors with entries  $a_{0,i}, b_{0,i}$ ; moreover, we set  $\mathbf{a} = \mathbf{X}\mathbf{a}_0$  and  $\mathbf{b} = \mathbf{X}\mathbf{b}_0$ . We use the Einstein notation, for which an implicit summation is performed when an index is repeated.

- Basic derivation rules:

$$\begin{aligned} \frac{\partial X_{kl}}{\partial X_{ij}} &= \delta_{ki} \delta_{jl}, \\ \frac{\partial (\mathbf{X}^{-1})_{kl}}{\partial X_{ij}} &= -(\mathbf{X}^{-1})_{ki} (\mathbf{X}^{-1})_{jl}, \\ \frac{\partial (\mathbf{X}^{-1})_{kl}}{\partial X_{ij}} &= -(\mathbf{X}^{-1})_{ki} (\mathbf{X}^{-1})_{jl}, \\ \frac{\partial \det \mathbf{X}}{\partial X_{ij}} &= \det \mathbf{X} (\mathbf{X}^{-T})_{ij}. \end{aligned}$$

- Linear form derivation rule:

$$\begin{aligned} \frac{\partial (\mathbf{a} \otimes \mathbf{b}_0)_{kl}}{\partial X_{ij}} &= \frac{\partial (\mathbf{X}\mathbf{a}_0 \mathbf{b}_0^T)_{kl}}{\partial X_{ij}} \\ &= \frac{\partial (X_{kn} a_{0,n} b_{0,l})}{\partial X_{ij}} \\ &= \delta_{ki} a_{0,j} b_{0,l} = \delta_{ki} (\mathbf{a}_0 \otimes \mathbf{b}_0)_{jl}. \end{aligned}$$

## Appendix A. Matrix calculus

---

- Quadratic forms derivation rule:

$$\begin{aligned}
\frac{\partial \operatorname{tr} \mathbf{X}^T \mathbf{X}}{\partial X_{ij}} &= 2X_{ij}, \\
\frac{\partial \mathbf{a}_0 \cdot \mathbf{X}^T \mathbf{X} \mathbf{b}_0}{\partial X_{ij}} &= \frac{\partial (a_{0,k} X_{nk} X_{nl} b_{0,l})}{\partial X_{ij}} \\
&= a_{0,k} (\delta_{ni} \delta_{kj} X_{nl} + X_{nk} \delta_{ni} \delta_{lj}) b_{0,l} \\
&= a_{0,j} X_{il} b_{0,l} + b_{0,j} X_{ik} a_{0,k} \\
&= a_{0,j} b_i + b_{0,j} a_i = (\mathbf{a} \otimes \mathbf{b}_0 + \mathbf{b} \otimes \mathbf{a}_0)_{ij}.
\end{aligned}$$

Let now  $\mathbf{Y} \in \mathbb{R}^{3 \times 3 \times 3}$ ,  $\mathbf{Z} \in \mathbb{R}^{3 \times 3 \times 3 \times 3}$  a third and a fourth order tensor with entries  $Y_{klij}$   $Z_{klij}$ , respectively, We then denote by

$$((\mathbf{Y})[\mathbf{X}])_k = Y_{kij} X_{ij}, \quad ((\mathbf{Z})[\mathbf{X}])_{kl} = Y_{klij} X_{ij},$$

the contractions  $(\mathbf{Y})[\mathbf{X}] \in \mathbb{R}^3$  and  $(\mathbf{Z})[\mathbf{X}] \in \mathbb{R}^{3 \times 3}$ .

# B Models

In this Appendix we list, for each core model, the functions and coefficients not explicitly reported in the main chapters. In the following,  $H_a(z)$  is the Heaviside function centered in  $a \in \mathbb{R}$ , while

$$H_a^M(z) = \frac{(1 + \tanh(M(z - a)))}{2}$$

stands for its smooth approximation depending on a constant parameter  $M \in \mathbb{R}^+$  (where a larger  $M$  corresponds to a sharper transition at  $z = a$ ). Its derivative is equal to

$$(H_a^M)'(z) = \frac{M(1 - \tanh^2(M(z - a)))}{2}.$$

## B.1 Ionic model and ionic currents terms

|       |       |         |       |         |        |          |           |
|-------|-------|---------|-------|---------|--------|----------|-----------|
| $v_o$ | $v_1$ | $v_1^-$ | $v_2$ | $v_2^-$ | $v_3$  | $v_{so}$ | $\hat{v}$ |
| 0.006 | 0.3   | 0.015   | 0.015 | 0.03    | 0.9087 | 0.65     | 1.58      |

|              |       |        |          |                         |                       |                 |
|--------------|-------|--------|----------|-------------------------|-----------------------|-----------------|
| $w_*^\infty$ | $k_2$ | $k_3$  | $k_{so}$ | $\tau_1^+ [\text{s}]$   | $\tau_2^+ [\text{s}]$ | $\tau_2^\infty$ |
| 0.94         | 65    | 2.0994 | 2        | $1.4506 \times 10^{-3}$ | $280 \times 10^{-3}$  | 0.07            |

|                           |                                 |                           |                                 |                           |                                 |
|---------------------------|---------------------------------|---------------------------|---------------------------------|---------------------------|---------------------------------|
| $\bar{\tau}_1 [\text{s}]$ | $\bar{\bar{\tau}}_1 [\text{s}]$ | $\bar{\tau}_2 [\text{s}]$ | $\bar{\bar{\tau}}_2 [\text{s}]$ | $\bar{\tau}_3 [\text{s}]$ | $\bar{\bar{\tau}}_3 [\text{s}]$ |
| $60 \times 10^{-3}$       | $1150 \times 10^{-3}$           | $70 \times 10^{-3}$       | $20 \times 10^{-3}$             | $2.7342 \times 10^{-3}$   | $3 \times 10^{-3}$              |

|                           |                                 |                              |                                    |                         |                        |
|---------------------------|---------------------------------|------------------------------|------------------------------------|-------------------------|------------------------|
| $\bar{\tau}_o [\text{s}]$ | $\bar{\bar{\tau}}_o [\text{s}]$ | $\bar{\tau}_{so} [\text{s}]$ | $\bar{\bar{\tau}}_{so} [\text{s}]$ | $\tau_{si} [\text{s}]$  | $\tau_{fi} [\text{s}]$ |
| $6 \times 10^{-3}$        | $6 \times 10^{-3}$              | $43 \times 10^{-3}$          | $0.2 \times 10^{-3}$               | $2.8723 \times 10^{-3}$ | $0.11 \times 10^{-3}$  |

Table B.1 – Values of the coefficients used for the minimal model [Bueno-Orovio et al., 2008]. The coefficients indicated in scientific notation were rescaled from the original work, from [ms] to [s].

## Appendix B. Models

---

- Time functions

$$\begin{aligned}
\tau_1^-(v) &= (1 - H_{v_1^-}(v))\bar{\tau}_1 + H_{v_1^-}(v)\bar{\bar{\tau}}_1, \\
\tau_2^-(v) &= (1 - H_{v_2^-}^{k_{so}}(v))\bar{\tau}_2 + H_{v_2^-}^{k_{so}}(v)\bar{\bar{\tau}}_2, \\
\tau_1^-(v) &= (1 - H_{v_2}(v))\bar{\tau}_3 + H_{v_2}(v)\bar{\bar{\tau}}_3, \\
\tau_1^-(v) &= (1 - H_{v_o}(v))\bar{\tau}_o + H_{v_o}(v)\bar{\bar{\tau}}_o, \\
\tau_{so}(v) &= (1 - H_{v_{so}}^{k_{so}}(v))\bar{\tau}_{so} + H_{v_{so}}^{k_{so}}(v)\bar{\bar{\tau}}_{so}.
\end{aligned}$$

- Model terms

$$\begin{aligned}
\boldsymbol{\alpha}(v) &= \left( \frac{1 - H_{v_1}(v)}{\tau_1^-(v)}, \quad \frac{1 - H_{v_2}(v)}{\tau_2^-(v)}, \quad \frac{1}{\tau_3(v)} \right)^T, \\
\boldsymbol{\beta}(v) &= \left( -\frac{H_{v_1}(v)}{\tau_1^+}, \quad -\frac{H_{v_2}(v)}{\tau_2^+}, \quad 0 \right)^T, \\
\mathbf{w}^\infty(v) &= \left( 1 - H_{v_1^-}(v), \quad H_{v_o}(v) \left( w_*^\infty - 1 + \frac{v}{\tau_2^\infty} \right) + 1 - \frac{v}{\tau_2^\infty}, \quad H_{v_3}^{k_3}(v) \right)^T.
\end{aligned}$$

- Minimal model ionic currents terms

$$\begin{aligned}
I^{ion}(v, w_1, w_2, w_3) &= I_{fi}(v, w_1) + I_{so}(v) + I_{si}(v, w_2, w_3), \\
I_{fi}(v, w_1) &= -\frac{w_1 H_{v_1}(v)(v - v_1)(\hat{v} - v)}{\tau_{fi}}, \\
I_{so}(v) &= \frac{(v - v_o)(1 - H_{v_2}(v))}{\tau_o(v)} + \frac{H_{v_2}(v)}{\tau_{so}(v)}, \\
I_{si}(v, w_2, w_3) &= -\frac{H_{v_2}(v)w_2w_3}{\tau_{si}}.
\end{aligned}$$

- Minimal model ionic currents Jacobian terms

$$\begin{aligned}
\frac{\partial I^{ion}}{\partial w_1}(v) &= -\frac{H_{v_1}(v)(v - v_1)(\hat{v} - v)}{\tau_{fi}}, \\
\frac{\partial I^{ion}}{\partial w_2}(v, w_3) &= -\frac{H_{v_2}(v)w_3}{\tau_{si}}, \\
\frac{\partial I^{ion}}{\partial w_3}(v, w_3) &= -\frac{H_{v_2}(v)w_2}{\tau_{si}}, \\
\frac{\partial I^{ion}}{\partial v}(v, w_1, w_2, w_3) &= -\frac{w_1(H'_{v_1}(v)(v - v_1)(\hat{v} - v) + H_{v_1}(v)(-2v + v_1 + \hat{v}))}{\tau_{fi}} \\
&\quad + \frac{((1 - H_{v_2}(v)) - (v - v_o)H'_{v_2}(v))\tau_o(v) - (v - v_o)(1 - H_{v_2}(v))\tau'_o(v)}{\tau_o^2(v)} \\
&\quad + \frac{H'_{v_2}(v)\tau_{so}(v) - H_{v_2}(v)\tau'_{so}(v)}{\tau_{so}^2(v)} - \frac{H'_{v_2}(v)w_2w_3}{\tau_{si}}.
\end{aligned}$$

- Semi-implicit splitting of the ionic currents

$$\begin{aligned}
 I_{w_1}^{ion}(v^*) &= -\frac{H_{v_1}(v^*)(v^* - v_1)(\widehat{v} - v^*)}{\tau_{fi}}, \\
 I_{w_3}^{ion}(v^*, w_2^*) &= -\frac{H_{v_2}(v^*)w_2^*}{\tau_{si}}, \\
 I_v^{ion}(v^*) &= \frac{(1 - H_{v_2}(v^*))}{\tau_o(v^*)}, \\
 \tilde{I}^{ion}(v^*) &= \frac{(1 - H_{v_2}(v^*))v_o}{\tau_o(v^*)} - \frac{H_{v_2}(v^*)}{\tau_{so}(v^*)}.
 \end{aligned}$$

## B.2 Monodomain and bidomain

| $\chi$ | $C_m$ | $\sigma_l [mm^2 s^{-1}]$ | $\sigma_t [mm^2 s^{-1}]$ |
|--------|-------|--------------------------|--------------------------|
| 1      | 1     | $1.2042 \times 10^2$     | $0.1761 \times 10^2$     |

| $\chi$ | $C_m$ | $\sigma_{E,l} [mm^2 s^{-1}]$ | $\sigma_{E,t} [mm^2 s^{-1}]$ | $\sigma_{I,l} [mm^2 s^{-1}]$ | $\sigma_{I,t} [mm^2 s^{-1}]$ |
|--------|-------|------------------------------|------------------------------|------------------------------|------------------------------|
| 1      | 1     | $1.2042 \times 10^2$         | $0.7044 \times 10^2$         | $2.4084 \times 10^2$         | $0.3522 \times 10^2$         |

Table B.2 – Coefficient used for the monodomain (top table) and the bidomain (bottom table) equations.

The term

$$\frac{\partial(J\mathbf{F}^{-1}\mathbf{D}_m\mathbf{F}^{-T}\nabla_0 v)}{\partial\mathbf{F}},$$

in Eq. (2.20) is a third order tensor, which is contracted with the second order  $\nabla_0\psi_s$  and the first order  $\nabla_0\psi_s$  ones, thus yielding a scalar. In order to display it, we write it in terms of its components

$$\left( \frac{\partial(J\mathbf{F}^{-1}\mathbf{D}_m\mathbf{F}^{-T}\nabla_0 v)}{\partial\mathbf{F}} \right)_{kij} = \frac{\partial(J\mathbf{F}^{-1}\mathbf{D}_m\mathbf{F}^{-T}\nabla_0 v)_k}{\partial F_{ij}}.$$

Hence

$$\begin{aligned}
 \left( \frac{\partial(J\mathbf{F}^{-1}\mathbf{D}_m\mathbf{F}^{-T}\nabla_0 v)}{\partial\mathbf{F}} \right)_{kij} &= \frac{\partial(J\mathbf{F}^{-1}\mathbf{D}_m\mathbf{F}^{-T})_{kl}}{\partial F_{ij}} (\nabla_0 v)_l \\
 &= (\mathbf{F}^{-T})_{ij} (\mathbf{D}_0 \nabla_0 v)_k \\
 &\quad - (\mathbf{F}^{-1})_{ki} (\mathbf{D}_0)_{jl} (\nabla_0 v)_l \\
 &\quad - (\mathbf{D}_0)_{lp} \delta_{qi} \delta_{pj} (\mathbf{F}^{-1})_{qk} (\nabla_0 v)_l,
 \end{aligned}$$

## Appendix B. Models

---

where  $\mathbf{D}_0 = J\mathbf{F}^{-1}\mathbf{D}_m\mathbf{F}^{-T}$ .

### B.3 Mechanical activation

|       |       |       |       |       |       |       |               |  |
|-------|-------|-------|-------|-------|-------|-------|---------------|--|
| $d_0$ | $d_1$ | $e_1$ | $d_2$ | $e_2$ | $d_3$ | $e_3$ |               |  |
| 4.33  | 2.57  | -2.05 | 1.33  | 0.30  | 0.10  | 0.22  | $\times 10^3$ |  |

|                          |                          |                     |       |          |               |                   |                   |                   |                   |
|--------------------------|--------------------------|---------------------|-------|----------|---------------|-------------------|-------------------|-------------------|-------------------|
| $SL_{min} [\mu\text{m}]$ | $SL_{max} [\mu\text{m}]$ | $l_0 [\mu\text{m}]$ | $c_0$ | $\alpha$ | $\varepsilon$ | $\hat{\mu}_{A,1}$ | $\hat{\mu}_{A,2}$ | $\hat{\mu}_{A,3}$ | $\hat{\mu}_{A,4}$ |
| 1.7                      | 2.6                      | 1.95                | 0.05  | -6       | 5             | 2.1               | 7                 | 12                | 500               |

Table B.3 – Coefficients of the truncated Fourier series approximating the force-length relationship (top table); minimum, maximum, and reference sarcomere length, calcium threshold and the tuning parameters. The parameter  $\hat{\mu}_A$  used for each of the four heartbeat phases is specified.

- Mechanical activation Jacobian terms

$$\begin{aligned}\frac{\partial \Phi(c, \gamma, \mathbf{d}_s)}{\partial c} &= \alpha(H'_{c_0}(c)(c - c_0)^2 + 2H_{c_0}(c)(c - c_0))R_{FL}(I_{4f}), \\ \frac{\partial \Phi(c, \gamma, \mathbf{d}_s)}{\partial \gamma} &= \sum_{j=1}^4 (-1)^j j(j+1)(j+2)I_{4f}\gamma^{j-1}, \\ \frac{\partial \Phi(c, \gamma, \mathbf{d}_s)}{\partial \mathbf{F}} &= \left( H_{c_0}(c)\alpha(c - c_0)^2 R'_{FL}(I_{4f}) + 2 \sum_{j=1}^5 (-1)^j j(j+1)(j+2)\gamma_f^j \right) (\mathbf{f} \otimes \mathbf{f}_0).\end{aligned}$$

- Semi-implicit splitting of the active force

$$\begin{aligned}\Phi_\gamma(c^*, \gamma^*, \mathbf{d}_s^*) &= -H_{c_0}(c^*)\alpha(c^* - c_0)^2 R_{FL}(I_{4f}^*), \\ \tilde{\Phi}(c^*, \gamma^*, \mathbf{d}_s^*) &= \sum_{j=1}^5 (-1)^j j(j+1)(j+2)I_{4f}^*(\gamma_f^*)^{j-1}.\end{aligned}$$

## B.4 Mechanics

| $a$ [Pa] | $b$   | $a_f$ [Pa] | $b_f$ | $a_s$ [Pa] | $b_s$  | $a_{fs}$ [Pa] | $b_{fs}$ | $B$ [Pa] | $\rho$ [g/mm <sup>3</sup> ] |
|----------|-------|------------|-------|------------|--------|---------------|----------|----------|-----------------------------|
| 59       | 8.023 | 18472      | 16.02 | 2481       | 11.120 | 216           | 11.436   | 5000     | 10 <sup>-3</sup>            |

| $K_{\perp}^{base}$ [Pa/mm] | $K_{\parallel}^{base}$ [Pa/mm] | $C_{\perp}^{base}$ [Pa·s/mm] | $C_{\parallel}^{base}$ [Pa·s/mm] |
|----------------------------|--------------------------------|------------------------------|----------------------------------|
| 1500                       | 10 <sup>-4</sup>               | 1                            | 0                                |

| $K_{\perp}^{epi}$ [Pa/mm] | $K_{\parallel}^{epi}$ [Pa/mm] | $C_{\perp}^{epi}$ [Pa·s/mm] | $C_{\parallel}^{epi}$ [Pa·s/mm] |
|---------------------------|-------------------------------|-----------------------------|---------------------------------|
| 10                        | 0                             | 5                           | 0                               |

Table B.4 – Parameters for the nearly incompressible Holzapfel-Ogden strain energy function (top table); density and boundary conditions coefficients (mid and bottom tables).

- Holzapfel-Ogden (passive) nearly incompressible strain energy function

$$\begin{aligned}
 \mathcal{W}(\mathbf{C}) &= \mathcal{W}_1(J^{-\frac{2}{3}}\mathcal{I}_1) + \mathcal{W}_{4f}(\mathcal{I}_{4f}) + \mathcal{W}_{4s}(\mathcal{I}_{4s}) + \mathcal{W}_{8fs}(\mathcal{I}_{8fs}) + \mathcal{W}_{vol}(J) \\
 &= \frac{a}{2b}e^{b(J^{-\frac{2}{3}}\mathcal{I}_1-3)} + \frac{a_f}{2b_f}\left[e^{b\langle\mathcal{I}_{4f}-1\rangle^2}-1\right] + \frac{a_s}{2b_s}\left[e^{b\langle\mathcal{I}_{4s}-1\rangle^2}-1\right] \\
 &\quad + \frac{a_{fs}}{2b_{fs}}\left[e^{b_{fs}\mathcal{I}_{8fs}^2}-1\right] + \frac{B}{2}(J-1)\log(J),
 \end{aligned}$$

where  $\langle x \rangle$  denotes the positive part of  $x$ .

- First Piola-Kirchhoff (passive) stress tensor

$$\begin{aligned}
 \mathbf{P}_E(\mathbf{d}_s) &= \mathbf{P}_E^1(\mathbf{d}_s) + \mathbf{P}_E^{4f}(\mathbf{d}_s) + \mathbf{P}_E^{4s}(\mathbf{d}_s) + \mathbf{P}_E^{8fs}(\mathbf{d}_s) + \mathbf{P}_E^{vol}(\mathbf{d}_s) \\
 &= \frac{\partial \mathcal{W}_1(J^{-\frac{2}{3}}\mathcal{I}_1^E)}{\partial \mathbf{F}_E} + \frac{\partial \mathcal{W}_{4f}(\mathcal{I}_{4f}^E)}{\partial \mathbf{F}_E} + \frac{\partial \mathcal{W}_{4s}(\mathcal{I}_{4s}^E)}{\partial \mathbf{F}_E} + \frac{\partial \mathcal{W}_{8fs}(\mathcal{I}_{8fs}^E)}{\partial \mathbf{F}_E} + \frac{\partial \mathcal{W}_{vol}(J)}{\partial \mathbf{F}_E} \\
 &= ae^{b(J^{-\frac{2}{3}}\mathcal{I}_1^E-3)}J^{-\frac{2}{3}}\left(\mathbf{F}_E - \frac{\mathcal{I}_1^E}{3}\mathbf{F}_E^{-T}\right) \\
 &\quad + 2a_fe^{b_f\langle\mathcal{I}_{4f}^E-1\rangle^2}\langle\mathcal{I}_{4f}^E-1\rangle(\mathbf{f}_E \otimes \mathbf{f}_0) \\
 &\quad + 2a_se^{b_s\langle\mathcal{I}_{4s}^E-1\rangle^2}\langle\mathcal{I}_{4s}^E-1\rangle(\mathbf{s}_E \otimes \mathbf{s}_0) \\
 &\quad + a_{fs}e^{b_{fs}(\mathcal{I}_{8fs}^E)^2}\mathcal{I}_{8fs}^E(\mathbf{f}_E \otimes \mathbf{s}_0 + \mathbf{s}_E \otimes \mathbf{f}_0) \\
 &\quad + \frac{B}{2}J\left(1 + \log(J) - \frac{1}{J}\right)\mathbf{F}_E^{-T},
 \end{aligned} \tag{B.1}$$

where

$$\mathbf{f}_E = \mathbf{F}_E \mathbf{f}_0, \quad \mathbf{s}_E = \mathbf{F}_E \mathbf{s}_0, \quad \mathbf{F}_E = \mathbf{F} \mathbf{F}_A^{-1}.$$

- First Piola-Kirchhoff (active and passive) stress tensor

$$\begin{aligned} \mathbf{P}(\mathbf{d}_s, \gamma_f) = & \left[ a e^{b(J^{-\frac{2}{3}} \mathcal{I}_1^E - 3)} J^{-\frac{2}{3}} \left( \mathbf{F}_E - \frac{\mathcal{I}_1^E}{3} \mathbf{F}_E^{-T} \right) \right. \\ & + 2a_f e^{b_f(\mathcal{I}_{4f}^E - 1)^2} \langle \mathcal{I}_{4f}^E - 1 \rangle (\mathbf{f}_E \otimes \mathbf{f}_0) \\ & + 2a_s e^{b_s(\mathcal{I}_{4s}^E - 1)^2} \langle \mathcal{I}_{4s}^E - 1 \rangle (\mathbf{s}_E \otimes \mathbf{s}_0) \\ & + a_{fs} e^{b_{fs}(\mathcal{I}_{8fs}^E)^2} \mathcal{I}_{8fs}^E (\mathbf{f}_E \otimes \mathbf{s}_0 + \mathbf{s}_E \otimes \mathbf{f}_0) \\ & \left. + \frac{B}{2} J \left( 1 + \log(J) - \frac{1}{J} \right) \mathbf{F}_E^{-T} \right] \mathbf{F}_A^{-1}, \end{aligned}$$

where

$$\begin{aligned} \mathbf{F}_A &= \mathbf{F}_A^T = \mathbf{I} + \gamma_f \mathbf{f}_0 \otimes \mathbf{f}_0 + \gamma_s(\gamma_f) \mathbf{s}_0 \otimes \mathbf{s}_0 + \gamma_n(\gamma_f) \mathbf{n}_0 \otimes \mathbf{n}_0, \\ \mathbf{F}_A^{-1} &= \mathbf{F}_A^{-T} = \mathbf{I} - \frac{\gamma_f}{1 + \gamma_f} \mathbf{f}_0 \otimes \mathbf{f}_0 - \frac{\gamma_s(\gamma_f)}{1 + \gamma_s(\gamma_f)} \mathbf{s}_0 \otimes \mathbf{s}_0 - \frac{\gamma_n(\gamma_f)}{1 + \gamma_n(\gamma_f)} \mathbf{n}_0 \otimes \mathbf{n}_0. \end{aligned}$$

- Holzapfel-Ogden (active and passive) Jacobian terms

$$\left( \frac{\partial \mathbf{P}(\mathbf{d}_s, \gamma_f)}{\partial \mathbf{F}_E} \right)_{klij} = \left( \frac{\partial \mathbf{P}_E(\mathbf{d}_s)}{\partial \mathbf{F}_E} \mathbf{F}_A^{-1} \right)_{klij} = \frac{\partial P_{kl}^E(\mathbf{d}_s)}{\partial F_{ip}^E} (\mathbf{F}_A^{-1})_{pj}.$$

$$\frac{\partial P_{kl}^E}{\partial F_{ij}^E} = \frac{\partial P_{kl}^{E,1}}{\partial F_{ij}^E} + \frac{\partial P_{kl}^{E,4f}}{\partial F_{ij}^E} + \frac{\partial P_{kl}^{E,4s}}{\partial F_{ij}^E} + \frac{\partial P_{kl}^{E,8fs}}{\partial F_{ij}^E} + \frac{\partial P_{kl}^{E,vol}}{\partial F_{ij}^E}.$$

$$\begin{aligned} \frac{\partial P_{kl}^{E,1}}{\partial F_{ij}^E} &= a \frac{\partial (e^{b(J^{-\frac{2}{3}} \mathcal{I}_1 - 3)})}{\partial F_{ij}^E} J^{-\frac{2}{3}} \left( F_{kl} - \frac{\mathcal{I}_1}{3} (\mathbf{F}^{-T})_{kl} \right) \\ &+ a e^{b(J^{-\frac{2}{3}} \mathcal{I}_1 - 3)} \frac{\partial J^{-\frac{2}{3}}}{\partial F_{ij}^E} \left( F_{kl} - \frac{\mathcal{I}_1}{3} (\mathbf{F}^{-T})_{kl} \right) \\ &+ a e^{b(J^{-\frac{2}{3}} \mathcal{I}_1 - 3)} J^{-\frac{2}{3}} \left( \frac{\partial F_{kl}}{\partial F_{ij}^E} - \frac{1}{3} \frac{\partial \mathcal{I}_1}{\partial F_{ij}^E} (\mathbf{F}^{-T})_{kl} - \frac{\mathcal{I}_1}{3} \frac{\partial (\mathbf{F}^{-T})_{kl}}{\partial F_{ij}^E} \right) \\ &= a e^{b(J^{-\frac{2}{3}} \mathcal{I}_1 - 3)} J^{-\frac{2}{3}} \\ &\quad \left\{ \left[ -\frac{2}{3} (b J^{-\frac{2}{3}} \mathcal{I}_1 + 1) (\mathbf{F}^{-T})_{ij} + 2b J^{-\frac{2}{3}} F_{ij} \right] \left( F_{kl} - \frac{\mathcal{I}_1}{3} (\mathbf{F}^{-T})_{kl} \right) \right. \\ &\quad \left. + \left[ \delta_{ki} \delta_{jl} - \frac{2}{3} F_{ij} (\mathbf{F}^{-T})_{kl} + \frac{\mathcal{I}_1}{3} (\mathbf{F}^{-T})_{il} (\mathbf{F}^{-T})_{kj} \right] \right\}. \end{aligned}$$



$$\begin{aligned}
 \frac{\partial P_{kl}^{E,4f}}{\partial F_{ij}} &= 2a_f \frac{\partial(e^{b_f(\mathcal{I}_{4f}-1)^2})}{\partial F_{ij}} (\mathcal{I}_{4f} - 1) (\mathbf{f} \otimes \mathbf{f}_0)_{kl} \\
 &\quad + 2a_f e^{b_f(\mathcal{I}_{4f}-1)^2} \frac{\partial(\mathcal{I}_{4f} - 1)}{\partial F_{ij}} (\mathbf{f} \otimes \mathbf{f}_0)_{kl} \\
 &\quad + 2a_f e^{b_f(\mathcal{I}_{4f}-1)^2} (\mathcal{I}_{4f} - 1) \frac{\partial(\mathbf{f} \otimes \mathbf{f}_0)_{kl}}{\partial F_{ij}} \\
 &= 2a_f e^{b_f(\mathcal{I}_{4f}-1)^2} \left\{ 2 \left( 2b_f (\mathcal{I}_{4f} - 1)^2 + 1 \right) (\mathbf{f} \otimes \mathbf{f}_0)_{kl} (\mathbf{f} \otimes \mathbf{f}_0)_{ij} + (\mathcal{I}_{4f} - 1) \delta_{ki} (\mathbf{f}_0 \otimes \mathbf{f}_0)_{jl} \right\}.
 \end{aligned}$$

$$\begin{aligned}
 \frac{\partial P_{kl}^{E,4s}}{\partial F_{ij}} &= 2a_s \frac{\partial(e^{b_s(\mathcal{I}_{4s}-1)^2})}{\partial F_{ij}} (\mathcal{I}_{4s} - 1) (\mathbf{s} \otimes \mathbf{s}_0)_{kl} \\
 &\quad + 2a_s e^{b_s(\mathcal{I}_{4s}-1)^2} \frac{\partial(\mathcal{I}_{4s} - 1)}{\partial F_{ij}} (\mathbf{s} \otimes \mathbf{s}_0)_{kl} \\
 &\quad + 2a_s e^{b_s(\mathcal{I}_{4s}-1)^2} (\mathcal{I}_{4s} - 1) \frac{\partial(\mathbf{s} \otimes \mathbf{s}_0)_{kl}}{\partial F_{ij}} \\
 &= 2a_s e^{b_s(\mathcal{I}_{4s}-1)^2} \left\{ 2 \left( 2b_s (\mathcal{I}_{4s} - 1)^2 + 1 \right) (\mathbf{s} \otimes \mathbf{s}_0)_{kl} (\mathbf{s} \otimes \mathbf{s}_0)_{ij} + (\mathcal{I}_{4s} - 1) \delta_{ki} (\mathbf{s}_0 \otimes \mathbf{s}_0)_{jl} \right\}.
 \end{aligned}$$

$$\begin{aligned}
 \frac{\partial P_{kl}^{E,8fs}}{\partial F_{ij}} &= a_{fs} \frac{\partial(e^{b_{fs}(\mathcal{I}_{8fs})^2})}{\partial F_{zq}} \mathcal{I}_{8fs} ((\mathbf{f} \otimes \mathbf{s}_0)_{kp} + (\mathbf{s} \otimes \mathbf{f}_0)_{kp}) \\
 &\quad + a_{fs} e^{b_{fs}(\mathcal{I}_{8fs})^2} \frac{\partial \mathcal{I}_{8fs}}{\partial F_{zq}} ((\mathbf{f} \otimes \mathbf{s}_0)_{kp} + (\mathbf{s} \otimes \mathbf{f}_0)_{kp}) \\
 &\quad + a_{fs} e^{b_{fs}(\mathcal{I}_{8fs})^2} \mathcal{I}_{8fs} \frac{\partial ((\mathbf{f} \otimes \mathbf{s}_0)_{kp} + (\mathbf{s} \otimes \mathbf{f}_0)_{kp})}{\partial F_{zq}} \\
 &= a_{fs} e^{b_{fs}\mathcal{I}_{8fs}^2} \left\{ (2b_{fs}\mathcal{I}_{8fs}^2 + 1) (\mathbf{f} \otimes \mathbf{s}_0 + \mathbf{s} \otimes \mathbf{f}_0)_{ij} (\mathbf{f} \otimes \mathbf{s}_0 + \mathbf{s} \otimes \mathbf{f}_0)_{kl} \right. \\
 &\quad \left. + \delta_{ki} \mathcal{I}_{8fs} ((\mathbf{f}_0 \otimes \mathbf{s}_0) + (\mathbf{s}_0 \otimes \mathbf{f}_0))_{jl} \right\}.
 \end{aligned}$$

$$\frac{\partial P_{kl}^{E,vol}}{\partial F_{ij}} = \frac{B}{2} J(2 + J \log(J)) \left( \mathbf{F}^{-T} \right)_{ij} \left( \mathbf{F}^{-T} \right)_{kl} - (J + J \log(J) - 1) \left( \mathbf{F}^{-T} \right)_{il} \left( \mathbf{F}^{-T} \right)_{kj}.$$



# Bibliography

- [Ahrens et al., 2005] Ahrens, J., Geveci, B., Law, C., Hansen, C., and Johnson, C. (2005). ParaView: An end-user tool for large-data visualization. *The visualization handbook*, 717.
- [Akhgari et al., 2017] Akhgari, M., Mobaraki, H., and Etemadi-Aleagha, A. (2017). Histopathological study of cardiac lesions in methamphetamine poisoning-related deaths. *DARU Journal of Pharmaceutical Sciences*, 25(1):5.
- [Aliev and Panfilov, 1996] Aliev, R. and Panfilov, A. (1996). A simple two-variable model of cardiac excitation. *Chaos, Solitons & Fractals*, 7(3):293–301.
- [Allgower and Georg, 2012] Allgower, E. and Georg, K. (2012). *Numerical continuation methods: an introduction*, volume 13. Springer Science & Business Media.
- [Altman and Dittmer, 1971] Altman, P. and Dittmer, D. (1971). Respiration and circulation. Technical report, Federation of American Societies for Experimental Biology Bethesda MD.
- [Ambrosi et al., 2011] Ambrosi, D., Arioli, G., Nobile, F., and Quarteroni, A. (2011). Electromechanical coupling in cardiac dynamics: the active strain approach. *SIAM Journal on Applied Mathematics*, 71(2):605–621.
- [Ambrosi and Pezzuto, 2012] Ambrosi, D. and Pezzuto, S. (2012). Active stress vs. active strain in mechanobiology: constitutive issues. *Journal of Elasticity*, 107(2):199–212.
- [Antiga et al., 2008] Antiga, L., Piccinelli, M., Botti, L., Ene-Iordache, B., Remuzzi, A., and Steinman, D. (2008). An image-based modeling framework for patient-specific computational hemodynamics. *Medical & biological engineering & computing*, 46(11):1097.
- [Ascher et al., 1997] Ascher, U., Ruuth, S., and Spiteri, R. (1997). Implicit-explicit runge-kutta methods for time-dependent partial differential equations. *Applied Numerical Mathematics*, 25(2-3):151–167.
- [Augustin et al., 2016] Augustin, C., Neic, A., Liebmann, M., Prassl, A., Niederer, S., Haase, G., and Plank, G. (2016). Anatomically accurate high resolution modeling of

## Bibliography

---

- human whole heart electromechanics: a strongly scalable algebraic multigrid solver method for nonlinear deformation. *Journal of computational physics*, 305:622–646.
- [Badia et al., 2008] Badia, S., Nobile, F., and Vergara, C. (2008). Fluid-structure partitioned procedures based on Robin transmission conditions. *Journal of Computational Physics*, 227(14):7027–7051.
- [Baillargeon et al., 2014] Baillargeon, B., Rebelo, N., Fox, D., Taylor, R. L., and Kuhl, E. (2014). The living heart project: a robust and integrative simulator for human heart function. *European Journal of Mechanics-A/Solids*, 48:38–47.
- [Barbarotta, 2014] Barbarotta, L. (2014). A mathematical and numerical study of the left ventricular contraction based on the reconstruction of a patient specific geometry.
- [Barbarotta et al., 2017] Barbarotta, L., Rossi, S., Dedè, L., and Quarteroni, A. (2017). Numerical validation of a transmurally heterogeneous orthotropic activation model for ventricular contraction. *MOX report*.
- [Bathe et al., 1999] Bathe, K., Zhang, H., and Ji, S. (1999). Finite element analysis of fluid flows fully coupled with structural interactions. *Computers & Structures*, 72(1-3):1–16.
- [Bauer and Bischof, 2008] Bauer, C. and Bischof, H. (2008). Edge based tube detection for coronary artery centerline extraction. *The Insight Journal*.
- [Bayer et al., 2012] Bayer, J., Blake, R., Plank, G., and Trayanova, N. (2012). A novel rule-based algorithm for assigning myocardial fiber orientation to computational heart models. *Annals of biomedical engineering*, 40(10):2243–2254.
- [Bazilevs et al., 2007] Bazilevs, Y., Calo, V., Cottrell, J., Hughes, T., Reali, A., and Scovazzi, G. (2007). Variational multiscale residual-based turbulence modeling for large eddy simulation of incompressible flows. *Computer Methods in Applied Mechanics and Engineering*, 197(1):173–201.
- [Bazilevs et al., 2008] Bazilevs, Y., Calo, V., Hughes, T., and Zhang, Y. (2008). Isogeometric fluid-structure interaction: theory, algorithms, and computations. *Computational Mechanics*, 43(1):3–37.
- [Bazilevs et al., 2009] Bazilevs, Y., Gohean, J., Hughes, T., Moser, R., and Zhang, Y. (2009). Patient-specific isogeometric fluid-structure interaction analysis of thoracic aortic blood flow due to implantation of the Jarvik 2000 left ventricular assist device. *Computer Methods in Applied Mechanics and Engineering*, 198(45-46):3534–3550.
- [Bazilevs et al., 2013] Bazilevs, Y., Takizawa, K., and Tezduyar, T. (2013). *Computational Fluid-Structure Interaction: Methods and Applications*. John Wiley & Sons.

- [Béchet et al., 2002] Béchet, E., Cuilliere, J., and Trochu, F. (2002). Generation of a finite element mesh from stereolithography (stl) files. *Computer-Aided Design*, 34(1):1–17.
- [Bordas et al., 2010] Bordas, R., Grau, V., Burton, R., Hales, P., Schneider, J., Gavaghan, D., Kohl, P., and Rodriguez, B. (2010). Integrated approach for the study of anatomical variability in the cardiac purkinje system: from high resolution mri to electrophysiology simulation. In *Engineering in Medicine and Biology Society (EMBC), 2010 Annual International Conference of the IEEE*, pages 6793–6796. IEEE.
- [Bourgault et al., 2009] Bourgault, Y., Coudiere, Y., and Pierre, C. (2009). Existence and uniqueness of the solution for the bidomain model used in cardiac electrophysiology. *Nonlinear analysis: Real world applications*, 10(1):458–482.
- [Boyett et al., 1991] Boyett, M., Frampton, J., and Kirby, M. (1991). The length, width and volume of isolated rat and ferret ventricular myocytes during twitch contractions and changes in osmotic strength. *Experimental Physiology*, 76(2):259–270.
- [Briggs et al., 2000] Briggs, W., Henson, V., and McCormick, S. (2000). *A multigrid tutorial*. SIAM.
- [Brooks and Hughes, 1982] Brooks, A. and Hughes, T. (1982). Streamline upwind/Petrov-Galerkin formulations for convection dominated flows with particular emphasis on the incompressible Navier-Stokes equations. *Computer methods in applied mechanics and engineering*, 32(1-3):199–259.
- [Brooks and Lu, 1972] Brooks, C. and Lu, H. (1972). *The sinoatrial pacemaker of the heart*. Charles C. Thomas Publisher.
- [Bueno-Orovio et al., 2008] Bueno-Orovio, A., Cherry, E., and Fenton, F. (2008). Minimal model for human ventricular action potentials in tissue. *Journal of Theoretical Biology*, 253(3):544–560.
- [Burman and Ern, 2003] Burman, E. and Ern, A. (2003). The discrete maximum principle for stabilized finite element methods. In *Numerical Mathematics and Advanced Applications*, pages 557–566. Springer.
- [Burns et al., 2002] Burns, R., Gibbons, R., Yi, Q., Roberts, R., Miller, T., Schaer, G., Anderson, J., and Yusuf, S. (2002). The relationships of left ventricular ejection fraction, end-systolic volume index and infarct size to six-month mortality after hospital discharge following myocardial infarction treated by thrombolysis. *Journal of the American College of Cardiology*, 39(1):30–36.
- [Cassidy et al., 1984] Cassidy, D., Vassallo, J., Marchlinski, F., Buxton, A., Untereker, W., and Josephson, M. (1984). Endocardial mapping in humans in sinus rhythm with normal left ventricles: activation patterns and characteristics of electrograms. *Circulation*, 70(1):37–42.

## Bibliography

---

- [Causin et al., 2005] Causin, P., Gerbeau, J., and Nobile, F. (2005). Added-mass effect in the design of partitioned algorithms for fluid–structure problems. *Computer Methods in Applied Mechanics and Engineering*, 194(42):4506–4527.
- [Cellier and Kofman, 2006] Cellier, F. and Kofman, E. (2006). *Continuous system simulation*. Springer Science & Business Media.
- [Chapelle et al., 2009] Chapelle, D., Fernández, M., Gerbeau, J., Moireau, P., Sainte-Marie, J., and Zemzemi, N. (2009). Numerical simulation of the electromechanical activity of the heart. *Functional Imaging and Modeling of the Heart*, pages 357–365.
- [Chen et al., 1997] Chen, C., Nevo, E., Fetters, B., Pak, P., Yin, F., Maughan, W., and Kass, D. (1997). Estimation of central aortic pressure waveform by mathematical transformation of radial tonometry pressure: validation of generalized transfer function. *Circulation*, 95(7):1827–1836.
- [Chen et al., 2012] Chen, M., Kaufman, A., and Yagel, R. (2012). *Volume graphics*. Springer Science & Business Media.
- [Chen and Womersley, 2006] Chen, X. and Womersley, R. (2006). Existence of solutions to systems of underdetermined equations and spherical designs. *SIAM Journal on Numerical Analysis*, 44(6):2326–2341.
- [Chen and Yamamoto, 1994] Chen, X. and Yamamoto, T. (1994). Newton-like methods for solving underdetermined nonlinear equations with nondifferentiable terms. *Journal of Computational and Applied Mathematics*, 55(3):311–324.
- [Cheng et al., 2005] Cheng, A., Langer, F., Rodriguez, F., Criscione, J., Daughters, G., Miller, D., and Ingels, N. (2005). Transmural cardiac strains in the lateral wall of the ovine left ventricle. *American Journal of Physiology-Heart and Circulatory Physiology*, 288(4):H1546–H1556.
- [Cherubini et al., 2008] Cherubini, C., Filippi, S., Nardinocchi, P., and Teresi, L. (2008). An electromechanical model of cardiac tissue: Constitutive issues and electrophysiological effects. *Progress in Biophysics and Molecular Biology*, 97(2):562–573.
- [Cho and Kensey, 1991] Cho, Y. and Kensey, K. (1991). Effects of the non-Newtonian viscosity of blood on flows in a diseased arterial vessel. part 1: steady flows. *Biorheology*, 28(3-4):241–262.
- [Cignoni et al., 2008] Cignoni, P., Callieri, M., Corsini, M., Dellepiane, M., Ganovelli, F., and Ranzuglia, G. (2008). Meshlab: an open-source mesh processing tool. In *Eurographics Italian Chapter Conference*, volume 2008, pages 129–136.
- [Codreanu et al., 2010] Codreanu, I., Robson, M., Golding, S., Jung, B. A., Clarke, K., and Holloway, C. (2010). Longitudinally and circumferentially directed movements of the left ventricle studied by cardiovascular magnetic resonance phase contrast velocity mapping. *Journal of Cardiovascular Magnetic Resonance*, 12(1):48.

- 
- [Colciago, 2014] Colciago, C. (2014). *Reduced order fluid-structure interaction models for haemodynamics applications*. PhD thesis, EPFL.
- [Colli Franzone et al., 2015a] Colli Franzone, P., Pavarino, L., and Scacchi, S. (2015a). Parallel multilevel solvers for the cardiac electro-mechanical coupling. *Applied Numerical Mathematics*, 95:140–153.
- [Colli Franzone et al., 2015b] Colli Franzone, P., Pavarino, L., and Scacchi, S. (2015b). Relationship between cardiac electrical and mechanical activation markers by coupling Bidomain and deformation models. In *International Conference on Functional Imaging and Modeling of the Heart*, pages 304–312. Springer.
- [Colli Franzone et al., 2016a] Colli Franzone, P., Pavarino, L., and Scacchi, S. (2016a). Joint influence of transmural heterogeneities and wall deformation on cardiac bioelectrical activity: a simulation study. *Mathematical biosciences*, 280:71–86.
- [Colli Franzone et al., 2017] Colli Franzone, P., Pavarino, L., and Scacchi, S. (2017). Effects of mechanical feedback on the stability of cardiac scroll waves: a bidomain electro-mechanical simulation study. *Chaos: An Interdisciplinary Journal of Nonlinear Science*, 27(9).
- [Colli Franzone et al., 2006] Colli Franzone, P., Pavarino, L. F., and Savaré, G. (2006). Computational electrocardiology: mathematical and numerical modeling. In *Complex Systems in Biomedicine*, pages 187–241. Springer.
- [Colli Franzone et al., 2016b] Colli Franzone, P., Pavarino, L. F., and Scacchi, S. (2016b). Bioelectrical effects of mechanical feedbacks in a strongly coupled cardiac electro-mechanical model. *Mathematical Models and Methods in Applied Sciences*, 26(01):27–57.
- [Costa et al., 2001] Costa, K., Holmes, J., and McCulloch, A. (2001). Modelling cardiac mechanical properties in three dimensions. *Philosophical Transactions of the Royal Society of London A: Mathematical, Physical and Engineering Sciences*, 359(1783):1233–1250.
- [Costa et al., 1999] Costa, K., Takayama, Y., McCulloch, A., and Covell, J. (1999). Laminar fiber architecture and three-dimensional systolic mechanics in canine ventricular myocardium. *American Journal of Physiology-Heart and Circulatory Physiology*, 276(2):H595–H607.
- [Costabal et al., 2017] Costabal, F., Concha, F., Hurtado, D., and Kuhl, E. (2017). The importance of mechano-electrical feedback and inertia in cardiac electromechanics. *Computer Methods in Applied Mechanics and Engineering*, 320:352–368.
- [Coupé et al., 2011] Coupé, P., Manjón, J. V., Fonov, V., Pruessner, J., Robles, M., and Collins, D. (2011). Patch-based segmentation using expert priors: Application to hippocampus and ventricle segmentation. *NeuroImage*, 54(2):940–954.

## Bibliography

---

- [Crosetto, 2011] Crosetto, P. (2011). Fluid–structure interaction problems in hemodynamics: parallel solvers, preconditioners, and applications. PhD thesis, EPFL, Switzerland, 2011.
- [Crosetto et al., 2011a] Crosetto, P., Deparis, S., Fourestey, G., and Quarteroni, A. (2011a). Parallel algorithms for fluid-structure interaction problems in haemodynamics. *SIAM Journal on Scientific Computing*, 33(4):1598–1622.
- [Crosetto et al., 2011b] Crosetto, P., Reymond, P., Deparis, S., Kontaxakis, D., Stergiopoulos, N., and Quarteroni, A. (2011b). Fluid–structure interaction simulation of aortic blood flow. *Computers & Fluids*, 43(1):46–57.
- [Crozier et al., 2016] Crozier, A., Augustin, C., Neic, A., Prassl, A., Holler, M., Fastl, T., Hennemuth, A., Bredies, K., Kuehne, T., and Bishop, M. (2016). Image-based personalization of cardiac anatomy for coupled electromechanical modeling. *Annals of biomedical engineering*, 44(1):58–70.
- [Dal et al., 2011] Dal, H., Göktepe, S., Kaliske, M., and Kuhl, E. (2011). A three-field, bi-domain based approach to the strongly coupled electromechanics of the heart. *Proceedings in Applied Mathematics and Mechanics*, 11(1):931–934.
- [Dal et al., 2013] Dal, H., Göktepe, S., Kaliske, M., and Kuhl, E. (2013). A fully implicit finite element method for bidomain models of cardiac electromechanics. *Computer Methods in Applied Mechanics and Engineering*, 253:323–336.
- [Davis et al., 1992] Davis, M., Donovan, J., and Hood, J. (1992). Stretch-activated single-channel and whole cell currents in vascular smooth muscle cells. *American Journal of Physiology-Cell Physiology*, 262(4):C1083–C1088.
- [De Hart et al., 2003] De Hart, J., Peters, G., Schreurs, P., and Baaijens, F. (2003). A three-dimensional computational analysis of fluid–structure interaction in the aortic valve. *Journal of biomechanics*, 36(1):103–112.
- [De Vito and Qian, 1995] De Vito, R. and Qian, J. (1995). Automatic identification of the long axis of the left ventricle from nuclear medicine spect data for use in myocardial perfusion studies. US Patent 5,421,331.
- [Demiray, 1976] Demiray, H. (1976). Stresses in ventricular wall. *Journal of Applied Mechanics*, 43(2):194–197.
- [Deparis et al., 2006] Deparis, S., Discacciati, M., Fourestey, G., and Quarteroni, A. (2006). Fluid–structure algorithms based on Steklov–Poincaré operators. *Computer Methods in Applied Mechanics and Engineering*, 195(41):5797–5812.
- [Deparis et al., 2016a] Deparis, S., Forti, D., Gervasio, P., and Quarteroni, A. (2016a). INTERNODES: an accurate interpolation-based method for coupling the galerkin solutions of pdes on subdomains featuring non-conforming interfaces. *Computers & Fluids*, 141:22–41.



- 
- [Deparis et al., 2016b] Deparis, S., Forti, D., Grandperrin, G., and Quarteroni, A. (2016b). FaCSI: A block parallel preconditioner for fluid-structure interaction in hemodynamics. *Journal of Computational Physics*, 327:700–718.
- [Deparis et al., 2014] Deparis, S., Forti, D., and Quarteroni, A. (2014). A rescaled localized radial basis function interpolation on non-cartesian and nonconforming grids. *SIAM Journal on Scientific Computing*, 36(6):A2745–A2762.
- [Dill and Costill, 1974] Dill, D. and Costill, D. (1974). Calculation of percentage changes in volumes of blood, plasma, and red cells in dehydration. *Journal of Applied Physiology*, 37(2):247–248.
- [Dokos et al., 2002] Dokos, S., Smaill, B., Young, A., and LeGrice, I. (2002). Shear properties of passive ventricular myocardium. *American Journal of Physiology-Heart and Circulatory Physiology*, 283(6):H2650–H2659.
- [Donea et al., 1982] Donea, J., Giuliani, S., and Halleux, J. (1982). An arbitrary Lagrangian-Eulerian finite element method for transient dynamic fluid-structure interactions. *Computer methods in applied mechanics and engineering*, 33(1-3):689–723.
- [Eck et al., 2016] Eck, V., Donders, W., Sturdy, J., Feinberg, J., Delhaas, T., Hellevik, L., and Huberts, W. (2016). A guide to uncertainty quantification and sensitivity analysis for cardiovascular applications. *International journal for numerical methods in biomedical engineering*, 32(8).
- [Elman et al., 2008] Elman, H., Howle, V., Shadid, J., Shuttleworth, R., and Tuminaro, R. (2008). A taxonomy and comparison of parallel block multi-level preconditioners for the incompressible Navier–Stokes equations. *Journal of Computational Physics*, 227(3):1790–1808.
- [Eriksson et al., 2013] Eriksson, T., Prassl, A., Plank, G., and Holzapfel, G. (2013). Influence of myocardial fiber/sheet orientations on left ventricular mechanical contraction. *Mathematics and Mechanics of Solids*, 18(6):592–606.
- [Ethier and Bourgault, 2008] Ethier, M. and Bourgault, Y. (2008). Semi-implicit time-discretization schemes for the bidomain model. *SIAM Journal on Numerical Analysis*, 46(5):2443–2468.
- [Faggiano et al., 2013] Faggiano, E., Antiga, L., Puppini, G., Quarteroni, A., Luciani, G., and Vergara, C. (2013). Helical flows and asymmetry of blood jet in dilated ascending aorta with normally functioning bicuspid valve. *Biomechanics and modeling in mechanobiology*, 12(4):801–813.
- [Fedele et al., 2015] Fedele, M., Faggiano, E., Barbarotta, L., Cremonesi, F., Formaggia, L., and Perotto, S. (2015). Semi-automatic three-dimensional vessel segmentation using a connected component localization of the region-scalable fitting energy. In

## Bibliography

---

- Image and Signal Processing and Analysis (ISPA), 2015 9th International Symposium on*, pages 72–77. IEEE.
- [Fedorov et al., 2012] Fedorov, A., Beichel, R., Kalpathy-Cramer, J., Finet, J., Fillion-Robin, J.C. and Pujol, S., Bauer, C., Jennings, D., Fennessy, F., and Sonka, M. (2012). 3D Slicer as an image computing platform for the Quantitative Imaging Network. *Magnetic Resonance Imaging*, 30(9):1323–1341.
- [Fernandez-Teran and Hurle, 1982] Fernandez-Teran, M. and Hurle, J. (1982). Myocardial fiber architecture of the human heart ventricles. *The Anatomical Record*, 204(2):137–147.
- [Fletcher et al., 1981] Fletcher, P., Pfeffer, J., Pfeffer, M., and Braunwald, E. (1981). Left ventricular diastolic pressure-volume relations in rats with healed myocardial infarction. effects on systolic function. *Circulation research*, 49(3):618–626.
- [Folk et al., 1999] Folk, M., Cheng, A., and Yates, K. (1999). HDF5: a file format and I/O library for high performance computing applications. In *Proceedings of supercomputing*, volume 99, pages 5–33.
- [Folk et al., 2011] Folk, M., Heber, G., Koziol, Q., Pourmal, E., and Robinson, D. (2011). An overview of the HDF5 technology suite and its applications. In *Proceedings of the EDBT/ICDT 2011 Workshop on Array Databases*, pages 36–47. ACM.
- [Formaggia et al., 2010] Formaggia, L., Quarteroni, A., and Veneziani, A. (2010). *Cardiovascular Mathematics: Modeling and Simulation of the Circulatory System*, volume 1. Springer Science & Business Media.
- [Forti, 2016] Forti, D. (2016). Parallel algorithms for the solution of large-scale fluid-structure interaction problems in hemodynamics. PhD thesis, EPFL, Switzerland.
- [Forti et al., 2016] Forti, D., Bukac, M., Quaini, A., Canic, S., and Deparis, S. (2016). A monolithic approach to fluid-composite structure interaction. *Journal of Scientific Computing*, pages 1–26.
- [Forti and Dedè, 2015] Forti, D. and Dedè, L. (2015). Semi-implicit BDF time discretization of the Navier-Stokes equations with VMS-LES modeling in a high performance computing framework. *Computers & Fluids*, 117:168–182.
- [Franzone et al., 2005] Franzone, P. C., Pavarino, L., and Taccardi, B. (2005). Simulating patterns of excitation, repolarization and action potential duration with cardiac bidomain and monodomain models. *Mathematical biosciences*, 197(1):35–66.
- [Frey, 2001] Frey, P. (2001). *Medit: an interactive mesh visualization software*. PhD thesis, INRIA.

- 
- [Gaudron et al., 1993] Gaudron, P., Eilles, C., Kugler, I., and Ertl, G. (1993). Progressive left ventricular dysfunction and remodeling after myocardial infarction. potential mechanisms and early predictors. *Circulation*, 87(3):755–763.
- [Gee et al., 2011] Gee, M., Küttler, U., and Wall, W. (2011). Truly monolithic algebraic multigrid for fluid–structure interaction. *International Journal for Numerical Methods in Engineering*, 85(8):987–1016.
- [Gee et al., 2006] Gee, M., Siefert, C., Hu, J., Tuminaro, R., and Sala, M. (2006). Ml 5.0 smoothed aggregation user’s guide. Technical report, Technical Report SAND2006-2649, Sandia National Laboratories.
- [Gerbeau and Vidrascu, 2003] Gerbeau, J. and Vidrascu, M. (2003). A quasi-Newton algorithm based on a reduced model for fluid-structure interaction problems in blood flows. *ESAIM: Mathematical Modelling and Numerical Analysis-Modélisation Mathématique et Analyse Numérique*, 37(4):631–647.
- [Gerbi et al., 2017] Gerbi, A., Dedè, L., and Quarteroni, A. (2017). A monolithic algorithm for the simulation of cardiac electromechanics in the human left ventricle. *Accepted for publication in Mathematics in Engineering*. (DOI: 10.3934/Mine.2018.1.1).
- [Gerbi et al., 2018] Gerbi, A., Dedè, L., and Quarteroni, A. (2018). Segregated algorithms for the numerical simulation of cardiac electromechanics in the left human ventricle. *Submitted to Journal of Scientific Computing*.
- [Gervasio et al., 2006] Gervasio, P., Saleri, F., and Veneziani, A. (2006). Algebraic fractional–step schemes with spectral methods for the incompressible navier–stokes equations. *Journal of Computational Physics*, 214(1):347–365.
- [Geuzaine and Remacle, 2009] Geuzaine, C. and Remacle, J. (2009). Gmsh: A 3D finite element mesh generator with built-in pre-and post-processing facilities. *International journal for numerical methods in engineering*, 79(11):1309–1331.
- [Giantesio and Musesti, 2017a] Giantesio, G. and Musesti, A. (2017a). A continuum model of skeletal muscle tissue with loss of activation. *arXiv preprint arXiv:1701.07823*.
- [Giantesio and Musesti, 2017b] Giantesio, G. and Musesti, A. (2017b). On the modeling of internal parameters in hyperelastic biological materials. *arXiv preprint arXiv:1609.08651*.
- [Gilbert et al., 2007] Gilbert, S., Benson, S., Li, P., and Holden, A. (2007). Regional localisation of left ventricular sheet structure: integration with current models of cardiac fibre, sheet and band structure. *European Journal of Cardio-Thoracic Surgery*, 32(2):231–249.
- [Godunov, 1959] Godunov, S. (1959). A difference method for numerical calculation of discontinuous solutions of the equations of hydrodynamics. *Matematicheskii Sbornik*, 89(3):271–306.

## Bibliography

---

- [Göktepe and Kuhl, 2010] Göktepe, S. and Kuhl, E. (2010). Electromechanics of the heart: a unified approach to the strongly coupled excitation–contraction problem. *Computational Mechanics*, 45(2-3):227–243.
- [Gordon et al., 1966] Gordon, A., Huxley, A., and Julian, F. (1966). The variation in isometric tension with sarcomere length in vertebrate muscle fibres. *The Journal of Physiology*, 184(1):170.
- [Grama, 2003] Grama, A. (2003). *Introduction to parallel computing*. Pearson Education.
- [Griffin et al., 2008] Griffin, B., Topol, E., Nair, D., and Ashley, K. (2008). *Manual of cardiovascular medicine*. Lippincott Williams & Wilkins.
- [Guccione et al., 1995] Guccione, J., Costa, K., and McCulloch, A. (1995). Finite element stress analysis of left ventricular mechanics in the beating dog heart. *Journal of biomechanics*, 28(10):1167–1177.
- [Guccione and McCulloch, 1991] Guccione, J. and McCulloch, A. (1991). Finite element modeling of ventricular mechanics. In *Theory of Heart*, pages 121–144. Springer.
- [Haralick and Shapiro, 1985] Haralick, R. and Shapiro, L. (1985). Image segmentation techniques. *Computer Vision, Graphics, and Image Processing*, 29(1):100–132.
- [Heidenreich et al., 2010] Heidenreich, E., Ferrero, J., Doblaré, M., and Rodríguez, J. (2010). Adaptive macro finite elements for the numerical solution of monodomain equations in cardiac electrophysiology. *Annals of biomedical engineering*, 38(7):2331–2345.
- [Hernández-Gascón et al., 2013] Hernández-Gascón, B., Grasa, J., Calvo, B., and Rodríguez, J. (2013). A 3D electro-mechanical continuum model for simulating skeletal muscle contraction. *Journal of theoretical biology*, 335:108–118.
- [Hirschvogel et al., 2017] Hirschvogel, M., Bassilious, M., Jagschies, L., Wildhirt, S., and Gee, M. (2017). A monolithic 3D–0D coupled closed-loop model of the heart and the vascular system: experiment-based parameter estimation for patient-specific cardiac mechanics. *International Journal for Numerical Methods in Biomedical Engineering*.
- [Hodgkin and Huxley, 1952] Hodgkin, A. and Huxley, A. (1952). A quantitative description of membrane current and its application to conduction and excitation in nerve. *The Journal of Physiology*, 117(4):500–544.
- [Hoffman and Cranefield, 1960] Hoffman, B. F. and Cranefield, P. F. (1960). *Electrophysiology of the Heart*. McGraw-Hill, Blakiston Division.
- [Holzapfel and Ogden, 2009] Holzapfel, G. and Ogden, R. (2009). Constitutive modelling of passive myocardium: a structurally based framework for material characterization. *Philosophical Transactions of the Royal Society of London A: Mathematical, Physical and Engineering Sciences*, 367(1902):3445–3475.

- [Holzapfel and Ogden, 2015] Holzapfel, G. and Ogden, R. (2015). On the tension-compression switch in soft fibrous solids. *European Journal of Mechanics-A/Solids*, 49:561–569.
- [Hoogendoorn et al., 2013] Hoogendoorn, C., Duchateau, N., Sánchez-Quintana, D., Whitmarsh, T., Sukno, F., De Craene, M., Lekadir, K., and Frangi, A. (2013). A high-resolution atlas and statistical model of the human heart from multislice CT. *IEEE transactions on medical imaging*, 32(1):28–44.
- [Hoshino et al., 1983] Hoshino, T., Fujiwara, H., Kawai, C., and Hamashima, Y. (1983). Myocardial fiber diameter and regional distribution in the ventricular wall of normal adult hearts, hypertensive hearts and hearts with hypertrophic cardiomyopathy. *Circulation*, 67(5):1109–1116.
- [Hoyt et al., 1989] Hoyt, R., Cohen, M., and Saffitz, J. (1989). Distribution and three-dimensional structure of intercellular junctions in canine myocardium. *Circulation Research*, 64(3):563–574.
- [Hron and Turek, 2006] Hron, J. and Turek, S. (2006). A monolithic FEM/multigrid solver for an ALE formulation of fluid-structure interaction with applications in biomechanics. In *Fluid-structure interaction*, pages 146–170. Springer.
- [Hsu et al., 1998] Hsu, E., Muzikant, A., Matulevicius, S., Penland, R., and Henriquez, C. (1998). Magnetic resonance myocardial fiber-orientation mapping with direct histological correlation. *American Journal of Physiology - Heart and Circulatory Physiology*, 274(5):H1627–H1634.
- [Hsu and Bazilevs, 2011] Hsu, M. and Bazilevs, Y. (2011). Blood vessel tissue prestress modeling for vascular fluid–structure interaction simulation. *Finite Elements in Analysis and Design*, 47(6):593–599.
- [Hu et al., 2001] Hu, H., Patankar, N., and Zhu, M. (2001). Direct numerical simulations of fluid–solid systems using the arbitrary Lagrangian–Eulerian technique. *Journal of Computational Physics*, 169(2):427–462.
- [Hughes et al., 2000] Hughes, T., Mazzei, L., and Jansen, K. (2000). Large eddy simulation and the variational multiscale method. *Computing and Visualization in Science*, 3(1-2):47–59.
- [Hughes et al., 2001] Hughes, T., Oberai, A., and Mazzei, L. (2001). Large eddy simulation of turbulent channel flows by the variational multiscale method. *Physics of fluids*, 13(6):1784–1799.
- [Humphrey et al., 1990] Humphrey, J., Strumpf, R., and Yin, F. (1990). Determination of a constitutive relation for passive myocardium: I. a new functional form. *Journal of Biomechanical Engineering*, 112(3):333–339.

## Bibliography

---

- [Humphrey and Yin, 1987] Humphrey, J. and Yin, F. (1987). On constitutive relations and finite deformations of passive cardiac tissue: I. a pseudostrain-energy function. *Journal of Biomechanical Engineering*, 109(4):298–304.
- [Hunter et al., 1997] Hunter, P., Nash, M., and Sands, G. (1997). Computational electromechanics of the heart. *Computational Biology of the Heart*, 12:347–407.
- [Huxley and Kress, 1985] Huxley, H. and Kress, M. (1985). Crossbridge behaviour during muscle contraction. *Journal of Muscle Research & Cell Motility*, 6(2):153–161.
- [Isgum et al., 2009] Isgum, I., Staring, M., Rutten, A., Prokop, M., V., M., and Van Ginneken, B. (2009). Multi-atlas-based segmentation with local decision fusion – application to cardiac and aortic segmentation in ct scans. *IEEE transactions on medical imaging*, 28(7):1000–1010.
- [Janela et al., 2010] Janela, J., Moura, A., and Sequeira, A. (2010). A 3d non-newtonian fluid–structure interaction model for blood flow in arteries. *Journal of Computational and Applied Mathematics*, 234(9):2783–2791.
- [Jarvik, 1981] Jarvik, R. (1981). The total artificial heart. *Scientific American*, 244(1):74–81.
- [Johnston et al., 2004] Johnston, B., Johnston, P., Corney, S., and Kilpatrick, D. (2004). Non-Newtonian blood flow in human right coronary arteries: steady state simulations. *Journal of Biomechanics*, 37(5):709–720.
- [Kamkin et al., 2000] Kamkin, A., Kiseleva, I., and Isenberg, G. (2000). Stretch-activated currents in ventricular myocytes: amplitude and arrhythmogenic effects increase with hypertrophy. *Cardiovascular research*, 48(3):409–420.
- [Katz, 2010] Katz, A. (2010). *Physiology of the Heart*. Lippincott Williams & Wilkins.
- [Keener and Sneyd, 1998] Keener, J. and Sneyd, J. (1998). *Mathematical Physiology*, volume 1. Springer.
- [Keyes et al., 2013] Keyes, D., McInnes, L., Woodward, C., Gropp, W., Myra, E., Pernice, M., Bell, J., Brown, J., Clo, A., and Connors, J. (2013). Multiphysics simulations: Challenges and opportunities. *The International Journal of High Performance Computing Applications*, 27(1):4–83.
- [Kircher et al., 1990] Kircher, B., Himelman, R., and Schiller, N. (1990). Noninvasive estimation of right atrial pressure from the inspiratory collapse of the inferior vena cava. *The American journal of cardiology*, 66(4):493–496.
- [Klabunde, 2011] Klabunde, R. (2011). *Cardiovascular physiology concepts*. Lippincott Williams & Wilkins.

- 
- [Krause et al., 2015] Krause, D., Dickopf, T., Potse, M., and Krause, R. (2015). Towards a large-scale scalable adaptive heart model using shallow tree meshes. *Journal of Computational Physics*, 298:79–94.
- [Krause et al., 2012] Krause, D., Potse, M., Dickopf, T., Krause, R., Auricchio, A., and Prinzen, F. (2012). Hybrid parallelization of a large-scale heart model. In *Facing the Multicore-Challenge II*, pages 120–132. Springer.
- [Krishnamoorthi et al., 2013] Krishnamoorthi, S., Sarkar, M., and Klug, W. (2013). Numerical quadrature and operator splitting in finite element methods for cardiac electrophysiology. *International Journal for Numerical Methods in Biomedical Engineering*, 29(11):1243–1266.
- [Krittian et al., 2010] Krittian, S., Janoske, U., Oertel, H., and Böhlke, T. (2010). Partitioned fluid–solid coupling for cardiovascular blood flow. *Annals of biomedical engineering*, 38(4):1426–1441.
- [Küttler et al., 2010] Küttler, U., Gee, M., Förster, C., Comerford, A., and Wall, W. (2010). Coupling strategies for biomedical fluid–structure interaction problems. *International Journal for Numerical Methods in Biomedical Engineering*, 26(3-4):305–321.
- [Lamponi, 2004] Lamponi, D. (2004). One dimensional and multiscale models for blood flow circulation. PhD thesis, EPFL, Switzerland.
- [Land et al., 2012] Land, S., Niederer, S., and Smith, N. (2012). Efficient computational methods for strongly coupled cardiac electromechanics. *IEEE Transactions on Biomedical Engineering*, 59(5):1219–1228.
- [Landajuela et al., 2017] Landajuela, M., Vergara, C., Gerbi, A., Dede’, L., Formaggia, L., and Quarteroni, A. (2017). Numerical approximation of the electromechanical coupling in the left ventricle with inclusion of the Purkinje network. *Accepted for publication in International Journal for Numerical Methods in Biomedical Engineering (DOI: 10.1002/cnm.2984)*.
- [Le Tallec and Mouro, 2001] Le Tallec, P. and Mouro, J. (2001). Fluid structure interaction with large structural displacements. *Computer methods in applied mechanics and engineering*, 190(24-25):3039–3067.
- [Lee and Schachter, 1980] Lee, D. and Schachter, B. (1980). Two algorithms for constructing a Delaunay triangulation. *International Journal of Computer & Information Sciences*, 9(3):219–242.
- [Lee and Liu, 1967] Lee, E. and Liu, D. (1967). Finite-strain elastic–plastic theory with application to plane-wave analysis. *Journal of Applied Physics*, 38(1):19–27.
- [Lee et al., 2010] Lee, H., Codella, N., Cham, M., Weinsaft, J. W., and Wang, Y. (2010). Automatic left ventricle segmentation using iterative thresholding and an active contour

## Bibliography

---

- model with adaptation on short-axis cardiac mri. *IEEE Transactions on Biomedical Engineering*, 57(4):905–913.
- [LeGrice et al., 2001] LeGrice, I., Hunter, P., Young, A., and Smaill, B. (2001). The architecture of the heart: a data-based model. *Philosophical Transactions of the Royal Society of London A: Mathematical, Physical and Engineering Sciences*, 359(1783):1217–1232.
- [Levick, 2013] Levick, J. (2013). *An introduction to cardiovascular physiology*. Butterworth-Heinemann.
- [Luo and Rudy, 1991] Luo, C. and Rudy, Y. (1991). A model of the ventricular cardiac action potential. Depolarization, repolarization, and their interaction. *Circulation Research*, 68(6):1501–1526.
- [Luo and Rudy, 1994] Luo, C. and Rudy, Y. (1994). A dynamic model of the cardiac ventricular action potential. I. Simulations of ionic currents and concentration changes. *Circulation Research*, 74(6):1071–1096.
- [Manzoni et al., 2016] Manzoni, A., Pagani, S., and Lassila, T. (2016). Accurate solution of Bayesian inverse uncertainty quantification problems combining reduced basis methods and reduction error models. *SIAM/ASA Journal on Uncertainty Quantification*, 4(1):380–412.
- [Marbán, 2002] Marbán, E. (2002). Cardiac channelopathies. *Nature*, 415(6868):213–218.
- [Masci et al., 2017] Masci, A., Alessandrini, M., Forti, D., Menghini, F., Dedé, L., Tommasi, C., Quarteroni, A., and Corsi, C. (2017). A patient-specific computational fluid dynamics model of the left atrium in atrial fibrillation: development and initial evaluation. In *International Conference on Functional Imaging and Modeling of the Heart*, pages 392–400. Springer.
- [Mayr et al., 2015] Mayr, M., Kloppel, T., Wall, W. A., and Gee, M. (2015). A temporal consistent monolithic approach to fluid-structure interaction enabling single field predictors. *SIAM Journal on Scientific Computing*, 37(1):B30–B59.
- [McCormick et al., 2013] McCormick, M., Nordsletten, D., Kay, D., and Smith, N. (2013). Simulating left ventricular fluid–solid mechanics through the cardiac cycle under lvad support. *Journal of Computational Physics*, 244:80–96.
- [McLachlan and Quispel, 2002] McLachlan, R. and Quispel, G. (2002). Splitting methods. *Acta Numerica*, 11:341–434.
- [Meyn, 1983] Meyn, K. (1983). Solution of underdetermined nonlinear equations by stationary iteration methods. *Numerische Mathematik*, 42(2):161–172.
- [Mildenberger et al., 2002] Mildenberger, P., Eichelberg, M., and Martin, E. (2002). Introduction to the DICOM standard. *European radiology*, 12(4):920–927.



- [Mitchell et al., 1992] Mitchell, G., Lamas, G., Vaughan, D., and Pfeffer, M. (1992). Left ventricular remodeling in the year after first anterior myocardial infarction: a quantitative analysis of contractile segment lengths and ventricular shape. *Journal of the American College of Cardiology*, 19(6):1136–1144.
- [Moghadam et al., 2011] Moghadam, M., Bazilevs, Y., Hsia, T., Vignon-Clementel, I., and Marsden, A. (2011). A comparison of outlet boundary treatments for prevention of backflow divergence with relevance to blood flow simulations. *Computational Mechanics*, 48(3):277–291.
- [Munteanu and Pavarino, 2009] Munteanu, M. and Pavarino, L. (2009). Decoupled Schwarz algorithms for implicit discretizations of nonlinear monodomain and bidomain systems. *Mathematical Models and Methods in Applied Sciences*, 19(07):1065–1097.
- [Murray et al., 2014] Murray, C., Ortblad, K., Guinovart, C., Lim, S., Wolock, T., Roberts, D., Dansereau, E., Graetz, N., Barber, R., and Brown, J. e. a. (2014). Global, regional, and national incidence and mortality for hiv, tuberculosis, and malaria during 1990–2013: a systematic analysis for the global burden of disease study 2013. *The Lancet*, 384(9947):1005–1070.
- [Mynard et al., 2012] Mynard, J., Davidson, M., Penny, D., and Smolich, J. (2012). A simple, versatile valve model for use in lumped parameter and one-dimensional cardiovascular models. *International Journal for Numerical Methods in Biomedical Engineering*, 28(6-7):626–641.
- [Nardinocchi and Teresi, 2007] Nardinocchi, P. and Teresi, L. (2007). On the active response of soft living tissues. *Journal of Elasticity*, 88(1):27–39.
- [Nash and Hunter, 2000] Nash, M. and Hunter, P. (2000). Computational mechanics of the heart. *Journal of Elasticity and the Physical Science of Solids*, 61(1-3):113–141.
- [Nickerson et al., 2005] Nickerson, D., Smith, N., and Hunter, P. (2005). New developments in a strongly coupled cardiac electromechanical model. *EP Europace*, 7(2):118–127.
- [Niederer et al., 2011] Niederer, S. et al. (2011). Verification of cardiac tissue electrophysiology simulators using an n-version benchmark. *Philosophical Transactions of the Royal Society A*, 369(1954):4331–4351.
- [Niederer and Smith, 2008] Niederer, S. and Smith, N. (2008). An improved numerical method for strong coupling of excitation and contraction models in the heart. *Progress in biophysics and molecular biology*, 96(1-3):90–111.
- [Nobile, 2001] Nobile, F. (2001). Numerical approximation of fluid–structure interaction problems with application to haemodynamics. PhD thesis, EPFL, Switzerland, 2001.

## Bibliography

---

- [Nobile et al., 2013] Nobile, F., Pozzoli, M., and Vergara, C. (2013). Time accurate partitioned algorithms for the solution of fluid–structure interaction problems in haemodynamics. *Computers & Fluids*, 86:470–482.
- [Nobile et al., 2012] Nobile, F., Quarteroni, A., and Ruiz-Baier, R. (2012). An active strain electromechanical model for cardiac tissue. *International Journal for Numerical Methods in Biomedical Engineering*, 28(1):52–71.
- [Noble, 1962] Noble, D. (1962). A modification of the hodgkin—huxley equations applicable to purkinje fibre action and pacemaker potentials. *The Journal of Physiology*, 160(2):317–352.
- [Nordsletten et al., 2011] Nordsletten, D., Niederer, S., Nash, M., Hunter, P., and Smith, N. (2011). Coupling multi–physics models to cardiac mechanics. *Progress in Biophysics and Molecular Biology*, 104(1):77–88.
- [Ogden, 1997] Ogden, R. W. (1997). *Non-linear elastic deformations*. Courier Corporation.
- [Opie, 2004] Opie, L. (2004). *Heart physiology: from cell to circulation*. Lippincott Williams & Wilkins.
- [Pagani, 2017] Pagani, S. (2017). *Reduced-order models for inverse problems and uncertainty quantification in cardiac electrophysiology*. PhD thesis, Politecnico di Milano.
- [Panfilov et al., 2005] Panfilov, A., Keldermann, R., and Nash, M. (2005). Self-organized pacemakers in a coupled reaction-diffusion-mechanics system. *Physical Review Letters*, 95(25):258104.
- [Patankar and Spalding, 1972] Patankar, S. and Spalding, D. (1972). A calculation procedure for heat, mass and momentum transfer in three-dimensional parabolic flows. *International Journal of Heat and Mass Transfer*, 15(10):1787–1806.
- [Patelli et al., 2017] Patelli, A., Dede, L., Lassila, T., Bartezzaghi, A., and Quarteroni, A. (2017). Isogeometric approximation of cardiac electrophysiology models on surfaces: An accuracy study with application to the human left atrium. *Computer Methods in Applied Mechanics and Engineering*, 317:248–273.
- [Pathmanathan et al., 2012] Pathmanathan, P., Bernabeu, M., Niederer, S., Gavaghan, D., and Kay, D. (2012). Computational modelling of cardiac electrophysiology: explanation of the variability of results from different numerical solvers. *International Journal for Numerical Methods in Biomedical Engineering*, 28(8):890–903.
- [Pathmanathan et al., 2010] Pathmanathan, P., Chapman, S., Gavaghan, D., and Whiteley, J. (2010). Cardiac electromechanics: the effect of contraction model on the mathematical problem and accuracy of the numerical scheme. *The Quarterly Journal of Mechanics and Applied Mathematics*, 27(11):1751–1770.

- 
- [Pavarino et al., 2015] Pavarino, L., Scacchi, S., and Zampini, S. (2015). Newton–Krylov–BDDC solvers for nonlinear cardiac mechanics. *Computer Methods in Applied Mechanics and Engineering*, 295:562–580.
- [Peters et al., 2007] Peters, J., Ecabert, O., Meyer, C., Schramm, H., Kneser, R., Groth, A., and Weese, J. (2007). Automatic whole heart segmentation in static magnetic resonance image volumes. *Medical Image Computing and Computer-Assisted Intervention–MICCAI*, (1):402–410.
- [Petersen et al., 2008] Petersen, K. B., Pedersen, M. S., et al. (2008). The matrix cookbook. *Technical University of Denmark*, 7(15):510.
- [Pezzuto, 2013] Pezzuto, S. (2013). Mechanics of the heart: constitutive issues and numerical experiments. PhD thesis, Politecnico di Milano, Italy, 2013.
- [Pezzuto and Ambrosi, 2014] Pezzuto, S. and Ambrosi, D. (2014). Active contraction of the cardiac ventricle and distortion of the microstructural architecture. *International Journal for Numerical Methods in biomedical Engineering*, 30(12):1578–1596.
- [Pezzuto et al., 2016] Pezzuto, S., Hake, J., and Sundnes, J. (2016). Space-discretization error analysis and stabilization schemes for conduction velocity in cardiac electrophysiology. *International journal for numerical methods in biomedical engineering*, 32(10).
- [Pfeffer and Braunwald, 1990] Pfeffer, M. and Braunwald, E. (1990). Ventricular remodeling after myocardial infarction. experimental observations and clinical implications. *Circulation*, 81(4):1161–1172.
- [Pinto and Boyden, 1999] Pinto, J. and Boyden, P. (1999). Electrical remodeling in ischemia and infarction. *Cardiovascular research*, 42(2):284–297.
- [Plotkowiak et al., 2008] Plotkowiak, M., Rodriguez, B., Plank, G., Schneider, J., Gavaghan, D., Kohl, P., and Grau, V. (2008). High performance computer simulations of cardiac electrical function based on high resolution MRI datasets. In *International Conference on Computational Science*, pages 571–580. Springer.
- [Potse et al., 2006] Potse, M., Dubé, B., Richer, J., Vinet, A., and Gulrajani, R. (2006). A comparison of monodomain and bidomain reaction-diffusion models for action potential propagation in the human heart. *IEEE Transactions on Biomedical Engineering*, 53(12):2425–2435.
- [Potse et al., 2014] Potse, M., Krause, D., Kroon, W., Murzilli, R., Muzzarelli, S., Regoli, F., Caiani, E., Prinzen, F., Krause, R., and Auricchio, A. (2014). Patient-specific modelling of cardiac electrophysiology in heart-failure patients. *Europace*, 16(suppl\_4):iv56–iv61.

## Bibliography

---

- [Provost et al., 2011] Provost, J., Lee, W., Fujikura, K., and Konofagou, E. (2011). Imaging the electromechanical activity of the heart in vivo. *Proceedings of the National Academy of Sciences*, 108(21):8565–8570.
- [Quaini, 2009] Quaini, A. (2009). Algorithms for fluid-structure interaction problems arising in hemodynamics. PhD thesis, EPFL, Switzerland.
- [Quarteroni, 2010] Quarteroni, A. (2010). *Numerical models for differential problems*, volume 2. Springer Science & Business Media.
- [Quarteroni et al., 2017a] Quarteroni, A., Lassila, T., Rossi, S., and Ruiz-Baier, R. (2017a). Integrated heart - coupling multiscale and multiphysics models for the simulation of the cardiac function. *Computer Methods in Applied Mechanics and Engineering*, 314:345–407.
- [Quarteroni et al., 2017b] Quarteroni, A., Manzoni, A., and Vergara, C. (2017b). The cardiovascular system: Mathematical modelling, numerical algorithms and clinical applications. *Acta Numerica*, 26:365–590.
- [Quarteroni et al., 2010] Quarteroni, A., Sacco, R., and Saleri, F. (2010). *Numerical mathematics*, volume 37. Springer Science & Business Media.
- [Quarteroni and Valli, 1994] Quarteroni, A. and Valli, A. (1994). *Numerical approximation of partial differential equations*. Springer.
- [Quarteroni and Valli, 1996] Quarteroni, A. and Valli, A. (1996). Domain decomposition methods for partial differential equations.
- [Quinn and Kohl, 2013] Quinn, T. and Kohl, P. (2013). Combining wet and dry research: experience with model development for cardiac mechano-electric structure-function studies. *Cardiovascular research*, 97(4):601–611.
- [Reese et al., 1995] Reese, T., Weisskoff, R., Smith, R., Rosen, B., Dinsmore, R., and Wedeen, V. (1995). Imaging myocardial fiber architecture in vivo with magnetic resonance. *Magnetic Resonance in Medicine*, 34(6):786–791.
- [Regazzoni et al., 2017] Regazzoni, F., Dede, L., and Quarteroni, A. (2017). Active contraction of cardiac cells: a model for sarcomere dynamics with cooperative interactions. *Submitted to Biomechanics and Modeling in Mechanobiology*.
- [Rocha et al., 2009] Rocha, B., Lino, B., dos Santos, R., Toledo, E., Barra, L., and Sundnes, J. (2009). A two dimensional model of coupled electromechanics in cardiac tissue. In *World Congress on Medical Physics and Biomedical Engineering, September 7-12, 2009, Munich, Germany*, pages 2081–2084. Springer.
- [Rossi, 2014] Rossi, S. (2014). *Anisotropic modeling of cardiac mechanical activation*. PhD thesis, EPFL.

- [Rossi et al., 2014] Rossi, S., Lassila, T., Ruiz-Baier, R., Sequeira, A., and Quarteroni, A. (2014). Thermodynamically consistent orthotropic activation model capturing ventricular systolic wall thickening in cardiac electromechanics. *European Journal of Mechanics-A/Solids*, 48:129–142.
- [Rossi et al., 2012] Rossi, S., Ruiz-Baier, R., Pavarino, L., and Quarteroni, A. (2012). Orthotropic active strain models for the numerical simulation of cardiac biomechanics. *International Journal for Numerical Methods in Biomedical Engineering*, 28(6-7):761–788.
- [Roth, 1997] Roth, B. (1997). Electrical conductivity values used with the bidomain model of cardiac tissue. *IEEE Transactions on Biomedical Engineering*, 44(4):326–328.
- [Rozanski et al., 1998] Rozanski, G., Xu, Z., Zhang, K., and Patel, K. (1998). Altered  $k^+$  current of ventricular myocytes in rats with chronic myocardial infarction. *American Journal of Physiology-Heart and Circulatory Physiology*, 274(1):H259–H265.
- [Rudy, 2008] Rudy, Y. (2008). Molecular basis of cardiac action potential repolarization. *Annals of the New York Academy of Sciences*, 1123(1):113–118.
- [Ruiz-Baier et al., 2014] Ruiz-Baier, R., Gizzi, A., Rossi, S., Cherubini, C., Laadhari, A., Filippi, S., and Quarteroni, A. (2014). Mathematical modelling of active contraction in isolated cardiomyocytes. *Mathematical Medicine and Biology*, 31(3):259–283.
- [Saad, 2003] Saad, Y. (2003). *Iterative methods for sparse linear systems*. SIAM.
- [Sabbah et al., 1986] Sabbah, H., Khaja, F., Brymer, J., McFarland, T., Albert, D., Snyder, J., Goldstein, S., and Stein, P. (1986). Noninvasive evaluation of left ventricular performance based on peak aortic blood acceleration measured with a continuous-wave Doppler velocity meter. *Circulation*, 74(2):323–329.
- [Sainte-Marie et al., 2006] Sainte-Marie, J., Chapelle, D., Cimrman, R., and Sorine, M. (2006). Modeling and estimation of the cardiac electromechanical activity. *Computers & Structures*, 84(28):1743–1759.
- [Sala and Heroux, 2005] Sala, M. and Heroux, M. (2005). Robust algebraic preconditioners with IFPACK 3.0. Technical report, Technical Report SAND-0662, Sandia National Laboratories.
- [Sankaran and Marsden, 2011] Sankaran, S. and Marsden, A. (2011). A stochastic collocation method for uncertainty quantification and propagation in cardiovascular simulations. *Journal of biomechanical engineering*, 133(3):031001.
- [Sansour, 2008] Sansour, C. (2008). On the physical assumptions underlying the volumetric-isochoric split and the case of anisotropy. *European Journal of Mechanics-A/Solids*, 27(1):28–39.

## Bibliography

---

- [Schmid et al., 2006] Schmid, H., Nash, M., Young, A., and Hunter, P. (2006). Myocardial material parameter estimation—a comparative study for simple shear. *Journal of Biomechanical Engineering*, 128(5):742–750.
- [Schroeder et al., 2004] Schroeder, W., Lorensen, B., and Martin, K. (2004). *The visualization toolkit: an object-oriented approach to 3D graphics*. Kitware.
- [Scollan et al., 1998] Scollan, D., Holmes, A., Winslow, R., and Forder, J. (1998). Histological validation of myocardial microstructure obtained from diffusion tensor magnetic resonance imaging. *American Journal of Physiology-Heart and Circulatory Physiology*, 275(6):H2308–H2318.
- [Shaw and Rudy, 1997] Shaw, R. and Rudy, Y. (1997). Electrophysiologic effects of acute myocardial ischemia: a theoretical study of altered cell excitability and action potential duration. *Cardiovascular research*, 35(2):256–272.
- [Shimkunas et al., 2013] Shimkunas, R., Zhang, Z., Wenk, J., Soleimani, M., Khazalpour, M., Acevedo-Bolton, G., Wang, G., Saloner, D., Mishra, R., and Wallace, A. (2013). Left ventricular myocardial contractility is depressed in the borderzone after posterolateral myocardial infarction. *The Annals of thoracic surgery*, 95(5):1619–1625.
- [Simo and Taylor, 1991] Simo, J. and Taylor, R. (1991). Quasi-incompressible finite elasticity in principal stretches. continuum basis and numerical algorithms. *Computer Methods in Applied Mechanics and Engineering*, 85(3):273–310.
- [Smith et al., 2011] Smith, N., de Vecchi, A., McCormick, M., Nordsletten, D., Camara, O., Frangi, A., Delingette, H., Sermesant, M., Relan, J., and Ayache, N. (2011). euHeart: personalized and integrated cardiac care using patient-specific cardiovascular modelling. *Interface focus*.
- [Smith et al., 2004] Smith, N., Nickerson, D., Crampin, E., and Hunter, P. (2004). Multiscale computational modelling of the heart. *Acta Numerica*, 13:371–431.
- [Spiteri and Dean, 2008] Spiteri, R. and Dean, R. (2008). On the performance of an Implicit–Explicit Runge–Kutta method in models of cardiac electrical activity. *IEEE Transactions on Biomedical Engineering*, 55(5):1488–1495.
- [Spodick, 1996] Spodick, D. (1996). *The pericardium: a comprehensive textbook*, volume 27. Informa Health Care.
- [Stålhand et al., 2011] Stålhand, J., Klarbring, A., and Holzapfel, G. (2011). A mechanochemical 3d continuum model for smooth muscle contraction under finite strains. *Journal of Theoretical Biology*, 268(1):120–130.
- [Streeter et al., 1970] Streeter, D., Vaishnav, R., Patel, D., Spotnitz, H., Ross, J., and Sonnenblick, E. (1970). Stress distribution in the canine left ventricle during diastole and systole. *Biophysical Journal*, 10(4):345–363.

- [Sugiura et al., 2012] Sugiura, S., Washio, T., Hatano, A., Okada, J., Watanabe, H., and Hisada, T. (2012). Multi-scale simulations of cardiac electrophysiology and mechanics using the university of tokyo heart simulator. *Progress in Biophysics and Molecular Biology*, 110(2):380–389.
- [Taber and Perucchio, 2000] Taber, L. and Perucchio, R. (2000). Modeling heart development. *Journal of Elasticity and the Physical Science of Solids*, 61(1-3):165–197.
- [Tagliabue et al., 2017] Tagliabue, A., Dede', L., and Quarteroni, A. (2017). Fluid dynamics of an idealized left ventricle: the extended nitsche's method for the treatment of heart valves as mixed time varying boundary conditions. *International Journal for Numerical Methods in Fluids*.
- [Takizawa et al., 2012] Takizawa, K., Bazilevs, Y., and Tezduyar, T. (2012). Space-time and ale-vms techniques for patient-specific cardiovascular fluid-structure interaction modeling. *Archives of Computational Methods in Engineering*, 19(2):171–225.
- [Takizawa et al., 2010] Takizawa, K., Christopher, J., Tezduyar, T., and Sathe, S. (2010). Space-time finite element computation of arterial fluid-structure interactions with patient-specific data. *International Journal for Numerical Methods in Biomedical Engineering*, 26(1):101–116.
- [ten Tusscher et al., 2004] ten Tusscher, K., Noble, D., Noble, P., and Panfilov, A. (2004). A model for human ventricular tissue. *American Journal of Physiology-Heart and Circulatory Physiology*, 286(4):H1573–H1589.
- [Tezduyar et al., 2008] Tezduyar, T., Sathe, S., Schwaab, M., and Conklin, B. (2008). Arterial fluid mechanics modeling with the stabilized space-time fluid-structure interaction technique. *International Journal for Numerical Methods in Fluids*, 57(5):601–629.
- [Tezduyar et al., 2006] Tezduyar, T., Sathe, S., and Stein, K. (2006). Solution techniques for the fully discretized equations in computation of fluid-structure interactions with the space-time formulations. *Computer Methods in Applied Mechanics and Engineering*, 195(41):5743–5753.
- [Thompson et al., 1998] Thompson, J., Soni, B., and Weatherill, N. (1998). *Handbook of grid generation*. CRC press.
- [Trayanova, 2011] Trayanova, N. (2011). Whole-heart modeling applications to cardiac electrophysiology and electromechanics. *Circulation Research*, 108(1):113–128.
- [Trayanova et al., 2010] Trayanova, N., Constantino, J., and Gurev, V. (2010). Models of stretch-activated ventricular arrhythmias. *Journal of Electrocardiology*, 43(6):479–485.
- [Trentin et al., 2015] Trentin, C., Faggiano, E., Conti, M., and Auricchio, F. (2015). An automatic tool for thoracic aorta segmentation and 3d geometric analysis. In *International Symposium on Image and Signal Processing and Analysis (ISPA)*, pages 60–65.

## Bibliography

---

- [Tricerri et al., 2015] Tricerri, P., Dedè, L., Deparis, S., Quarteroni, A., Robertson, A., and Sequeira, A. (2015). Fluid-structure interaction simulations of cerebral arteries modeled by isotropic and anisotropic constitutive laws. *Computational Mechanics*, 55(3):479–498.
- [Usyk et al., 2002] Usyk, T., LeGrice, I., and McCulloch, A. (2002). Computational model of three-dimensional cardiac electromechanics. *Computing and Visualization in Science*, 4(4):249–257.
- [Usyk and McCulloch, 2003] Usyk, T. and McCulloch, A. (2003). Electromechanical model of cardiac resynchronization in the dilated failing heart with left bundle branch block. *Journal of Electrocardiology*, 36:57–61.
- [Van Brummelen, 2009] Van Brummelen, E. (2009). Added mass effects of compressible and incompressible flows in fluid-structure interaction. *Journal of Applied mechanics*, 76(2):021206.
- [Vassallo et al., 1986] Vassallo, J., Cassidy, D., Miller, J., Buxton, A., Marchlinski, F., and Josephson, M. (1986). Left ventricular endocardial activation during right ventricular pacing: effect of underlying heart disease. *Journal of the American College of Cardiology*, 7(6):1228–1233.
- [Vergara et al., 2014] Vergara, C., Palamara, S., Catanzariti, D., Nobile, F., Faggiano, E., Pangrazzi, C., Centonze, M., Maines, M., Quarteroni, A., and Vergara, G. (2014). Patient-specific generation of the purkinje network driven by clinical measurements of a normal propagation. *Medical and Biological Engineering and Computing*, 52(10):813.
- [Vezhnevets and Konouchine, 2005] Vezhnevets, V. and Konouchine, V. (2005). Grow-Cut: Interactive multi-label nd image segmentation by cellular automata. In *GraphiCon proceedings*, volume 1, pages 150–156. Citeseer.
- [Wallace et al., 1963] Wallace, A., Skinner J.R., N., and Mitchell, J. (1963). Hemodynamic determinants of the maximal rate of rise of left ventricular pressure. *American Journal of Physiology-Legacy Content*, 205(1):30–36.
- [Wang et al., 2013] Wang, H., Gao, H., Luo, X., Berry, C., Griffith, B., Ogden, R., and Wang, T. (2013). Structure-based finite strain modelling of the human left ventricle in diastole. *International journal for numerical methods in biomedical engineering*, 29(1):83–103.
- [Westerhof et al., 2009] Westerhof, N., Lankhaar, J., and Westerhof, B. (2009). The arterial Windkessel. *Medical & Biological Engineering & Computing*, 47(2):131–141.
- [White et al., 1987] White, H., Norris, R., Brown, M., Brandt, P., Whitlock, R., and Wild, C. (1987). Left ventricular end-systolic volume as the major determinant of survival after recovery from myocardial infarction. *Circulation*, 76(1):44–51.



- 
- [Whiteley, 2006] Whiteley, J. (2006). An efficient numerical technique for the solution of the monodomain and bidomain equations. *Biomedical Engineering, IEEE Transactions on*, 53(11):2139–2147.
- [Wink and Roerdink, 2004] Wink, A. and Roerdink, J. (2004). Denoising functional mr images: a comparison of wavelet denoising and gaussian smoothing. *IEEE transactions on medical imaging*, 23(3):374–387.
- [Wong and Rautaharju, 1968] Wong, A. and Rautaharju, P. (1968). Stress distribution within the left ventricular wall approximated as a thick ellipsoidal shell. *American heart journal*, 75(5):649–662.
- [Wong and Kuhl, 2014] Wong, J. and Kuhl, E. (2014). Generating fibre orientation maps in human heart models using poisson interpolation. *Computer Methods in Biomechanics and Biomedical Engineering*, 17(11):1217–1226.
- [Xu et al., 2007] Xu, Y., Zhang, H., Li, H., and Hu, G. (2007). An improved algorithm for vessel centerline tracking in coronary angiograms. *Computer methods and programs in biomedicine*, 88(2):131–143.
- [Yin et al., 1996] Yin, F., Chan, C., and Judd, R. (1996). Compressibility of perfused passive myocardium. *American Journal of Physiology-Heart and Circulatory Physiology*, 271(5):H1864–H1870.
- [Yin et al., 1987] Yin, F., Strumpf, R., Chew, P., and Zeger, S. (1987). Quantification of the mechanical properties of noncontracting canine myocardium under simultaneous biaxial loading. *Journal of Biomechanics*, 20(6):577–589.
- [Zhang et al., 2006] Zhang, H., Maslov, K., Stoica, G., and Wang, L. (2006). Functional photoacoustic microscopy for high-resolution and noninvasive in vivo imaging. *Nature biotechnology*, 24(7):848.
- [Zheng et al., 2007] Zheng, Y., Barbu, A., Georgescu, B., Scheuering, M., and Comaniciu, D. (2007). Fast automatic heart chamber segmentation from 3D CT data using marginal space learning and steerable features. In *International Conference on Computer Vision (ICCV)*, pages 1–8. IEEE.
- [Zhuang et al., 2010] Zhuang, X., Rhode, K., Razavi, R., Hawkes, D., and Ourselin, S. (2010). A registration-based propagation framework for automatic whole heart segmentation of cardiac MRI. *IEEE Transactions on Medical Imaging*, 29(9):1612–1625.
- [Zienkiewicz and Zhu, 1992] Zienkiewicz, O. and Zhu, J. (1992). The superconvergent patch recovery and a posteriori error estimates. Part 1: the recovery technique. *International Journal for Numerical Methods in Engineering*, 33(7):1331–1364.



# Antonello Gerbi

## Curriculum Vitae

Avenue d'Echallens 61  
Lausanne, Switzerland 1004  
☎ (+41) 78 893 2163  
✉ antonello.gerbi@gmail.com  
January 30th, 1988

### Education

- Nov 2014– **Ph.D. student in Mathematics**,  
Present *Ecole Polytechnique Fédérale de Lausanne, Switzerland*,  
Laboratory: Chair of Modeling and Scientific Computing,  
Thesis title: Numerical approximation of cardiac electro-fluid-mechanical models:  
coupling strategies for large-scale simulation.  
Advisor: Prof. Alfio Quarteroni. Co-advisor: Prof. Luca Dede'
- Feb 2012– **Erasmus programme student**,  
Jul 2012 *Universidade do Porto, Portugal*.
- Sep 2010– **Master Degree in Mathematical Engineering (Computational Sciences)**,  
Oct 2014 *Politecnico di Milano, Italy*,  
Grade: 110/110 cum laude,  
Thesis title: On the Cahn-Hilliard-Oono equation with dynamic boundary conditions.  
Advisor: Prof. Maurizio Grasselli
- Sep 2007– **Bachelor Degree in Mathematical Engineering**,  
Sep 2010 *Politecnico di Milano, Italy*.

### Research activity

#### Publications

- M. Landajuela, C. Vergara, **A. Gerbi**, L. Dede', L. Formaggia, A. Quarteroni, *Numerical approximation of the electromechanical coupling in the left ventricle with inclusion of the Purkinje network*. Accepted for publication in International Journal for Numerical Methods in Biomedical Engineering (DOI: 10.1002/cnm.2984).
- A. Gerbi**, L. Dede', A. Quarteroni, *A monolithic algorithm for the simulation of cardiac electromechanics in the human left ventricle*. Accepted for publication in Mathematics in Engineering. (DOI: 10.3934/Mine.2018.1.1).
- A. Gerbi**, L. Dede', A. Quarteroni, *Segregated algorithms for the numerical simulation of cardiac electromechanics in the left human ventricle*, Submitted to Journal of Scientific Computing.

#### Contributed talks

- A. Gerbi**, L. Dede', D. Forti, A. Quarteroni, *Coupled mathematical and numerical models for integrated simulations of the left ventricle*, PASC 2016, Lausanne, Switzerland, June 8-10, 2016.

**A. Gerbi**, L. Dede', D. Forti, A. Quarteroni, *Mathematical and numerical models for integrated heart simulations*, SIMAI 2016, Milano, Italy, September 13-16, 2016.

**A. Gerbi**, L. Dede', A. Quarteroni, *Numerical modeling of the integrated electro-mechano-fluid problem for the left ventricle*, CMBE 2017, Pittsburgh, USA, April 10-12, 2017.

**A. Gerbi**, L. Dede', A. Quarteroni, *An integrated electro-mechano-fluid model for cardiac simulations*, PASC 2017, Lugano, Switzerland, June 26-28, 2017.

**A. Gerbi**, L. Dede', S. Deparis, A. Quarteroni, *The LifeV Finite Elements library: recent developments and cardiovascular applications*, ENUMATH 2017, Voss, Norway, September 25-29, 2017.

#### Journal reviewer

CAIM - Communications in Applied and Industrial Mathematics.

## Teaching

### Courses assistantship

- *Introduction to the Finite Element Method*, Prof. A. Quarteroni, fall semesters 2015 and 2016.
- *Analyse numérique*, Prof. A. Quarteroni, spring semesters 2015, 2016 and 2017.
- *Mathématiques II*, Prof. Michel Cibils, spring semester 2018.

### Supervised projects and theses

- *Optimal control of the Cahn-Hilliard equation*, Stefano Guarino, spring 2015 semester project.
- *A numerical study of the blood flow through the aortic valve: comparison of Newtonian and non-Newtonian models*, Nicholas Alan Molyneaux, fall 2015 semester project.
- *Numerical modeling of the electric field in neurons*, Julie Favre, spring 2016 semester project (in collaboration with the Blue Brain Project).
- *Electromechanical modelling of the human heart in bi-ventricle geometries*, Luca Azzolin, spring 2018 master thesis in Mathematical Engineering (Politecnico di Milano) - Thesis co-advisor.

## Languages

|            |                      |  |
|------------|----------------------|--|
| Italian    | <b>Mother tongue</b> |  |
| English    | <b>Excellent</b>     | <i>FCE and TOEIC certificates (C1)</i> |
| French     | <b>Intermediate</b>  |  |
| Portuguese | <b>Intermediate</b>  | <i>CIPLE certificate (A2)</i>          |

